

WL-TR-94-4109

PROCESS CONTROL OF MICROSTRUCTURE
IN MANUFACTURING

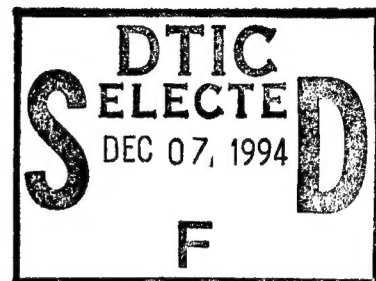


RAMANA V GRANDHI

WRIGHT STATE UNIVERSITY
DAYTON OH 45435-0001

JUNE 1994

FINAL REPORT FOR 09/01/90-12/01/93



APPROVED FOR PUBLIC RELEASE; DISTRIBUTION IS UNLIMITED.

MATERIALS DIRECTORATE
WRIGHT LABORATORY
AIR FORCE MATERIEL COMMAND
WRIGHT PATTERSON AFB OH 45433-7734

19941201 051

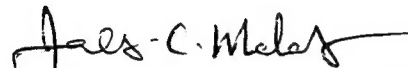
DTIC 07/94 1201 051
19941201 051

NOTICE

WHEN GOVERNMENT DRAWINGS, SPECIFICATIONS, OR OTHER DATA ARE USED FOR ANY PURPOSE OTHER THAN IN CONNECTION WITH A DEFINITELY GOVERNMENT-RELATED PROCUREMENT, THE UNITED STATES GOVERNMENT INCURS NO RESPONSIBILITY OR ANY OBLIGATION WHATSOEVER. THE FACT THAT THE GOVERNMENT MAY HAVE FORMULATED OR IN ANY WAY SUPPLIED THE SAID DRAWINGS, SPECIFICATIONS, OR OTHER DATA, IS NOT TO BE REGARDED BY IMPLICATION OR OTHERWISE IN ANY MANNER CONSTRUED, AS LICENSING THE HOLDER OR ANY OTHER PERSON OR CORPORATION, OR AS CONVEYING ANY RIGHTS OR PERMISSION TO MANUFACTURE, USE, OR SELL ANY PATENTED INVENTION THAT MAY IN ANY WAY BE RELATED THERETO.

THIS REPORT IS RELEASEABLE TO THE NATIONAL TECHNICAL INFORMATION SERVICE (NTIS). AT NTIS IS WILL BE AVAILABLE TO THE GENERAL PUBLIC, INCLUDING FOREIGN NATIONS.

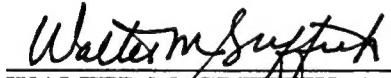
THIS TECHNICAL REPORT HAS BEEN REVIEWED AND IS APPROVED FOR PUBLICATION.



JAMES C. MALAS
Project Monitor, Material Process Design
Integration and Operations Division
Materials Directorate



ALLAN W. GUNDERSON
Materials Behavior Branch
Metals and Ceramics Division
Materials Directorate



WALTER M. GRIFFITH, Asst Chief
Metals and Ceramics Division
Materials Directorate

IF YOUR ADDRESS HAS CHANGED, IF YOU WISH TO BE REMOVED FROM OUR MAILING LIST, OR IF THE ADDRESSEE IS NO LONGER EMPLOYED BY YOUR ORGANIZATION, PLEASE NOTIFY, WL/MLLN, WRIGHT-PATTERSON AFB OH 45433-7817 TO HELP US MAINTAIN A CURRENT MAILING LIST.

COPIES OF THIS REPORT SHOULD NOT BE RETURNED UNLESS RETURN IS REQUIRED BY SECURITY CONSIDERATIONS, CONTRACTUAL OBLIGATIONS, OR NOTICE ON A SPECIFIC DOCUMENT.

REPORT DOCUMENTATION PAGE

Form Approved
OMB No. 0704-0188

Public reporting burden for this collection of information is estimated to average 1 hour per response, including the time for reviewing instructions, searching existing data sources, gathering and maintaining the data needed, and completing and reviewing the collection of information. Send comments regarding this burden estimate or any other aspect of this collection of information, including suggestions for reducing this burden, to Washington Headquarters Services, Directorate for Information Operations and Reports, 1215 Jefferson Davis Highway, Suite 1204, Arlington, VA 22202-4302, and to the Office of Management and Budget, Paperwork Reduction Project (0704-0188), Washington, DC 20503.

1. AGENCY USE ONLY (Leave blank)	2. REPORT DATE	3. REPORT TYPE AND DATES COVERED
	June 1994	Final Report 14 Sep 90-31 Dec 93
4. TITLE AND SUBTITLE		5. FUNDING NUMBERS
Process Control of Microstructure in Manufacturing		C F33615-90-C-5950 PE 61102F, 62102F PR 2306 TA P7 WU 12
6. AUTHOR(S)		
Ramana V. Grandhi		
7. PERFORMING ORGANIZATION NAME(S) AND ADDRESS(ES)		8. PERFORMING ORGANIZATION REPORT NUMBER
Wright State University Dayton, OH 45435-0001		N/A
9. SPONSORING / MONITORING AGENCY NAME(S) AND ADDRESS(ES)		10. SPONSORING / MONITORING AGENCY REPORT NUMBER
Materials Directorate Wright Laboratory Air Force Materiel Command Wright Patterson AFB OH 45433-7734		WL-TR-94-4109
11. SUPPLEMENTARY NOTES		
12a. DISTRIBUTION / AVAILABILITY STATEMENT		12b. DISTRIBUTION CODE
Approved for public release; distribution is unlimited.		
13. ABSTRACT (Maximum 200 words)		
<p>This report presents a systematic methodology for the design of optimal process parameters for forging processes. The procedure for construction of a state space model utilizing nonlinear rigid-viscoplastic finite element formulation is developed. A coupled state space model is built to represent the deformation and thermal behavior of the material, with nodal velocities and nodal temperatures as the state variables, and die velocity as input to the system. The output variables of the state space system are the effective strain rate and critical nodal temperature. The linear quadratic regulator (LQR) theory with finite time control is used in designing the ram velocity and initial die temperature. Model reduction schemes are adopted in generating reduced order analytical models from the full size state space representation. The methodology developed is demonstrated on axisymmetric and plane strain forging cases. The performance of the procedure is evaluated using measures such as temperature and strain rate variation within the billet, load requirement, and total process time.</p>		
14. SUBJECT TERMS		15. NUMBER OF PAGES 250
Process Control, Metal Forming , Forging Process, Modern Control Theory, Finite Elements		16. PRICE CODE
17. SECURITY CLASSIFICATION OF REPORT	18. SECURITY CLASSIFICATION OF THIS PAGE	19. SECURITY CLASSIFICATION OF ABSTRACT
UNCLASSIFIED	UNCLASSIFIED	UNCLASSIFIED
20. LIMITATION OF ABSTRACT		UL

FOREWORD

This technical report presents the work performed under Contract No. F33615-90-C-5950 for the Wright Patterson Air Force Base, Ohio. The report is published for imparting technical information only and does not necessarily represent the recommendations, conclusions, or approval of the Air Force. The project was managed by Dr. James C. Malas of Wright Laboratory, Wright Patterson Air Force Base, Ohio. Wright State University (WSU) was the prime contractor for the project, with UES, Inc. as subcontractor, and Dr. Dennis Irwin, as consultant.

The principal investigator, Dr. Ramana V. Grandhi, would like to thank Dr. James C. Malas for his constant advice and direction during the contract period. The technical assistance of Dr. Anil Chaudhary, and Prof. Dennis Irwin, during the course of this work, is greatly appreciated. The discussions with Dr. Lee Semiatin and Mr. James T. Morgan of Wright Laboratory, Dr. Harold Gegel and Dr. Venkat Seetharaman of UES, Inc., and Prof. Raghavan Srinivasan of WSU were very valuable to the project.

Dr. Grandhi was assisted by the following team of graduate assistants at WSU in developing and conducting the research work:

Mr. Anand Kumar (currently with Italimpianti of America, Inc., Pittsburg, PA)

Mr. H. Cheng (currently with Systems Research Laboratories, Dayton, OH)

Mr. Ramesh Thiagarajan (currently with Bell Helicopter, Dallas, TX)

Mr. Shyam Sanjeev Kumar

Mr. Ed Wright

Mr. Tom Johnson

Accession For	
NTIS	CRA&I <input checked="" type="checkbox"/>
DTIC	TAB <input type="checkbox"/>
Unannounced <input type="checkbox"/>	
Justification _____	
By _____	
Distribution / _____	
Availability Codes	
Dist	Avail and/or Special
A-1	

SUMMARY

This research work developed a systematic methodology for the design of optimal process parameters for forging processes. The methodology uses a multi-disciplinary approach involving advanced modeling methods, finite element techniques, nonlinear mechanics and modern control theory, for maintaining the forging system variables within 'favorable' processing windows. Appendix A gives an overview of the project goals and tasks, and also describes in brief the tasks accomplished in this work and their organization in this report. Chapter 1 introduces the objectives and goals of this research work, and the design/analysis methods used to achieve these goals. It also includes a section surveying the earlier work done in this area. Chapter 2 gives a brief description of the nonlinear rigid viscoplastic finite element method, and presents the mathematical derivation of the deformation state space model from the finite element equations. In addition, this chapter also describes the finite element based condensation procedure used to reduce the number of degrees of freedom of the deformation state space model. The procedure for development of the thermal state space model from the finite element governing equations is described in Chapter 3 of the report. This chapter also presents the procedure for condensation of the thermal state space model to reduce the order of the state space system. Chapter 4 describes the development of the coupled thermomechanical state space model, and the construction of the control output matrix. Chapter 5 explains the design strategy used for optimizing the process parameters based on the linear quadratic regulator (LQR) theory. This chapter gives a detailed description of the procedure used in solving the state space equations, and also presents the methodology used in designing the initial die temperature. The logic used in selecting weighting matrices for the LQR control scheme is also described in Chapter 5. The methodology developed was tested and validated using a variety of forging simulations under different operating conditions. These test cases and

numerical examples are presented in Chapter 6 of this report. While dealing with large scale finite element models involving a large number of degrees of freedom, generally, numerical difficulties are encountered during the implementation process. To avoid such situations and to reduce the time and effort during computation, reduced order models need to be used. Chapter 7 describes in detail the model reduction methods studied and utilized during the course of this work. This chapter also presents the comparative evaluation of several order reduction methods and the basis for selection of the Balanced Model Reduction (BMR) as suitable for use in this work. The control law and weighting matrix selection had to be modified for use with the reduced order models. The procedure for doing this, and a few case studies to validate the conclusions drawn are also presented in Chapter 7. Chapter 8 presents more complicated and large-scale simulation examples to demonstrate the effectiveness of the model reduction methodology developed. After the control-based methodology was developed, approximations were made and introduced into the program to reduce the computational time involved in the process. Chapter 9 presents the results of these studies and describes the effect of using one state space model for the entire simulation, and the effect of using smoothed (approximate) die velocity schedules during the simulation.

To summarize the entire procedure, the nonlinear rigid viscoplastic finite element method is used for deformation and thermal analyses. A coupled state space model is then built to represent the deformation and thermal behavior of the material, with nodal velocities and nodal temperatures as the state variables. A finite element based condensation technique is used for reducing the order of the system to facilitate numerical analysis. Sophisticated model reduction techniques are used to further reduce the order of the state space system. The desired (favorable) forging conditions are obtained by imposing constraints on effective strain-rate and temperature variation within the deforming material. The linear quadratic regulator (LQR) theory with finite time control is used in designing the ram velocity and initial die temperature.

TABLE OF CONTENTS

Foreword	i
Summary	ii
Table of Contents	iv
List of Figures	vii
List of Tables	x
1 Introduction	1
1.1 Need for process control in metal forming	1
1.2 Process parameters and physical/microstructural properties	3
1.3 Metal forming simulation using the finite element method (FEM)	6
1.4 Design of optimal process parameters	10
1.5 Reduced order models	14
2 State Space Model for Deformation Analysis	17
2.1 Basis for the finite element formulation	17
2.2 Finite element equations	20
2.3 Frictional force as the finite element load vector	25
2.4 Condensation of the system during deformation analysis	28
2.5 State space model for deformation analysis	34
3 State Space Model for Thermal Analysis	36
3.1 Finite element equations for heat transfer	36
3.2 State space model for thermal analysis	42
3.3 Condensation of the thermal state space model	45
4 Coupled Thermo-mechanical State Space Model	49
4.1 Construction of the control output matrix	49

4.2 Coupled state space system	51
5 Process Parameter Design Using Optimal Control Theory	54
5.1 Design strategy	54
5.2 Initial die temperature design	63
5.3 LQR design scheme	65
5.4 Selection of weighting matrices for control	70
6 Numerical Examples - Full Size State Space Model	71
6.1 Model validation	72
6.2 Temperature gradient reduction	83
6.3 Isothermal design	88
6.4 Temperature range reduction	91
6.5 Initial die temperature design	98
7 Reduced Order State Space Models	106
7.1 Introduction to model reduction	106
7.2 Aggregation method	110
7.3 Modal analysis method	113
7.3.1 Davison's method	115
7.3.2 Marshall's method	116
7.3.3 Nicholson's method	117
7.4 Balanced model reduction (BMR) method	119
7.4.1 Construction of the balanced model	119
7.4.2 Construction of the transformation matrix	120
7.4.3 Construction of the reduced model	122
7.5 Control law for reduced order models	122
7.6 Performance evaluation and selection of reduced order models	130
7.6.1 H-block compression - Frictionless case	130

7.6.2 H-block compression - Friction case	142
7.7 Analysis of results	151
8 Numerical Examples - Reduced Order Models	154
8.1 Isothermal design - IBR disk forging	155
8.2 Non-isothermal design - Engine disk forging	166
9 Practical Aspects in Process Control Design	173
9.1 Smoothened die velocity profiles	173
9.2 Stability and validity of the state space models	174
9.3 Eigenmode analysis for process characterization	185
10 Summary and Conclusions	204
11 References	207
Appendix A - Project Overview	220
Appendix B - User's Manual for COPP	223
Appendix C - User's Manual for Reduced Order Models	235

LIST OF FIGURES

Fig 1. Secant and tangent stiffness	24
Fig 2. Contact boundary conditions	27
Fig 3. System condensation	30
Fig 4. FEM discretization of the die body	37
Fig 5. Thermal boundary conditions	39
Fig 6. Design scheme flow chart	62
Fig 7. Engine disk forging - FEM simulation	73
Fig 8. FEM discretization of the billet	74
Fig 9. Validation of the state space model	76
Fig 10. Temperature gradient reduction - Strain rates	85
Fig 11. Temperature gradient reduction - Die velocities	86
Fig 12. Temperature gradient reduction - Temperature profiles	87
Fig 13. Isothermal design - Strain rates	89
Fig 14. Isothermal design - Die velocities	90
Fig 15. Temperature variance reduction - Strain rates	93
Fig 16. Temperature variance reduction - Die velocities	94
Fig 17. Temperature variance reduction - Node 18 temperature profiles	96
Fig 18. Temperature variance reduction - Load stroke curves	97
Fig 19. Initial die temperature adjustment	102
Fig 20. Initial die temperature design - Strain rates	103
Fig 21. Initial die temperature design - Die velocities	104
Fig 22. Initial die temp. design - Node 18 temp. profiles	105
Fig 23. Process parameter design using reduced order models	109
Fig 24. FEM discretization - Frictionless case	131

Fig 25. Comparison of velocities using reduced models and full model	134
Fig 26. Comparison of desired and controlled strain rates	136
Fig 27. FEM discretization - Friction case	144
Fig 28. Comparison of velocities using reduced models and full model	145
Fig 29. Comparison of desired and controlled strain rates	152
Fig 30. Simulation of IBR disk forging	156
Fig 31. Finite element model of Integrated Blade and Rotor disk	157
Fig 32. Die velocity profile for IBR disk forging (strain rate = 0.5)	159
Fig 33. Strain rate profile for IBR disk forging (strain rate = 0.5)	160
Fig 34. Comparison of strain rates for IBR forging using reduced order model	162
Fig 35. Die velocity profiles - Designed and constant velocity cases	163
Fig 36. Strain rate profiles - Designed and constant velocity cases	164
Fig 37. Comparison of designed velocities and contact nodes vs. stroke	165
Fig 38. Comparison of strain rates for IBR disk	167
Fig 39. Finite element model of die and billet for engine disk	169
Fig 40. Comparison of strain rates for engine disk forging	170
Fig 41. Comparison of die velocities for engine disk forging	171
Fig 42. Comparison of nodal temps. (node 18) for engine disk forging	172
Fig 43. Engine disk forging - Velocity profiles	175
Fig 44. Engine disk forging - Strain rate profiles	176
Fig 45. Channel section forging - Velocity profiles	177
Fig 46. Channel section forging - Strain rate profiles	178
Fig 47. Die velocities using constant and varying system matrices	181
Fig 48. Strain rates using constant and varying system matrices	182
Fig 49. Die velocities using constant and varying weighting matrices	183
Fig 50. Strain rates using constant and varying weighting matrices	184
Fig 51. Eigenvalue spectrum of a generic elemental stiffness matrix	187

Fig 52. H-Block compression: Finite element model	195
Fig 53. Stability predictions for H-Block compression (Step 1)	196
Fig 54. Stability predictions for H-Block compression (Step 15)	197
Fig 55. Plane strain compression: Finite element model	199
Fig 56. Stability predictions for plane strain compression (Step 1)	200
Fig 57. Stability predictions for plane strain compression (Step 10)	201
Fig A1. Process control of metal forming operations - Project Overview	221
Fig A2. Description and organization of the metal forming process control work	222

LIST OF TABLES

Table 1. Model validation: State space model vs. ALPID	77
Table 2. Performance of the optimal control design scheme	95
Table 3. Comparison of optimized velocities for aggregation method	137
Table 4. Comparison of optimized velocities for BMR model	138
Table 5. Comparison of optimized velocities for Marshall's method	139
Table 6. Comparison of optimized velocities for Davison's method	140
Table 7. Comparison of optimized velocities for Nicholson's method	141
Table 8. Comparison of optimized velocities for BMR model	146
Table 9. Comparison of optimized velocities for aggregation method	147
Table 10. Comparison of optimized velocities for Marshall's method	148
Table 11. Comparison of optimized velocities for Davison's method	149
Table 12. Comparison of optimized velocities for Nicholson's method	150

CHAPTER 1

Introduction

1.1 Need for process control in metal forming

In today's metal forming industry new materials are being widely introduced and used for an ever-broadening scope of applications. The increasing demand for new, high performance materials has augmented the need for superior processing methods. Computer-aided design techniques have generally been found to be the most effective and efficient way to meet this challenge and are used widely. In this work, the nonlinear rigid viscoplastic finite element method has been used for simulation and analysis of forging processes. Even though this work focuses on forging, the methodology featured in this report is general purpose and is applicable to any of the unit forming processes.

During manufacturing the mechanical and service properties of the final product are dependent to a large extent on the prior processing history. As such, one of the most important tasks is the selection and control of critical process parameters that would ensure required part quality along with specific mechanical and physical characteristics. Therefore, there is a need to develop an optimal processing strategy that would result in defect-free, high quality products on a repeatable basis.

Forging is a thermomechanical plastic deformation process wherein the work-piece is deformed from a relatively simple geometry to a predetermined complex shape by the application of compressive forces. Forging differs from other shaping methods in that the flow of metal is intended to produce specific material properties in the final product. The forging operation can be visualized as a system with a large number of interacting factors like starting billet shape, interface frictional conditions, temperature of workpiece and dies, velocity of the die, and geometry of the final part. These parameters strongly influence the thermal and flow behavior of the deforming material and have a direct impact on the spatial and temporal distribution of field variables like strain-rate, total effective strain, and nodal temperatures. The properties and integrity of the final formed product are, in turn, functions of the field components of the metal forming system. It is thus necessary to monitor and control the essential field variables like strain, strain-rate, and temperature to obtain the desired microstructure and service properties in the final product. Also, non-conventional and difficult-to-process materials generally have a narrow range of processing conditions in the strain, strain-rate, and temperature space where they can be processed successfully without any formation of defects. To maintain the field variables within these 'favorable' processing regions, optimal design of process parameters such as die velocity and initial die/billet temperature must be carried out.

1.2 Process parameters and physical/microstructural properties

Generally, metal forming processes may be divided into two categories: massive forming and sheet metal forming. The massive forming processes include operations such as forging, extrusion, and rolling. Although this work is generic in nature and is applicable to all the unit forming processes, the main focus is on isothermal/nonisothermal forging. In these processes there is a strong relationship between macroscopic (physical) properties, microstructure, and process parameters. This is strongly supported by earlier work done in this area. For instance, in the design of aircraft engine disks, attempts have been made to obtain desired properties in the final product by generating different microstructures in different regions of the disk [1]. Though detailed relationships between microstructure and physical properties have not yet been fully established, it has been shown through experiments that physical properties depend to a large extent on the microstructure of the material, and if the workpiece is not processed in the right manner and under appropriate operating conditions, defective products and/or unwanted physical characteristics in the final product may result.

In metal forming processes, it has generally been found that process parameters play an important role in the forming of a specific microstructure in the workpiece. For example, Devadas et. al. [2], modeled the microstructure and mechanical properties of steel during hot rolling. These models have been used

to predict grain size and characterize static and dynamic recrystallization during the rolling process. Most of these models have been found to be sensitive to change in process parameters such as strain, strain-rate, and temperature. Sastry et. al. [3] studied the relationship between metallurgical properties and process parameters during the superplastic forming of titanium alloys. This work showed that the percentage of equilibrium α phase in the microstructure is related to strain-rate, strain-rate sensitivity, and temperature. Dadras and Thomas [4] conducted experiments to study the deformation behavior of Ti-6242 (Ti-6Al-2Sn-4Zr-2Mo-0.1Si) alloy during the upset forging of specimens starting with $(\alpha + \beta)$ or β microstructure. They found that the volume percentage of primary α microstructure in the specimen is influenced by the deformation temperature. This further illustrated and emphasized the importance of temperature effects during deformation. Recently, Cohen and Durham [5] correlated the effect of change in strain-rate to the final microstructure during hot working processes. The dependence of the resulting microstructure on various temperatures and strain-rates was analyzed while carrying out compression tests on a carbon steel material. Seetharaman et. al. [6] analyzed the effect of strain, strain-rate, and temperature on the microstructure of a gamma Ti-Al alloy during extrusion. During this work, the relationship between microstructural parameters (grain size and grain distribution) and process parameters (effective strain-rate, effective strain, and flow stress) was obtained using experimentally collected data. This further proved that both strain-rate and temperature have a strong influence on the microstructure and properties of a given material.

Besides microstructure, workability is also an important characteristic in analyzing metal forming processes. Workability is the capacity of a material to deform without failure. It depends on: (1) process parameters (such as temperature, strain-rates, stresses, and strain history), and (2) material variables (such as composition and initial microstructure). The current work proposes that it is crucial to select proper processing conditions and process parameters to achieve the desired microstructure and workability level in the deforming workpiece. For a given billet material and geometry the following major process parameters have to be determined to obtain optimal forging conditions:

- Die material
- Initial die/workpiece temperatures
- Ram speed
- Lubricant
- Preform geometry and position
- Die geometry
- Type and size of the forging press

In the past, the design of process parameters for metal forming operations was done on a trial and error basis, and was dependent to a large extent on the experience of the die designers, metallurgists and process engineers. This method was expensive, time consuming, and not very reliable. With the development of sophisticated numerical techniques, computer aided design and analysis methods have become very popular and are in use widely.

1.3 Metal forming simulation using the finite element method (FEM)

With advancement in computer technology and development of sophisticated processing methods, the use of computer-aided techniques for process simulation and process design has increased considerably. Some of the well known metal forming simulation and analysis methods are the slab method, the upper-bound method, the slip-line field method, and the finite element analysis (FEA) method.

The slab method is based on the equilibrium of a slab of the deforming body and assumes a simplified stress distribution along the slab. Biswas and Rooks [8] evaluated the loads and stresses for metal forming processes based on this method using an approach in which the various deformation stages are uncoupled and analyzed separately. Lui and Das [9] also used the slab method for evaluating the loads and stresses in axisymmetric forgings. Although this method is quick and gives reasonable results [10,11], its main shortcoming is that it is restricted to the evaluation of loads and stresses for simple geometries only.

The upper bound method [12,13] assumes a velocity field describing metal flow during the forming operation. Based on this velocity field, the total forming energy and the forming load are then calculated. By including one or more parameters in the considered velocity field, it is possible to determine and optimize the upper-bound velocity field. The optimal process parameters are determined by minimizing the total forming energy with respect to these parameters [14]. This approach has earlier been used in the analysis of axisymmetric forgings, plate rolling, and extrusion processes [15-19].

Due to the rapid development of computers and numerical algorithms, the finite element method (FEM) has become very popular for simulating and analyzing metal forming problems. Most of the FE analyses in this field are based on the rigid-plastic and rigid-viscoplastic theories. For rigid-plastic materials, it is assumed that flow stress is a function of strain, strain-rate, and temperature, and that the elastic response of the material is negligible. The rigid-viscoplastic theory was generalized by Zienkiewicz et. al. [20,21] and is capable of modeling hot, rate-dependent processes. This generalization provides the theory for analyzing the deformation of Ti-alloys which are strain-rate sensitive materials.

Lee and Kobayashi [22,23] developed the rigid-plastic finite element method using variational principles for a material obeying Von Mises' yield criterion with isotropic kinematic hardening. In the early 80's, Oh et. al. [24,25] refined the rigid-viscoplastic formulation to solve a wide variety of problems using the finite element method. These efforts resulted in the development of a generalized

computer program ALPID [26] (Analysis of Large Plastic Incremental Deformation), which has the capability to perform a wide range of 2-D metal forming simulations.

A variety of metal forming problems have been solved using the finite element analysis method. Reference 27 gives a broad and detailed coverage of the application of FEM in metal forming research. It contains plane strain problems (such as bulk forging, sheet rolling, plate bending and side pressing), axisymmetric forgings (such as disk forging and ring compression), steady-state processes such as extrusion and drawing; sheet metal forming operations, and the forging of porous metals. Duggirala [28] also used ALPID in the analysis of flashless ring gear blanks and axle shafts.

Besides the rigid-plastic and rigid-viscoplastic finite element analysis, some researchers also used other plastic theories. Dexter [29] studied the mechanisms involved in forging using the elastic-viscoplastic finite element analysis. The stress and strain values, especially at the die-workpiece interface, and the critical loads for the potential failure of forging die can be obtained by this method of analysis. The updated Lagrangian Jaumann Formulation of FEM, which includes elastic deformation and tends to be elastic-plastic or elastic-viscoplastic in nature, has also been used in metal forming [30]. It has successfully been applied to the problems of extrusion, drawing, rolling and sheet metal forming.

Finite element analysis and simulation has been further enhanced and developed by several researchers to handle nonisothermal processing conditions. Wu

and Oh developed the program ALPIDT [31] which interfaces ALPID with a thermal analysis module, and can perform coupled thermo-viscoplastic deformation analyses. Oh et. al. [32] used ALPIDT to analyze the hot die forging of Ti6242 alloys. They found that the distortion in the FE mesh was more severe during hot-die forging than in isothermal forging. Clearly, the effect of temperature, possibly combined with the strain-rate effect, caused the metal flow to differ under the two forging conditions. Zienkiewicz et. al. [33] studied and performed a coupled thermal analysis for steady-state extrusion operations. Tang et. al. [34] analyzed the shell nosing problem using this approach. Coupled analysis using the updated Lagrangian approach also has been reported in earlier work [35].

In this work, the finite element method has been chosen as the primary numerical analysis tool. The nonlinear rigid viscoplastic finite element program ALPID has been used for simulation and analysis purposes because it has the following capabilities:

1. Obtaining detailed solutions of mechanics in a deforming body with sufficient accuracy for practical purposes. The solution contains velocities, strains, stresses, strain-rates, temperatures, contact pressure distributions, die load and die temperatures.
2. Handling arbitrary boundary conditions.

3. Including the friction effect at the die-workpiece interface in both deformation and thermal calculations.
4. Graphics display for post-processing.
5. Analyzing a large variety of problems by simply changing the input data.

1.4 Design of optimal process parameters

Compared to traditional design methods in the metal forming field, numerical analysis and design techniques are less time consuming and expensive. In the past, considerable research has been conducted in designing and selecting optimum process parameters using numerical approaches.

Boer et. al. [36] developed a process model based on the slab method to calculate stress and strain distributions in the deforming workpiece. Thermal analysis was performed using finite element methods and a simplified non-dimensional analysis. Using the above strategy, and minimizing the stress ratio parameter, optimal ram velocity profiles and initial die temperature were obtained for both isothermal and hot die forgings (using NIM80A material). Lanka and Grandhi [37] developed the Conformal Mapping Method to design intermediate die shapes for 2-D and 3-D forgings. This is a geometry mapping technique wherein the staging criteria are identified based on the stress ratio parameter. Malas [38] developed an approach for process parameter design using a linear relationship between the ram velocity and strain-rate as an approximation to maintain the

billet variables within stable processing regions. Hong [39] designed a control scheme based on a finite element analysis model. This model utilizes the local thickness of the deforming blank as a measured variable to track a desired trajectory. Kobayashi et. al. [27], and Park et. al. [40] developed the “backward tracing” technique which is based on the reversal of material flow during simulation. Using this method preforms were designed for shell nosing, plane-strain rolling, and axisymmetric forging problems. Han et. al. [41] combined this idea with a numerical optimization approach, and designed optimal intermediate die shapes for isothermal forging processes by minimizing the strain-rate variance in the deforming workpiece. This technique is called the “Backward Deformation Optimization Method”, and includes sensitivity analysis, besides introducing a criterion for nodal separation from the surface of the die during backward deformation simulation. Grandhi et. al. [42] then introduced an optimal control design algorithm into the process parameter design procedure. The metal forming process was modeled and condensed into the state space form, and a suitable optimal control algorithm was used in designing the process parameters. Optimum ram velocity schedules for maintaining specified strain-rates in the billet were generated by this approach for an isothermal disk forging.

During conventional hot die forging, there is a complex thermal interplay between the workpiece, die(s) and the atmosphere. There is heat generation due to the dissipation of deformation energy, and friction. At the same time there is heat loss from the system due to conduction between the billet and die. In addition, there is also heat loss due to convection and radiation between the billet

and the environment. As a result, the processed material may experience severe temperature gradients along the interface of the die and billet, which could lead to the formation of surface defects. Thermal disparities and temperature changes in the workpiece may also induce phase transformations and changes in the grain structure. These changes, in turn, affect the flow stress and metal flow as well as other process variables. Furthermore, severe temperature gradients result in large thermal stresses leading to material failure. Quenching is an example where thermally induced stresses can cause warping and cracking of the finished parts. In view of these effects, this research extended the isothermal study in reference 42 to handle nonisothermal situations like hot die forging.

The objective of this work is to build a numerical model representing the metal forming system, and design optimal process parameters (ram velocity and initial die temperature) that satisfy the following requirements:

1. Maintain the strain-rate at a certain value at a given location (element) in the billet.
2. Maintain the temperature at the critical spot (node) above some value.
3. Reduce the temperature range in the billet.
4. Reduce the temperature gradient at the interface of die and billet.
5. Force the strain-rate and temperature to follow desired trajectories.

The above requirements have significant practical meaning, as explained in the later sections of this report. If these requirements can be satisfied, maintaining the process parameters within favorable processing regions becomes easy.

The coupled deformation and thermal analysis code, ALPID, is modified to build the state space model and then condensed to obtain a reduced order model. An optimal finite time controller design algorithm has been integrated with the ALPID code to calculate the required (optimal) process parameters. The results show that the above methodology is quite successful in achieving the required objectives. But developing the state space model from the finite element equations and solving the resulting set of equations is a non-trivial task, especially while dealing with large scale systems. While simulating realistic manufacturing processes, it is necessary to use large-scale finite element models with a large number of degrees of freedom. In such instances, the corresponding state space model also has a large number of states. This is likely to cause numerical difficulties during implementation, besides being computationally expensive and tedious. In such situations, model reduction techniques have to be used to reduce the order of the system before designing the controllers. The following section gives a brief introduction and description of model reduction techniques.

1.5 Reduced order models

Balas [43], surveyed different model reduction methods applied to the control of large space structures. He presented a mathematical framework to survey the general topics in control theory (for large space structures) like optimal control, reduced-order models, spillover compensation, reduced order controllers, and other related topics. These numerical techniques are widely used in aircraft and space structure control work by many researchers. Marshall [44] described in detail the numerical strategies used for the reduction of large models using the modal analysis approach. Akoi [45,46] applied economic aggregation techniques to solve large scale control problems. Rao, et. al. [47] applied the balanced truncation and modal aggregation methods to large flexible structures, where the FE model of the structure in the state space form is used to design robust controllers for structural systems. Safonov, et. al. [48] used the modal truncation and Hankel-norm techniques to reduce a 116-state model to a 4-state model, while designing a robust multivariable controller for suppressing active vibration in large space structures. Ben Jaafar, et. al. [49] had earlier applied model reduction techniques to thermal diffusion problems. In that work, the Eitelberg, Marshall, and Aggregation methods were applied to a finite element model describing heat transmission in thermal diffusion problems. Wanxie, et. al. [50] used the relationship between the generalized variational approach and LQ control theory to successfully reduce the size of an eigenvalue problem by half. Chang and Engblom [51] used the Rayleigh-Ritz method to reduce the model of a structure under uniform loading for non-linear dynamic response predictions.

In most of the above applications, the model reduction techniques used tend to retain the dynamic response of the original system. For the current analysis, the objective during model reduction is to derive a reduced order system that is both controllable and observable. In addition, it must be ensured that the reduced model retains the properties/characteristics of the full model. Gregory [52] constructed a reduced model for lightly damped structures using balanced model reduction (BMR) techniques. He reduced a full state model having 114 states to a reduced model having 26 states, and concluded that the BMR technique (effectively) retains the stability, controllability and observability of the full model. Yae and Inman [53], also concluded that the BMR technique retains the properties of the full state model for multi-body systems and can be used for control applications. This was also confirmed by Adams et. al. [54], who used the BMR method in flight control applications.

In this work, the following three broad methods of model reduction were studied:

- a. Aggregation Method [55]
- b. Modal analysis methods [56]
- c. Balanced model reduction [57]

After the reduced order state space models are developed, a control law based on the differential Riccati equation is adopted to design optimal die velocities for

the metal forming process, like in the case of the full state model. The detailed formulation involved in deriving reduced order models is explained at a later stage in this report.

The following chapters describe in detail the process control strategy developed and the mathematical formulations involved in setting up and solving the optimal control problem. Appendix B and Appendix C provide information on the program developed (COPP - Control of Optimal Processing Parameters) for implementing this methodology.

CHAPTER 2

State Space Model for Deformation Analysis

2.1 Basis for the finite element formulation

The finite element method (FEM) used in this work is based on the flow formulation. This approach assumes that during metal forming the plastic strains usually outweigh elastic strains and the idealization of rigid-plastic or rigid-viscoplastic material behavior is acceptable. In other words, phenomena associated with elasticity are completely neglected in this method of analysis.

The original problem associated with the deformation process of rigid viscoplastic materials is a boundary-value problem and the formulation is briefly described below [22,23,27]:

Consider a body (workpiece) having volume V and a boundary surface S . The boundary surface S may be divided into three distinct parts given by:

$$S = S_u + S_F + S_c \quad (2.1)$$

where S_u is the surface with prescribed velocity \bar{u} , S_F is the portion of the workpiece with traction F prescribed, and S_c is the tool-workpiece interface surface where the frictional stress f acts. The body is composed of a rigid plastic material which obeys the Von Mises yield criterion and its associated flow rule. The deformation of the body V is now characterized by the following field equations.

Equilibrium conditions for deformation analysis (neglecting body forces) are given by:

$$\sigma_{ij,j} = 0 \quad (2.2)$$

where σ_{ij} is the ij^{th} component of the Cauchy stress tensor. In the above equation, a recurring letter suffix indicates the sum, and the comma denotes partial differentiation.

Compatibility conditions are given by the following strain rate-velocity relation:

$$\dot{\varepsilon}_{ij} = \frac{1}{2} (u_{i,j} + u_{j,i}) \quad (2.3)$$

where, $\dot{\varepsilon}_{ij}$ is the ij^{th} -component of the strain-rate tensor, u_i is a velocity component, and the comma represents differentiation.

The constitutive equation giving the stress-strain rate relationship is [27]:

$$\sigma'_{ij} = \frac{2}{3} \frac{\bar{\sigma}}{\dot{\varepsilon}} \dot{\varepsilon}_{ij} \quad (2.4)$$

where σ'_{ij} is a component of the deviatoric stress, $\bar{\sigma}$ and $\dot{\varepsilon}$ are the effective stress and effective strain rates, respectively, defined by $\bar{\sigma} = \sqrt{\frac{3}{2} \sigma_{ij}' \sigma_{ij}'}$ and $\dot{\varepsilon} = \sqrt{\frac{2}{3} \dot{\varepsilon}_{ij} \dot{\varepsilon}_{ij}}$. The flow stress, in general, is a function of total strain, strain-rate, temperature, and microstructure S , and may be represented as:

$$\bar{\sigma} = f(T, \bar{\varepsilon}, \dot{\varepsilon}, S) \quad (2.5)$$

The boundary condition for this system representing equilibrium of stresses is given by:

$$\sigma_{ij} n_i = F_j, \quad \text{on } S_F \quad (2.6)$$

where n_i is the i th-component of the unit normal vector to the body surface and F_j is the j th-component of the prescribed surface traction. The velocity boundary condition is given by:

$$u_i = \bar{u}_i, \quad \text{on } S_u \quad (2.7)$$

where \bar{u}_i is the i th-component of prescribed velocity. Solutions to this problem are the stress and velocity distributions that satisfy the governing equations and the boundary conditions. The governing equations include the equilibrium equations, the yield criterion, and the compatibility conditions derived from the flow rule. Since it is difficult to obtain a complete solution that satisfies all the field equations, various approximate methods are used to solve the above problem, one of them being the finite element method. The basic principles and concepts involved in the finite element method are the variational principle and discretization.

The finite element governing equation for metal forming analysis may be derived from the potential energy functional [27],

$$\pi = \int_V \bar{\sigma} \dot{\varepsilon} dV - \int_{S_F} F_i u_i dS \quad (2.8)$$

where the first term represents the rate of total plastic work done and the second term represents the rate of work expended due to surface traction. The variational principle requires that among admissible velocities u_i that satisfy the conditions of compatibility and incompressibility (as well as the velocity boundary conditions) the actual solution gives the above functional a stationary value. In other words, the solution of the original boundary value problem is obtained

from the solution of the dual variational problem, where the first order variation of the above functional vanishes, i.e.,

$$\delta\pi = \int_V \bar{\sigma} \delta \dot{\varepsilon} dV - \int_{S_F} F_i \delta u_i dS = 0 \quad (2.9)$$

Metal deformation occurs at a constant volume. Therefore, the admissible velocity u_i needs to satisfy the incompressibility constraint. This is embedded into the variational principle functional (Eq. (2.9)) by introducing the penalty constant K (which is a very large positive quantity) into the equation as,

$$\delta\pi = \int_V \bar{\sigma} \delta \dot{\varepsilon} dV + K \int_V \dot{\varepsilon}_V \delta \dot{\varepsilon}_V dV - \int_{S_F} F_i \delta u_i dS = 0 \quad (2.10)$$

where $\dot{\varepsilon}_V = \dot{\varepsilon}_{ii}$ is the volumetric strain rate. The development of the finite element equations from the above equation is described in the next section.

2.2 Finite element equations

The discretization of the variational principle functional described above is done using the standard procedure of the finite element method. The primary unknown for the solution of Eq. (2.10) (which represents a quasi-static plastic deformation process) is the velocity field associated with it. This velocity field, u , is approximated by shape functions in terms of nodal point velocity values as,

$$u = \mathbf{N}_D^T \mathbf{v} \quad (2.11)$$

where \mathbf{N}_D is the shape function matrix for deformation analysis, and \mathbf{v} is the nodal velocity vector for the element under consideration. For two-dimensional,

four-noded, quadrilateral elements having two degrees of freedom per node, \mathbf{v} is a 8×1 vector given by,

$$\mathbf{v}^T = [v_1 \ v_2 \ v_3 \ \dots v_8]$$

Eq. (2.10) may now be expressed in terms of the nodal point velocities \mathbf{v} and their variations $\delta\mathbf{v}$. Using the variational principle, from the arbitrariness of δv_I , a set of nonlinear algebraic equations (stiffness equations) are obtained as given below [27]:

$$\frac{\partial \pi}{\partial v_I} = \sum_j \left(\frac{\partial \pi}{\partial v_I} \right)_{(j)} = 0 \quad (2.12)$$

where (j) represents the quantity at the j th element. The capital-letter suffix, I , refers to the nodal point number. The above equation is actually determined by first obtaining the elemental equations and then assembling them under appropriate constraints to obtain a set of global stiffness equations in the standard finite element form,

$${}^n\mathbf{K} {}^n\mathbf{V} = {}^n\mathbf{F} \quad (2.13)$$

where \mathbf{K} is the global stiffness matrix, \mathbf{F} is the load vector (described in detail in the next section), \mathbf{V} is the global velocity vector, and n is the counter representing the iteration number at every time step. This problem is similar to a standard finite element analysis problem, but its special feature is that the geometry of the boundary, and hence the boundary condition, keeps changing as the die stroke increases. \mathbf{K} and \mathbf{F} are both functions of \mathbf{V} , resulting in a highly nonlinear system of equations. Therefore, the analysis path of the forging process is traced in an incremental manner by considering a series of discrete equilibrium states,

each corresponding to a specific value of time. The n^{th} discrete equilibrium state is assumed to correspond to the time value t , and the subsequent or $(n + 1)^{th}$ equilibrium state, is assumed to correspond to time $(t + \Delta t)$. The geometry configuration at time $(t + \Delta t)$ is updated from time (t) . This is known *a priori* from the solution of the previous time step (t) . The velocity distribution for configuration $(t + \Delta t)$ is unknown and calculated in an implicit iterative manner until a converged solution is obtained.

The solution to Eq. (2.12) or Eq. (2.13) is generally obtained iteratively using the Newton-Raphson method. The method consists of linearization and application of convergence criteria to obtain the final solution. If the converged point is $\mathbf{v} = \mathbf{v}_0$, a Taylor series expansion can be made about \mathbf{v}_0 as follows:

$$\left[\frac{\partial \pi}{\partial v_I} \right]_{\mathbf{v}=\mathbf{v}_0} + \left[\frac{\partial^2 \pi}{\partial v_I \partial v_J} \right]_{\mathbf{v}=\mathbf{v}_0} \Delta v_J = 0 \quad (2.14)$$

where Δv_J is the first order correction of the velocity \mathbf{v} . The linearized system of equations may be written as:

$$\mathbf{K} \Delta \mathbf{v} = \mathbf{f} \quad (2.15)$$

where \mathbf{K} is again the material and process dependent stiffness matrix, and \mathbf{f} is the residual of the nodal point force vector. This equation may further be rearranged and expanded as,

$$\mathbf{K}_S \mathbf{v} + \mathbf{K}_t \Delta \mathbf{v} = \mathbf{F} \quad (2.16)$$

where \mathbf{K}_S and \mathbf{K}_t are called the secant stiffness and tangent (or gradient) stiffness matrices, respectively (Fig. 1). \mathbf{K}_S and \mathbf{K}_t are calculated based on the current

solution of Eq. (2.13) and treated as constant matrices for time t to $(t + \Delta t)$. Here again, \mathbf{F} is the finite element load vector. Once the solution of Eq. (2.14) for the velocity correction term ($\Delta \mathbf{v}$) is obtained, the current velocity \mathbf{v}_0 is updated as $(\mathbf{v}_0 + \alpha \Delta \mathbf{v})$, where α is a constant between 0 and 1, and is called the deceleration coefficient. Iteration is continued until the velocity correction terms become negligible and the convergence criteria are met.

To calculate the first and second derivatives in Eq. (2.14), the effective strain rate ($\dot{\epsilon}$) and volumetric strain rate ($\dot{\epsilon}_V$) must be expressed in terms of the nodal velocities. This is done by means of the strain-rate matrix \mathbf{B}_s , defined by [27],

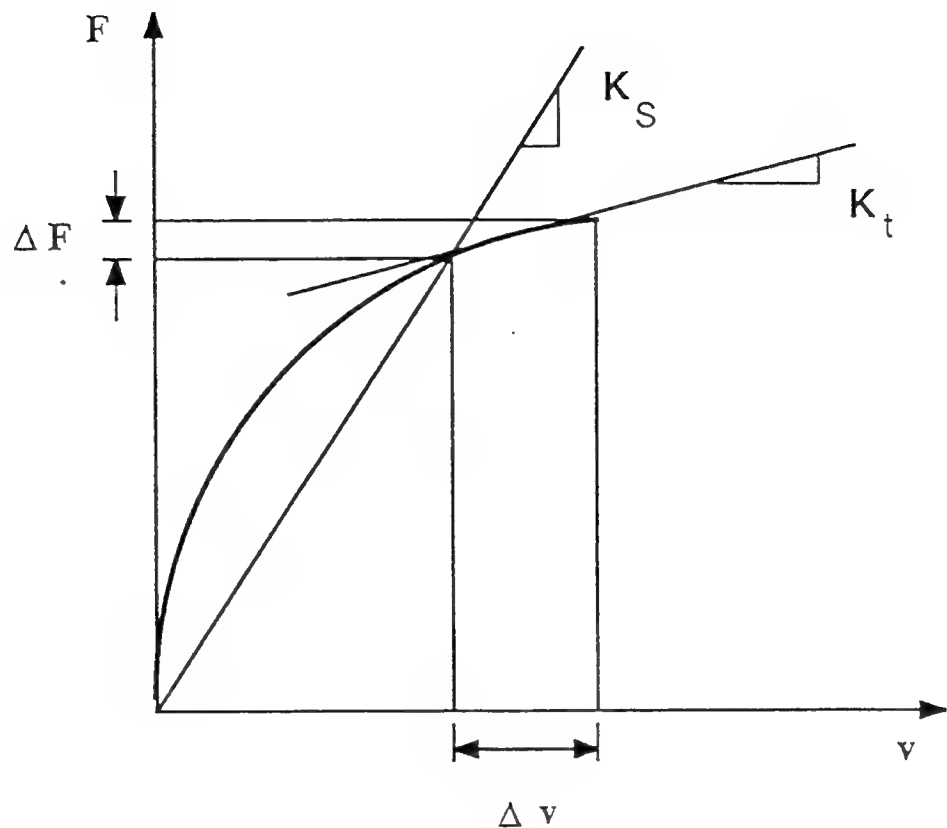
$$\dot{\epsilon} = \mathbf{B}_s \mathbf{v} \quad (2.17)$$

where $\dot{\epsilon}$ is the strain-rate vector which contains the normal strain-rate and engineering shear strain-rate components. The effective strain-rate, in turn, can be expressed in terms of the strain-rate vector as [27]:

$$\begin{aligned} (\dot{\epsilon})^2 &= \dot{\epsilon}^T \mathbf{D} \dot{\epsilon} \\ &= \mathbf{v}^T \mathbf{B}_s^T \mathbf{D} \mathbf{B}_s \mathbf{v} \\ &= \mathbf{v}^T \mathbf{P} \mathbf{v} \end{aligned} \quad (2.18)$$

where $\mathbf{P} = \mathbf{B}_s^T \mathbf{D} \mathbf{B}_s$. \mathbf{D} is a diagonal matrix that has $\frac{2}{3}$ and $\frac{1}{3}$ as its components, corresponding to the normal and shear strain-rates, respectively. Also, the volumetric strain-rate is defined as:

$$\dot{\epsilon}_V = C_i v_i \quad (2.19)$$



F = Force

v = Velocity

K_s = Secant Stiffness Matrix

K_t = Tangent Stiffness Matrix

Figure 1: Secant and tangent stiffness

where $C_i = B_{1i} + B_{2i} + B_{3i}$, and B_{ij} is an element of the strain-rate matrix \mathbf{B}_s . Using the above formulae, the first and second order derivatives in Eq. (2.14) may be expressed as [27],

$$\frac{\partial \pi}{\partial v_i} = \int_V \frac{\bar{\sigma}}{\dot{\bar{\varepsilon}}} P_{ij} v_j dV + \int_V K C_j v_j C_i dV - \int_{S_F} F_j N_{ji} dS \quad (2.20)$$

and,

$$\frac{\partial^2 \pi}{\partial v_i \partial v_j} = \int_V \frac{\bar{\sigma}}{\dot{\bar{\varepsilon}}} P_{ij} dV + \int_V \left(\frac{1}{\dot{\bar{\varepsilon}}} \frac{\partial \bar{\sigma}}{\partial \dot{\bar{\varepsilon}}} - \frac{\bar{\sigma}}{\dot{\bar{\varepsilon}}^2} \right) \frac{1}{\dot{\bar{\varepsilon}}} P_{ik} v_k v_m P_{mj} dV + \int_V K C_j C_i dV \quad (2.21)$$

The detailed derivation of the above equations and explanation of the terms involved may be obtained from reference 27.

2.3 Frictional force as the finite element load vector

The frictional condition at the die-material interface greatly influences metal flow during most forming processes and merits proper analysis and treatment. In the current procedure, friction stress f_f , which appears in the load vector of the finite element governing equation, is given by,

$$f_f = - \int_{S_c} m k \frac{u_r}{|u_r|} dS \quad (2.22)$$

where m is the friction factor, k is the shear strength of the material, and u_r is the sliding velocity at the die workpiece interface (S_c).

During finite element analysis, a coordinate transformation is made to transfer the die-workpiece contact nodal velocities onto a local coordinate system

which has one axis normal to the die surface and the other axis along the die surface (Fig. 2). A shape function is used to interpolate u_r [58] as,

$$u_r = \frac{1}{2} (1 - r) v_{r(j)} + \frac{1}{2} (1 + r) v_{r(l)} \quad (2.23)$$

where $v_{r(j)}$ and $v_{r(l)}$ are the relative sliding velocities at nodes j and l, respectively. At node j, the sliding velocity can be expressed in the local coordinate system as,

$$v_{r(j)} = v_{T(j)} - v_{dT(j)} \quad (2.24)$$

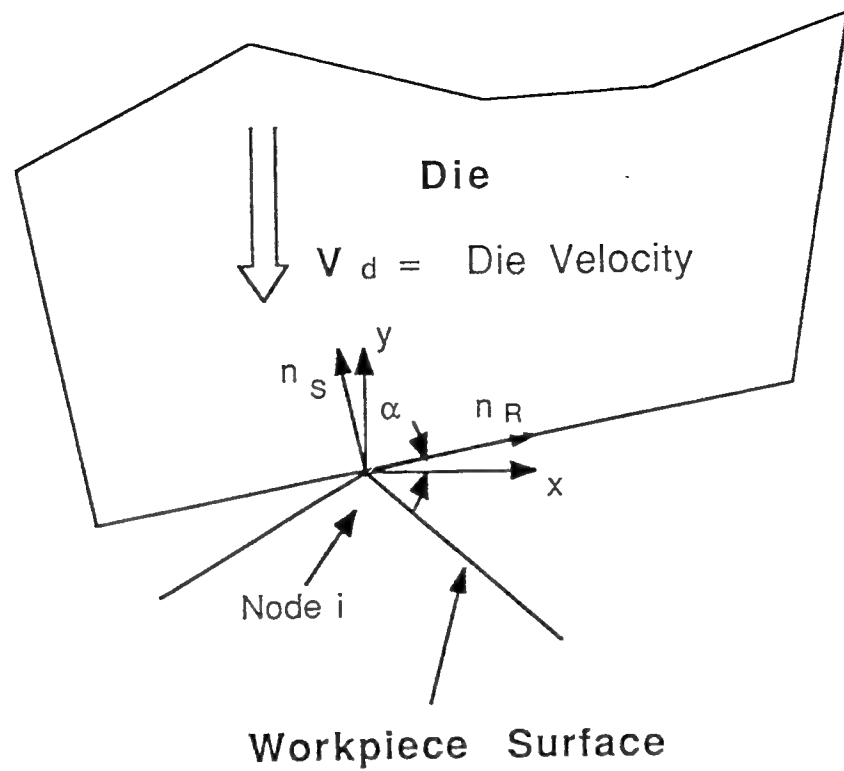
where $v_{T(j)}$ is the tangential nodal velocity along the die surface, and $v_{dT(j)}$ is the tangential component of the die velocity at boundary node j. Then, Eq. (2.22) becomes:

$$\begin{aligned} f_f &= - \int_{S_c} m k N_f^T \frac{\mathbf{v}_r}{|\mathbf{u}_r|} dS \\ &= - \int_{S_c} m k N_f^T \frac{\mathbf{v}_T}{|u_r|} dS + \int_{S_c} m k N_f^T \frac{\mathbf{v}_{dT}}{|u_r|} dS \end{aligned} \quad (2.25)$$

where N_f is the shape function. \mathbf{v}_T and \mathbf{v}_{dT} are given below:

$$\mathbf{v}_T^T = [v_{T(j)} \ v_{T(l)}] \quad \mathbf{v}_{dT}^T = [v_{dT(j)} \ v_{dT(l)}]$$

Eq. (2.25) gives the friction force along the die surface for the segment between node j and node l. The first term of Eq. (2.25) is added to the stiffness matrix \mathbf{K}_s because it contains the nodal velocity. The second term stays on the right side of the finite element governing equation, and appears as the load vector in Eq. (2.16). During the design phase, this term is transformed into the control



n_s = Inward unit normal to the die continuum at the contact node i

n_R = Unit vector tangent to the die continuum at the contact node i

(n_s, n_R) = Local coordinates

(x, y) = Global coordinates

Figure 2: Contact boundary conditions

input as it contains die velocity, which is one of the major design parameters in this work.

2.4 Condensation of the system during deformation analysis

In general, while simulating metal forming processes, large-scale finite element models are required to capture in detail the thermo-mechanical behavior of the deforming material. In this work four-noded isoparametric quadrilateral elements have been used for discretization of the workpiece and the die. Each of these nodes has two degrees of freedom. Because each nodal degree of freedom corresponds to one algebraic equation, the number of equations to be solved during analysis would be very large if many elements are used to describe the problem. This would result in a large size state space model, adding to the difficulty and computational expense in integrating FEM with an optimal control algorithm. In addition, most control design algorithms are efficient and effective only while handling 50 or less state variables. Beyond this limit, numerical difficulty may be encountered during the computation and implementation process. There is thus a need for reducing the nodal degrees of freedom of the metal forming system represented by Eq. (2.16).

A systematic condensation procedure has been developed wherein some of the important degrees of freedom of the system, including the nodal degrees of freedom for the ‘element of interest’, are retained, and those for the rest of the elements are condensed out of the system. ‘Element of interest’ actually refers

to the element(s) constituting critical regions in the billet where it is desired to achieve and maintain specific processing conditions.

To condense Eq. (2.16), the velocity field \mathbf{V} has been divided into the following five zones (Fig. 3):

\mathbf{V}_T : Tangential nodal velocities along the die surface.

\mathbf{V}_N : Nodal velocities with direction normal to the die surface.

\mathbf{V}_C : Fixed nodal degrees of freedom due to symmetric boundary condition.

\mathbf{V}_I : Nodal velocities of the element(s) of interest.

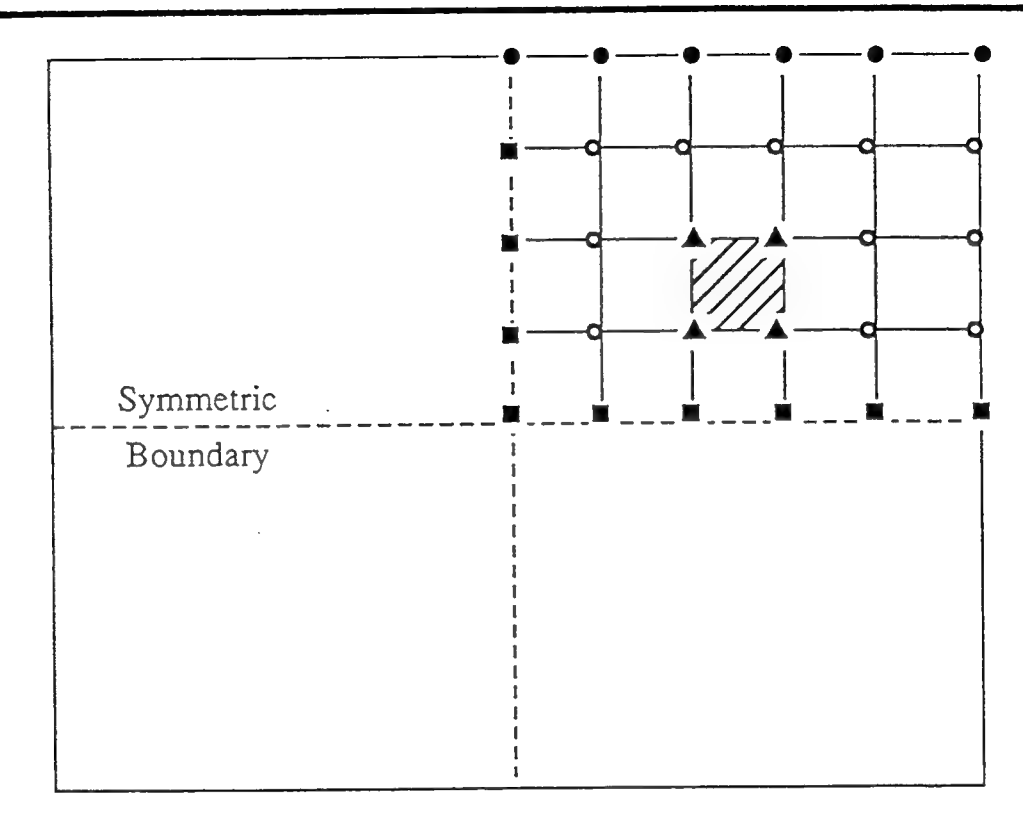
\mathbf{V}_B : Nodal velocities of the other elements.

Eq. (2.16) can now be rewritten based on the above definitions as,

$$\begin{aligned}
 & \begin{bmatrix} K_{s11} & K_{s12} & K_{s13} & K_{s14} & K_{s15} \\ K_{s21} & K_{s22} & K_{s23} & K_{s24} & K_{s25} \\ K_{s31} & K_{s32} & K_{s33} & K_{s34} & K_{s35} \\ K_{s41} & K_{s42} & K_{s43} & K_{s44} & K_{s45} \\ K_{s51} & K_{s52} & K_{s53} & K_{s54} & K_{s55} \end{bmatrix} \begin{bmatrix} \mathbf{V}_T \\ \mathbf{V}_N \\ \mathbf{V}_I \\ \mathbf{V}_B \\ \mathbf{V}_C \end{bmatrix} \\
 & + \begin{bmatrix} K_{t11} & K_{t12} & K_{t13} & K_{t14} & K_{t15} \\ K_{t21} & K_{t22} & K_{t23} & K_{t24} & K_{t25} \\ K_{t31} & K_{t32} & K_{t33} & K_{t34} & K_{t35} \\ K_{t41} & K_{t42} & K_{t43} & K_{t44} & K_{t45} \\ K_{t51} & K_{t52} & K_{t53} & K_{t54} & K_{t55} \end{bmatrix} \begin{bmatrix} \Delta \mathbf{V}_T \\ \Delta \mathbf{V}_N \\ \Delta \mathbf{V}_I \\ \Delta \mathbf{V}_B \\ \Delta \mathbf{V}_C \end{bmatrix} = \begin{bmatrix} \mathbf{F}_T \\ \mathbf{F}_N \\ 0 \\ 0 \\ 0 \end{bmatrix} \quad (2.26)
 \end{aligned}$$

where \mathbf{K}_{sij} and \mathbf{K}_{tij} are submatrices of \mathbf{K}_s and \mathbf{K}_t , and are determined based on their location in the billet. \mathbf{F}_T is the load vector associated with the friction force, and \mathbf{F}_N is the load vector related to the normal force at the die/billet interface.

Upper Die



Bottom Die

- = Nodes at the die contact boundary (V_T and V_N)
- = Nodes at the symmetric boundary (V_C)
- ▲ = Nodes of the element of interest (V_I)
- = Nodes of the rest elements (V_B)

Figure 3: System condensation

Assuming die velocity is represented by \mathbf{V}_d , the tangential and normal die velocities at the contact boundary are:

$$Normal \quad \mathbf{V}_{dN} = \mathbf{T}_y \mathbf{V}_d \quad (2.27)$$

$$Tangential \quad \mathbf{V}_{dT} = \mathbf{T}_x \mathbf{V}_d \quad (2.28)$$

where \mathbf{T}_x and \mathbf{T}_y are the transformation vectors which contain the direction cosines of the local coordinates at every die contacting node. Referring to Fig. 2, at the contact node i , the transformation vectors are given by,

$$T_{xi} = \sin \alpha_i \quad (2.29)$$

$$T_{yi} = \cos \alpha_i \quad (2.30)$$

In the nodal velocity discretization scheme described above, \mathbf{V}_N is always equal to \mathbf{V}_{dN} , the normal component of the die velocity. Therefore, it is reasonable to set $\Delta \mathbf{V}_N$ to zero. At surfaces having symmetric boundary conditions, the velocity components are zero in the direction of symmetry. So, we also have \mathbf{V}_C and $\Delta \mathbf{V}_C$ equal to $\mathbf{0}$. These terms can therefore be dropped from the system equations. We are then left with the following boundary conditions:

$$\mathbf{V}_C = \mathbf{0} \quad \Delta \mathbf{V}_C = \mathbf{0}$$

$$\mathbf{V}_N = \mathbf{V}_{dN} = \mathbf{T}_y \mathbf{V}_d \quad \Delta \mathbf{V}_N = \mathbf{0}$$

By applying these boundary conditions in Eq. (2.26) and deleting the corresponding rows and columns, we have,

$$\begin{bmatrix} K_{S11} & K_{S13} & K_{s14} \\ K_{S31} & K_{S33} & K_{s34} \\ K_{S41} & K_{S43} & K_{s44} \end{bmatrix} \begin{bmatrix} \mathbf{V}_T \\ \mathbf{V}_I \\ \mathbf{V}_B \end{bmatrix} + \begin{bmatrix} K_{t11} & K_{t13} & K_{t14} \\ K_{t31} & K_{t33} & K_{t34} \\ K_{t41} & K_{t43} & K_{t44} \end{bmatrix} \begin{bmatrix} \Delta \mathbf{V}_T \\ \Delta \mathbf{V}_I \\ \Delta \mathbf{V}_B \end{bmatrix}$$

$$= \begin{bmatrix} \mathbf{F}_T - \mathbf{K}_{s12}\mathbf{V}_N \\ -K_{s32}\mathbf{V}_N \\ -K_{s42}\mathbf{V}_N \end{bmatrix} \quad (2.31)$$

On the right side of Eq. (2.31), \mathbf{F}_T is obtained from the friction force calculation of Eq. (2.25) as,

$$\begin{aligned} f_T &= \int_{S_c} m k \mathbf{N}_f^T \frac{V_{dT}}{|u_r|} dS \\ &= \int_{S_c} m k \mathbf{N}_f^T \frac{\mathbf{T}_x}{|u_r|} dS \ V_d \\ &= h_s V_d \end{aligned} \quad (2.32)$$

where $V_{dT} = \mathbf{T}_x V_d$, and $h_s = \int_{S_c} m k \mathbf{N}_f^T \frac{\mathbf{T}_x}{|u_r|} dS$. Evaluating the above friction term along the whole interface, we have,

$$\mathbf{F}_T = \mathbf{H}_s V_d \quad (2.33)$$

The load vector may now be written as,

$$\begin{bmatrix} \mathbf{F}_T - \mathbf{K}_{s12}\mathbf{V}_N \\ -K_{s32}\mathbf{V}_N \\ K_{s42}\mathbf{V}_N \end{bmatrix} = \begin{bmatrix} H_s - K_{s12}T_y \\ -K_{s32}T_y \\ K_{s42}T_y \end{bmatrix} V_d \quad (2.34)$$

To solve and condense \mathbf{V}_B from Eq. (2.31), a forward difference approach is used to calculate $\Delta\mathbf{V}_B$, where,

$$\Delta\mathbf{V}_B = \mathbf{V}_B - \bar{\mathbf{V}}_B \quad (2.35)$$

Here, \mathbf{V}_B is the nodal velocity at time $(t + \Delta t)$ and $\bar{\mathbf{V}}_B$ is the nodal velocity at time t . $\bar{\mathbf{V}}_B$ is a known vector and treated as a constant vector in the time interval $(t, t + \Delta t)$. By substituting Eq. (2.35) into the 3rd row of Eq. (2.31), we have,

$$\mathbf{V}_B = [\mathbf{K}_{s44} + \mathbf{K}_{t44}]^{-1}$$

$$[-K_{s41}V_T - K_{s43}V_I - K_{t41}\Delta V_T - K_{t43}\Delta V_I - K_{s42}V_N + K_{t44}\bar{V}_B]$$

Substituting this solution into the first and second rows of Eq. (2.31) gives the following reduced order equation:

$$\begin{bmatrix} \bar{K}_{s11} & \bar{K}_{s12} \\ \bar{K}_{s21} & \bar{K}_{s22} \end{bmatrix} \begin{bmatrix} V_T \\ V_I \end{bmatrix} + \begin{bmatrix} \bar{K}_{t11} & \bar{K}_{t12} \\ \bar{K}_{t21} & \bar{K}_{t22} \end{bmatrix} \begin{bmatrix} \Delta V_T \\ \Delta V_I \end{bmatrix} = \begin{bmatrix} \bar{G}_1 \\ \bar{G}_2 \end{bmatrix} V_d + \begin{bmatrix} \bar{W}_1 \\ \bar{W}_2 \end{bmatrix} \quad (2.36)$$

where the submatrices and vectors are:

$$\bar{K}_{s11} = K_{s11} - (K_{s14} + K_{t14})(K_{s44} + K_{t44})^{-1}K_{s41}$$

$$\bar{K}_{s12} = K_{s13} - (K_{s14} + K_{t14})(K_{s44} + K_{t44})^{-1}K_{s43}$$

$$\bar{K}_{s21} = K_{s31} - (K_{s34} + K_{t34})(K_{s44} + K_{t44})^{-1}K_{s41}$$

$$\bar{K}_{s22} = K_{s33} - (K_{s34} + K_{t34})(K_{s44} + K_{t44})^{-1}K_{s43}$$

$$\bar{K}_{t11} = K_{t11} - (K_{s14} + K_{t14})(K_{s44} + K_{t44})^{-1}K_{t41}$$

$$\bar{K}_{t12} = K_{t13} - (K_{s14} + K_{t14})(K_{s44} + K_{t44})^{-1}K_{t43}$$

$$\bar{K}_{t21} = K_{t31} - (K_{s14} + K_{t14})(K_{s44} + K_{t44})^{-1}K_{t41}$$

$$\bar{K}_{t22} = K_{t33} - (K_{s14} + K_{t14})(K_{s44} + K_{t44})^{-1}K_{t43}$$

$$\bar{G}_1 = H_s - K_{s12}T_y + (K_{s14} + K_{t14})(K_{s44} + K_{t44})^{-1}K_{s42}T_y$$

$$\bar{G}_2 = -K_{s32}T_y + (K_{s34} + K_{t34})(K_{s44} + K_{t44})^{-1}K_{s42}T_y$$

$$\bar{W}_1 = -(K_{s14} + K_{t14})(K_{s44} + K_{t44})^{-1}K_{t44}\bar{V}_B + K_{t14}\bar{V}_B$$

$$\bar{W}_2 = -(K_{s34} + K_{t34})(K_{s44} + K_{t44})^{-1}K_{t44}\bar{V}_B + K_{t34}\bar{V}_B$$

In Eq. (2.36), only V_T and V_I are retained. These are the nodal degrees of freedom needed in the process parameter design. The rest of the nodal degrees

of freedom are either eliminated or condensed. In this way, the order of the state space system is greatly reduced.

2.5 State space model for deformation analysis

In Eq. (2.36) if $\bar{\mathbf{K}}_s$, $\bar{\mathbf{K}}_t$, $\bar{\mathbf{G}}$ and $\bar{\mathbf{W}}$ are defined as follows,

$$\begin{aligned}\bar{\mathbf{K}}_s &= \begin{pmatrix} \bar{\mathbf{K}}_{s11} & \bar{\mathbf{K}}_{s12} \\ \bar{\mathbf{K}}_{s21} & \bar{\mathbf{K}}_{s22} \end{pmatrix} \\ \bar{\mathbf{K}}_t &= \begin{pmatrix} \bar{\mathbf{K}}_{t11} & \bar{\mathbf{K}}_{t12} \\ \bar{\mathbf{K}}_{t21} & \bar{\mathbf{K}}_{t22} \end{pmatrix} \\ \bar{\mathbf{G}} &= \begin{pmatrix} \bar{\mathbf{G}}_1 \\ \bar{\mathbf{G}}_2 \end{pmatrix}, \quad \bar{\mathbf{W}} = \begin{pmatrix} \bar{\mathbf{W}}_1 \\ \bar{\mathbf{W}}_2 \end{pmatrix}\end{aligned}$$

and if,

$$\mathbf{V}_S^T = [\mathbf{V}_T^T \ \mathbf{V}_I^T] \quad \Delta \mathbf{V}_S^T = [\Delta \mathbf{V}_T^T \ \Delta \mathbf{V}_I^T]$$

then equation (2.36) may be written as,

$$\bar{\mathbf{K}}_s \mathbf{V}_S + \bar{\mathbf{K}}_t \Delta \mathbf{V}_S = \bar{\mathbf{G}} \mathbf{V}_d + \bar{\mathbf{W}}$$

or,

$$\bar{\mathbf{K}}_t \Delta \mathbf{V}_S = -\bar{\mathbf{K}}_s \mathbf{V}_S + \bar{\mathbf{G}} \mathbf{V}_d + \bar{\mathbf{W}}$$

By multiplying and dividing the left side of the above equation by Δt , we have,

$$[\Delta t \bar{\mathbf{K}}_t] \frac{\Delta \mathbf{V}_S}{\Delta t} = -\bar{\mathbf{K}}_s \mathbf{V}_S + \bar{\mathbf{G}} \mathbf{V}_d + \bar{\mathbf{W}}$$

Now, by applying the limit, $\Delta t \rightarrow 0$, we have,

$$[\Delta t \bar{\mathbf{K}}_t] \frac{d \mathbf{V}_S}{dt} = -\bar{\mathbf{K}}_s \mathbf{V}_S + \bar{\mathbf{G}} \mathbf{V}_d + \bar{\mathbf{W}} \quad (2.37)$$

where Δt is the time increment from one simulation step to the next. The above equation is in the standard state space format. By defining the plant matrix as,

$$\mathbf{A}_D = -[\Delta t \bar{\mathbf{K}}_t]^{-1} [\bar{\mathbf{K}}_s]$$

the input matrix as,

$$\mathbf{B}_D = [\Delta t \bar{\mathbf{K}}_t]^{-1} [\bar{\mathbf{G}}]$$

and the constant perturbation vector (due to condensation) as,

$$\mathbf{W}_D = [\Delta t \bar{\mathbf{K}}_t]^{-1} [\bar{\mathbf{W}}]$$

the condensed state space model for deformation analysis (Eq. (2.37)) may be rewritten as:

$$\frac{d\mathbf{V}_S}{dt} = \mathbf{A}_D \mathbf{V}_S + \mathbf{B}_D V_d + \mathbf{W}_D \quad (2.38)$$

where \mathbf{V}_S is the state vector containing the nodal velocities associated with the element of interest and the nodal velocities of the die-contacting boundary nodes. The plant matrix, input matrix, and perturbation vector have been described above, and V_d (die velocity) is the input (scalar) to the system represented in the above equation.

CHAPTER 3

State Space Model for Thermal Analysis

3.1 Finite element equations for heat transfer

The consideration of temperature effects in metal forming is very important because thermal effects accompanying the deformation process strongly influence the mechanical and material properties of the final product. In addition to deformation analysis, nonisothermal metal forming simulation needs a comprehensive thermal analysis procedure to determine the temperature distribution in the billet and die domains. The thermal analysis involves several separate bodies like the die, workpiece, and lubricant, and takes into account the thermal interplay between each of them. The die and billet are discretized (Fig. 4), and finite element analysis for each of these bodies is conducted separately. Heat transfer between the distinct bodies through the region of contact is modeled by enforcing consistent heat transfer boundary conditions. Generally, for nonisothermal forming processes, a coupled thermo-viscoplastic analysis is carried out wherein it is necessary to simultaneously solve the material flow problem (for a given temperature distribution) and the heat transfer equations. This section gives an overview of the thermal analysis procedure for metal forming simulation using the finite element method [27,34].

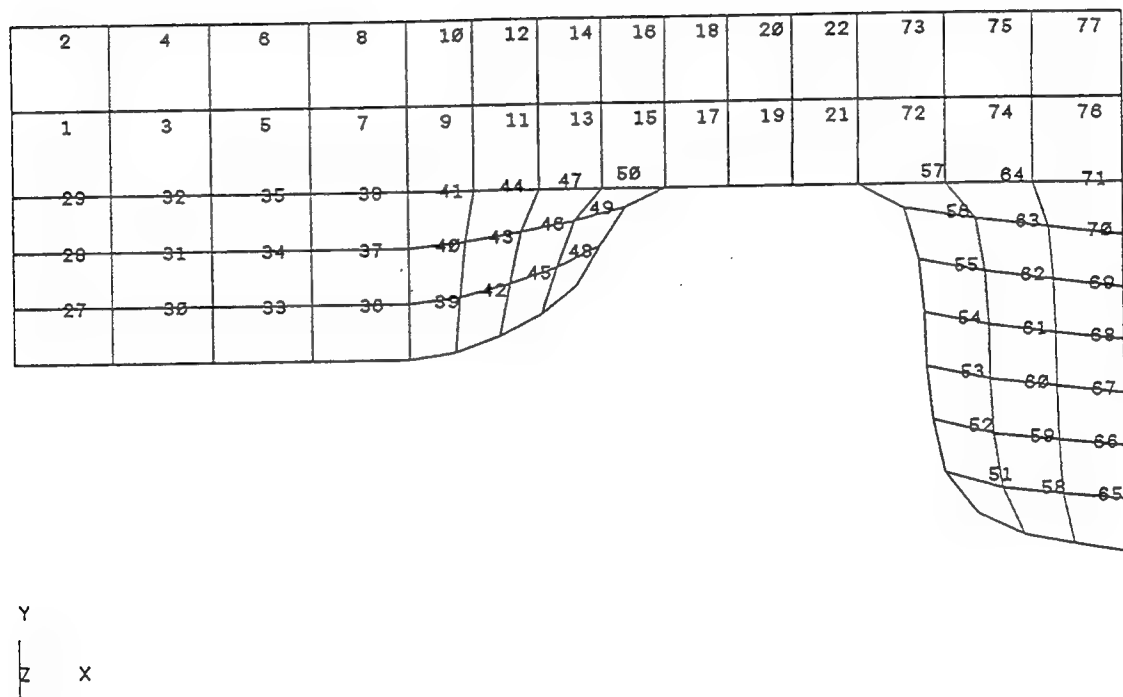


Figure 4: FEM discretization of the die body

Consider a body in thermal equilibrium under a specific set of prescribed thermal boundary conditions (Fig. 5). The energy balance equation for heat transfer analysis is given by,

$$\nabla \cdot \mathbf{q} - \dot{r} + \rho c \frac{dT}{dt} = 0 \quad (3.1)$$

where ρ and c are the mass density and specific heat, respectively; \dot{r} is the heat generation rate, T is the current temperature, and t refers to time. Also, \mathbf{q} is the heat flux, and can be written using Fourier's law of heat transfer as,

$$\mathbf{q} = -\mathbf{k}_c \cdot \nabla T \quad (3.2)$$

where \mathbf{k}_c denotes thermal conductivity, and ∇T is the spatial gradient of temperature. In Eq. (3.1), $\nabla \cdot \mathbf{q}$ refers to the divergence of heat flux, which is given by, $\nabla \cdot \mathbf{q} = \frac{\partial q_m}{\partial X_m}$, where X_m is the m -coordinate value for a generic point P in the body domain. If the heat generation in the deforming body is assumed to be due to plastic deformation only, then,

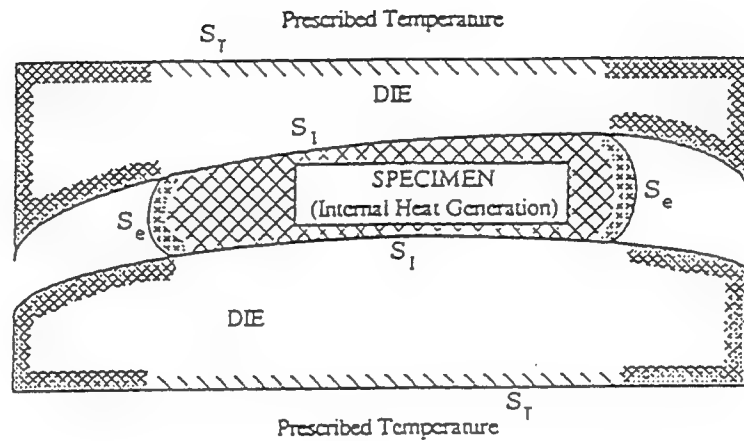
$$\dot{r} = \kappa \sigma_{ij} \dot{\varepsilon}_{ij} \quad (3.3)$$

where the heat generation efficiency κ represents the fraction of mechanical energy transformed into heat (which is generally assumed to be 0.9). In this work, two types of boundary conditions are considered over the body surface (Fig. 5). On surface S_T , the temperature is prescribed as:

$$T = \tilde{T} \quad \text{on} \quad S_T \quad (3.4)$$

Interface Heat Transfer Between
the Specimen and Die

Convection and
Radiation Boundary
Conditions



Convection and
Radiation Boundary
Conditions

Interface Heat Transfer Between
the Specimen and Die

Define:

S_e = Portion of S_q where convection and radiation boundary conditions are specified.

S_I = Portion of S_q where interface heat transfer conditions are applied.

$$S_q = S_e + S_I$$

Figure 5: Thermal boundary conditions

On surface S_q , the heat flux is specified as:

$$\mathbf{n} \cdot \mathbf{q} + \tilde{q} = 0 \quad \text{on} \quad S_q = S_I + S_e \quad (3.5)$$

where \mathbf{q} is the heat flux due to conduction, and \mathbf{n} is a unit vector acting normal to the body surface in an outwards direction. \tilde{q} represents heat flux due to convection (and/or radiation) boundary conditions and heat generated due to friction in the die-workpiece contact area. S_I is the die-workpiece interface, and S_e represents the surface exposed to the environment.

Using the Galerkin weighted residual approach, with δT (i. e., virtual temperature increment) as the weighting function, a weak form of Eq. (3.1) is obtained as [27],

$$\int_V \left[\nabla \cdot (\mathbf{k}_c \cdot \nabla T) + \dot{r} - \rho c \frac{dT}{dt} \right] \delta T dV + \int_S (\tilde{q} + \mathbf{n} \cdot \mathbf{q}) \delta T dS = 0 \quad (3.6)$$

where S is the total surface area of the body ($S = S_T + S_q$), and V is the current volume of the body. Solutions to problems of this nature require that the temperature field satisfies the prescribed boundary conditions and Eq. (3.6) for an arbitrary perturbation δt .

To implement the finite element procedure, the temperature field in Eq. (3.6) is discretized and approximated as,

$$T = \mathbf{N}_T^T \mathbf{T} \quad (3.7)$$

For a quadrilateral element, the shape function vector, \mathbf{N} , and the vector of nodal temperatures, \mathbf{T} , are given by,

$$\mathbf{N}_T^T = [q_1 \ q_2 \ q_3 \ q_4] \quad \mathbf{T}^T = [T_1 \ T_2 \ T_3 \ T_4]$$

where q_i is the shape function, and T_i is the nodal temperature. By substituting Eq. (3.7) into Eq. (3.6) and expanding, the finite element governing equation for heat transfer analysis is obtained, as shown below:

$$\mathbf{C}_T \dot{\mathbf{T}} + \mathbf{K}_c \mathbf{T} = \mathbf{Q}_T \quad (3.8)$$

where \mathbf{C}_T is the heat capacity matrix, \mathbf{K}_c is the heat conduction matrix, \mathbf{Q}_T is the heat flux vector, and \mathbf{T} is the vector of nodal point temperatures.

The transient thermal behavior of the body is captured in an incremental manner by considering a series of discrete thermal equilibrium states, each corresponding to a specific value of time. The n^{th} discrete equilibrium state is assumed to correspond to the time value (t) and the subsequent, or $(n + 1)^{th}$ equilibrium state is assumed to correspond to time $(t + \Delta t)$ where Δt is the (current) time increment value. Therefore, for a particular \mathbf{C}_T and \mathbf{K}_c , Eq. (3.8) is used to obtain the temperature solution in the interval $(t, t + \Delta t)$. Then, \mathbf{C}_T and \mathbf{K}_c are updated, and the procedure is repeated for the next time step.

In Eq. (3.8), the heat flux vector \mathbf{Q}_T has several components and is expressed as:

$$\mathbf{Q}_T = \int_V \kappa (\bar{\sigma} \dot{\bar{\varepsilon}}) \mathbf{N}_T dV + \int_{S_e} \sigma \epsilon (T_e^4 - T_s^4) \mathbf{N}_T dS \quad (3.9)$$

$$+ \int_{S_e} h (T_e - T_s) \mathbf{N}_T dS + \int_{S_I} h_{lub} (T_d - T_w) \mathbf{N}_T dS + \int_{S_I} q_f \mathbf{N}_T dS$$

where S_e refers to the surface where convection and radiation boundary conditions are specified. S_I is the surface where interface heat transfer conditions apply.

The first term on the right side of Eq. (3.9) is the heat generated by plastic deformation within the deforming body. The second term defines the heat radiated between the workpiece and environment, where σ is the Stefan-Boltzman constant, ϵ is the emissivity, and T_e and T_s are environment and surface temperatures, respectively. The third term describes the heat convected from the body to the environment with heat convection coefficient h . The fourth term represents the heat conducted between the die/workpiece through their interface. T_d and T_w are die and workpiece temperatures, respectively, and h_{lub} is the heat transfer coefficient for the lubricant. The last term is the contribution of the heat generated due to friction along the die-workpiece interface, q_f being the surface heat generation rate due to friction.

3.2 State space model for thermal analysis

From the finite element governing equations for thermal analysis, a state space model representing the thermal aspects of the metal forming process is constructed. To build the state space model for thermal analysis, Eq. (3.8) first must be expressed in terms of the state variables, namely the nodal velocities and nodal temperatures. The most difficult task in achieving this is the representation of the thermal load vector of Eq. (3.8) in terms of the state variables. This is done by considering one term at a time from Eq. (3.9). The procedure is described below:

$$(1) \int_V \kappa(\bar{\sigma}\dot{\bar{\varepsilon}}) \mathbf{N}_T dV$$

Using Eq. (2.18) to describe $\dot{\bar{\varepsilon}}$, we have,

$$\begin{aligned}
 \int_V \kappa(\bar{\sigma}\dot{\bar{\varepsilon}}) \mathbf{N}_T dV &= \int_V \frac{\kappa\bar{\sigma}}{\dot{\bar{\varepsilon}}} \dot{\bar{\varepsilon}}^2 \mathbf{N}_T dV \\
 &= \int_V \frac{\kappa\bar{\sigma}}{\dot{\bar{\varepsilon}}} \mathbf{N}_T \mathbf{v}^T \mathbf{P} dV \mathbf{v} \\
 &\doteq \int_V \frac{\kappa\bar{\sigma}}{\dot{\bar{\varepsilon}}} \mathbf{N}_T \mathbf{v}_*^T \mathbf{P} dV \mathbf{v} \\
 &= \mathbf{K}_E \mathbf{v}
 \end{aligned} \tag{3.10}$$

where \mathbf{v} is the nodal velocity vector for the element under consideration (unknown), $\mathbf{K}_E = \int_V \frac{\kappa\bar{\sigma}}{\dot{\bar{\varepsilon}}} \mathbf{N}_T \mathbf{v}_*^T \mathbf{P} dV$, and \mathbf{v}_* is the vector of nodal velocities (known quantity) at the beginning of the current time step. \mathbf{K}_E is therefore constant for the current time step.

$$(2) \int_{S_e} \sigma \epsilon (T_e^4 - T_s^4) \mathbf{N}_T dS$$

It is generally tedious to linearize a fourth order term such as the radiation heat transfer term shown above. In addition, the magnitude of the radiation term was found to be insignificant when compared to the other heat transfer terms. It has thus been neglected for the course of this work.

$$(3) \int_{S_e} h(T_e - T_s) \mathbf{N}_T dS$$

$$\begin{aligned}
 \int_{S_e} h(T_e - T_s) \mathbf{N}_T dS &= \int_{S_e} h \mathbf{N}_T dS T_e - \int_{S_e} h \mathbf{N}_T T_s dS \\
 &= \int_{S_e} h \mathbf{N}_T dS T_e - \int_{S_e} h \mathbf{N}_T \mathbf{N}_T^T dS \mathbf{T}_s \\
 &= \mathbf{H}_e T_e - \mathbf{K}_B \mathbf{T}_s
 \end{aligned} \tag{3.11}$$

where $\mathbf{H}_e = \int_{S_e} h \mathbf{N}_T dS$, and $\mathbf{K}_B = \int_{S_e} h \mathbf{N}_T \mathbf{N}_T^T dS$.

$$(4) \quad \int_{S_I} h_{lub} (T_d - T_w) \mathbf{N}_T dS$$

Similar to the procedure used in (3), this term can be expressed as,

$$\int_{S_I} h_{lub} (T_d - T_w) \mathbf{N}_T dS = \mathbf{H}_d T_d - \mathbf{K}_w \mathbf{T}_w \quad (3.12)$$

where $\mathbf{H}_d = \int_{S_I} h_{lub} \mathbf{N}_T dS$, and $\mathbf{K}_w = \int_{S_I} h_{lub} \mathbf{N}_T \mathbf{N}_T^T dS$.

$$(5) \quad \int_{S_I} q_f \mathbf{N}_T dS$$

The heat generated due to friction, q_f , is calculated as,

$$q_f = f_f |u_r|$$

where f_f is the frictional stress, and from Eq. (2.25),

$$f_f = -mk \mathbf{N}_f^T \frac{\mathbf{v}_r}{|u_r|}$$

Now, we have,

$$\begin{aligned} \int_{S_I} q_f \mathbf{N}_T dS &= \int_{S_I} -mk \mathbf{N}_T \mathbf{N}_f^T dS \mathbf{v}_r \\ &= \int_{S_I} -mk \mathbf{N}_T \mathbf{N}_f^T dS \mathbf{v}_T + \int_{S_I} mk \mathbf{N}_T \mathbf{N}_f^T \mathbf{T}_x dS V_d \\ &= -\mathbf{K}_f \mathbf{v}_T + \mathbf{B}_{DT} V_d \end{aligned} \quad (3.13)$$

where $\mathbf{K}_f = \int_{S_I} mk \mathbf{N}_T \mathbf{N}_f^T dS$, and $\mathbf{B}_{DT} = \int_{S_I} mk \mathbf{N}_T \mathbf{N}_f^T \mathbf{T}_x dS$. The explanation of some of the terms described above may be obtained from section 2.3 describing

the interface frictional stresses. Substituting Eqs.(3.10) through (3.13) into Eq. (3.9), and expanding, we have,

$$\mathbf{Q}_T = \mathbf{K}_E \mathbf{v} - \mathbf{K}_f \mathbf{v}_T - \mathbf{K}_B \mathbf{T}_s - \mathbf{K}_w \mathbf{T}_w + \mathbf{H}_d T_d + \mathbf{H}_e T_e + \mathbf{B}_{DT} V_d \quad (3.14)$$

Also, from Eq. (3.8), we have,

$$\frac{d\mathbf{T}}{dt} = -\mathbf{C}_T^{-1} \mathbf{K}_c \mathbf{T} + \mathbf{C}_T^{-1} \mathbf{Q}_T \quad (3.15)$$

Substituting Eq. (3.14) into Eq. (3.15) and rearranging the terms, the full size state space model for thermal analysis is obtained as,

$$\frac{d\mathbf{T}}{dt} = \mathbf{A}_{DT} \mathbf{V} + \mathbf{A}_T \mathbf{T} + \mathbf{B}_{DT} V_d + \mathbf{W}_T \quad (3.16)$$

where \mathbf{A}_{DT} consists of the matrices \mathbf{K}_E , \mathbf{K}_f , and \mathbf{C}_T ; \mathbf{V} represents the velocity field explained in section 2.4; \mathbf{A}_T is built from \mathbf{K}_S , \mathbf{K}_w , \mathbf{K}_c and \mathbf{C}_T ; and \mathbf{W}_T consists of $\mathbf{H}_d T_d$ and $\mathbf{H}_e T_e$. Similar to the deformation state space model, all the matrices in Eq. (3.16) are built at time step t , and are assumed to be constant for the time interval Δt .

3.3 Condensation of the thermal state space model

In nonisothermal forging analysis, the analytical (state space) model represents a coupled deformation-thermal system which has both nodal velocities and nodal temperatures as the nodal degrees of freedom. The total number of finite element equations to solve is (comparatively) much higher than in isothermal analysis. It is thus necessary to condense the thermal state space system to reduce the number of degrees of freedom involved. Eq. (3.16) has two distinct

parts: $\mathbf{A}_{DT}\mathbf{V}$, related to deformation, and $\mathbf{A}_T\mathbf{T}$, related to temperature effects. Therefore, system condensation is performed in two stages, one related to velocity field condensation and the other dealing with temperature field condensation.

(1) Condensation of the velocity field:

Similar to the condensation of the deformation model, the velocity field is partitioned into five zones, and \mathbf{A}_{DT} is expanded based on these zones as,

$$\mathbf{A}_{DT}\mathbf{V} = \mathbf{A}_{DT1}\mathbf{V}_T + \mathbf{A}_{DT2}\mathbf{V}_N + \mathbf{A}_{DT3}\mathbf{V}_I + \mathbf{A}_{DT4}\mathbf{V}_B + \mathbf{A}_{DT5}\mathbf{V}_C \quad (3.17)$$

Now, from Eq. (2.16), we have,

$$\mathbf{K}_s\mathbf{v} + \mathbf{K}_t\Delta\mathbf{v} = \mathbf{F}$$

Because $\Delta\mathbf{v}$ is small compared to \mathbf{v} , and because $\mathbf{A}_{DT}\mathbf{V}$ is not a significant part of the heat flux in a hydraulic press forging process, the term $\mathbf{K}_t\Delta\mathbf{v}$ is left out to simplify the thermal condensation process. Now, we can solve for \mathbf{V}_B from the above two equations as,

$$\mathbf{V}_B = \mathbf{K}_{s44}^{-1} [-\mathbf{K}_{s41}\mathbf{V}_T - \mathbf{K}_{s43}\mathbf{V}_I - \mathbf{K}_{s42}\mathbf{T}_y V_d] \quad (3.18)$$

In addition,

$$\mathbf{V}_N = \mathbf{T}_y V_d$$

Substituting \mathbf{V}_N and \mathbf{V}_B into Eq. (3.17) and setting $\mathbf{V}_C = 0$ (symmetric boundary condition), we have,

$$\mathbf{A}_{DT}\mathbf{V} = \bar{\mathbf{A}}_{DT1}\mathbf{V}_T + \bar{\mathbf{A}}_{DT2}\mathbf{V}_I + \mathbf{B}'_{DT}V_d$$

where,

$$\bar{\mathbf{A}}_{DT1} = \mathbf{A}_{DT1} - \mathbf{A}_{DT4}\mathbf{K}_{s44}^{-1}\mathbf{K}_{s41}$$

$$\bar{\mathbf{A}}_{DT2} = \mathbf{A}_{DT3} - \mathbf{A}_{DT4} \mathbf{K}_{s44}^{-1} \mathbf{K}_{s43}$$

$$\mathbf{B}'_{DT} = (\mathbf{A}_{DT2} - \mathbf{A}_{DT4} \mathbf{K}_{s44}^{-1} \mathbf{K}_{s42}) \mathbf{T}_y$$

Substituting these expressions into Eq. (3.16) and setting

$$\bar{\mathbf{A}}_{DT} = [\bar{\mathbf{A}}_{DT1} \quad \bar{\mathbf{A}}_{DT2}] \quad \bar{\mathbf{B}}_{DT} = \mathbf{B}'_{DT} + \mathbf{B}_{DT},$$

the thermal state space model after velocity condensation may be represented as:

$$\frac{dT}{dt} = \bar{\mathbf{A}}_{DT} \begin{bmatrix} \mathbf{V}_T \\ \mathbf{V}_I \end{bmatrix} + \mathbf{A}_T \mathbf{T} + \bar{\mathbf{B}}_{DT} \mathbf{V}_d + \mathbf{W}_T \quad (3.19)$$

Here, the retained velocity field consists of nodal velocities of the die-contacting boundary nodes and nodal velocities of the nodes constituting the element of interest.

(2) Condensation of the temperature field:

The second stage of condensation is done with respect to the temperature field so as to retain the 'critical' nodal temperatures. To be consistent with the deformation condensation, the 'critical' nodal temperatures are identified as temperatures of the nodes at the die-workpiece boundary, and temperatures of the nodes constituting the element of interest. In accordance, the temperature field is divided into two zones. The first one consists of the temperatures of interest \mathbf{T}_I , which in turn includes the nodal temperatures at the die-billet interface and the nodal temperatures of the element(s) of interest. The rest of the nodal temperatures are put into the second group represented as \mathbf{T}_M . Eq. (3.19) is now partitioned and rearranged as follows:

$$\frac{d}{dt} \begin{bmatrix} \mathbf{T}_I \\ \mathbf{T}_M \end{bmatrix} = \begin{bmatrix} \bar{\mathbf{A}}_{DT11} & \bar{\mathbf{A}}_{DT12} \\ \bar{\mathbf{A}}_{DT21} & \bar{\mathbf{A}}_{DT22} \end{bmatrix} \begin{bmatrix} \mathbf{V}_T \\ \mathbf{V}_I \end{bmatrix} + \begin{bmatrix} \mathbf{A}_{T11} & \mathbf{A}_{T12} \\ \mathbf{A}_{T21} & \mathbf{A}_{T22} \end{bmatrix} \begin{bmatrix} \mathbf{T}_I \\ \mathbf{T}_M \end{bmatrix} + \begin{bmatrix} \bar{\mathbf{B}}_{DT1} \\ \bar{\mathbf{B}}_{DT2} \end{bmatrix} \mathbf{V}_d + \begin{bmatrix} \mathbf{W}_{T1} \\ \mathbf{W}_{T2} \end{bmatrix} \quad (3.20)$$

Assume \mathbf{T}_M is the unknown temperature field at $(t + \Delta t)$ and $\bar{\mathbf{T}}_M$ constitutes the known temperatures at time t . Using the forward difference scheme, we have,

$$\frac{d\mathbf{T}_M}{dt} = \frac{\mathbf{T}_M - \bar{\mathbf{T}}_M}{\Delta t}$$

Substituting the above expression into the 2nd row of Eq. (3.20) and solving for \mathbf{T}_M , we get,

$$\begin{aligned} \mathbf{T}_M = & \Delta t [\mathbf{I} - \Delta t \mathbf{A}_{T22}]^{-1} [\bar{\mathbf{A}}_{DT21} \mathbf{V}_T + \bar{\mathbf{A}}_{DT22} \mathbf{V}_I + \mathbf{A}_{T21} \mathbf{T}_I + \bar{\mathbf{B}}_{DT2} V_d + \mathbf{W}_{T2}] \\ & + [\mathbf{I} - \Delta t \mathbf{A}_{T22}]^{-1} \bar{\mathbf{T}}_M \end{aligned} \quad (3.21)$$

where \mathbf{I} is the unit (or identity) matrix. By substituting Eq. (3.21) into the 1st row of Eq. (3.20) and rearranging, the following equation is obtained:

$$\frac{d\mathbf{T}_I}{dt} = \bar{\mathbf{K}}_{DT} \begin{bmatrix} \mathbf{V}_T \\ \mathbf{V}_I \end{bmatrix} + \bar{\mathbf{K}}_{TP} \mathbf{T}_I + \bar{\mathbf{B}}_{TP} V_d + \bar{\mathbf{W}}_{TP} \quad (3.22)$$

where,

$$\bar{\mathbf{K}}_{DT} = [\bar{\mathbf{K}}_{DT1} \ \bar{\mathbf{K}}_{DT2}]$$

$$\bar{\mathbf{K}}_{DT1} = \bar{\mathbf{A}}_{DT11} + \mathbf{A}_{T12} \Delta t [\mathbf{I} - \Delta t \mathbf{A}_{T22}]^{-1} \bar{\mathbf{A}}_{DT21}$$

$$\bar{\mathbf{K}}_{DT2} = \bar{\mathbf{A}}_{DT12} + \mathbf{A}_{T12} \Delta t [\mathbf{I} - \Delta t \mathbf{A}_{T22}]^{-1} \bar{\mathbf{A}}_{DT22}$$

$$\bar{\mathbf{K}}_{TP} = \mathbf{A}_{T11} + \mathbf{A}_{T12} \Delta t [\mathbf{I} - \Delta t \mathbf{A}_{T22}]^{-1} \mathbf{A}_{T21}$$

$$\bar{\mathbf{B}}_{TP} = \bar{\mathbf{B}}_{DT1} + \mathbf{A}_{T12} \Delta t [\mathbf{I} - \Delta t \mathbf{A}_{T22}]^{-1} \bar{\mathbf{B}}_{DT2}$$

$$\bar{\mathbf{W}}_{TP} = \mathbf{W}_{T1} + \mathbf{A}_{T12} \Delta t [\mathbf{I} - \Delta t \mathbf{A}_{T22}]^{-1} \mathbf{W}_{T2} + \mathbf{A}_{T12} [\mathbf{I} - \Delta t \mathbf{A}_{T22}]^{-1} \bar{\mathbf{T}}_M$$

Eq. (3.22) represents the condensed state space model for thermal analysis. Here again, all the matrices are built at time t and are considered to be invariant for the time interval Δt .

CHAPTER 4

Coupled Thermo-mechanical State Space Model

4.1 Construction of the control output matrix

As mentioned earlier, for this work the effective strain rate of the element of interest has been identified as an important process variable to be monitored and controlled. At the same time, since nodal velocities (explained earlier) have been chosen as the state variables, it is necessary to formulate an output equation to represent the strain rate in terms of the nodal velocities. The relationship between the strain rate and nodal velocities is a nonlinear function over the entire domain of the process. Therefore, at every simulation time step a linearization is performed to formulate the output equation.

Let \mathbf{v} represent the nodal velocities of the nodes constituting the element of interest. Also assume the current state space model is built with the velocity field \mathbf{v}_* and is valid until time t . Then, in the next time step (t to $t + \Delta t$), the velocity field may be described as,

$$\mathbf{v} = \mathbf{v}_* + \Delta\mathbf{v} \quad (4.1)$$

From Eq. (2.18) and Eq. (4.1),

$$\begin{aligned} \dot{\varepsilon}^2 &= \mathbf{v}^T \mathbf{P} \mathbf{v} \\ &= (\mathbf{v}_* + \Delta\mathbf{v})^T \mathbf{P} (\mathbf{v}_* + \Delta\mathbf{v}) \\ &= \mathbf{v}_*^T \mathbf{P} \mathbf{v}_* + \Delta\mathbf{v}^T \mathbf{P} \mathbf{v}_* + \mathbf{v}_*^T \mathbf{P} \Delta\mathbf{v} + \Delta\mathbf{v}^T \mathbf{P} \Delta\mathbf{v} \end{aligned} \quad (4.2)$$

Because the last term in the above equation is a higher order term, it may be neglected. The second term can be expanded as,

$$\begin{aligned}
 \Delta \mathbf{v}^T \mathbf{P} \mathbf{v}_* &= \sum_j \left(\sum_i \Delta v_i P_{ij} \right) v_{*j} \\
 &= \sum_i \left(\sum_j v_{*j} P_{ij} \right) \Delta v_i \\
 &= \mathbf{v}_*^T \mathbf{P}^T \Delta \mathbf{v}
 \end{aligned} \tag{4.3}$$

From Chapter 2, \mathbf{P} is equal to $\mathbf{B}_s^T \mathbf{D} \mathbf{B}_s$, and \mathbf{D} is a diagonal matrix implying $\mathbf{P}^T = \mathbf{P}$. Now, from Eq. (4.3),

$$\begin{aligned}
 \Delta \mathbf{v}^T \mathbf{P} \mathbf{v}_* &= \mathbf{v}_*^T \mathbf{P}^T \Delta \mathbf{v} \\
 &= \mathbf{v}_*^T \mathbf{P} \Delta \mathbf{v}
 \end{aligned} \tag{4.4}$$

By substituting these relations into Eq. (4.2),

$$\begin{aligned}
 \dot{\varepsilon}^2 &= \mathbf{v}_*^T \mathbf{P} \mathbf{v}_* + 2 \mathbf{v}_*^T \mathbf{P} \Delta \mathbf{v} \\
 &= \mathbf{v}_*^T \mathbf{P} \mathbf{v}_* + 2 \mathbf{v}_*^T \mathbf{P} \Delta \mathbf{v} + \mathbf{v}_*^T \mathbf{P} \mathbf{v}_* - \mathbf{v}_*^T \mathbf{P} \mathbf{v}_* \\
 &= 2 \mathbf{v}_*^T \mathbf{P} \mathbf{v}_* + 2 \mathbf{v}_*^T \mathbf{P} \Delta \mathbf{v} - \mathbf{v}_*^T \mathbf{P} \mathbf{v}_* \\
 &= 2 \mathbf{v}_*^T \mathbf{P} (\mathbf{v}_* + \Delta \mathbf{v}) - \mathbf{v}_*^T \mathbf{P} \mathbf{v}_* \\
 &= 2 \mathbf{v}_*^T \mathbf{P} \mathbf{v} - \mathbf{v}_*^T \mathbf{P} \mathbf{v}_*
 \end{aligned} \tag{4.5}$$

Now, by defining,

$$2 \mathbf{v}_*^T \mathbf{P} = \mathbf{c}_1 \quad \mathbf{v}_*^T \mathbf{P} \mathbf{v}_* = \mathbf{e}_1$$

a linearized relationship between effective strain rate and nodal velocities is obtained, given by,

$$(\dot{\varepsilon})^2 = \mathbf{c}_1 \mathbf{v} - \mathbf{e}_1 \tag{4.6}$$

4.2 Coupled state space system

In the state space model for deformation analysis, the state vector is given by $[\mathbf{V}_T^T \ \mathbf{V}_I^T]^T$. If the strain-rate squared of the element of interest (element I) is defined as $\dot{\varepsilon}_I^2$, the following output equation for deformation analysis is obtained:

$$\dot{\varepsilon}_I^2 = \mathbf{C}_1 \begin{bmatrix} \mathbf{V}_T \\ \mathbf{V}_I \end{bmatrix} + \mathbf{E}_1 \quad (4.7)$$

Strain-rate squared is used as the output variable instead of the strain-rate because it is difficult to obtain a linearized relationship between $\dot{\varepsilon}$ and \mathbf{v} . Also, since $\dot{\varepsilon}$ is always positive, $\dot{\varepsilon}^2$ gives almost the same information as $\dot{\varepsilon}$. The \mathbf{c}_1 and \mathbf{e}_1 in Eq. (4.6) have been placed in the corresponding rows and columns of \mathbf{C}_1 and \mathbf{E}_1 , which are in turn related to the nodal velocities associated with the element of interest. In the thermal state space model, the state vector \mathbf{T}_I contains the nodal temperatures of the die-contacting boundary nodes, and the nodal temperatures of the element(s) of interest. Theoretically (and from an implementation point of view), it is difficult to include all of these temperatures in the optimal design. One effective way to circumvent this problem is to select one critical nodal temperature from the set \mathbf{T}_I to be the output variable. For example, if the objective is to keep all the nodal temperatures above a certain value, then the lowest nodal temperature could be selected as the critical nodal temperature. With the critical nodal temperature controlled, the rest of nodal temperatures would also be in the desired temperature range. If the critical temperature is T_C , the output equation for the thermal analysis becomes,

$$T_C = \mathbf{C}_2 \mathbf{T}_I \quad (4.8)$$

where, \mathbf{C}_2 is a matrix with the diagonal element(s) equal to 1, corresponding to the critical nodal temperature, while the rest of the diagonal elements are zeros.

In this study, the state vector is defined as \mathbf{x} , where,

$$\mathbf{x}^T = [\mathbf{V}_S^T \ \mathbf{T}_I^T] \quad (4.9)$$

and \mathbf{V}_S and \mathbf{T}_I are the state variables corresponding to deformation and thermal analysis, respectively. \mathbf{V}_S includes the nodal velocities of the die-contacting boundary nodes and the nodal velocities of the nodes constituting the element of interest. \mathbf{T}_I contains the nodal temperatures of the boundary nodes and the nodal temperatures of the nodes forming the element of interest.

The output vector for the coupled thermo-mechanical system is defined as \mathbf{y} , where,

$$\mathbf{y}^T = [\dot{\varepsilon}_I^2 \ T_C^T] \quad (4.10)$$

Here, $\dot{\varepsilon}_I$ is the strain rate of the element of interest (explained earlier), and T_C is the critical nodal temperature as discussed above.

With the above definitions, a coupled thermo-mechanical state space model for nonisothermal metal forming processes can be obtained by grouping together the deformation state space model of Eq. (2.38) and the thermal state space model of Eq. (3.22). Then,

$$\begin{aligned} \dot{\mathbf{x}} &= \mathbf{A}\mathbf{x} + \mathbf{B}\mathbf{V}_d + \mathbf{W} \\ \mathbf{y} &= \mathbf{C}\mathbf{x} + \mathbf{E} \end{aligned} \quad (4.11)$$

where \mathbf{A} is the plant matrix and is given by,

$$\mathbf{A} = \begin{bmatrix} \mathbf{A}_D & \mathbf{0} \\ \bar{\mathbf{K}}_{DT} & \bar{\mathbf{K}}_{TP} \end{bmatrix}$$

\mathbf{B} is the input matrix given by,

$$\mathbf{B}^T = \begin{bmatrix} \mathbf{B}_D^T & \bar{\mathbf{B}}_{TP}^T \end{bmatrix}$$

\mathbf{W} is a constant vector given by,

$$\mathbf{W}^T = \begin{bmatrix} \mathbf{W}_D^T & \bar{\mathbf{W}}_{TP}^T \end{bmatrix}$$

\mathbf{C} is the output matrix, where,

$$\mathbf{C} = \begin{bmatrix} \mathbf{C}_1 & \mathbf{0} \\ \mathbf{0} & \mathbf{C}_2 \end{bmatrix}$$

and \mathbf{E} is a constant vector in $(t, t + \Delta t)$ given by,

$$\mathbf{E}^T = \begin{bmatrix} \mathbf{E}_1^T & \mathbf{0}^T \end{bmatrix}$$

It should be noted that \mathbf{W} contains certain terms coming from the condensation procedure. In keeping these terms, the error between the condensed model and the full size model is reduced considerably, especially for large scale problems. Comparing with standard state space models generally used in control system theory, Eq. (4.6) may be treated as a system with constant perturbation \mathbf{W} . The model is built and updated at each time step of the simulation. A unique feature of this system is that the geometry of the workpiece and the boundary condition keeps changing with progress in deformation. Because of this, the dimension of the plant matrix and other matrices representing the system also changes with increasing stroke.

CHAPTER 5

Process Parameter Design Using Optimal Control Theory

5.1 Design strategy

To establish an effective design strategy, it is important to understand the essential characteristics of the system and the relationship between the various interacting parameters and field variables. Chapters 2, 3 and 4 described the different field variables and design parameters being considered, and the relationship between them. This section describes the setting up of the optimal control problem for forging processes and the general strategy adopted for solving it.

In this work, the design goal is to monitor and control two important process variables associated with the deformation process, namely effective strain rate and nodal temperature. Effective strain-rate is directly dependent on nodal velocities; it is therefore an instantaneous quantity and may be directly influenced by changes in the die velocity. However, there are some system dependent constraints on how effectively the strain rate may be controlled while simulating the forging process. The metal working process, though nonlinear in nature, is treated in a piecewise continuous manner by linearizing it at every simulation time step. The deformation analysis therefore does not allow a large change in effective strain in one time step of the simulation. This constraint is represented by the maximum strain increment per step in ALPID. In addition, there are other constraints such as the forging machine's acceleration capability. But it is

an accepted fact in the metal forming field that strain rate in the billet may be controlled by suitably adjusting the die velocity. Therefore, a design methodology based on control theory is developed to design optimal ram velocity schedules that meet the design requirements on the strain rate. Generally, the design objective is to maintain the effective strain-rate at some desired value, or within a range of desired values. Considering that the strain-rate at time t may be far away from the desired value, to achieve the above objective a tracking problem needs to be formulated, wherein the desired value may be reached after a finite number of steps, and from then on maintained at this value. At each time step, an optimal die velocity is generated based on the desired strain-rate value at that step, which is defined as z_{1i} , where 'i' stands for the current step number. z_{1i} is decided by the final desired strain-rate value ($\dot{\varepsilon}_d$), the effective strain-rate value from the previous step ($\dot{\varepsilon}_{i-1}$), and the specified constraints. This may be stated mathematically as,

$$z_{1i} = \begin{cases} \dot{\varepsilon}_{i-1} \pm m_x \dot{\varepsilon}_{i-1}, & |z_{1i} - \dot{\varepsilon}_d| > 0.03\dot{\varepsilon}_d \\ \dot{\varepsilon}_d, & |z_{1i} - \dot{\varepsilon}_d| < 0.03\dot{\varepsilon}_d \end{cases} \quad (5.1)$$

where m_x is a suitable percentage value (usually less than 5%) based on the machine's acceleration capability and the strain increment limit [58].

Temperature design is a much more difficult and complicated issue than velocity design. From chapter 3 it is observed that nodal temperatures are influenced by a number of heat generation and heat transfer terms. The first term in Eq. (3.9) (deformation heat generation) is dependent on the type of forging process used. This term plays a more important role in high speed forging processes like mechanical press forging (about 20 in/sec ram velocity) or hammer (about 80 in/sec ram velocity) forging. For these processes changing the die velocity in the

middle of the process is virtually impossible because of the high inertia of the die and the very short processing time involved. Therefore, in this study we confine ourselves to conventional forging processes utilizing hydraulic presses having ram velocities below 5 in/sec. Earlier, Boer et. al. [59] designed a varying die velocity profile for processing NIM80A material and implemented it on a hydraulic machine with a microcomputer as the controller. Since hydraulic presses operate at relatively low die velocities, the deformation heat generation is not very significant. Generally, while performing forging using hydraulic-type machines, the temperature in the middle of the billet increases by 30 to 40°F, while on the boundary surface this effect is totally counteracted by the die chilling effect, which is explained below.

The last four terms in Eq. (3.9) mainly affect the boundary surface temperature. Among these terms, the radiation heat term is neglected because it has an insignificant magnitude when compared to the other terms. Also, if the process does not last very long, the convection heat loss is again not very significant. At the boundaries, the friction heat has some influence on the temperature, but is still not the dominant term. The dominant factor is the heat conducted between the billet and die through the interface. Because the die temperature is usually much lower than that of the billet (up to 1000°F at times) the heat transfer due to conduction between these two bodies is very large, and a severe temperature gradient exists at the die-workpiece boundary. This phenomenon is called the die chilling effect. Compared to the 40°F increase in temperature in the middle of the billet due to deformation heat generation, the boundary temperature has a 300 to 400°F reduction in temperature due to the die chilling effect. Due to

the large temperature gradient between the center of the billet and the contact boundary, severe thermal stresses are induced which can radically increase die wear. The die chilling effect also affects the microstructure and mechanical properties of the workpiece because the resulting temperature gradient could result in a non-uniform distribution of service properties in the billet. Therefore, in this study, one of the primary goals is to determine a method to alleviate the die chilling effect. Since this phenomenon occurs mainly at the boundaries, only the treatment of boundary nodal temperatures was taken up during this work.

The difficulties involved in boundary nodal temperature control are apparent from its following two characteristics. First, temperature is an accumulated value and not an instantaneous quantity like strain rate. Second, it is not directly influenced by the die velocity. So, changes made in die velocity at some instant in time do not immediately affect the temperature. In this work, the objective selected for temperature control is to reduce the temperature range in the workpiece material. This is desirable because it would result in a more uniform distribution of mechanical properties in the final product. Since temperature is not easily controllable, for the scope of this work the goal is confined to raising the nodal temperatures above a specified value rather than trying to maintain them at the given value. To achieve the above objectives, the design scheme is again formulated as a tracking problem, and the lowest boundary nodal temperature is selected as the design parameter to achieve this goal. The logic behind this is if the lowest boundary temperature is maintained above a certain value, all the other boundary nodal temperatures would also be above the specified value.

Similar to strain-rate control, we define the desired nodal temperature at step i as z_{2i} , which can be generated in two ways. One way is to use the following formula:

$$z_{2i} = T_{i-1} + gd_{i-1}(1 - n) \Delta t \quad (5.2)$$

where T_{i-1} is the nodal temperature at step (i-1), and gd_{i-1} is the temperature gradient at step (i-1). n is a positive percentage value usually less than 3% and is again determined based on the machine capabilities and the strain increment limit. The objective of Eq. (5.2) is to reduce the temperature range by reducing the temperature gradient at each simulation step. Though it cannot give an accurate control of temperature, it is quite suitable for nonisothermal design involving die velocity as the lone design variable. The other method of defining the desired nodal temperature is by inputting a known polynomial approximation of the required temperature into the design scheme, as discussed later in the report.

In the nonisothermal design process, the output vector contains at least two output variables: the effective strain-rate and the nodal temperature. Without the initial die temperature parameter (explained later), the only control input is the die velocity. From control system theory, this is a single input multiple output (SIMO) system. The forging system also contains a constant vector \mathbf{W} in the system equation, which may be treated as a constant perturbation term [60]. For problems of this nature, several kinds of optimal control schemes have been developed. For example, the robust servomechanism design in reference 61 uses two servocompensators so that the resulting system is stable, and the steady-state error is zero for all kinds of disturbances. That means the disturbance could occur

in the system matrices, input/output vectors, or the feedback channels. The Proportional plus Integral state feedback design in reference 60 uses an integral feedback to eliminate the steady-state error caused by a known or unknown constant disturbance. However, the above two design schemes have the basic requirement that the number of control inputs should not be less than the number of system outputs. Therefore, this scheme cannot be utilized in the current SIMO problem.

In this work, the linear quadratic regulator (LQR) theory is used as a design tool for determining the optimal (forging) process parameters. LQR theory is one of the most popular design methods in optimal control. It is a proportional feedback design and can be used for SIMO and SISO systems. In this study, a terminal condition is also introduced into the standard LQR quadratic performance index to improve the error characteristics of the system. From Eq. (4.11), for step i which lasts from time t to $(t + \Delta t)$, the desired value vector may be defined as,

$$\mathbf{z}_i^T = [z_{1i} \ z_{2i}]$$

and the error vector may be expressed as,

$$\mathbf{e}_i(t) = \mathbf{z}_i - \mathbf{y}_i(t) \quad t \in (t, t + \Delta t)$$

Now, the following performance index may be used in the optimal design scheme:

$$J = \frac{1}{2} \mathbf{e}_i^T(\Delta t) \mathbf{M} \mathbf{e}_i(\Delta t) + \frac{1}{2} \int_0^{\Delta t} [\mathbf{e}_i^T(t) \mathbf{Q} \mathbf{e}_i(t) + \mathbf{U}_i^T(t) \mathbf{R} \mathbf{U}_i(t)] dt \quad (5.3)$$

where \mathbf{M} , \mathbf{Q} , and \mathbf{R} are the weighting matrices for the terminal condition, error, and input term, respectively, and \mathbf{U}_i is the input vector. For the isothermal case,

or in cases where only die velocity design is considered, $\mathbf{U}_i(t) = [V_{di}(t)]$. If initial die temperature design is also performed, $\mathbf{U}_i^T(t) = [V_{di}(t) \ \Delta T_{di}(t)]$, where ΔT_{di} is the initial die temperature adjustment parameter. Minimization of Eq. (5.3) gives [60]:

$$\mathbf{U}_i(t) = -\mathbf{R}^{-1}\mathbf{B}^T [\mathbf{K}_i(t)\mathbf{x}(t) - \mathbf{g}_i(t)] \quad (5.4)$$

where $\mathbf{K}_i(t)$ and $\mathbf{g}_i(t)$ are the solutions to the differential Riccati equations given by,

$$\begin{aligned} \dot{\mathbf{K}}_i(t) &= -\mathbf{K}_i(t)\mathbf{A} - \mathbf{A}^T\mathbf{K}_i(t) + \mathbf{K}_i(t)\mathbf{B}\mathbf{R}^{-1}\mathbf{B}^T\mathbf{K}_i(t) - \mathbf{C}^T\mathbf{Q}\mathbf{C} \\ \dot{\mathbf{g}}_i(t) &= [\mathbf{K}_i(t)\mathbf{B}\mathbf{R}^{-1}\mathbf{B}^T - \mathbf{A}^T]\mathbf{g}_i(t) - \mathbf{C}^T\mathbf{Q}\mathbf{z}_i + \mathbf{K}_i(t)\mathbf{W}\mathbf{r} \end{aligned} \quad (5.5)$$

In Eq. (5.5), \mathbf{K}_i and \mathbf{g}_i are time dependent, and are not constant because of the finite time integral in the performance index. However, if the output is more than the control input, there may be no solution for the infinite time optimal tracking problem [60]. Eq. (5.4) gives a solution series in the time interval $(t, t + \Delta t)$. To make the process more efficient and for reducing the computational time, the average of this solution series is taken as the optimal design. i.e.,

$$\mathbf{U}_i^{opt} = \frac{\sum_j^n \mathbf{U}_i(t_j)}{n} \quad t_j \in (t, t + \Delta t) \quad (5.6)$$

where n is the number of smaller time intervals into which step i is divided for solving Eq. (5.5). For most cases, it has been observed that Eq. (5.6) is a reasonably good and acceptable assumption.

To give an overview of the methodology, the state space model is developed based on the finite element simulation, and then the LQR design scheme is used

to design the optimal process parameters. This is an off-line design scheme, and the purpose is to use control theory as a design tool rather than to design a practical control system. The emphasis is on obtaining die velocity profiles and the initial die temperature, rather than in stabilizing the control loops as done in classical control system design. The entire design scheme developed is illustrated in Fig. 6.

During nonisothermal forging process design, the strain-rate control and the temperature control may have a conflicting requirement on the die velocity. For example, the strain rate control may need the die velocity to be reduced; at the same time the temperature control may actually require the die velocity to be increased. In such a situation the strain-rate control is given higher priority because the strain-rate is more sensitive to changes in the die velocity. Therefore, in this design scheme, if the above mentioned conflict occurs, the die velocity is decided based on the strain-rate. Actually, temperature is not an easily controllable quantity and the main contribution of the optimal die velocity design to the thermal aspect of the process is in reducing the temperature range in the deforming billet by reducing the die-workpiece contact time. This may not always be possible, though, and a more effective way to directly influence the interface temperature is by designing an appropriate initial die temperature for the process.

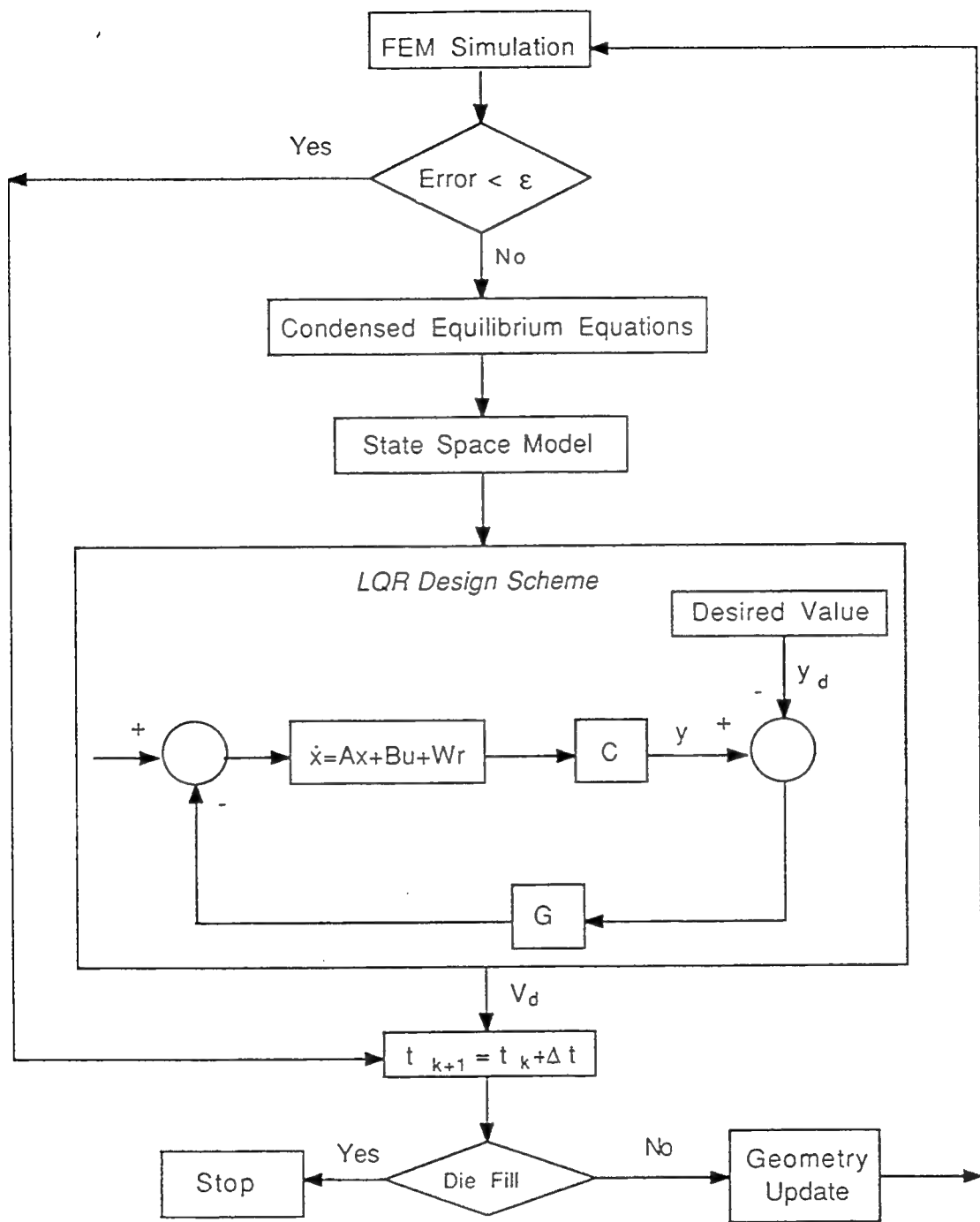


Figure 6: Design scheme flow chart

5.2 Initial die temperature design

Because of the strong die chilling effect during hydraulic press forging, the most efficient way to influence the boundary nodal temperatures and reduce the temperature range in the workpiece is by designing the initial die temperature. Since the entire design methodology is based on the LQR design scheme, it is preferable to continue to apply the LQR method for initial die temperature design also. But, LQR is a step by step design scheme, while initial die temperature is a single value and needs to be specified at the beginning of the process. To solve this problem, the following design approach is proposed.

In this scheme, a new design variable called die temperature adjustment (ΔT_d) is introduced. By adding ΔT_d to the present die temperature (T_d) the total die temperature is given by ($T_d + \Delta T_d$), and Eq. (3.12) may now be written as,

$$\int_{S_I} h_{lub} (T_d + \Delta T_d - T_w) \mathbf{N}_T dS = \mathbf{H}_d T_d + \mathbf{H}_d \Delta T_d - \mathbf{K}_w \mathbf{T}_w$$

By using this equation instead of Eq. (3.12) in developing the state space model, the modified state equation may be written as,

$$\dot{\mathbf{x}} = \mathbf{A}\mathbf{x} + \begin{bmatrix} \mathbf{B}_D & \mathbf{0} \\ \bar{\mathbf{B}}_{TP} & \mathbf{H}_d \end{bmatrix} \begin{bmatrix} V_d \\ \Delta T_d \end{bmatrix} + \mathbf{W}r \quad (5.7)$$

The difference between Eq. (4.11) and Eq. (5.7) is that in the latter, the input matrix \mathbf{B} has been expanded and now there are two input variables instead of one. If $\Delta T_d = 0$, then Eq. (5.7) will yield the same results as Eq. (4.11). The term $\mathbf{H}_d \Delta T_d$ actually changes the temperature gradient at each step by a certain amount. \mathbf{H}_d mainly contains shape functions and heat transfer coefficients and

does not change much during the whole process. For a case in which the temperature gradient needs to be reduced by the same amount at each time step (by applying the ΔT_d correction), nearly the same ΔT_d value may be expected from the LQR design scheme. This suggests that to achieve the design objective, the actual initial die temperature should be changed by the average value of ΔT_d for all the time steps. i.e.,

$$\Delta T_{d0} = \frac{\sum_i^n \Delta T_d}{n} \quad (5.8)$$

where i is the design step count and n is the total number of design steps. It has been found that with the (new) initial die temperature ($T_d + \Delta T_{d0}$) designed in this manner, the boundary nodal temperature may be altered sufficiently to meet the design requirement.

To implement this scheme, the key issue during initial die temperature design is how to generate a desired nodal temperature profile which not only satisfies the design requirement, but also gives nearly the same temperature gradient change at each design step. Through parametric studies it was found that for hydraulic press forging, the temperature curve of a die-contacting node is nearly a straight line. Therefore, we may with reasonable accuracy use a 3rd order polynomial to approximate the temperature path of a particular node with respect to time. Then, by changing the coefficient of the first order term in the polynomial, we can generate the desired temperature profile. The problem now becomes one of tracking the desired temperature profile. The above design scheme works successfully if the die temperature is not very close to the billet temperature, and if the die velocity does not vary by a significant amount. These conditions hold good in most hot die forging cases. The detailed procedure for designing

the initial die temperature is explained in the numerical examples section of this report.

5.3 LQR design scheme

In Eq. (4.11) \mathbf{E} is a constant vector and can be grouped into the left side of the output equation, with the vector of desired values. Now, the state space model representing the system may be written as,

$$\dot{\mathbf{x}} = \mathbf{Ax} + \mathbf{Bu} + \mathbf{W} \quad (5.9)$$

$$\mathbf{y} = \mathbf{Cx} \quad (5.10)$$

where the state vector \mathbf{x} has a dimension n , the input vector \mathbf{u} has a dimension m and the output vector \mathbf{y} has a dimension p . n , m , and p refer to the number of states, number of inputs, and number of outputs in the system, respectively. Then, \mathbf{A} (system matrix) is a $n \times n$ matrix, \mathbf{B} (input matrix) is a $n \times m$ matrix, and \mathbf{C} (output matrix) is a $p \times n$ matrix. \mathbf{W} is a known vector resulting from the finite element condensation procedure. During the derivation, to make the notations simple, the integration limits are set as $t_0 = t_k$ and $T = t_k + \Delta t$, where t_0 and T are the lower and upper integration limits in the performance index equation. If the desired output is \mathbf{z} , and the error vector is $\mathbf{e} = \mathbf{z} - \mathbf{y}$, the performance index is given by,

$$J = \frac{1}{2} \mathbf{e}^T(T) \mathbf{M} \mathbf{e}(T) + \frac{1}{2} \int_{t_0}^T [\mathbf{e}^T(t) \mathbf{Q}(t) \mathbf{e}(t) + \mathbf{u}^T(t) \mathbf{R} \mathbf{u}(t)] dt$$

where \mathbf{Q} is a $n \times n$ semi-positive definite matrix for weighting the error vector, \mathbf{R} is a $m \times m$ positive definite matrix for weighting the input vector, and \mathbf{M} is

a semi-positive definite matrix used for weighting the terminal condition. The method of selection of these weighting matrices is explained in section 5.4 of this chapter. Some important steps in the derivation of the optimal control scheme are described below [49]. The error vector, \mathbf{e} , may be written as,

$$\mathbf{e} = \mathbf{z} - \mathbf{Cx} \quad (5.11)$$

By following the standard state space equation solving procedure, and by substituting Eq. (5.11) into the performance index, the Hamiltonian function may be written as,

$$\mathbf{H} = \frac{1}{2}[\mathbf{z} - \mathbf{Cx}]^T \mathbf{Q} [\mathbf{z} - \mathbf{Cx}] + \frac{1}{2}\mathbf{u}^T \mathbf{R} \mathbf{u} + \mathbf{x}^T \mathbf{A}^T \lambda + \mathbf{u}^T \mathbf{B}^T \lambda + \mathbf{W}^T \lambda$$

where λ is a Lagrange multiplier. From the condition, $\frac{\partial \mathbf{H}}{\partial \mathbf{u}} = \mathbf{0}$, we have,

$$\mathbf{R} \mathbf{u} + \mathbf{B}^T \lambda = \mathbf{0}$$

$$\mathbf{u} = -\mathbf{R}^{-1} \mathbf{B}^T \lambda \quad (5.12)$$

From $\dot{\lambda} = -\frac{\partial \mathbf{H}}{\partial \mathbf{x}}$, we have,

$$\dot{\lambda} = -\mathbf{C}^T \mathbf{Q} \mathbf{C} \mathbf{x} + \mathbf{C}^T \mathbf{Q} \mathbf{z} - \mathbf{A}^T \lambda \quad (5.13)$$

By substituting Eq. (5.12) into Eq. (5.9),

$$\dot{\mathbf{x}} = \mathbf{A} \mathbf{x} - \mathbf{B} \mathbf{R}^{-1} \mathbf{B}^T \lambda + \mathbf{W} \quad (5.14)$$

Now, by defining the following terms,

$$\mathbf{S} = \mathbf{B} \mathbf{R}^{-1} \mathbf{B}^T$$

$$\mathbf{V} = \mathbf{C}^T \mathbf{Q} \mathbf{C}$$

$$\mathbf{P} = \mathbf{C}^T \mathbf{Q}$$

we can group Eq. (5.13) and Eq. (5.14) as,

$$\begin{bmatrix} \dot{\mathbf{x}} \\ \dot{\lambda} \end{bmatrix} = \begin{bmatrix} \mathbf{A} & -\mathbf{S} \\ -\mathbf{V} & -\mathbf{A}^T \end{bmatrix} \begin{bmatrix} \mathbf{x} \\ \lambda \end{bmatrix} + \begin{bmatrix} \mathbf{W}r \\ \mathbf{Pz} \end{bmatrix} \quad (5.15)$$

This represents a $2n \times 2n$ system, where n is the number of states in the state space model.

If Φ is the state transition matrix, the solution to Eq. (5.15) is given by,

$$\begin{bmatrix} \mathbf{x}(T) \\ \lambda(T) \end{bmatrix} = \Phi(T, t) \left(\begin{bmatrix} \mathbf{x}(t) \\ \lambda(t) \end{bmatrix} + \int_t^T \Phi^{-1}(\tau, t) \begin{bmatrix} \mathbf{W}(\tau)r(\tau) \\ \mathbf{P}(\tau)\mathbf{z}(\tau) \end{bmatrix} d\tau \right) \quad (5.16)$$

i.e.,

$$\begin{bmatrix} \mathbf{x}(T) \\ \lambda(T) \end{bmatrix} = \Phi(T, t) \begin{bmatrix} \mathbf{x}(t) \\ \lambda(t) \end{bmatrix} + \begin{bmatrix} \mathbf{g}_1(t) \\ \mathbf{g}_2(t) \end{bmatrix} \quad (5.17)$$

The $2n$ boundary conditions corresponding to the current system are,

$$\begin{aligned} t &= t_0, \quad \mathbf{x}(t_0) = \xi \\ \lambda(T) &= \frac{\partial}{\partial \mathbf{x}(T)} \left[\frac{1}{2} \mathbf{e}^T(T) \mathbf{M} \mathbf{e}(T) \right] \\ t &= T; \\ &= \mathbf{C}^T(T) \mathbf{M} \mathbf{C}(T) \mathbf{x}(T) - \mathbf{C}^T(T) \mathbf{M} \mathbf{z}(T) \end{aligned}$$

Now, by defining $\mathbf{C}^T(T) \mathbf{M} \mathbf{C}(T) = \mathbf{G}(T)$, we have,

$$\lambda(T) = \mathbf{G}(T) \mathbf{x}(T) - \mathbf{C}^T(T) \mathbf{M} \mathbf{z}(T) \quad (5.18)$$

Also, say,

$$\Phi(T, t) = \begin{bmatrix} \Phi_{11} & \Phi_{12} \\ \Phi_{21} & \Phi_{22} \end{bmatrix}$$

Then, Eq. (5.17) becomes,

$$\begin{bmatrix} \mathbf{x}(T) \\ \lambda(T) \end{bmatrix} = \begin{bmatrix} \Phi_{11} & \Phi_{12} \\ \Phi_{21} & \Phi_{12} \end{bmatrix} \begin{bmatrix} \mathbf{x}(T) \\ \lambda(T) \end{bmatrix} + \begin{bmatrix} \mathbf{g}_1(t) \\ \mathbf{g}_2(t) \end{bmatrix}$$

Substituting Eq. (5.18) into the above equation, we have:

$$\lambda(t) = [\Phi_{22} - \mathbf{G}\Phi_{12}]^{-1} \left([\mathbf{G}\Phi_{11} - \Phi_{21}] \mathbf{x}(t) + [\mathbf{G}\mathbf{g}_1(t) - \mathbf{g}_2(t) - \mathbf{C}^T(T) \mathbf{M}\mathbf{z}] \right)$$

Now, by assuming,

$$\mathbf{K}(t) = [\Phi_{22} - \mathbf{G}\Phi_{12}]^{-1} [\mathbf{G}\Phi_{11} - \Phi_{21}] \quad (5.19)$$

$$\mathbf{g}(t) = [\Phi_{22} - \mathbf{G}\Phi_{12}]^{-1} [\mathbf{G}\mathbf{g}_1(t) - \mathbf{g}_2(t) - \mathbf{C}^T(T) \mathbf{M}\mathbf{z}] \quad (5.20)$$

we have,

$$\lambda = \mathbf{K}(t) \mathbf{x}(t) - \mathbf{g}(t) \quad (5.21)$$

where $\mathbf{K}(t)$ is a $n \times n$ time-varying matrix, and $\mathbf{g}(t)$ is a n -dimensional vector.

By differentiating Eq. (5.21) with respect to t , we have,

$$\dot{\lambda} = \dot{\mathbf{K}}\mathbf{x} + \mathbf{K}\dot{\mathbf{x}} - \dot{\mathbf{g}} \quad (5.22)$$

Then, substituting Eq. (5.21) into Eq. (5.14), we get,

$$\dot{\mathbf{x}} = [\mathbf{A} - \mathbf{SK}] \mathbf{x} + \mathbf{Sg} + \mathbf{Wr} \quad (5.23)$$

Now, substituting Eq. (5.23) into Eq. (5.22), we get,

$$\dot{\lambda} = [\dot{\mathbf{K}} + \mathbf{KA} - \mathbf{KSK}] \mathbf{x} + \mathbf{KSg} + \mathbf{KW}r - \dot{\mathbf{g}} \quad (5.24)$$

Substituting Eq. (5.21) into Eq. (5.13), $\dot{\lambda}$ may also be written as,

$$\dot{\lambda} = [-\mathbf{V} - \mathbf{A}^T \mathbf{K}] \mathbf{x} + \mathbf{A}^T \mathbf{g} + \mathbf{P} \mathbf{z} \quad (5.25)$$

Comparing Eq. (5.24) and Eq. (5.25), we have,

$$\dot{\mathbf{K}} = -\mathbf{K} \mathbf{A} - \mathbf{A}^T \mathbf{K} + \mathbf{K} \mathbf{S} \mathbf{K} - \mathbf{V}$$

i.e.,

$$\dot{\mathbf{K}} = -\mathbf{K} \mathbf{A} - \mathbf{A}^T \mathbf{K} + \mathbf{K} \mathbf{B} \mathbf{R}^{-1} \mathbf{B}^T \mathbf{K} - \mathbf{C}^T \mathbf{Q} \mathbf{C} \quad (5.26)$$

and,

$$\dot{\mathbf{g}} = [\mathbf{K} \mathbf{B} \mathbf{R}^{-1} \mathbf{B}^T - \mathbf{A}^T] \mathbf{g} - \mathbf{C}^T \mathbf{Q} \mathbf{z} + \mathbf{K} \mathbf{W} \mathbf{r} \quad (5.27)$$

The above equations are the differential Riccati equations mentioned in section (5.1). The corresponding boundary condition for this system is:

$$\lambda(T) = \mathbf{K}(T) \mathbf{x}(T) - \mathbf{g}(T)$$

$$\lambda(T) = \mathbf{C}^T(T) \mathbf{M} \mathbf{C}(T) - \mathbf{C}^T \mathbf{M} \mathbf{z}(T)$$

where,

$$\begin{aligned} \mathbf{K}(T) &= \mathbf{C}^T(T) \mathbf{M} \mathbf{C}(T) \\ \mathbf{g}(T) &= \mathbf{C}^T(T) \mathbf{M} \mathbf{z}(T) \end{aligned} \quad (5.28)$$

By solving Eq. (5.26) and Eq. (5.27) together with the boundary conditions from Eq. (5.28), the optimal design solution may be obtained. While computing the solutions of Eq. (5.26) and Eq. (5.27), the Pade approximation [47] method has been used in determining the state transformation matrix Φ . Eqs. (5.19) and (5.20) are then used to calculate \mathbf{K} and \mathbf{g} [48].

5.4 Selection of weighting matrices for control

The selection of weighting matrices during optimal control is a very difficult issue, and no general method exists which is applicable to all kinds of systems and problems. Generally, weighting matrices are determined by a trial and error process or are based on parametric studies. In nonisothermal forging process design, the boundary conditions may change significantly from one time step to the next, so that the system equations could be totally different between steps. Therefore, using constant weighting matrices for different design problems is practically impossible. In this study, the following matrices are used during process parameter design as the weighting matrices [65]:

$$\mathbf{Q} = \text{diag} \left[\frac{1}{\mathbf{e}_{max}^2} \right]$$

$$\mathbf{M} = 100\mathbf{Q}$$

$$\mathbf{R} = \begin{bmatrix} \frac{\mathbf{Q}_{11}}{r} & 0 \\ 0 & 0.01 \end{bmatrix}$$

Here, r is a positive value varying between 1 and 100, and is automatically decided by the computer program based on the deviation of the process parameters from their respective desired values. This quantity actually forces the change of the design parameters within fixed constraints. Usually, an isothermal design uses a large value of r compared to a nonisothermal design process. For plane strain cases in general, and for complex problems it was found that the above weighting matrix scheme was resulting in numerical difficulties during implementation. For such cases, the weighting matrices were constrained within certain finite bounds determined using systematic parametric studies.

CHAPTER 6

Numerical Examples - Full Size State Space Model

A general purpose computer program COPP (Control of Optimal Processing Parameters) has been developed to implement the design techniques described in this work. This program is built on the rigid viscoplastic finite element program ALPID (Analysis of Large Plastic Incremental Deformation). In addition to using ALPID subroutines for analysis purposes, a design and control module has been developed and built into the program for designing the optimal process parameters. Along with the ALPID input file, COPP requires a small design input data file, the format of which is presented in Appendix (B). Appendix B also contains a detailed user's manual with examples for running this program. In general, COPP has the following capabilities:

1. ALPID simulation for both isothermal and nonisothermal processes.
2. Optimal die velocity design for isothermal process.
3. Optimal die velocity design for nonisothermal process.
4. Initial die temperature design for nonisothermal process.

This chapter presents a few numerical examples to support and substantiate the theory presented in earlier sections of the report. The case of an axisymmetric engine disk forging (Fig. 7) is considered under different operating conditions. The material used for the simulation is Ti-6242 (Titanium alloy), which is a strain-rate sensitive material. Due to its symmetry, only a quarter section of the cylindrical billet is modeled. Discretization of the billet continuum was performed using 50 isoparametric quadrilateral elements (Fig. 8), and the die was modeled using 73 finite elements. A constant shear friction factor of 0.3 was used at the die-billet interface. A billet temperature of $1735^{\circ}F$ and a die temperature of $600^{\circ}F$ was specified at the beginning of the process. A total die stroke of 0.50 inch was required to complete the forging operation as shown in Fig. 7.

6.1 Model validation

The accuracy of the state space model in representing the metal forming system has been tested extensively and validated using ALPID simulation results. The testing was done for both isothermal and nonisothermal processes using varying frictional conditions, different die velocities, and for a range of different materials. The response of the state space system was found to be in close conformance with the ALPID simulation results. One such example is presented here to establish the effectiveness of the state space model in capturing the deformation characteristics of the forging process.

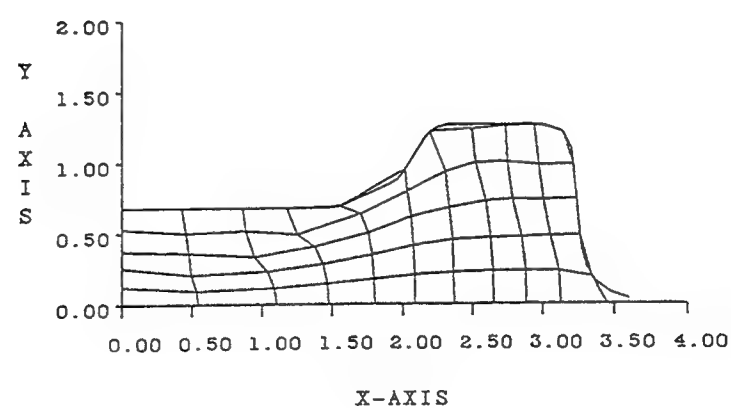
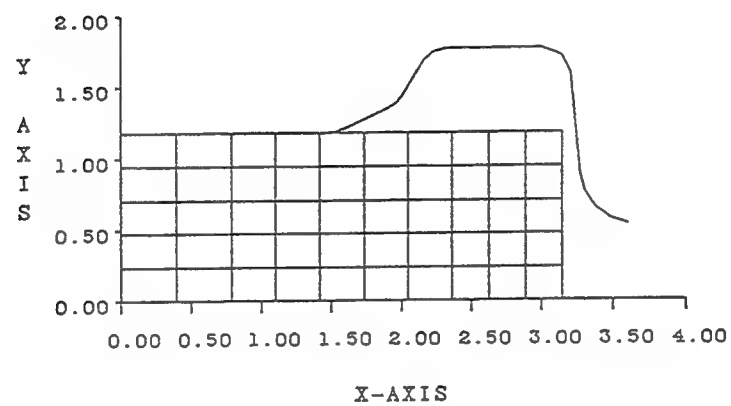
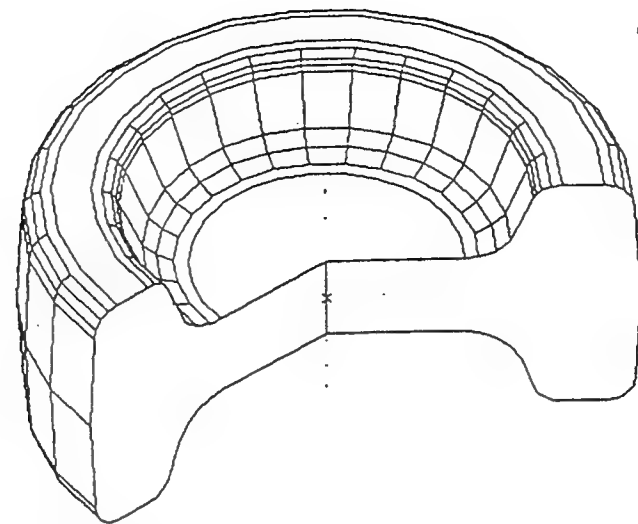


Figure 7: Engine disk forging - FEM simulation

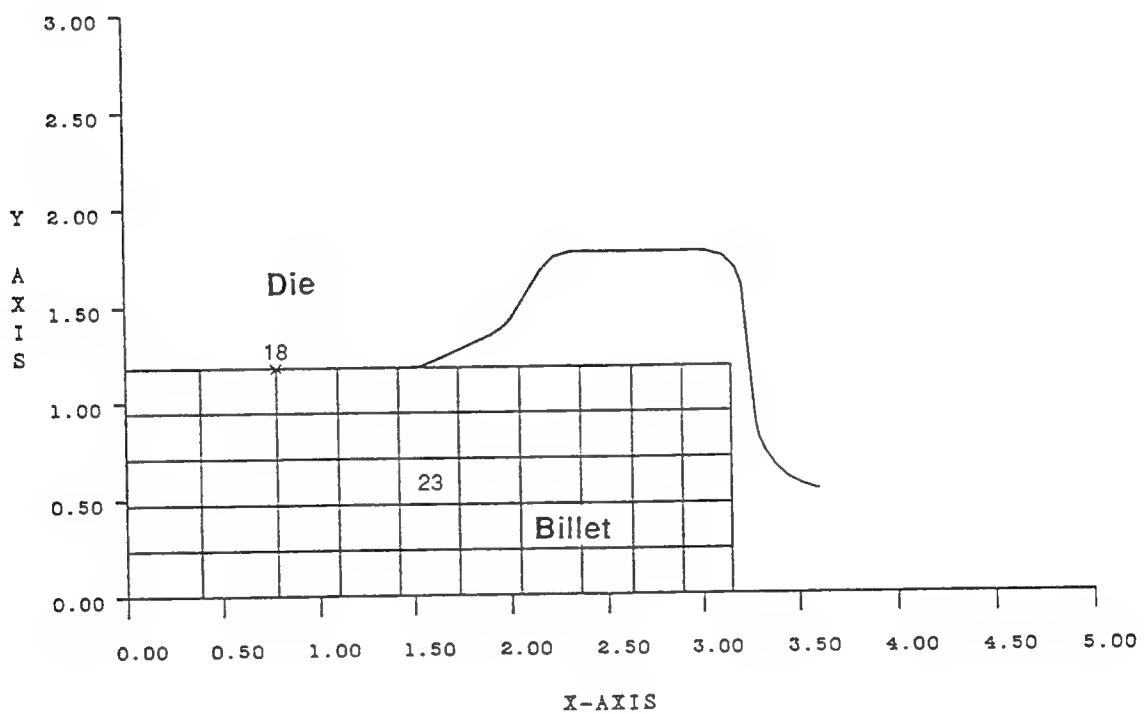


Figure 8: FEM discretization of the billet

Consider the forging of the engine disk described earlier. Element 23 is selected as the element of interest. The rationale behind this is, due to its location in the workpiece, element 23 is always under deformation and is also likely to go through a number of modes of deformation. As a result this element is very sensitive to changes in the die velocity and is a good candidate to be selected as the control element. As shown in Fig. 9, the state space model is built at 18% reduction when the stroke is 0.33 inch and the die velocity is 1.0 in/sec. In the current state space system, 17 state variables are used for describing the nodal velocities. Of these, 9 are the tangential nodal velocities of the die-contacting boundary nodes and the rest are nodal velocities of element 23. In addition, 14 states are used to describe the nodal temperatures. Among these, 10 are nodal temperatures of the die-contacting nodes, and the other four are temperatures of the nodes constituting element 23. The full size state space model thus has 31 state variables. Now, a small perturbation of 0.0025 in/sec is given to the die velocity to activate the response of the state space model. At the same time, this change in die velocity is also implemented in ALPID. The results from the state space system and those from ALPID (which serves as the reference) are then tabulated and compared (Table 1). The results presented in Table 1 show that the temperature field and the nodal velocity field (for element 23) generated by the state space system closely match with those of the ALPID simulation.

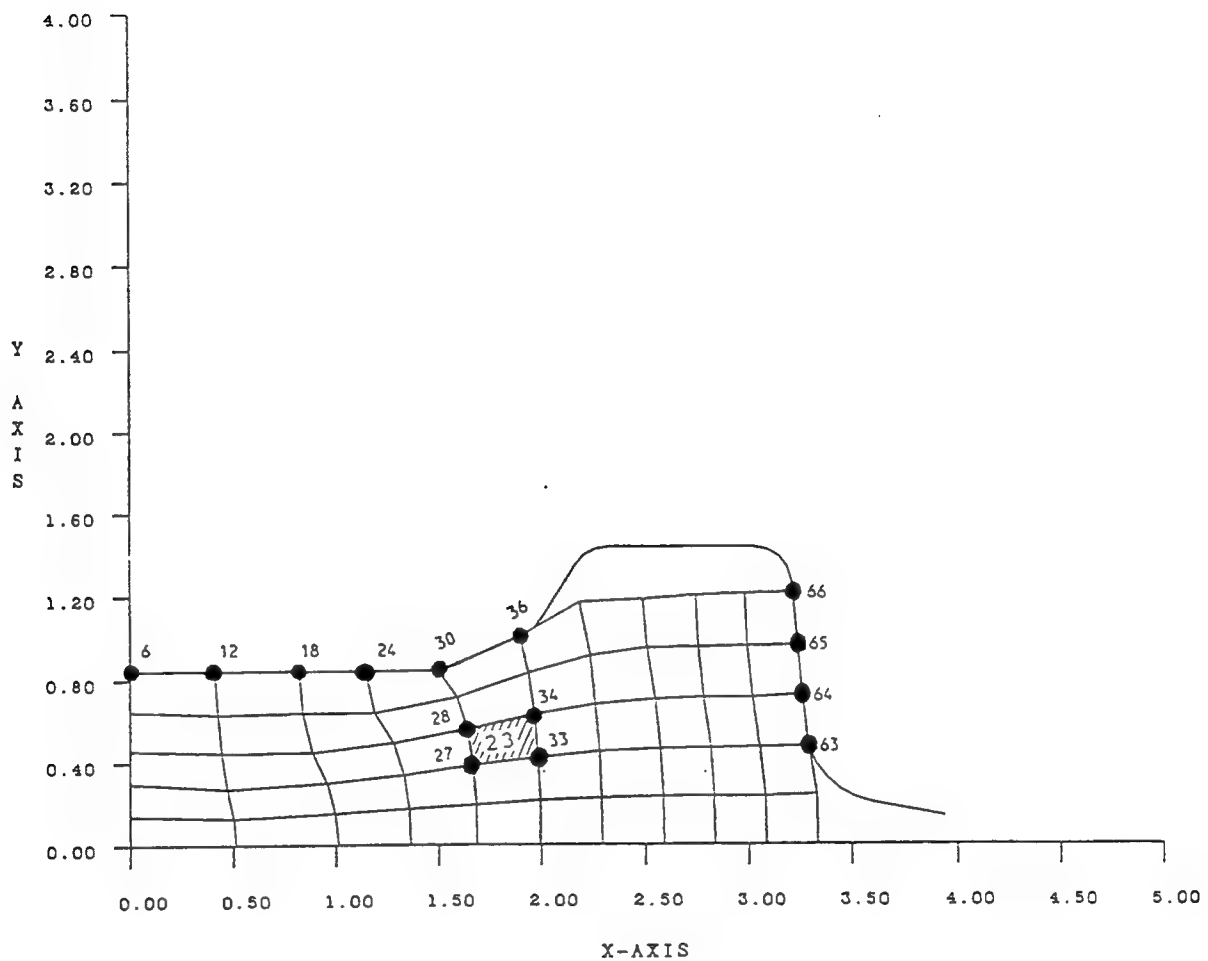


Figure 9: Validation of the state space model

Table 1. Model Validation: State space model vs. ALPID**t=0.33292 + 0.0 (sec)****Velocity Field (in/sec)**

N.O.F.	State Space Model	ALPID	Error (%)
23	0.10078E+00	0.10078E+00	—
35	0.15708E+00	0.15708E+00	—
47	0.20641E+00	0.20641E+00	—
59	0.14646E+00	0.14646E+00	—
71	0.14127E-01	0.14127E-01	—
125	-0.11512E+00	-0.11512E+00	—
127	-0.26875E+00	-0.26875E+00	—
129	-0.29317E+00	-0.29317E+00	—
131	-0.33610E+00	-0.33610E+00	—
53	0.86712E+00	0.86712E+00	—
54	-0.30277E+00	-0.30277E+00	—
55	0.73772E+00	0.73772E+00	—
56	-0.52864E+00	-0.52864E+00	—
65	0.83599E+00	0.83599E+00	—
66	-0.14027E+00	-0.14027E+00	—
67	0.75102E+00	0.75102E+00	—
68	-0.21921E+00	-0.21921E+00	—

N.O.F.: Nodal degree of freedom

Table 1. (Continued)

t=0.33292 + 0.0 (sec)

Temperature Field ($^{\circ}$ F)

N.O.F.	State Space Model	ALPID	Error (%)
6	0.17418E+04	0.17418E+04	—
12	0.15857E+04	0.15857E+04	—
18	0.15509E+04	0.15509E+04	—
24	0.15602E+04	0.15602E+04	—
27	0.17465E+04	0.17465E+04	—
28	0.17491E+04	0.17491E+04	—
30	0.15454E+04	0.15454E+04	—
33	0.17421E+04	0.17421E+04	—
34	0.17433E+04	0.17433E+04	—
36	0.16389E+04	0.16389E+04	—
63	0.17079E+04	0.17079E+04	—
64	0.16738E+04	0.16738E+04	—
65	0.16513E+04	0.16513E+04	—
66	0.16337E+04	0.16337E+04	—

N.O.F.: Nodal degree of freedom

Table 1. (Continued)

$t=0.33292 + 0.005 \text{ (sec)}$

Velocity Field (in/sec)

N.O.F.	State Space Model	ALPID	Error (%)
23	0.10090E+00	0.10562E+00	4.4684
35	0.15719E+00	0.16308E+00	3.6095
47	0.20655E+00	0.21551E+00	4.1550
59	0.14656E+00	0.15717E+00	6.7457
71	0.14061E-01	0.14151E-01	0.6354
125	-0.11519E+00	-0.12870E+00	10.4985
127	-0.26891E+00	-0.27671E+00	2.8208
129	-0.29331E+00	-0.29747E+00	1.3996
131	-0.33622E+00	-0.33604E+00	0.0537
53	0.86752E+00	0.88153E+00	1.5902
54	-0.30291E+00	-0.30300E+00	0.0301
55	0.73804E+00	0.75044E+00	1.6529
56	-0.52889E+00	-0.53073E+00	0.3459
65	0.83638E+00	0.84936E+00	1.5283
66	0.14034E+00	-0.13878E+00	1.1298
67	0.75135E+00	0.76265E+00	1.4823
68	-0.21932E+00	-0.21743E+00	0.8694

N.O.F.: Nodal degree of freedom

Table 1. (Continued)

$t=0.33292 + 0.005 \text{ (sec)}$

Temperature Field ($^{\circ}\text{F}$)

N.O.F.	State Space Model	ALPID	Error (%)
6	0.17420E+04	0.17420E+04	0.0006
12	0.15840E+04	0.15842E+04	0.0103
18	0.15489E+04	0.15488E+04	0.0072
24	0.15584E+04	0.15582E+04	0.0096
27	0.17467E+04	0.17466E+04	0.0044
28	0.17494E+04	0.17494E+04	0.0039
30	0.15432E+04	0.15430E+04	0.0122
33	0.17423E+04	0.17423E+04	0.0032
34	0.17435E+04	0.17434E+04	0.0058
36	0.16370E+04	0.16366E+04	0.0235
63	0.17063E+04	0.17060E+04	0.0172
64	0.16713E+04	0.16714E+04	0.0023
65	0.16490E+04	0.16490E+04	0.0014
66	0.16312E+04	0.16311E+04	0.0047

N.O.F.: Nodal degree of freedom

Table 1. (Continued) **$t=0.33292 + 0.01 \text{ (sec)}$** **Velocity Field (in/sec)**

N.O.F.	State Space Model	ALPID	Error (%)
23	0.10099E+00	0.10842E+00	6.8529
35	0.15728E+00	0.16655E+00	5.5713
47	0.20665E+00	0.22100E+00	6.4914
59	0.14664E+00	0.16244E+00	9.7278
71	0.14011E-01	0.15191E-01	7.7659
125	-0.11524E+00	-0.13458E+00	14.3705
127	-0.26902E+00	-0.27961E+00	3.7885
129	-0.29342E+00	-0.29832E+00	1.6414
131	-0.33634E+00	-0.33486E+00	0.4417
53	0.86784E+00	0.88620E+00	2.0716
54	-0.30302E+00	-0.30269E+00	0.1094
55	0.73830E+00	0.75574E+00	2.3080
56	-0.52910E+00	-0.53030E+00	0.2280
65	0.83671E+00	0.85311E+00	1.9227
66	-0.14040E+00	-0.13830E+00	1.5162
67	0.75161E+00	0.76531E+00	1.7895
68	-0.21940E+00	-0.21693E+00	1.1403

N.O.F.: Nodal degree of freedom

Table 1. (Continued)

$t=0.33292 + 0.01 \text{ (sec)}$

Temperature Field ($^{\circ}\text{F}$)

N.O.F.	State Space Model	ALPID	Error (%)
6	0.17423E+04	0.17423E+04	0.0010
12	0.15824E+04	0.15827E+04	0.0212
18	0.15469E+04	0.15467E+04	0.0138
24	0.15565E+04	0.15562E+04	0.0185
27	0.17470E+04	0.17468E+04	0.0088
28	0.17497E+04	0.17496E+04	0.0078
30	0.15409E+04	0.15406E+04	0.0232
33	0.17425E+04	0.17424E+04	0.0064
34	0.17437E+04	0.17435E+04	0.0116
36	0.16350E+04	0.16343E+04	0.0455
63	0.17047E+04	0.17041E+04	0.0373
64	0.16689E+04	0.16690E+04	0.0050
65	0.16466E+04	0.16466E+04	0.0031
66	0.16286E+04	0.16285E+04	0.0102

N.O.F.: Nodal degree of freedom

It may be noticed, however, that boundary nodes behave differently from the interior nodes and tend to have greater error margins. The error in the velocities of the boundary nodes is due to the complex effects of friction, temperature gradient, and changes in boundary conditions. In spite of these errors we still have very accurate velocity field modeling for elements within the boundary. Therefore, in the present design scheme, elements at the boundary are generally not selected as elements of interest.

Based on the above example and other similar cases, we may conclude that the state space model is capable of satisfying the design requirements and can be used as an effective numerical model for design of the process parameters. It was also observed that, overall, the state space model was found to give more accurate results for the frictionless case as compared to the friction case. Also, the results of the isothermal model were generally found to be better than those of the nonisothermal state space model.

6.2 Temperature gradient reduction

One of the primary design objectives in this work is to reduce the temperature gradient at the boundaries, because this would alleviate the thermal stresses induced at the boundaries due to the die chilling effect. This example illustrates the influence of temperature gradient reduction on the boundary nodal temperatures. The design requirements are chosen arbitrarily just to illustrate the method. It is assumed that the temperature gradient at node 18 needs to be reduced, and the effective strain-rate of element 23 ($\dot{\varepsilon}_{23}$) is to be maintained at 2.0 1/sec. The only design parameter is the die velocity. The process is started

with a relatively low die velocity of 0.5 in/sec, which results in $\dot{\varepsilon}_{23}$ around 0.25 1/sec. This gives enough room to change the die velocity by large amounts to illustrate the effectiveness of the current method. For comparison purposes, two sets of designs are carried out, and the results are presented in Figs. 10 through 12.

The first design, called 'Design I', does not include temperature gradient reduction, and merely involves controlling the strain rate. The output variable of Design I is $\dot{\varepsilon}_{23}$. The second design, 'Design II', is similar to Design I, but in addition involves a temperature gradient reduction of 3% at every time step, and has node 18's temperature added into the output vector. Eqs. (5.1) and (5.2) are used to obtain the desired $\dot{\varepsilon}_{23}$ and T_{18} , respectively. The weighting matrices are the same for the two designs, except that Design II has an additional weighting factor corresponding to the temperature output. During Design I die velocity increases at a steady rate till $\dot{\varepsilon}_{23}$ reaches 2.0 1/sec at a stroke of 0.23 inch. In Design II, the strain-rate increases faster than in Design I because of the effect of temperature gradient reduction. To reduce the temperature gradient the heat generation rate needs to be faster than normal. This can be achieved only by increasing the die velocity. As a result, the strain rate also increases at a faster rate and reaches the required value quicker than in the previous case. When the stroke approaches 0.13 inch, a sudden jump in the strain-rate occurs because the workpiece comes in contact with the far end of the die. Consequently, $\dot{\varepsilon}_{23}$ overshoots the desired value of 2.0 1/sec. The die velocity is now reduced to bring $\dot{\varepsilon}_{23}$ back to 2.0 1/sec. The desired value is finally achieved at a stroke of 0.17 inch. Examining the temperature profiles in Fig. 12, it is observed that before

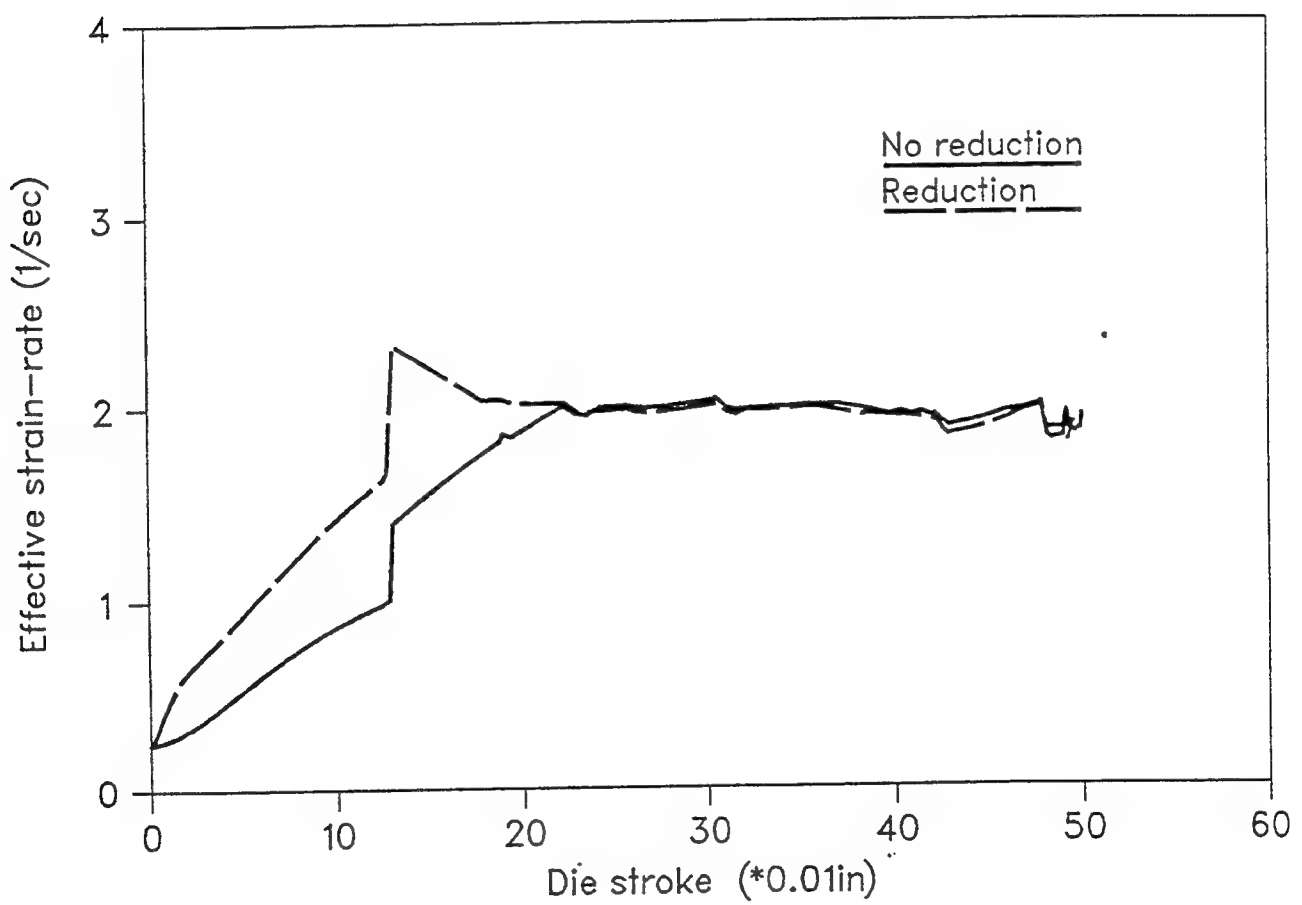


Figure 10: Temperature gradient reduction - Strain rates

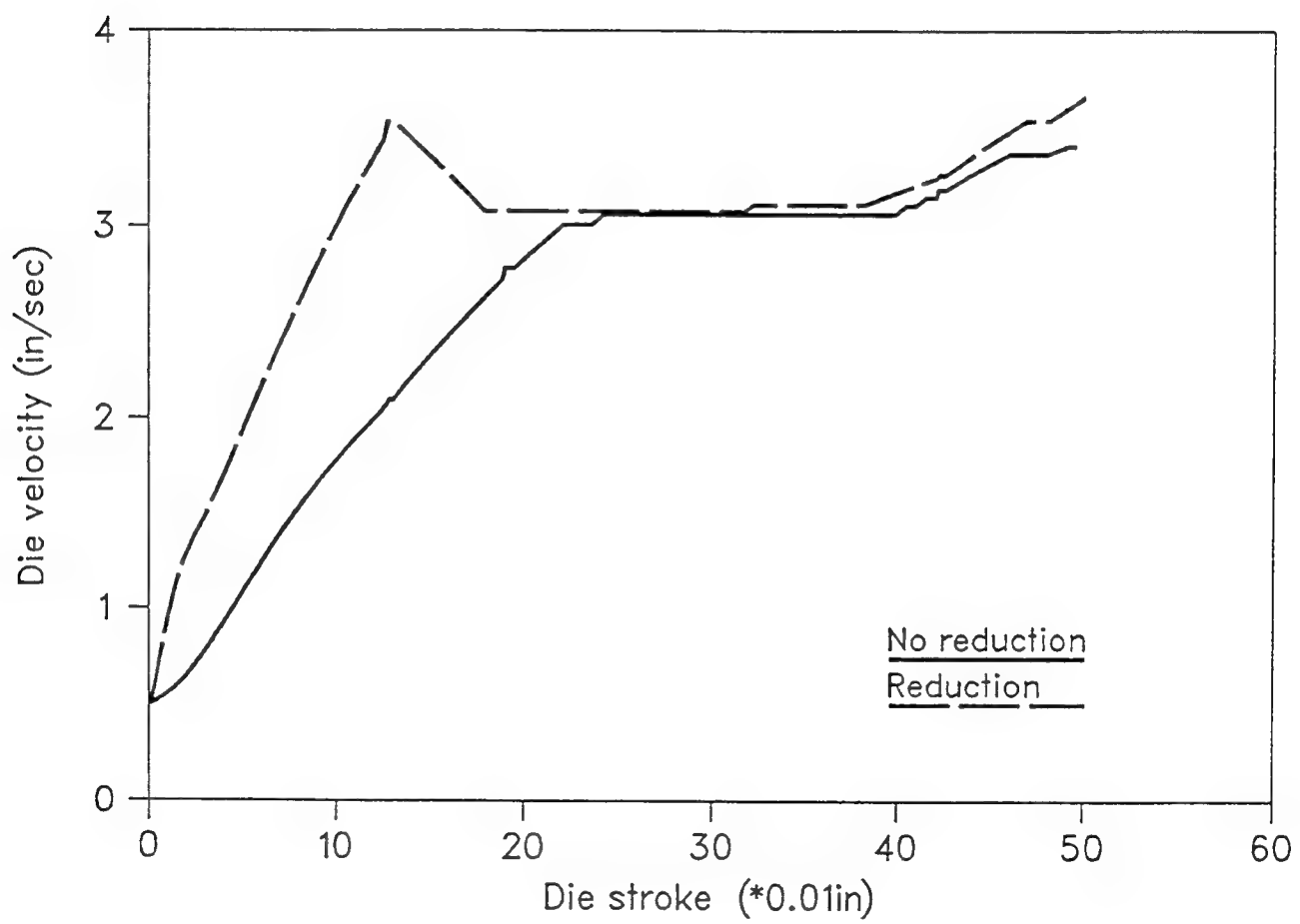


Figure 11: Temperature gradient reduction - Die velocities

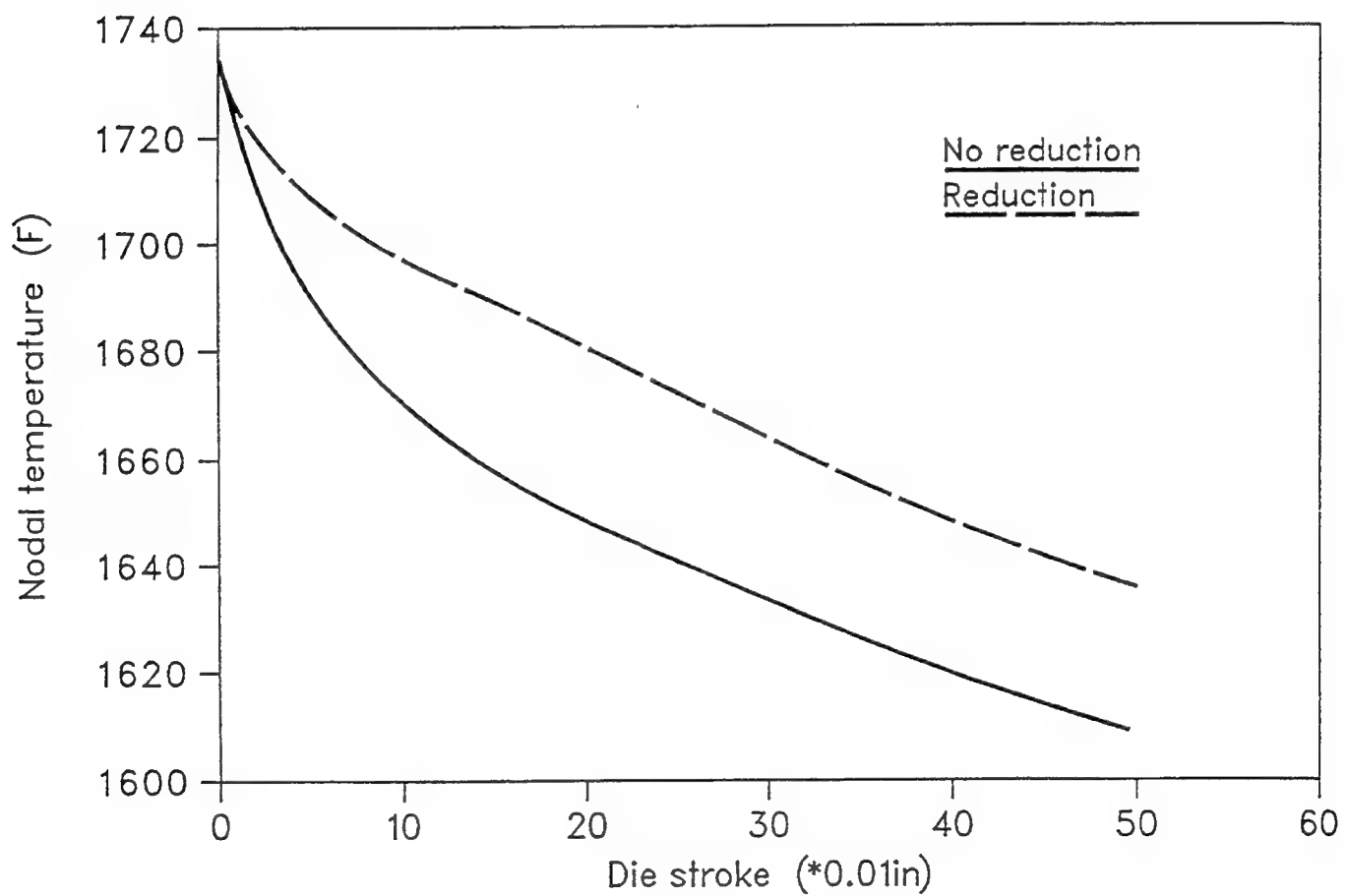


Figure 12: Temperature gradient reduction - Temperature profiles

a stroke of 0.20 inch, the temperature gradient shows a definite reduction in the second case. But after that, the gradients of both curves are nearly the same because the die velocities in both cases are almost the same. At the end of the process, the temperature of node 18 is $1609^{\circ}F$ in Design I and $1635^{\circ}F$ in Design II, a $26^{\circ}F$ increase in the latter case. It may be concluded that temperature gradient reduction results in an increase in temperature of the die-contacting boundary nodes. It should be noted, though, that this increase is largely a result of the reduced die-workpiece contact time because the die velocity is higher in Design II than in Design I. This example shows that using the optimal design scheme, a suitable die velocity profile may be generated that maintains the strain rate of critical elements at the desired value and at the same time reduces the temperature gradient at the die-workpiece interface.

6.3 Isothermal design

This example uses the same engine disk forging model described earlier. An isothermal design is presented which requires the effective strain-rate of element 23 to be maintained at 0.1 1/sec . The starting die velocity is about 0.25 in/sec , corresponding to an $\dot{\varepsilon}_{23}$ value of 0.125 1/sec . Fig. 13 shows that this starting $\dot{\varepsilon}_{23}$ value is quickly reduced to 0.1 1/sec because the design scheme calls for a reduction in the die velocity. During the initial stages of forging the change in $\dot{\varepsilon}_{23}$ is relative small, but around a stroke of 0.13 inch a large jump (nearly a 50% increase) in $\dot{\varepsilon}_{23}$ may be noticed. This is because of the sudden change in the deformation mode of the workpiece as it comes in contact with the far end of the die. However, as shown in Fig. 14, the design scheme is robust and effective, and

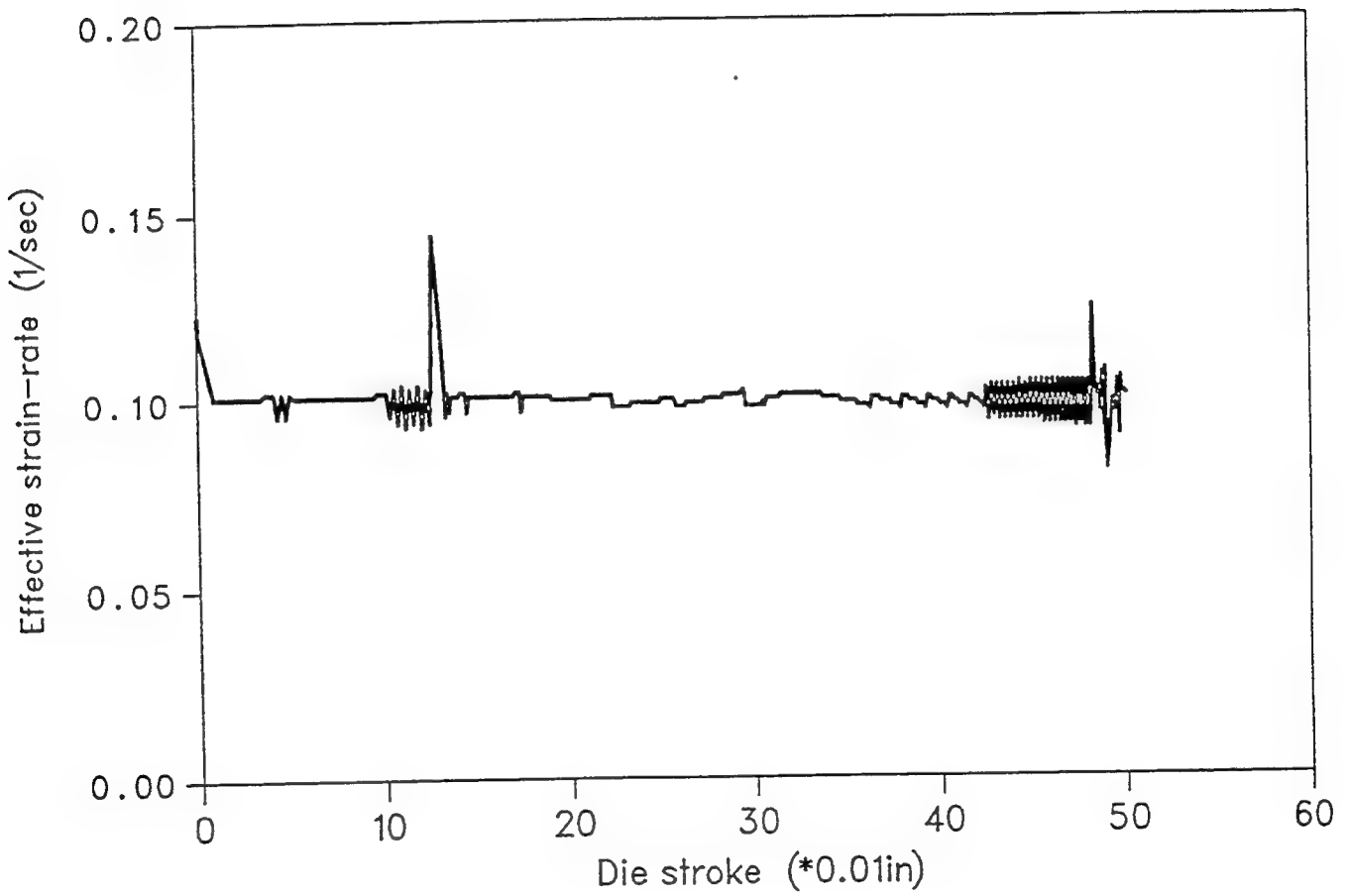


Figure 13: Isothermal design - Strain rates

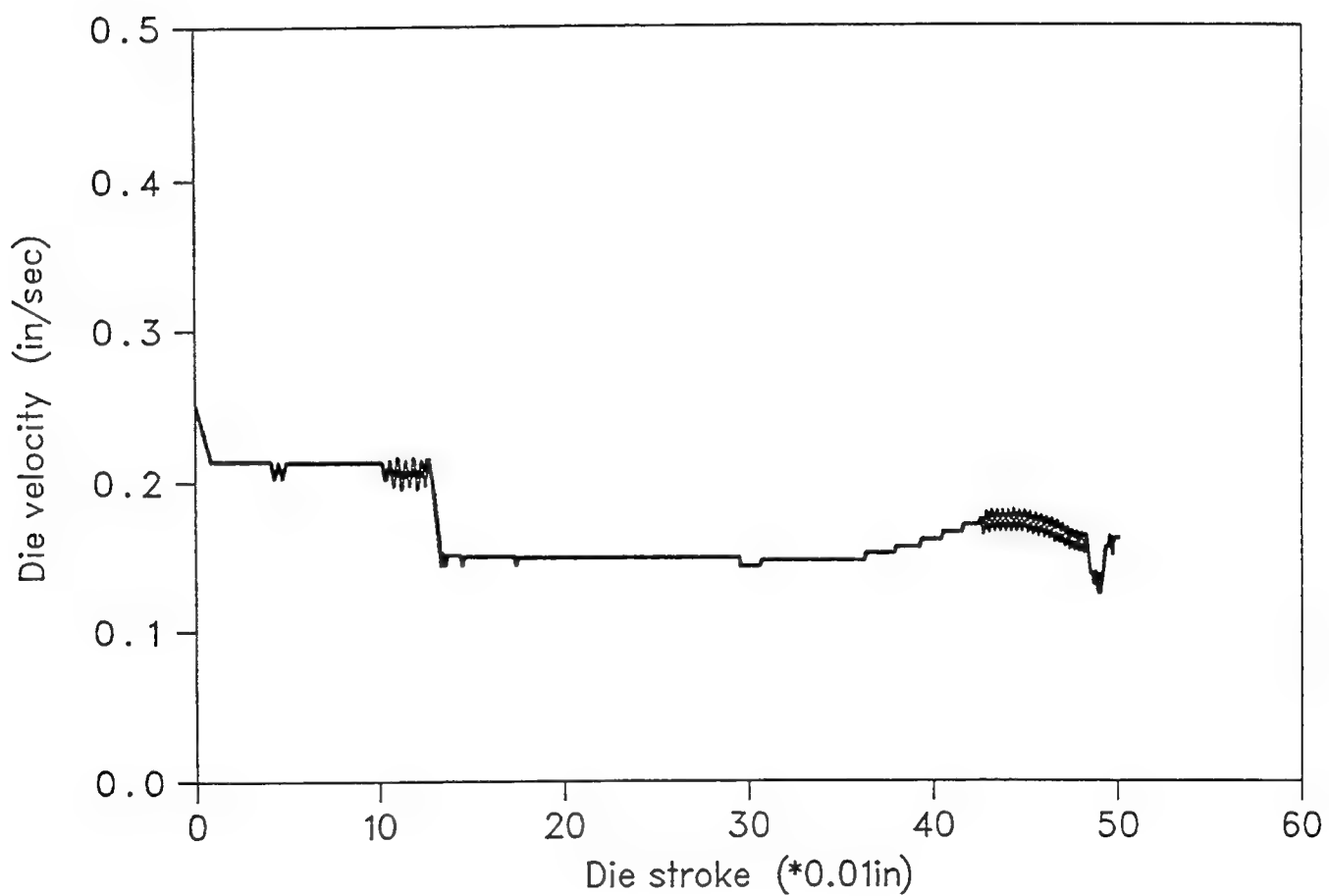


Figure 14: Isothermal design - Die velocities

immediately reduces the die velocity and brings the effective strain-rate back to 0.1 1/sec in a short time without much oscillation. Near the end of the process, though, some instability is observed, causing a considerable amount of oscillation in both the die velocity and strain-rate. This could be due to the complex nature of forces that come into play during the die filling process.

6.4 Temperature range reduction

In most hot die forging processes, one of the design objectives is to reduce the temperature range in the billet as much as possible. This improves the temperature distribution and results in a more uniform distribution of properties in the final workpiece. The following numerical example is presented to illustrate how the above objective may be met using the proposed design methodology. The optimization problem is stated as:

$$\text{Minimize : } |T_{\max} - T_{\min}| \quad (6.1)$$

$$\text{Subject to : } \dot{\varepsilon}_{\max} \leq 2.5 \text{ 1/sec} \quad (6.2)$$

$$\text{Design variable : } V_d$$

where Eq. (6.2) applies a constraint that requires the maximum effective strain-rate in the billet to be no more than 2.5 1/sec. The present design scheme is used to generate an optimum ram velocity profile to solve the problem stated above. The optimal results are then compared with the constant velocity results to demonstrate the effectiveness of the proposed design methodology.

Through finite element simulations it was found that node 18 possesses the lowest temperature in the billet throughout the process. This is because node 18

remains in contact with the die from beginning to end, and the strain rate in the vicinity of node 18 is not very high. The temperature range in Eq. (6.1) may now be approximated to $(T_{max} - T_{18})$, where T_{18} is the temperature of node 18. The design scheme has the ability to automatically select the element possessing the largest strain-rate as the element of interest and design an optimal die velocity schedule based on the strain rate constraint imposed. Fig. 15 gives the strain-rate schedule for the element(s) having the largest strain rate in the workpiece at any given time step, and Fig. 16 gives the corresponding optimal die velocity profile. With a starting value of 2.1 in/sec, the designed ram velocity gradually reduces keeping $\dot{\varepsilon}_{max}$ around 2.5 1/sec for the entire process. The designed ram velocity profile gives the largest value of die velocity that can be used without violating the constraint of Eq. (6.2). Hence, the profile also gives the minimum contact time between the die and billet. By minimizing the contact time, the total heat loss and the temperature range in the workpiece are also reduced. At the end of the process, node 18's temperature (the lowest temperature in the billet) is $1574^{\circ}F$ and the maximum temperature in the billet is $1777^{\circ}F$, giving a temperature range of $203^{\circ}F$.

For comparison, the above example was also simulated using a constant die velocity. Because $\dot{\varepsilon}_{max}$ gradually increases under a constant die velocity, the largest constant die velocity which can be used without exceeding the constraint is 1.25 in/sec. By examining Figs. 15 and 16 it may be observed that even though for most of the process $\dot{\varepsilon}_{max}$ is far below 2.5 1/sec limit, we can use a constant die velocity no larger than 1.25 in/sec; otherwise $\dot{\varepsilon}_{max}$ would violate the strain rate constraint towards the end of the stroke.

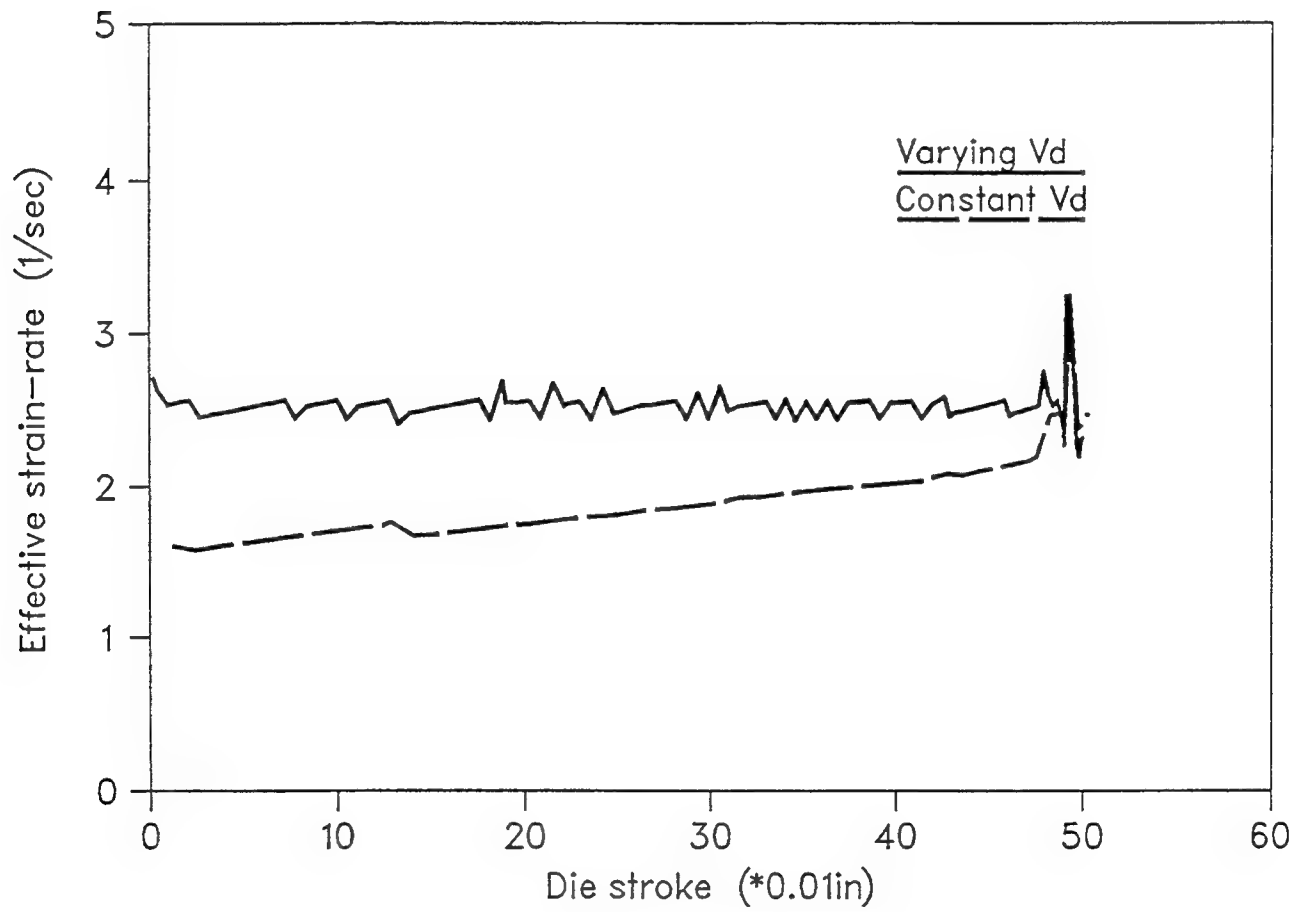


Figure 15: Temp. variance reduction - Strain rates

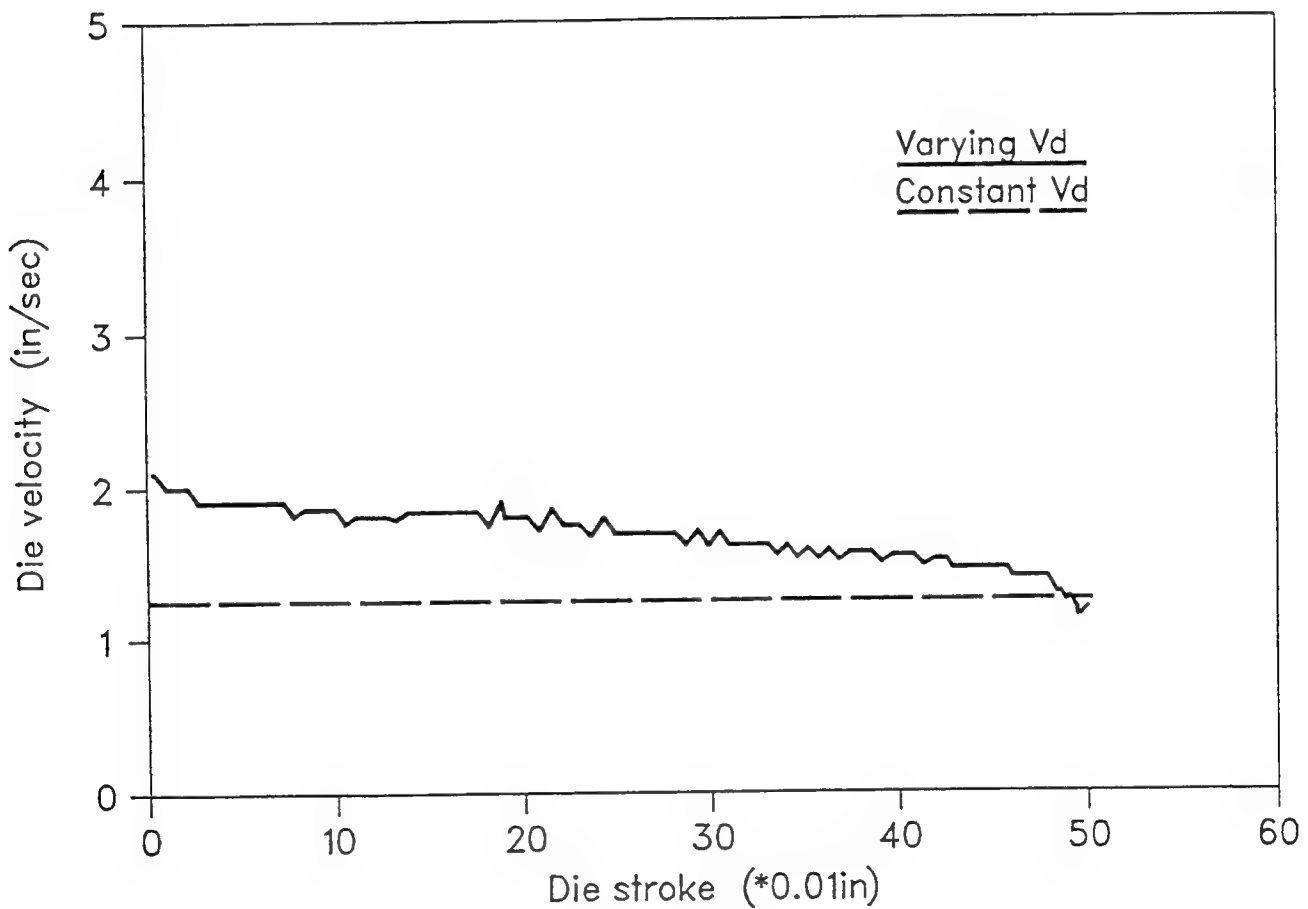


Figure 16: Temp. variance reduction - Die velocities

In this example the constant velocity is lower than the optimal ram velocity for most of the forging process (Fig. 16). This results in a longer die-workpiece contact time in the former case. At the end of the simulation it may be observed that node 18 has a temperature of $1533^{\circ}F$, and the maximum temperature in the billet is $1775^{\circ}F$. The temperature range thus turns out to be $242^{\circ}F$. Fig. 17 clearly illustrates the difference in temperature profiles (of node 18) for the two cases, and Fig. 18 gives the corresponding load-stroke curves. There is only a slight increase in load while using the optimal die velocity because the design scheme is based on the minimum energy concept. This example shows that by using this design scheme, an optimal die velocity profile can be generated to minimize the die-workpiece contact time and the temperature range in the deforming workpiece. Table 2 lists some of the performance benefits derived by using this methodology.

Table 2. Performance of the optimal control design scheme

	Optimum Velocity	Constant Velocity
Max. Temp. ($^{\circ}F$)	1777	1775
Min. Temp. ($^{\circ}F$)	1574	1533
Temp. Range ($^{\circ}F$)	203	242
Range Reduced (%)	16	—
Process Time (sec)	0.300	0.402
Time Reduced (%)	25.4	—

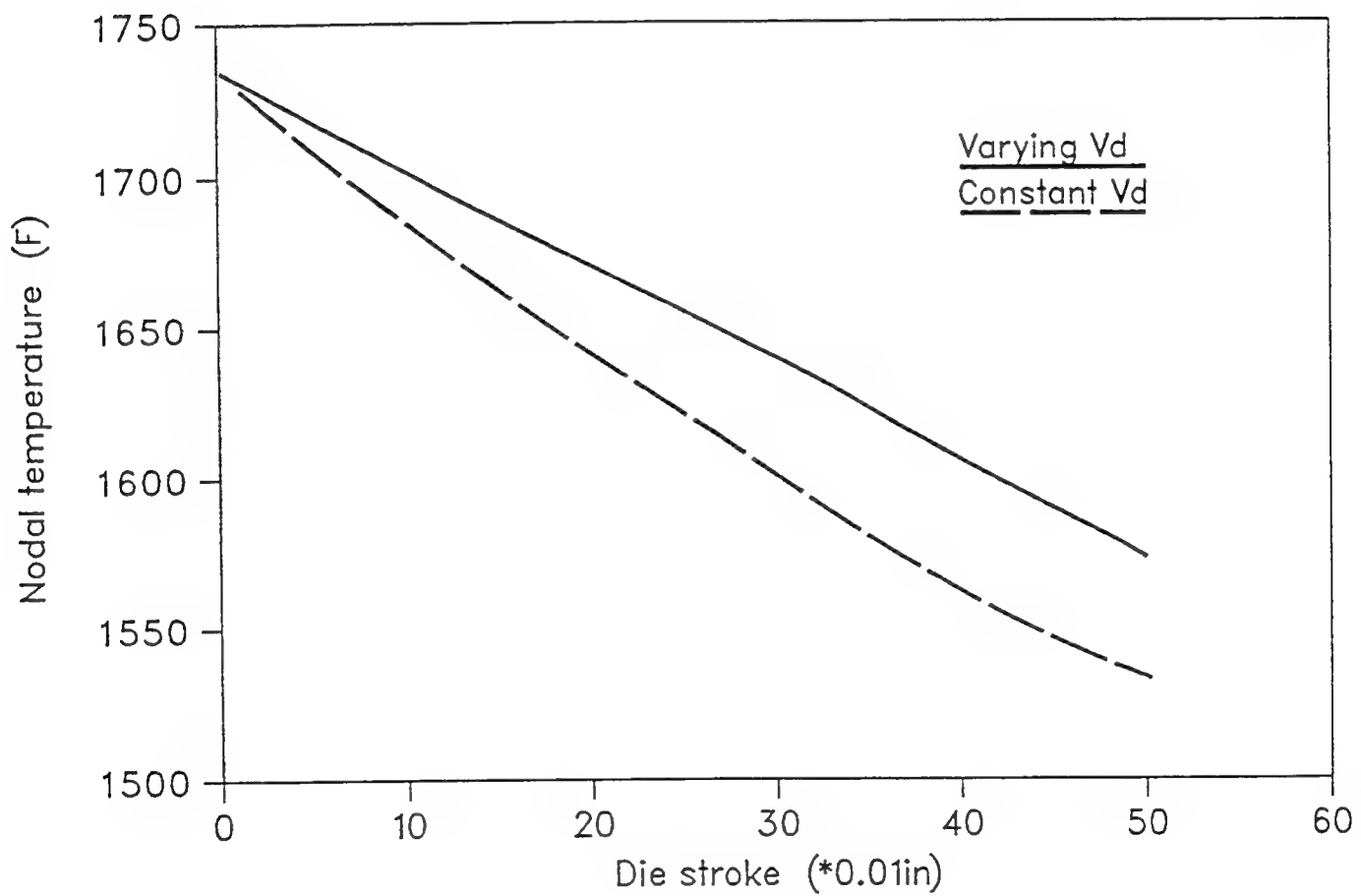


Figure 17: Temp. variance reduction - Node 18 temp. profiles

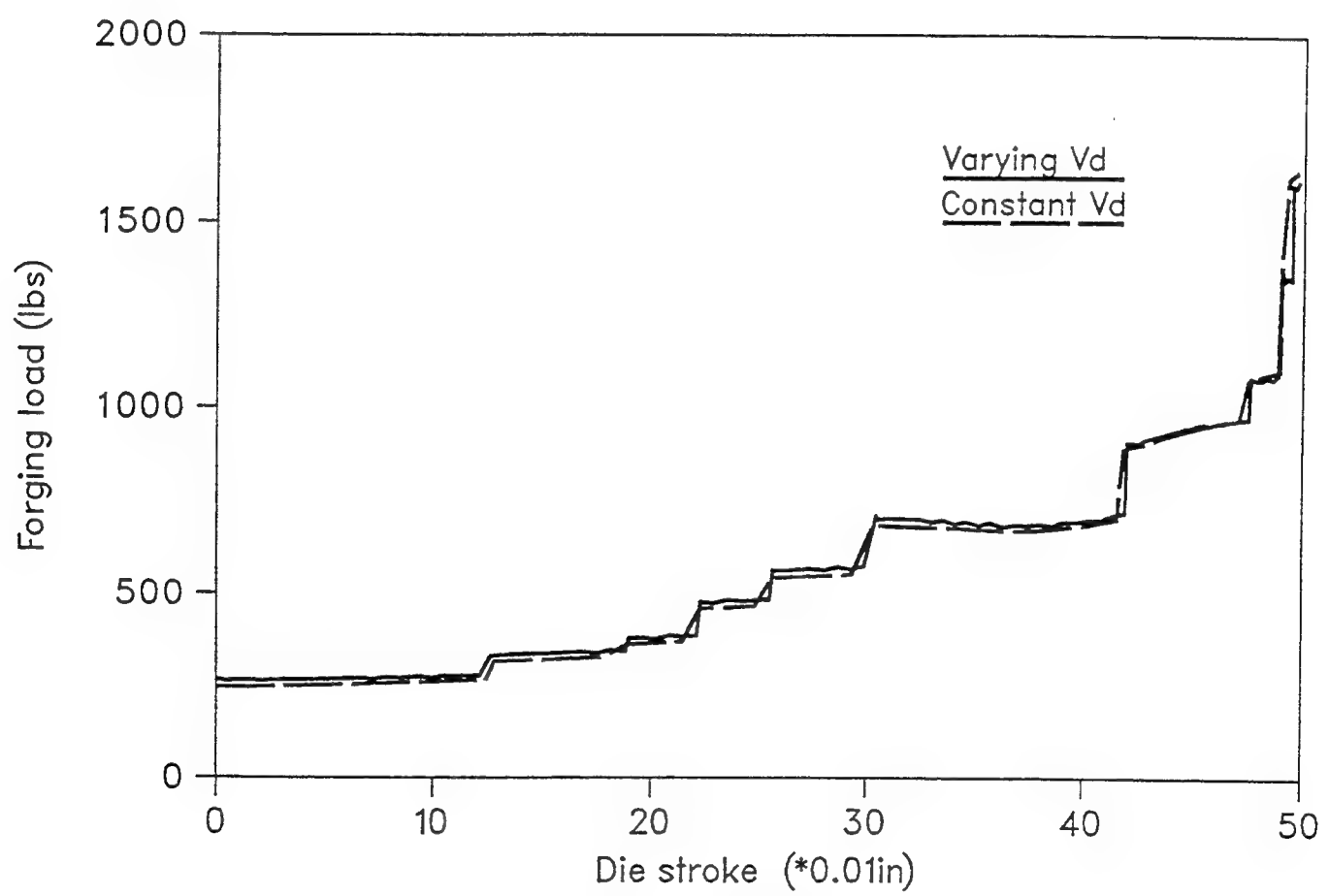


Figure 18: Temp. variance reduction - Load stroke curves

6.5 Initial die temperature design

In forging processes, selection of initial die temperature is an important but difficult decision to make. This numerical example describes how the proposed design methodology could be used to obtain an optimal initial die temperature value. The design problem for this example may be stated as follows:

$$\text{Objective : } T_{18} > 1560^{\circ}\text{F} \quad (6.3)$$

$$\text{Subject to : } \dot{\varepsilon}_{23} = 0.7 \text{ 1/sec} \quad (6.4)$$

Design variables : T_d and V_d

where $\dot{\varepsilon}_{23}$ is the effective strain-rate of element 23 (critical element as explained earlier), and T_d is the initial die temperature. Because node 18 (critical node) possesses the lowest temperature in the billet, Eq. (6.3) is equivalent to raising the temperature of the whole billet above 1560°F . The design is carried out in three steps, each necessitating an independent finite element simulation.

Step 1. Generating the desired nodal temperature profile.

In this step, the design is conducted using only die velocity as the design variable. The initial die temperature used is 600°F . The purpose of this step is to: (1) check whether Eq. (6.3) can be satisfied without changing the initial die temperature, and (2) generate a suitable polynomial representing the temperature path of node 18 that satisfies the constraints of Eq. (6.4). The design is started when the die velocity, V_d , is equal to 1.4 in/sec, corresponding to $\dot{\varepsilon}_{23}$ equal to 0.698 1/sec. Checking the results at the end of the simulation, the temperature

of node 18 temperature was found to be $1519^{\circ}F$. Figs. 20 through 22 give the profiles of $\dot{\varepsilon}_{23}$, V_d and T_{18} , respectively for this example. It may be observed from Fig. 20 that the strain rate constraint of Eq. (6.4) is satisfied for the entire process under the optimal die velocity (V_d) in Fig. 21. At the same time, Fig. 22 shows that the temperature constraint of Eq. (6.3) is not satisfied. This calls for an increase in the initial die temperature so as to bring the temperature of node 18 to the required value. To represent the desired temperature profile, a 3rd order polynomial is used to fit the path of T_{18} as,

$$T_{18} = 1735 - 641.37t + 355.5t^2 - 25.1t^3 \quad (6.5)$$

In Eq. (6.5) the first order term is the dominant term influencing the temperature gradient. To raise the nodal temperature, therefore, the coefficient of the first order term has to be changed to an appropriate value. By setting $T_{18} = 1560^{\circ}F$ at end of the process, the new first order coefficient (from Eq. (6.5)) was calculated as -550. Substituting this back into Eq. (6.5) we have,

$$T_{18} = 1735 - 550t + 355.5t^2 - 25.1t^3 \quad (6.6)$$

Eq. (6.6) gives the desired temperature profile for node 18 during the initial die temperature adjustment design.

Step 2. Adjusting the initial die temperature

With Eq. (6.6) as the desired temperature profile, the design in step 1 is repeated using an additional design variable ΔT_d , which is the initial die temperature adjustment parameter. The other conditions remain the same as in Step 1. The value of ΔT_d at every time step is calculated using the proposed design

scheme and presented in Fig. 19. By using Eq. (5.8) to average the ΔT_d values at each simulation time step, a mean initial die temperature adjustment value of $172^\circ F$ is obtained (represented by the dashed line in Fig. 19). The actual initial die temperature which satisfies all the design constraints is thus $772^\circ F$.

Step 3. Redesign using the new initial die temperature

This step is merely a repeat of step 1 with the new initial die temperature value of $772^\circ F$ (instead of $600^\circ F$). From Figs. 20 and 21, the profiles of the die velocity and $\dot{\varepsilon}_{23}$ are similar before and after initial die temperature design. This shows that changing the initial die temperature does not affect the strain-rate of the control element significantly. The temperature of node 18, though, is very sensitive to the change in initial die temperature as observed in Fig. 22. With a $172^\circ F$ higher initial die temperature, the final temperature of node 18 is $1557^\circ F$, very close to the design requirement of $1560^\circ F$ (a difference of about 7.5%). The temperature gradient of the boundary nodes (node 18 in particular) is thus reduced. At the same time, it was also observed that the temperature range was reduced from $256^\circ F$ to $218^\circ F$, a drop of about 14%.

This example shows that the proposed method for initial die temperature (adjustment) design works well, and can be effectively used to reduce the temperature range/temperature gradient in the deforming workpiece. Noting that the increase in boundary nodal temperatures is not linearly proportional to the increase in initial die temperature, solving a design problem such as the one posed in this example would be very difficult and cumbersome without a systematic methodology and/or strategy like the one described in this section. One

of the major advantages of the method described here is that the design can be performed in three simulation steps instead of going through a number of trial and error steps as is done normally. This could save a considerable amount of time, effort, and money during the entire design process.

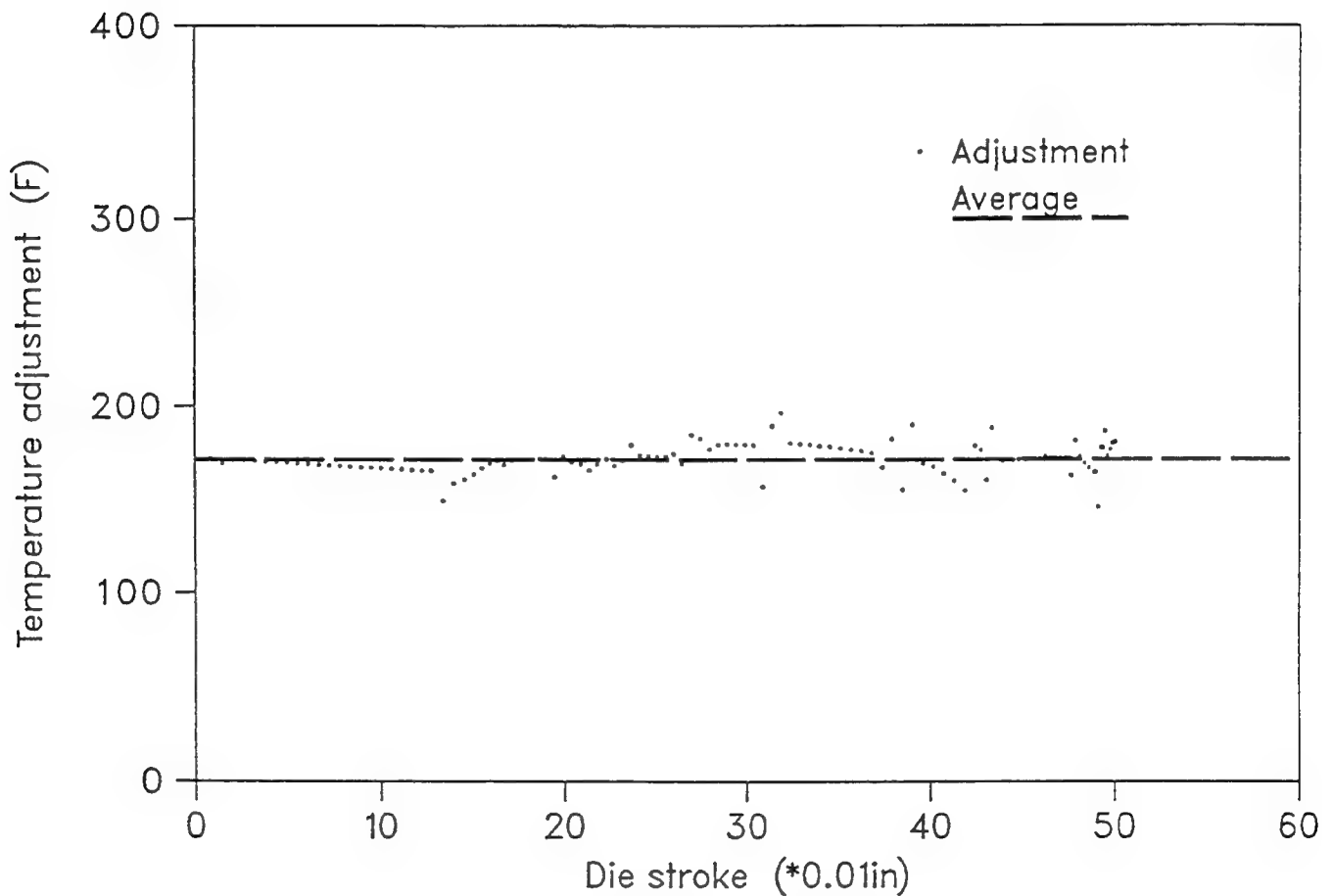


Figure 19: Initial die temperature adjustment

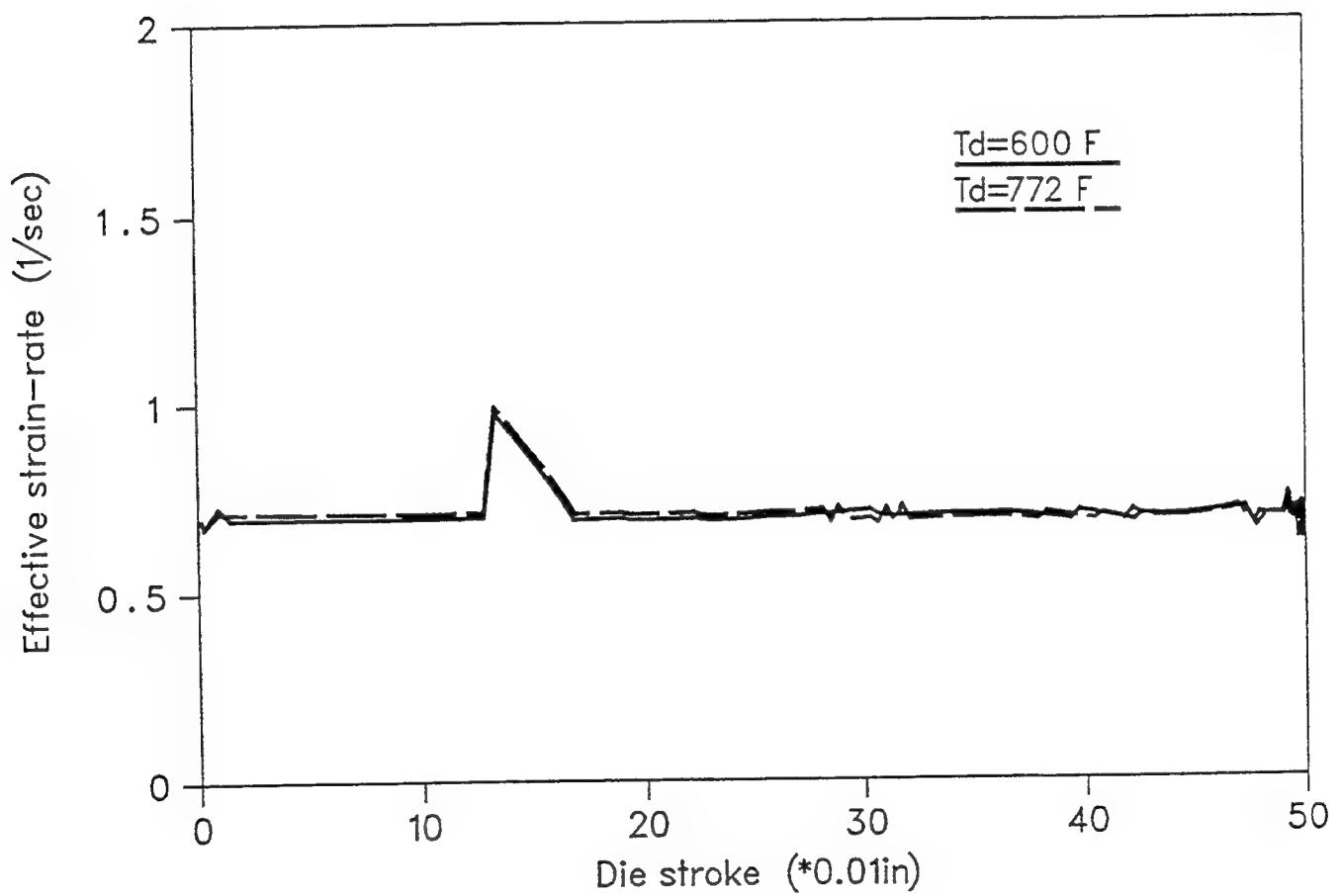


Figure 20: Initial die temp. design - Strain rates

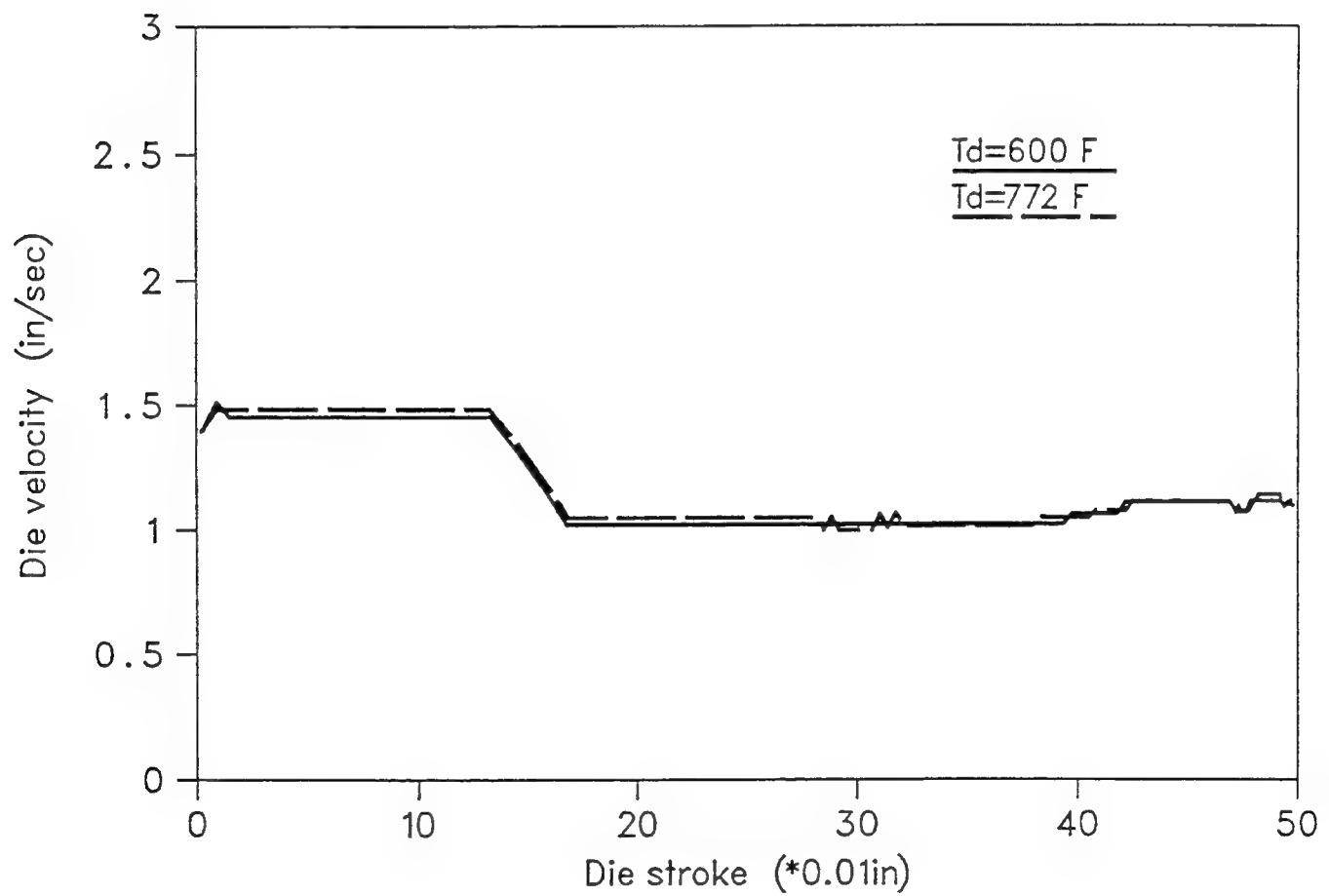


Figure 21: Initial die temp. design - Die velocities

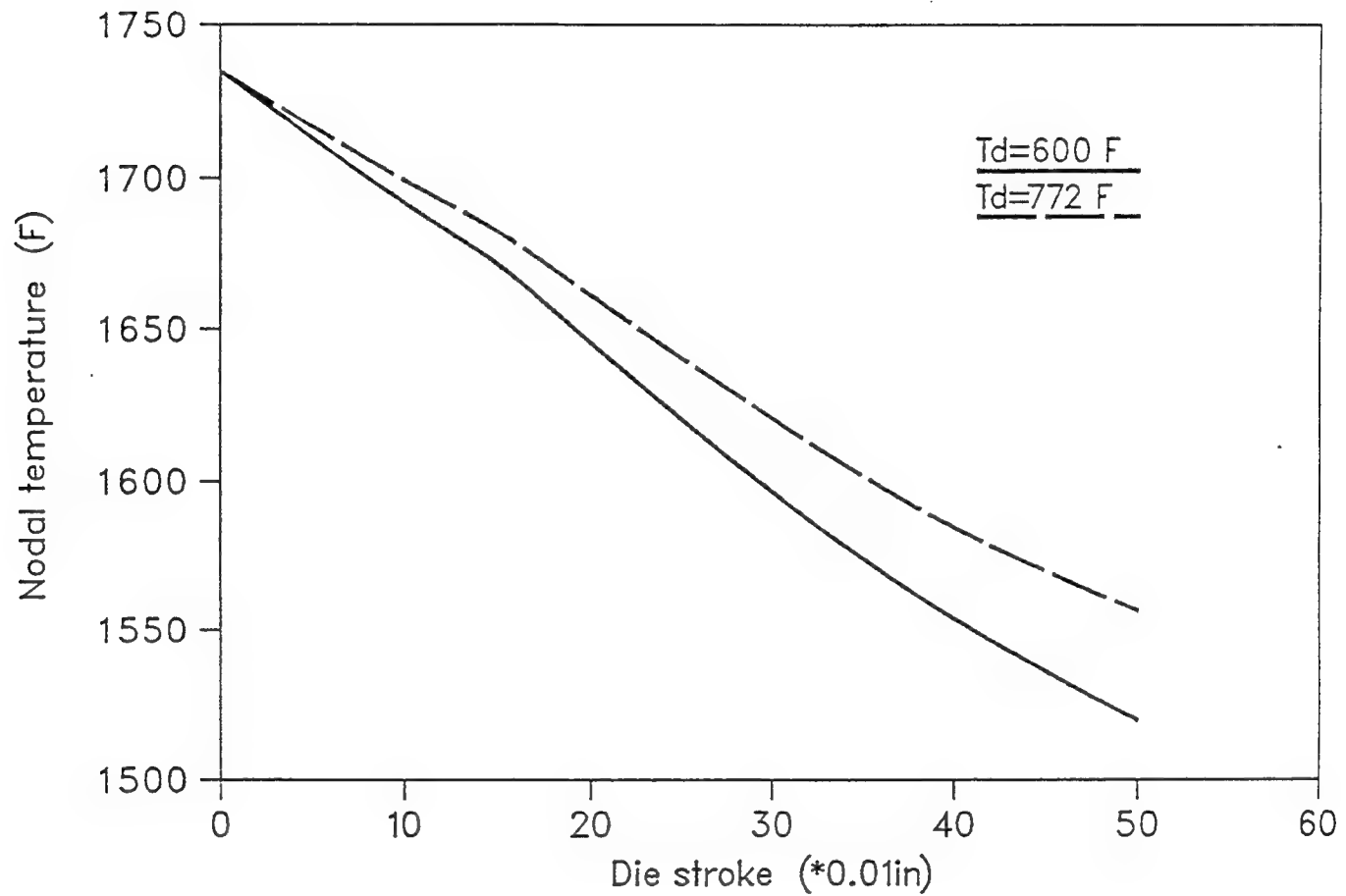


Figure 22: Initial die temp. design - Node 18 temp. profiles

CHAPTER 7

Reduced Order State Space Models

7.1 Introduction to model reduction

In general, large scale finite element models are used for simulating and analyzing metal forming processes to capture in detail information regarding the thermo-mechanical behavior of the deforming material. The condensation scheme explained earlier reduces and transforms the finite element model to a state space model by retaining the tangential nodal velocities and temperatures of the die contacting nodes, and the nodal degrees of freedom of the critical element (in the deforming material) as states. Despite the condensation process, a large model results when analyzing large scale practical forming problems. Further, for on-line control applications, it is desirable to have smaller models capable of accurately representing the thermo-mechanical behavior of the metal forming process. Since the state space model is built using the converged finite element solution at each time step, it may be considered a reasonably accurate representation of the metal forming process [66,67].

The highly nonlinear finite element model of the metal forming process is linearized and modeled in the state space form as,

$$\dot{\mathbf{x}} = \mathbf{Ax} + \mathbf{Bu}$$

$$\mathbf{y} = \mathbf{Cx} \quad (7.1)$$

where \mathbf{A} is the plant matrix, \mathbf{B} is the input matrix, and \mathbf{C} is the output matrix to convert the state vector \mathbf{x} into the desired output \mathbf{y} . u is the input vector, which in this case is the ram velocity. Eq. (7.1) is derived from the stiffness matrix and force vectors of the metal forming process. The state space models are built using the converged solution at the end of each simulation time step. The conversion of the finite element equations to state space form takes into account the symmetric boundary conditions and the other relevant boundary conditions of the physical system. The force vector used includes the effects due to friction and reaction forces. The reaction forces are due to the symmetric boundary conditions applied during the finite element modeling. The nodal velocities of the boundary nodes and the nodal velocities of the element of interest (whose strain rate is to be controlled) are considered as states. The elemental strain rate is the output, and it is maintained within a predetermined and prespecified range. The output matrix, \mathbf{C} , is defined as the matrix to convert the nodal velocities into the strain rate of the element of interest. The control problem is posed as a tracking problem, and since the output is to be tracked, the objective of the control law is to minimize the performance index in such a way that the error is minimized and the end conditions are met.

The aim of reducing the original model is to get an equivalent linear state space system of a dimension considerably smaller than that of the original system. Since the control problem is a tracking problem, the reduced model should necessarily be controllable. In addition, the reduced system should be observable in order to implement this methodology as a feedback on-line control scheme.

The methodology for obtaining reduced order state space models and their subsequent use in designing optimal die velocity schedules is described in the flow chart of Fig. 23.

Reduced order models can generally be obtained using several methods available in relevant literature. The following are two broad classifications of currently available order reduction techniques:

- i. The first classification uses the mode concept of linear models. The aim here is to keep the dominant eigenvalues of the full model, i.e., the eigenvalues most influential on the system dynamic behavior. The modal analysis method and the aggregation method belong to this classification.
- ii. The second classification includes the approaches based on preserving the same degree of controllability and observability product (σ_i) as in the full model. The Balanced Model Reduction (BMR) method belongs to this category, where the reduction is applied by deleting the smallest singular values, σ_i , of the balanced state space configuration.

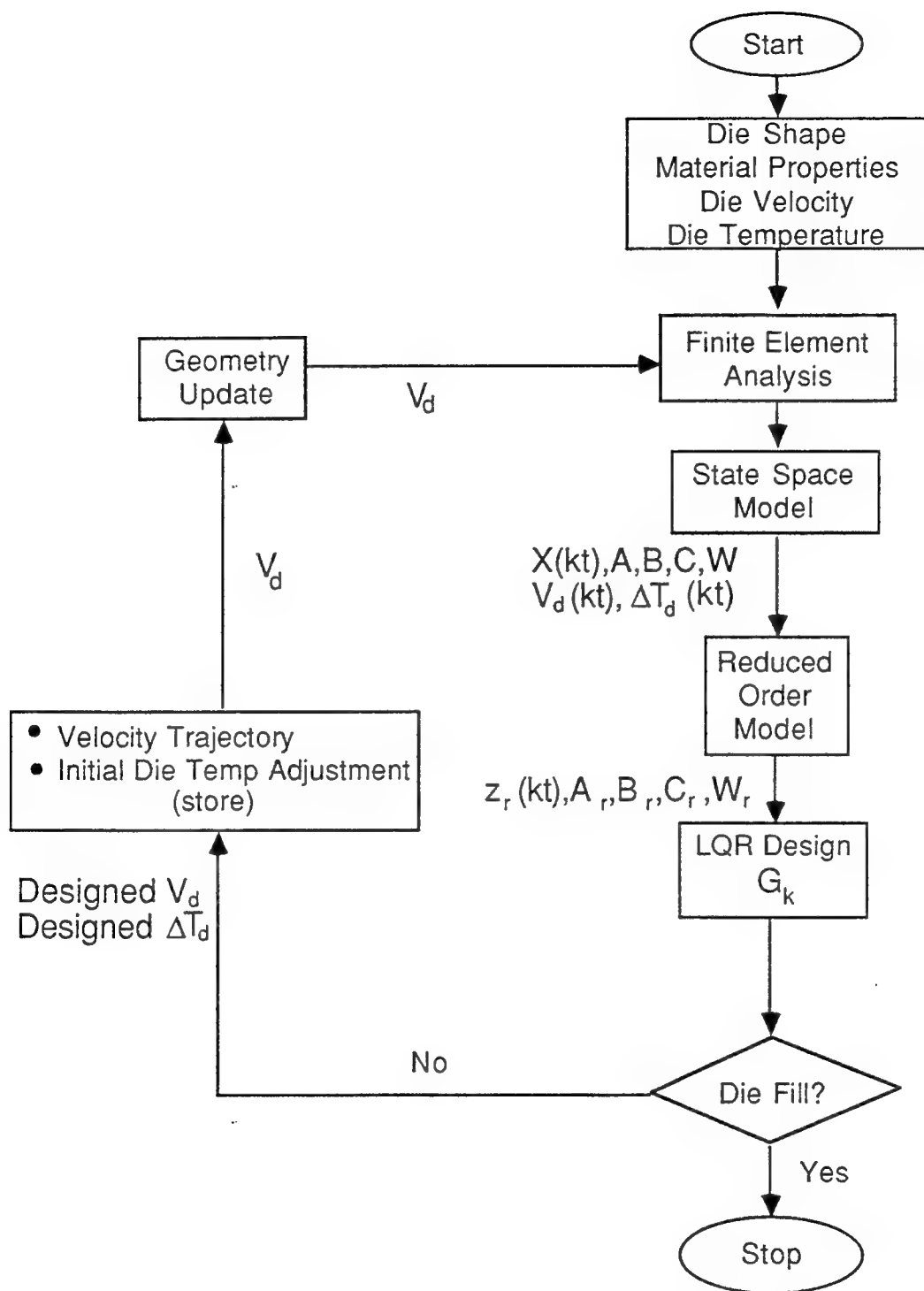


Figure 23: Process parameter design using reduced order models

7.2 Aggregation method

Aggregation techniques replace the initial system model with a reduced order model that preserves the dominant system characteristics. In this method, the important assumption is that the reduced state vector (\mathbf{x}_r) and the full state vector \mathbf{x} are related linearly by an aggregation matrix, \mathbf{P} , of dimension $(m \times p)$, having rank m . Here, m is the number of states in the reduced order model, and p represents the number of states in the full-size model. The aggregated model is not a part of the full state model. Instead, it is a linear combination of the states of the full model [55]. Some salient features of this technique are described below. In this method it is assumed there exists an aggregation matrix (\mathbf{P}) such that,

$$\mathbf{x}_r = \mathbf{P}\mathbf{x} \quad (7.2)$$

where \mathbf{x}_r is the reduced state vector, and \mathbf{x} is the full state vector. Also, $\mathbf{x} \in \mathbf{R}^p$, $\mathbf{x}_r \in \mathbf{R}^m$ and $\mathbf{P} \in \mathbf{R}^{(m \times p)}$. Now, the aggregated state space model can be constructed as,

$$\begin{aligned} \dot{\mathbf{x}}_r &= \mathbf{A}_r \mathbf{x}_r + \mathbf{B}_r u \\ \mathbf{y}_r &= \mathbf{C}_r \mathbf{x}_r \end{aligned} \quad (7.3)$$

where $\mathbf{A}_r \in \mathbf{R}^{(m \times m)}$, $\mathbf{B}_r \in \mathbf{R}^{(m \times 1)}$ and $\mathbf{C}_r \in \mathbf{R}^{(1 \times m)}$ are the aggregated plant, input and output matrices, respectively. Since the input and output are scalars (for the isothermal case), \mathbf{B}_r and \mathbf{C}_r take the sizes described above. In order to derive the aggregated model from the full state model, the relationship between the full

model, aggregated model, and the transformation matrix must be determined.

By substituting Eq. (7.2) in Eq. (7.3), we have,

$$\mathbf{P}\dot{\mathbf{x}} = \mathbf{A}_r\mathbf{P}\mathbf{x} + \mathbf{B}_r\mathbf{u} \quad (7.4)$$

By premultiplying Equation (7.1) with \mathbf{P} and equating the coefficient matrix of \mathbf{x} and the coefficient matrix of \mathbf{u} , with those of Equation (7.4), we get,

$$\mathbf{A}_r\mathbf{P} = \mathbf{P}\mathbf{A}$$

$$\mathbf{B}_r = \mathbf{P}\mathbf{B} \quad (7.5)$$

The selection of \mathbf{P} is important to establish a proper relationship between the full state model and aggregated model. Generally, this matrix is computed based on the contribution of the eigenvalues to the output vector. If λ represents the eigenvalues of \mathbf{A} , and \mathbf{v} represents their associated eigenvectors, then,

$$\mathbf{A}\mathbf{v} = \lambda\mathbf{v} \quad (7.6)$$

Premultiplying both sides of Equation (7.6) by the aggregation matrix, \mathbf{P} ,

$$\mathbf{P}(\mathbf{A}\mathbf{v}) = \lambda\mathbf{P}\mathbf{v} \quad (7.7)$$

Substituting for $\mathbf{P}\mathbf{A}$ from Equation (7.5) into Equation (7.7),

$$\mathbf{A}_r(\mathbf{P}\mathbf{v}) = \lambda(\mathbf{P}\mathbf{v}) \quad (7.8)$$

This equation shows that the eigenvalues of the matrix \mathbf{A}_r are m aggregated eigenvalues of the matrix \mathbf{A} . The same is true in case of the eigenvectors also. Hence, it may be seen that the selection of the aggregation matrix significantly influences the performance of the reduced model with respect to the full model.

Since the aggregation matrix is a transformation matrix which is selected based on eigenvalues, the selection is carried out using the modal matrix of the full system. The canonical form of the states is expressed as,

$$\mathbf{x} = \mathbf{M}\mathbf{w} \quad (7.9)$$

where \mathbf{w} is the transformed state variable in eigenspace and \mathbf{M} is the modal matrix containing the eigenvectors of the matrix \mathbf{A} . By substituting Equation (7.9) into Equation (7.1), the full-size state space system in the transformed form is written as,

$$\dot{\mathbf{w}} = \mathbf{\Lambda}\mathbf{w} + \mathbf{\Gamma}u \quad (7.10)$$

where,

$$\mathbf{\Lambda} = \mathbf{M}^{-1}\mathbf{A}\mathbf{M} = \begin{pmatrix} \mathbf{\Lambda}_1 & \mathbf{0} \\ \mathbf{0} & \mathbf{\Lambda}_2 \end{pmatrix} \quad (7.11)$$

$$\mathbf{\Gamma} = \mathbf{M}^{-1}\mathbf{B} = \begin{pmatrix} \mathbf{\Gamma}_1 \\ \mathbf{\Gamma}_2 \end{pmatrix} \quad (7.12)$$

Here, $\mathbf{\Lambda}$ is a diagonal matrix of the eigenvalues of \mathbf{A} , $\mathbf{\Lambda}_1$ contains the dominant eigenvalues and $\mathbf{\Lambda}_2$ is made up of the non-dominant eigenvalues of the system. Because of the properties of the stiffness matrix, the plant always has distinct eigenvalues. $\mathbf{\Gamma}_1 \in \mathbf{R}^{(m \times m)}$ and $\mathbf{\Gamma}_2 \in \mathbf{R}^{(p-m) \times (p-m)}$ are the transformed forms of the input matrix of the full state model. In the partitioned form the full state space system is written as,

$$\begin{pmatrix} \dot{\mathbf{w}}_1 \\ \dot{\mathbf{w}}_2 \end{pmatrix} = \begin{pmatrix} \mathbf{\Lambda}_1 & \mathbf{0} \\ \mathbf{0} & \mathbf{\Lambda}_2 \end{pmatrix} \begin{pmatrix} \mathbf{w}_1 \\ \mathbf{w}_2 \end{pmatrix} + \begin{pmatrix} \mathbf{\Gamma}_1 \\ \mathbf{\Gamma}_2 \end{pmatrix} u \quad (7.13)$$

From this, the decomposition of the transformed states into m reduced states is performed as described below:

$$\dot{\mathbf{w}}_1 = \mathbf{\Lambda}_1\mathbf{w}_1 + \mathbf{\Gamma}_1u \quad (7.14)$$

where w_1 represents states that are to be retained for the reduced model of size m , and is defined as $w_1 = (I_m \ 0)w$. Also, substituting for w from Equation (7.9), we get $Px = (I_m \ 0)M^{-1}x$. Now, the transformation matrix P can be defined as,

$$P = (I_m \ 0)M^{-1} \quad (7.15)$$

Because the goal of model reduction is to reduce the size of the original model, but still obtain results comparable to that of the full model, the output matrix C_r also must be defined in terms of the aggregation matrix. Hence, the reduced output matrix is given by,

$$C_r = CP^+ \quad (7.16)$$

where P^+ is the pseudo inverse of the aggregation matrix P .

7.3 Modal analysis method

In the aggregation method the states (reduced) are a linear combination of the full state model. The modal analysis method, unlike the aggregation method, is based on transforming the system matrices in such a way that the characteristics of the entire system (full-size) are included in the reduced model. The full state model is represented in eigenspace using the relation in Equation (7.9), where the transformation is done using the modal matrix, M . Equation (7.1) is valid for one simulation time step of the metal forming process. Because the system

(Eq. (7.1)) is now linear and time invariant for that time step (interval), it can be partitioned in the following form,

$$\begin{pmatrix} \dot{x}_1 \\ \dot{x}_2 \end{pmatrix} = \begin{pmatrix} A_1 & A_2 \\ A_3 & A_4 \end{pmatrix} \begin{pmatrix} x_1 \\ x_2 \end{pmatrix} + \begin{pmatrix} B_1 \\ B_2 \end{pmatrix} u \quad (7.17)$$

where $x_1 \in \mathbb{R}^m$ is the state vector whose modes are to be retained, $x_2 \in \mathbb{R}^{(p-m)}$ is the state vector whose modes are to be neglected, and m is known *a priori*. The matrices A_1, A_2, A_3, A_4, B_1 and B_2 are constant. Accordingly, the modal matrix, M , can also be represented in the partitioned form as,

$$M = \begin{pmatrix} M_1 & M_2 \\ M_3 & M_4 \end{pmatrix} \quad (7.18)$$

From Eq. (7.9), $x = [x^T_1 \ x^T_2]^T$ is the original form and $w = [w^T_1 \ w^T_2]^T$ is the transformed form. In the partitioned form, w_1 includes the states of dominant eigenvalues and w_2 includes states of non-dominant eigenvalues of the system. Now, the original system is represented in the transformed coordinates as explained in equations (7.10) - (7.12). The states in eigenspace are further expanded using the matrix properties and the relationship between the matrices of M and their inverses. The dominant and non-dominant states are expressed as,

$$\begin{aligned} \dot{w}_1 &= M_1^{-1} [A_1 M_1 + A_2 M_3] w_1 \\ &+ \left[(M_1 - M_2 M_4^{-1} M_3) B_1 - M_1^{-1} M_2 (M_4 - M_3 M_1^{-1} M_2)^{-1} B_2 \right] u \end{aligned} \quad (7.19)$$

$$\begin{aligned} \dot{w}_2 &= M_4^{-1} [A_3 M_2 + A_4 M_4] w_2 \\ &+ \left[-M_4^{-1} M_3 (M_4 - M_2 M_4^{-1} M_3)^{-1} B_1 + (M_4 - M_3 M_1^{-1} M_2)^{-1} B_2 \right] u \end{aligned} \quad (7.20)$$

From the above two expressions the reduced order models may be derived. Based on the modal analysis technique, there are three methods by which model reduction is done:

1. Davison's method
2. Marshall's method
3. Nicholson's method

All the above methods retain the dominant eigenvalues of the original system. Further, all three methods assume that all the non-dominant eigenvalues are in Λ_2 . Because the design is a tracking problem, the output matrix is also modified accordingly, to get reasonable results. Some distinct features of these methods are discussed below.

7.3.1 Davison's method

This method makes use of the fact that Λ_2 contains only non-dominant eigenvalues. w_2 is derived from the approximation $\dot{w}_2 = 0$ and is replaced in terms of x_1 and u . By substituting this approximation back into Equation (7.10) and rearranging the terms, the reduced system is written as,

$$\begin{aligned} A_r &= A_1 + A_2 M_3 M_1^{-1} \\ B_r &= M_1 \left(M_1 - M_2 M_4^{-1} M_3 \right)^{-1} B_1 - M_2 \left(M_4 - M_3 M_1^{-1} M_2 \right)^{-1} B_2 \end{aligned} \quad (7.21)$$

Because the output of the reduced model depends on the retained states x_1 , the output matrix is also partitioned as,

$$y = [C_1 \ C_2] \begin{pmatrix} x_1 \\ x_2 \end{pmatrix} = [C_1 \ C_2] \begin{pmatrix} M_1 & M_2 \\ M_3 & M_4 \end{pmatrix} \begin{pmatrix} w_1 \\ w_2 \end{pmatrix} \quad (7.22)$$

where \mathbf{C}_1 and \mathbf{C}_2 are the partitioned output matrices spanning the dominant and non-dominant states, respectively. By rearranging and substituting for the non-dominant states, \mathbf{x}_2 , the output is written as,

$$\mathbf{y} = [\mathbf{C}_1 + \mathbf{C}_2 \mathbf{M}_3 \mathbf{M}_1^{-1}] \mathbf{x}_1 + \{\mathbf{C}_2 [\mathbf{M}_3 \mathbf{M}_1^{-1} \mathbf{M}_2 - \mathbf{M}_4] \mathbf{\Lambda}_2^{-1} \mathbf{\Gamma}_2\} \mathbf{u} = \mathbf{C}_r \mathbf{x}_1 + \mathbf{D}_r \mathbf{u} \quad (7.23)$$

7.3.2. Marshall's method

This method is derived from Equation (7.17) and equations (7.10) - (7.12). From Equation (7.17), $\dot{\mathbf{x}}_1$ can be defined as,

$$\dot{\mathbf{x}}_1 = \mathbf{A}_1 \mathbf{x}_1 + \mathbf{A}_2 \mathbf{x}_2 + \mathbf{B}_1 \mathbf{u} \quad (7.24)$$

By partitioning Equation (7.9) and extracting the terms related to \mathbf{x}_2 , we get,

$$\mathbf{x}_2 = \mathbf{M}_3 \mathbf{w}_1 + \mathbf{M}_4 \mathbf{w}_2 \quad (7.25)$$

Now, rearranging Equation (7.25), the dominant states in the modal coordinates are obtained as,

$$\mathbf{w}_1 = \mathbf{M}_1^{-1} \mathbf{x}_1 - \mathbf{M}_1^{-1} \mathbf{M}_2 \mathbf{w}_2 \quad (7.26)$$

Using the condition $\dot{\mathbf{w}}_2 = 0$, \mathbf{w}_2 can be determined in the modal coordinates as,

$$\mathbf{w}_2 = -\mathbf{\Lambda}_2^{-1} \mathbf{\Gamma}_2 \mathbf{u} \quad (7.27)$$

By substituting Equations (7.26) and (7.27) in Equation (7.25), and substituting the result in Equation (7.24), the reduced system is derived as,

$$\mathbf{A}_r = \mathbf{A}_1 + \mathbf{A}_2 \mathbf{M}_3 \mathbf{M}_1^{-1}$$

$$\mathbf{B}_r = \mathbf{B}_1 - \mathbf{A}_2 \left[\mathbf{M}_4 - \mathbf{M}_3 \mathbf{M}_1^{-1} \mathbf{M}_2 \right] \mathbf{\Lambda}_2^{-1} \mathbf{\Gamma}_2 \quad (7.28)$$

In modal coordinates the output is written as in Equation (7.22). Now, substituting for \mathbf{w}_2 from Equation (7.27), the output (in terms of reduced states) may be written as,

$$\mathbf{y} = [\mathbf{C}_1 \mathbf{M}_1 + \mathbf{C}_2 \mathbf{M}_3] \mathbf{w}_1 - [\mathbf{C}_1 \mathbf{M}_2 + \mathbf{C}_2 \mathbf{M}_4] \mathbf{\Lambda}_2^{-1} \mathbf{\Gamma}_2 \mathbf{u} = \mathbf{C}_r \mathbf{w}_1 + \mathbf{D}_r \mathbf{u} \quad (7.29)$$

7.3.3. Nicholson's method

In this method the reduced system is derived by completely neglecting the effect of \mathbf{w}_2 on the system. By assuming that the non-dominant states do not have any influence on the dominant states, and substituting for \mathbf{x}_2 in terms of \mathbf{x}_1 , the reduced model is constructed. Based on this assumption, Equation (7.18) is modified as,

$$\begin{pmatrix} \mathbf{x}_1 \\ \mathbf{x}_2 \end{pmatrix} = \begin{pmatrix} \mathbf{M}_1 & 0 \\ \mathbf{M}_3 & 0 \end{pmatrix} \begin{pmatrix} \mathbf{w}_1 \\ \mathbf{w}_2 \end{pmatrix} \quad (7.30)$$

By substituting Equation (7.30) in Equation (7.17) and rearranging, we get,

$$\dot{\mathbf{x}}_1 = \mathbf{M}_1 \mathbf{\Lambda}_1 \mathbf{M}_1^{-1} \mathbf{x}_1 + \mathbf{M}_1 \mathbf{\Gamma}_1 \mathbf{u} \quad (7.31)$$

The reduced model may now be described as,

$$\begin{aligned} \mathbf{A}_r &= \mathbf{A}_1 + \mathbf{A}_2 \mathbf{M}_3 \mathbf{M}_1^{-1} \\ \mathbf{B}_r &= \mathbf{M}_1 (\mathbf{I}_m \quad 0_{m \times (p-m)}) \mathbf{M}^{-1} \mathbf{B} \end{aligned} \quad (7.32)$$

The neglected (non-dominant) states are given by,

$$\dot{\mathbf{x}}_2 = \mathbf{M}_3 \mathbf{M}_1^{-1} \mathbf{x}_1 \quad (7.33)$$

The output matrix for the reduced system may be derived as,

$$\mathbf{y} = [\mathbf{C}_1 + \mathbf{C}_2 \mathbf{M}_3 \mathbf{M}_1^{-1}] \mathbf{x}_1 = \mathbf{C}_r \mathbf{x}_1 \quad (7.34)$$

7.4 Balanced model reduction (BMR) method

7.4.1 Construction of the balanced model

The BMR method belongs to the second classification of order reduction methods described in section 7.1. Generally, it is desirable to have a system that is both controllable and observable, called the balanced system. The BMR method is a state selection procedure in the grammian-balanced coordinate system of the full state space model. The grammian-balanced system is called the internally balanced system of the full system. The reduced model is derived by retaining only the most controllable and observable states of the internally balanced system. The internally balanced system is constructed using a transformation matrix, $[T_b]$, which exists only if the plant matrix of the full state space model is asymptotically stable. The state space model for metal forming processes is always stable because the plant matrix is negative definite, as may be observed from chapter 2. If the transformation matrix exists, then, the states in the balanced coordinate system are given by,

$$x_b = T_b^{-1}x \quad (7.35)$$

Now, the balanced state space form of Equation (7.1) is expressed as,

$$\begin{aligned} x_b &= A_b x_b + B_b u + W_b \\ y &= C_b x_b \end{aligned} \quad (7.36)$$

where $A_b = T_b^{-1}AT_b$, $B_b = T_b^{-1}$, $C_b = CT_b$ and $W_b = T_b^{-1}W$. A system is called internally balanced or grammian balanced if,

$$\bar{P}_c = \bar{P}_o = \Sigma = \text{diag} [\sigma_1^2, \sigma_2^2, \dots, \sigma_n^2] \quad (7.37)$$

where the σ_i 's are Hankel singular values of the balanced system and Σ is a diagonal matrix containing σ_i^2 . \bar{P}_c and \bar{P}_o are the controllability and observability grammians of the system, which are the solutions of the following Lyapunov equations:

$$A_b \bar{P}_c + \bar{P}_c A^T b + B_b B^T b = 0$$

and

$$A^T b \bar{P}_o + \bar{P}_o A_b + C^T b C_b = 0 \quad (7.38)$$

The balanced state space model (Equation 7.36) is actually the controllable subspace of the condensed (full-size) state space model of the metal forming process (Equation 7.1).

7.4.2 Construction of the transformation matrix [57]

The controllability and observability grammians (P_c and P_o) of the full state space model may be obtained as solutions of the following Lyapunov equations:

$$A P_c + P_c A^T + B B^T = 0$$

and

$$A^T P_o + P_o A + C^T C = 0. \quad (7.39)$$

By factorizing the controllability grammian P_c using singular value decomposition, we have,

$$P_c = U_1 \Sigma_1 U_1^T \quad (7.40)$$

From the properties of singular value decomposition, the product $U_1 U_1^T$ results in an identity matrix, and Σ_1 is a diagonal matrix having the singular values of the matrix P_c as its diagonal terms. Σ_1 will normally have n_c non-zero values. From the non-zero values of Σ_1 , the controllable subspace of the system can be extracted by partitioning the matrix U as $[U_{11} \ U_{12}]$, where $U_{11} \in \mathbb{R}^{n \times n_c}$ spans the controllable subspace and $U_{12} \in \mathbb{R}^{n \times (n-n_c)}$ spans the uncontrollable subspace of the system. If all the states are controllable, then $n_c = n$. Using the information specified above, the controllable subspace may be retained as,

$$T_1 = U_{11} \Sigma_{11}^{\frac{1}{2}} \quad (7.41)$$

By factorizing the product $T_1^T P_o T_1$ using singular value decomposition [56,57,68],

$$T_1^T P_o T_1 = U_2 \Sigma_2 U_2^T \quad (7.42)$$

where the non-zero portion of the singular value matrix, Σ_2 , spans the observable part of the controllable subspace of the system, represented as Σ_{22} . By partitioning U_2 similar to the operation in Equation (7.40), the controllable-observable subspace is constructed as,

$$T_2 = U_{21} \Sigma_{22}^{-\frac{1}{2}} \quad (7.43)$$

From T_1 and T_2 , the transformation matrix for balanced model reduction (T_b) is derived as,

$$T_b = T_1 T_2 \quad (7.44)$$

7.4.3 Construction of the reduced model

As explained by Moore [68], in cases where σ_m^2 is considerably larger than $\sigma_{(m+1)}^2$, the subspace \mathbf{x}_r behaves like it is both controllable and observable. If the mechanics of Kalman's minimal realization theory are applied to the internally balanced model, with \mathbf{x}_r used as a working approximation of \mathbf{x}_b , then, the resulting lower order model is generically stable and internally balanced. Now, by truncating the smallest singular values (σ_i) of the balanced system, the reduced model may be defined by,

$$\begin{aligned}\mathbf{A}_r &= (\mathbf{I}_m \quad 0) \mathbf{A}_b \begin{pmatrix} \mathbf{I}_m \\ 0 \end{pmatrix} \\ \mathbf{B}_r &= (\mathbf{I}_m \quad 0) \mathbf{B}_b \\ \mathbf{C}_r &= \mathbf{C}_b \begin{pmatrix} \mathbf{I}_m \\ 0 \end{pmatrix}\end{aligned}\tag{7.45}$$

7.5 Control law for reduced order models

The performance of reduced order models can be measured using many criteria. The objective of model reduction in this case is to design optimal input velocities while using a smaller state space system. Hence, comparing the die velocities designed using the full and reduced models is a good measure to evaluate the performance of the reduced order models. The control law used for the full-size state space model [66,67] cannot be directly applied to the reduced models (Equations (3.23) and (3.29)), because the reduced models have an extra

term (**D**) in the output equation. In this section, a control law suitable for use with reduced order models is developed. The input velocities are designed using a finite time control law with output tracking.

For a time-invariant linear system, the state space representation may be given by,

$$\dot{\mathbf{x}} = \mathbf{f}[\mathbf{x}(t), \mathbf{u}(t), t] = \mathbf{A}\mathbf{x} + \mathbf{B}\mathbf{u} + \mathbf{W} \quad \text{and} \quad \mathbf{y} = \mathbf{C}\mathbf{x} + \mathbf{D}\mathbf{u} \quad (7.46)$$

where **A**, **B**, **W**, **C**, **D**, **x** describe the full system and **A_r**, **B_r**, **W_r**, **C_r**, **D_r**, **x_r** describe the reduced system. The design is done off-line as explained earlier. The problem is posed as an output tracking problem and the output tracked is the strain rate of the element of interest. $\dot{\epsilon}_d$ is the desired strain rate trajectory to be tracked, and **y** is the output of the system. The error term (**e**) is given by $\mathbf{e} = \dot{\epsilon}_d - \mathbf{C}\mathbf{x} - \mathbf{D}\mathbf{u}$. This error signal is used as the state feedback while designing the velocity schedule. For control, it is desirable to bring the system from a given initial state **x₀** to an acceptable terminal state by designing a suitable control input **u**. The control is achieved by minimizing a performance index consisting of positive definite quadratic terms for the terminal condition, tracking error, and control input, respectively. This is represented mathematically as,

$$\min \quad J = \phi[\mathbf{x}(t_f), t_f] + \int_{t_0}^{t_f} \mathbf{L}[\mathbf{x}(t), \mathbf{u}(t), t] dt \quad (7.47)$$

where $\phi[\mathbf{x}(t_f), t_f] = \frac{1}{2}\mathbf{e}^T(t_f)\mathbf{S}\mathbf{e}(t_f)$ and $\mathbf{L}[\mathbf{x}(t), \mathbf{u}(t), t] = \frac{1}{2}[\mathbf{e}^T(t)\mathbf{Q}\mathbf{e}(t) + \mathbf{u}^T\mathbf{R}\mathbf{u}]$. **S** and **R** are positive definite weighting matrices which weight the terminal condition and the control, respectively, and **Q** is a positive semi-definite matrix which weights the states. Here, the problem is to design the control input, **u(t)**, such

that the Equation (7.47) is minimized. To find an optimal $u(t)$, the system differential equation (Eq. (7.46)) is combined with Equation (7.47) by means of a Lagrange multiplier function, $\lambda(t)$, as shown below:

$$J = \phi[x(t_f), t_f] + \int_{t_0}^{t_f} [L[x(t), u(t), t] + \lambda^T(t) \{f[x(t), u(t), t] - \dot{x}\}] dt \quad (7.48)$$

$\lambda(t)$ is a function of the states $x(t)$. For numerical convenience a scalar function H called the Hamiltonian, is defined as [69]:

$$H[x(t), u(t), t] = L[x(t), u(t), t] + \lambda^T(t) f[x(t), u(t), t] \quad (7.49)$$

By substituting Equation (7.49) in Equation (7.48) and integrating the resulting equation, the function to be minimized is:

$$J = \phi[x(t_f), t_f] - \lambda^t(t_f) x(t_f) + \lambda^t(t_0) x(t_0) + \int_{t_0}^{t_f} \{H[x(t), u(t), t] + \dot{\lambda}^t(t) x(t)\} dt \quad (7.50)$$

Now consider the variation of J due to variations in the control $u(t)$, for the fixed time interval t_0 to t_f . Mathematically,

$$\delta J = \left[\left(\frac{\partial \phi}{\partial x} - \lambda^t \right) \delta x \right]_{t_f} + [\lambda^T \delta x]_{t_0} + \int_{t_0}^{t_f} \left\{ \left[\frac{\partial H}{\partial x} + \dot{\lambda}^t \right] \delta x + \frac{\partial H}{\partial u} \delta u \right\} dt \quad (7.51)$$

By setting the coefficients of δx to zero in the above equation, the necessary and sufficient conditions for minimizing the performance index can be derived as,

$$\dot{\lambda}^T(t) = -\frac{\partial H}{\partial x} \quad \text{and} \quad \frac{\partial H}{\partial u} = 0 \quad (7.52)$$

The corresponding boundary condition may be given as,

$$\lambda^T(t_f) = \frac{\partial \phi}{\partial x} \quad (7.53)$$

The optimal $u(t)$ which minimizes the performance index (Eq. (7.47)) can be obtained by solving Equations (7.46), (7.52), and (7.53) simultaneously. The Hamiltonian function, H , is now derived as,

$$\begin{aligned}
 H &= \frac{1}{2} [e^T Q e + u^T R u] + \lambda^T [Ax + Bu + W] \\
 &= \frac{1}{2} [ZQZ - x^T C^T QZ - u^T D^T QZ - ZQCx + x^T C^T QCx + u^T D^T QCx] \\
 &\quad + \frac{1}{2} [-ZQDu + x^T C^T QDu + u^T D^T QDu + u^T Ru] + \lambda^T Ax + \lambda^T Bu + \lambda^T W
 \end{aligned} \tag{7.54}$$

where Z is the desired strain rate $\dot{\epsilon}_d$. Taking the partial derivative of Equation (7.54) with respect to x and setting the result equal to $-\dot{\lambda}$, one of the Euler-Lagrange equations may be constructed as,

$$\dot{\lambda} = -A^T \lambda - C^T QCx + C^T QZ - C^T QDu \tag{7.55}$$

Now, taking the partial derivative of Equation (7.54) with respect to u and setting the result equal to zero, the optimal control law may be derived as,

$$u(t) = -[D^T QD + R]^{-1} [D^T QZ - D^T QCx(t) + B^T \lambda(t)] \tag{7.56}$$

Substituting for $u(t)$ from Equation (7.56) into Equation (7.46), we have,

$$\dot{x}(t) = H_1 x(t) + H_2 \lambda(t) + V_1(t) \tag{7.57}$$

where,

$$H_1 = A + B [D^T QD + R]^{-1} D^T QC$$

$$H_2 = -B [D^T QD + R]^{-1} B^T$$

$$V_1(t) = W - B [D^T QD + R]^{-1} D^T QZ(t)$$

Substituting for $u(t)$ from Equation (7.56) into Equation (7.55), we get,

$$\dot{\lambda}(t) = \mathbf{H}_3 x(t) + \mathbf{H}_4 \lambda(t) + \mathbf{V}_2(t) \quad (7.58)$$

where,

$$\begin{aligned}\mathbf{H}_3 &= -\mathbf{C}^T \mathbf{Q} \mathbf{C} - \mathbf{C}^T \mathbf{Q} \mathbf{D} [\mathbf{D}^T \mathbf{Q} \mathbf{D} + \mathbf{R}]^{-1} \mathbf{D}^T \mathbf{Q} \mathbf{C} \\ \mathbf{H}_4 &= -\mathbf{A}^T + \mathbf{C}^T \mathbf{Q} \mathbf{D} [\mathbf{D}^T \mathbf{Q} \mathbf{D} + \mathbf{R}]^{-1} \mathbf{B}^T \\ \mathbf{V}_2 &= \mathbf{C}^T \mathbf{Q} \mathbf{Z} + \mathbf{C}^T \mathbf{Q} \mathbf{D} [\mathbf{D}^T \mathbf{Q} \mathbf{D} + \mathbf{R}]^{-1} \mathbf{D}^T \mathbf{Q} \mathbf{Z}(t)\end{aligned}$$

Combining Equations (7.57) and (7.58), we get,

$$\begin{pmatrix} \dot{x}(t) \\ \dot{\lambda}(t) \end{pmatrix} = \begin{pmatrix} \mathbf{H}_1 & \mathbf{H}_2 \\ \mathbf{H}_3 & \mathbf{H}_4 \end{pmatrix} \begin{pmatrix} x(t) \\ \lambda(t) \end{pmatrix} + \begin{pmatrix} \mathbf{V}_1(t) \\ \mathbf{V}_2(t) \end{pmatrix} \quad (7.59)$$

There are $2n$ number of equations in Equation (7.59), where n is the number of states in Equation (7.46). Now, the solution of Equation (7.59) may be obtained as,

$$\begin{pmatrix} x(t_f) \\ \lambda(t_f) \end{pmatrix} = \Phi(t_f, t) \begin{pmatrix} x(t) \\ \lambda(t) \end{pmatrix} + \Phi(t_f, t) \int_{t_0}^{t_f} \Phi^{-1}(\tau, t) \begin{pmatrix} \mathbf{V}_1(\tau) \\ \mathbf{V}_2(\tau) \end{pmatrix} d\tau \quad (7.60)$$

where Φ is the state transition matrix (explained earlier). For convenience, Equation (7.60) can be rewritten as,

$$\begin{pmatrix} x(t_f) \\ \lambda(t_f) \end{pmatrix} = \Phi(t_f, t) \begin{pmatrix} x(t) \\ \lambda(t) \end{pmatrix} + \begin{pmatrix} \mathbf{g}_1(t) \\ \mathbf{g}_2(t) \end{pmatrix} \quad (7.61)$$

The two terms on the right side of Equation (7.61) are computed using the Pade approximation technique [63]. In Equation (7.61) there are two unknowns ($x(t_f)$ and $\lambda(t)$) out of which only $\lambda(t)$ is needed for the design of the system input (Equation 7.56). To solve for these unknowns $2n$ boundary conditions are needed. These are specified as,

at $t = t_0$, $x(t_0)$ is known

$$\text{at } t = t_f, \lambda(t_f) = \frac{\partial \phi^T}{\partial x}$$

By partitioning Φ in Equation (7.61) into four parts, Equation (7.61) can be rewritten as,

$$\begin{pmatrix} x(t_f) \\ \lambda(t_f) \end{pmatrix} = \begin{pmatrix} \Phi_{11} & \Phi_{12} \\ \Phi_{21} & \Phi_{22} \end{pmatrix} \begin{pmatrix} x(t) \\ \lambda(t) \end{pmatrix} + \begin{pmatrix} g_1(t) \\ g_2(t) \end{pmatrix} \quad (7.62)$$

From the boundary condition (Equation 7.53) and the definition of ϕ , $\lambda(t_f)$ may be defined as:

$$\begin{aligned} \lambda(t_f) &= \frac{\partial}{\partial x(t_f)} \left\{ \frac{1}{2} [Z^T - x^T C^T - u^T D^T] S [Z - Cx - Du] \right\} \\ &= \left[-C^T - \frac{\partial u^T}{\partial x} D^T \right] S [Z - Cx - Du] + [Z^T - x^T C^T - u^T D^T] S \left[-C - D \frac{\partial u}{\partial x} \right] \\ &= -C^T S Z + C^T S C x + C^T S D u + \frac{\partial u^T}{\partial x} [D^T S D u + D^T S C x - D^T S Z] \end{aligned} \quad (7.63)$$

Using the definition of u from Equation (7.56),

$$\frac{\partial u^T}{\partial x} = C^T Q D \kappa^{-T} = \alpha \quad (7.64)$$

where $\kappa = D^T Q D + R$. Substituting Equation (7.64) in Equation (7.63) and grouping the terms, we have,

$$\begin{aligned} \lambda(t_f) &= [-C^T S - \alpha D^T S] Z + [C^T S C + \alpha D^T S C] x + [C^T S D + \alpha D^T S D] u \\ &= \tau_1 Z + \tau_2 x + \tau_3 u \end{aligned} \quad (7.65)$$

Again substituting for u from Equation (7.56), we have,

$$\lambda(t_f) = \tau_1 Z + \tau_2 x + \tau_3 [-\kappa^{-1} D^T Q C Z + \kappa^{-1} D^T Q C x - \kappa^{-1} B^T \lambda(t)] \quad (7.66)$$

Rearranging and regrouping the above equation, we get,

$$[I + \tau_3 \kappa^{-1} B^T] \lambda(t_f) = [\tau_1 - \tau_3 \kappa^{-1} D^T Q C] Z(t_f) + [\tau_2 + \tau_3 \kappa^{-1} D^T Q C] x(t_f) \quad (7.67)$$

or,

$$\begin{aligned}\lambda(t_f) &= [I + \tau_3 \kappa^{-1} B^T]^{-1} \{ [\tau_1 - \tau_3 \kappa^{-1} D^T Q] Z(t_f) + [\tau_2 + \tau_3 \kappa^{-1} D^T Q C] x(t_f) \} \\ &= \eta_1 Z(t_f) + \eta_2 x(t_f)\end{aligned}\quad (7.68)$$

where

$$\begin{aligned}\eta_1 &= [I + \tau_3 \kappa^{-1} B^T]^{-1} [\tau_1 - \tau_3 \kappa^{-1} D^T Q] \\ \eta_2 &= [I + \tau_3 \kappa^{-1} B^T]^{-1} [\tau_2 + \tau_3 \kappa^{-1} D^T Q C]\end{aligned}$$

By expanding the matrices in equation (7.62), we get,

$$\begin{aligned}x(t_f) &= \Phi_{11}x(t) + \Phi_{12}\lambda(t) + g_1(t) \\ \lambda(t_f) &= \Phi_{21}x(t) + \Phi_{22}\lambda(t) + g_2(t)\end{aligned}\quad (7.69)$$

From equation (7.68),

$$\lambda(t_f) = \eta_1 Z(t_f) + \eta_2 x(t_f) \quad (7.70)$$

Substituting for $x(t_f)$ (in the above equation) from Equation (7.69), we get,

$$\lambda(t_f) = \eta_1 \Phi_{11}x(t) + \eta_1 \Phi_{12}\lambda(t) + \eta_1 g_1(t) + \eta_2 Z(t_f) \quad (7.71)$$

Substituting the above equation back into Equation (7.69), we get,

$$\eta_1 \Phi_{11}x(t) + \eta_1 \Phi_{12}\lambda(t) + \eta_1 g_1(t) + \eta_2 Z(t_f) = \Phi_{21}x(t) + \Phi_{22}\lambda(t) + g_2(t) \quad (7.72)$$

By rearranging the terms in the above equation, we get,

$$[\Phi_{22} - \eta_1 \Phi_{12}] \lambda(t) = [\eta_1 \Phi_{11} - \Phi_{21}] x(t) + [\eta_1 g_1(t) - g_2(t) + \eta_2 Z(t_f)] \quad (7.73)$$

From equation (7.73), the $\lambda(t)$ needed for input design in Equation (7.56) may be derived as,

$$\lambda(t) = [\Phi_{22} - \eta_1 \Phi_{12}]^{-1} \{ [\eta_1 \Phi_{11} - \Phi_{21}] x(t) + [\eta_1 g_1(t) - g_2(t) + \eta_2 Z(t_f)] \} \quad (7.74)$$

or,

$$\lambda(t) = L(t)x(t) - g(t) \quad (7.75)$$

where $Z(t)$ is the desired output, and L and g are solutions of the differential Riccati equations shown below:

$$\begin{aligned} -LH_1 - H_1^T L + LH_2 L + H_4 &= \dot{L} \\ -[LH_2 - H_1^T] g - V_2 + LV_1 &= \dot{g} \end{aligned} \quad (7.76)$$

The boundary conditions for the above system of equations are given as, $L(t_f) = \eta_1$ and $g(t_f) = \eta_2 Z(t_f)$, which are constant known values. With these boundary conditions, solving Equation (7.76) iteratively, the control law for designing the process parameters may be obtained.

To a large extent, the design obtained using this control law depends on the proper selection of the weighting matrices (Eq. (7.48)). Since this is a vital issue in getting an acceptable design, the weighting matrices have to be carefully designed so as to obtain meaningful inputs. In this work, the weighting matrices Q , R , and S are determined as follows [69]:

$$\begin{aligned} S^{-1} &= n \times \text{max. of diagonal of } e(t_f)e^T(t_f), \\ Q^{-1} &= n(t_f - t_o) \times \text{max. of diagonal of } e(t)e^T(t), \\ R^{-1} &= n(t_f - t_o) \times \text{max. of diagonal of } u(t)u^T(t). \end{aligned} \quad (7.77)$$

where $e(t_f)$ is known from the desired design values. The values of $e(t)$ and $u(t)$ are calculated at every simulation time step along with the iterative solution process.

7.6 Performance evaluation and selection of reduced order models

The order of the full-size state space model was reduced using the methods discussed in earlier sections of this chapter. A comparative study was then carried out to evaluate which model reduction method was best suited for metal forming applications. Two numerical examples were used to perform the comparative study of the model reduction methods studied. The selection of a suitable reduced order model was based on the designed die velocities. Of the two examples presented here, the first example has no friction specified, while the second example uses a shear friction factor of 0.3.

7.6.1 H-block compression - Frictionless case

A closed die forging was simulated to deform a cylindrical billet into a H-block using two dies. The die had a height to web ratio of 0.5. A cylindrical billet of radius of 60 mm and height 40 mm was used as the starting workpiece. Due to its symmetry, only one half of the workpiece was modeled. The discretized workpiece had 96 elements and 117 nodes (Fig. 24). The simulation was carried out with an initial die velocity of 0.1 mm/sec for the upper die, while the bottom die was

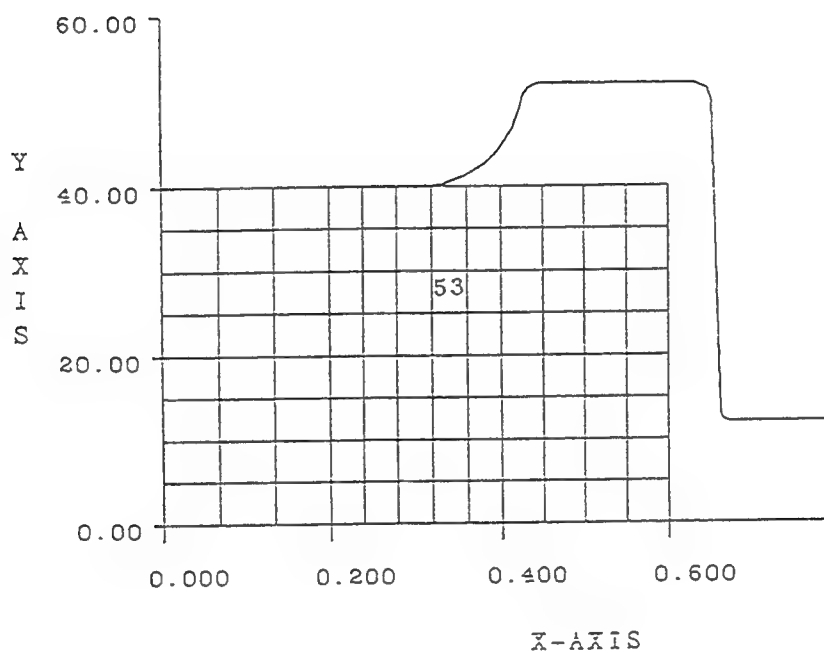


Figure 24: FEM discretization - Frictionless case

kept stationary. A rate sensitive billet material was used for the simulation. The constitutive (flow) equation for the material is given as:

$$\bar{\sigma} = k \dot{\epsilon}^g \dot{\epsilon}^h \quad (7.78)$$

where k is a proportionality constant used in the flow formulation, g is the rate sensitivity factor, and h is the effective strain exponent. For this example the values of k , g , and h were 10, 0.1, and 0.0, respectively. The strain rate of a single element was controlled, and element number 53 was chosen as the element of interest. This element was considered critical because it goes through a number of modes of deformation during the simulation due to its location in the billet. In this example the friction factor at the die/billet interface was assumed to be zero.

During the start of the simulation, seven nodes were touching the (moving) die. For each of these nodes, the normal component of velocity is a known quantity and is not considered as a degree of freedom. In addition, there are four nodes associated with the element of interest, each having two degrees of freedom. Since the degrees of freedom of the system are also considered as the states during state space modeling, this results in a full-size state space model with 15 states. The initial strain rate of element 53 was $0.0044/\text{sec}$ and the desired strain rate was $0.005/\text{sec}$. The 15 initial states were reduced to 4 using the model reduction methods described earlier. The number of states in the reduced model was decided from the controllability grammians of the full matrix. In this case, only four grammians had significant magnitude and the rest were very small, resulting in four states in the reduced order model. Since a transformation matrix was used to construct the reduced models, the weighting matrices were

modified using these transformation matrices, so as to have a uniform testing condition for all the models. The control scheme was applied for designing the die velocity using the state space models derived using the Aggregation, Davison, Marshall, Nicholson and BMR approaches. The design of velocities was carried out for 20 simulation time steps.

The comparative results are shown in Fig. 25. In this figure, the optimal die velocities are plotted as a function of time for 20 time steps (0.4 sec). The simulations were conducted using a time step of 0.02 sec. At each time step the state space model (A, B and C) is built based on the current billet geometry, die velocity (designed in the previous step), and the prevailing frictional conditions. For the first step the die velocity is taken from the input information specified. A finite time control law based on the linear quadratic regulator (LQR) theory is used to design the die velocities using the full state model. These results are used as a reference against which the results of the reduced order model are compared. The designed velocities (Fig. 25) show a sharp increase in the initial phase of deformation and then gradually stabilize with time as the strain rate approaches the desired value. From the full model, the earlier mentioned reduced-order systems are generated and an optimal die velocity is again designed. It may be observed that the velocities designed using the BMR model match very closely those of the full model. The maximum percentage error in the design was 0.3%. This percentage error was observed in the initial stages of the velocity design, and the error decreased as the simulation progressed. In the Aggregation model, the initial results (first three steps) followed the trend of the full model. But, after that the designed velocities displayed a trend quite different from that of

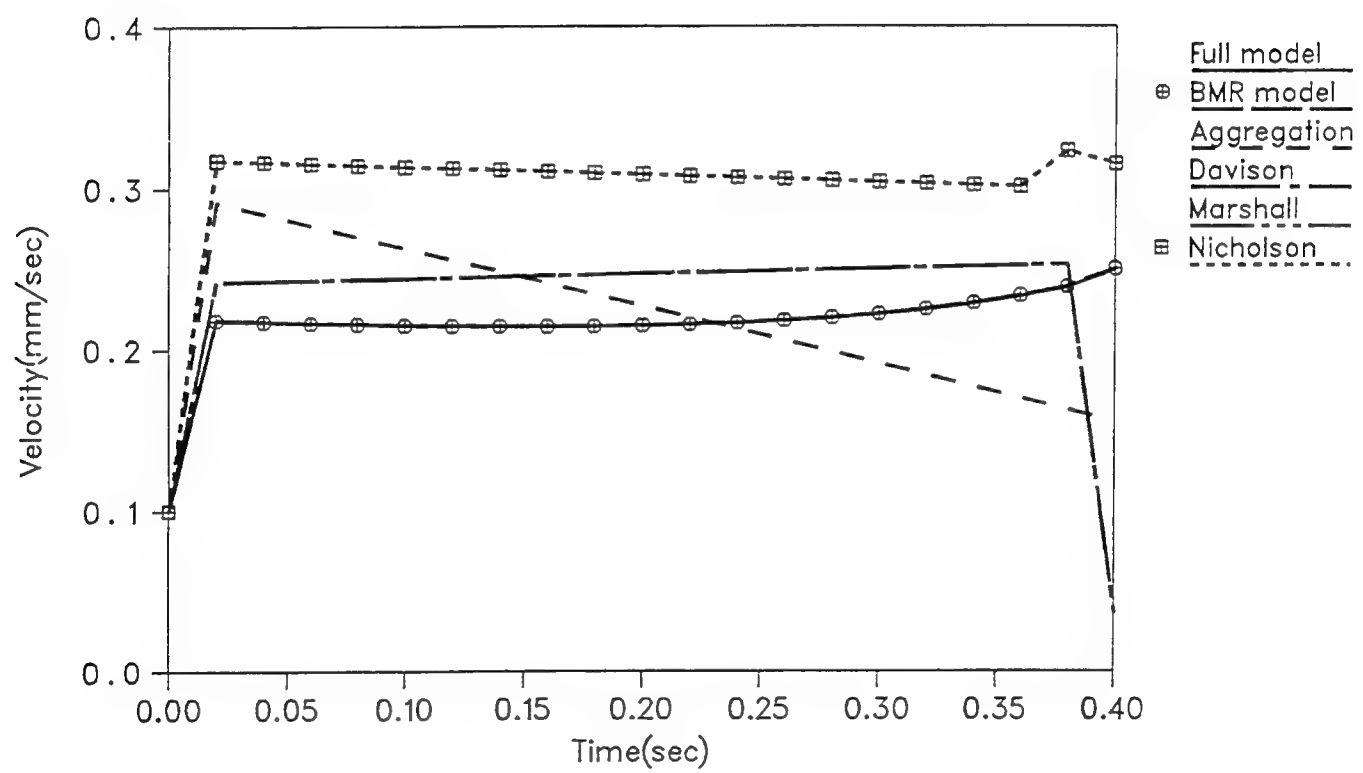


Figure 25: Comparison of velocities using reduced models and full model

the full model. This was probably because the transformation (during reduction) did not retain the controllable characteristics of the full model. Further, in the case of the Aggregation model, the performance of the reduced model improved as the number of retained states was increased. Davison's model resulted in a velocity trend similar to that of the full model except at the last time step of the simulation. In this case the designs do not match because only the first four modes are retained in the reduced system. Though the full model is compensated for within the reduced system, the initial response of the unretained states may result in a mismatch in the results. The results of Marshall's and Nicholson's method are similar, and to a large extent the trend of the full state model is maintained, in both cases. Because these models are derived from model transformations, the numerical correspondence with the full model is not exact. In these methods the proper selection and grouping of the dominant modes of the system largely influence the system characteristics and output.

For the first example, the reduced model built using the BMR scheme retains the controllable and observable characteristics of the full model. As a result, the velocities designed using the BMR model and full model match very closely. The velocities designed using the Aggregation, BMR, Marshall, Davison and Nicholson methods along with results of the full model are tabulated in Tables (3) through (7), respectively. The forging simulation was carried out using these velocities and the finite element model described earlier. The resulting strain rate trajectories obtained are depicted in Fig. (26).

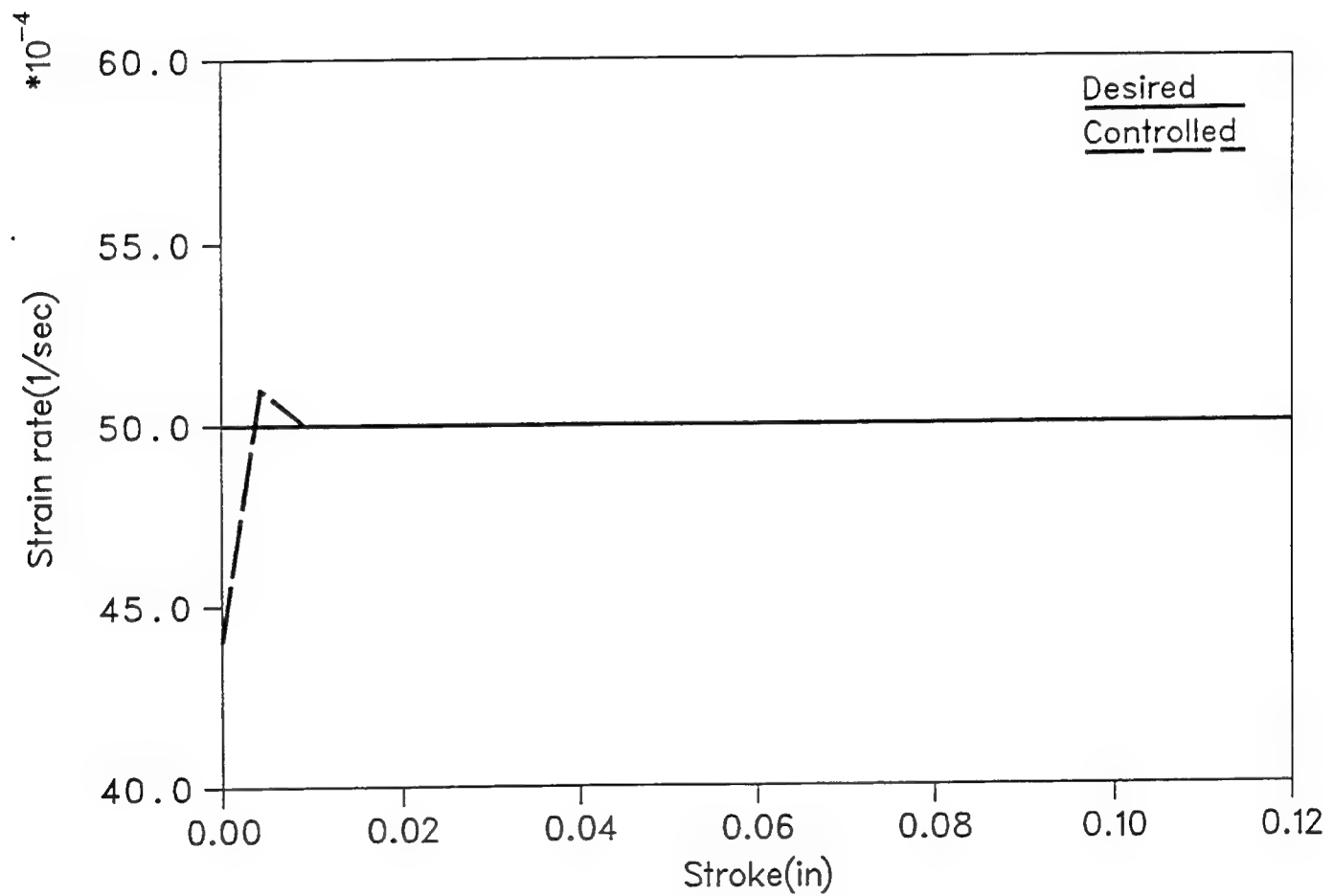


Figure 26: Comparison of desired and controlled strain rates

Table 3. Comparison of optimized velocities for aggregation method (Frictionless case)

Step No.	Time (sec)	Full model (mm/sec)	Red. Model (mm/sec)	% Error
1	0.02	0.1069	0.0221	79.3265
2	0.04	0.1102	0.0238	78.4029
3	0.06	0.1137	0.0256	77.4846
4	0.08	0.1173	0.0277	76.3853
5	0.10	0.1211	0.0301	75.1445
6	0.12	0.1251	0.0328	73.7810
7	0.14	0.1293	0.0359	72.2351
8	0.16	0.1337	0.0395	70.4562
9	0.18	0.1384	0.0435	68.5694
10	0.20	0.1433	0.0483	66.2945
11	0.22	0.1485	0.0539	63.7037
12	0.24	0.1540	0.0606	60.6494
13	0.26	0.1599	0.0687	57.0356
14	0.28	0.1661	0.0788	52.5587
15	0.30	0.1727	0.0916	46.9600
16	0.32	0.1797	0.1086	39.5659
17	0.34	0.1873	0.1323	29.3647
18	0.36	0.1953	0.1677	14.1321
19	0.38	0.2039	0.2267	-11.1820
20	0.40	0.2132	0.3457	-62.1482

Table 4. Comparison of optimized velocities for BMR model (Frictionless case)

Step No.	Time (sec)	Full Model (mm/sec)	Red. Model (mm/sec)	% error
1	0.02	-0.2497	-0.2504	-0.2803
2	0.04	-0.2387	-0.2393	-0.2514
3	0.06	-0.2333	-0.2338	-0.2143
4	0.08	-0.2288	-0.2292	-0.1748
5	0.10	-0.2252	-0.2255	-0.1332
6	0.12	-0.2223	-0.2225	-0.0900
7	0.14	-0.2200	-0.2202	-0.0909
8	0.16	-0.2182	-0.2184	-0.0917
9	0.18	-0.2169	-0.2170	-0.0461
10	0.20	-0.2160	-0.2160	0.0000
11	0.22	-0.2153	-0.2153	0.0000
12	0.24	-0.2150	-0.2149	0.0465
13	0.26	-0.2149	-0.2148	0.0465
14	0.28	-0.2150	-0.2149	0.0465
15	0.30	-0.2153	-0.2151	0.0929
16	0.32	-0.2157	-0.2155	0.0927
17	0.34	-0.2163	-0.2161	0.0925
18	0.36	-0.2169	-0.2167	0.0922
19	0.38	-0.2177	-0.2175	0.0919
20	0.40	-0.2186	-0.2183	0.1372

Table 5. Comparison of optimized velocities for Marshall's method (Frictionless case)

Step No.	Time (sec)	Full model (mm/sec)	Red. Model (mm/sec)	% Error
1	0.02	0.1069	0.1787	-67.1656
2	0.04	0.1102	0.1846	-67.5136
3	0.06	0.1137	0.1908	-67.8100
4	0.08	0.1173	0.1973	-68.2012
5	0.10	0.1211	0.2041	-68.5384
6	0.12	0.1251	0.2111	-68.7450
7	0.14	0.1293	0.2186	-69.0642
8	0.16	0.1337	0.2263	-69.2595
9	0.18	0.1384	0.2345	-69.4364
10	0.20	0.1433	0.2431	-69.6441
11	0.22	0.1485	0.2521	-69.7643
12	0.24	0.1540	0.2616	-69.8701
13	0.26	0.1599	0.2715	-69.7936
14	0.28	0.1661	0.2821	-69.8374
15	0.30	0.1727	0.2932	-69.7742
16	0.32	0.1797	0.3049	-69.6717
17	0.34	0.1873	0.3173	-69.4074
18	0.36	0.1953	0.3305	-69.2268
19	0.38	0.2039	0.3445	-68.9554
20	0.40	0.2132	0.3594	-68.5741

Table 6. Comparison of optimized velocities for Davison's method (Frictionless case)

Step No.	Time (sec)	Full model (mm/sec)	Red. Model (mm/sec)	% Error
1	0.02	0.1069	0.1318	-23.2928
2	0.04	0.1102	0.1408	-27.7677
3	0.06	0.1137	0.1504	-32.2779
4	0.08	0.1173	0.1605	-36.8287
5	0.10	0.1211	0.1712	-41.3708
6	0.12	0.1251	0.1825	-45.8833
7	0.14	0.1293	0.1945	-50.4254
8	0.16	0.1337	0.2072	-54.9738
9	0.18	0.1384	0.2207	-59.4653
10	0.20	0.1433	0.2350	-63.9916
11	0.22	0.1485	0.2503	-68.5522
12	0.24	0.1540	0.2666	-73.1169
13	0.26	0.1599	0.2841	-77.6735
14	0.28	0.1661	0.3028	-82.2998
15	0.30	0.1727	0.3229	-86.9716
16	0.32	0.1797	0.3445	-91.7084
17	0.34	0.1873	0.3679	-96.4229
18	0.36	0.1953	0.3933	-101.3825
19	0.38	0.2039	0.4210	-106.4738
20	0.40	0.2132	0.4512	-111.6323

Table 7. Comparison of optimized velocities for Nicholson's method (Frictionless case)

Step No.	Time (sec)	Full model (mm/sec)	Red. Model (mm/sec)	% Error
1	0.02	0.1069	0.1318	-23.2928
2	0.04	0.1102	0.1408	-27.7677
3	0.06	0.1137	0.1504	-32.2779
4	0.08	0.1173	0.1605	-36.8287
5	0.10	0.1211	0.1712	-41.3708
6	0.12	0.1251	0.1825	-45.8833
7	0.14	0.1293	0.1945	-50.4254
8	0.16	0.1337	0.2072	-54.9738
9	0.18	0.1384	0.2207	-59.4653
10	0.20	0.1433	0.2350	-63.9916
11	0.22	0.1485	0.2503	-68.5522
12	0.24	0.1540	0.2666	-73.1169
13	0.26	0.1599	0.2841	-77.6735
14	0.28	0.1661	0.3028	-82.2998
15	0.30	0.1727	0.3229	-86.9716
16	0.32	0.1797	0.3445	-91.7084
17	0.34	0.1873	0.3679	-96.4229
18	0.36	0.1953	0.3933	-101.3825
19	0.38	0.2039	0.4210	-106.4738
20	0.40	0.2132	0.4512	-111.6323

7.6.2 H-block compression - Friction case

In this example, a closed die forging of an H-block from a cylindrical billet was simulated using one die. The billet considered for simulation had a height of 2.45 inches and a radius of 2.45 inches. Due to the existing symmetric conditions, only a quarter of the die and workpiece were modeled. During modeling the workpiece was discretized into 240 nodes and 203 elements (Fig. 27). The die had a height to web ratio of 1.0. The same material as used in the previous example was used for this simulation. The frictional condition at the billet-die interface was specified by using a constant shear friction factor of 0.3. The simulation was initiated with an initial die velocity of 0.1 in/sec. The control of a single element was considered and a desired strain rate of 0.05/sec in element number 153 was taken as the control objective. This element is critical because it is adjacent to the die-billet contact surface, and is sensitive to the frictional conditions at the die-billet interface. During the first step of simulation, 25 nodes were touching the die. Each of these nodes has one degree of freedom as explained in the previous example. In addition, the element of interest is associated with four nodes having two degrees of freedom each. This results in a full-size (condensed) state space system with 33 states. At the end of the second time step, 29 nodes were touching the die. As explained above, this would result in a state space model having 37 states. By applying the model reduction techniques explained earlier, the number of states was reduced to 10. In this case, the number of states in the reduced model was decided by the controllability grammians. In the current example the first 10 grammians had

significant values compared to the rest, resulting in a reduced order model having 10 states.

To evaluate the performance of the reduced order models, the input velocities were designed using the full model and compared with those of the reduced models. Because the strain rate desired was very low compared to the initial strain rate of element 153, the design trend using the full model revealed that the die velocities decreased rapidly as the simulation progressed. The consolidated results and comparisons of the designed velocities are depicted in Fig. (28). The simulations were carried out using a time step of 0.02 sec for 20 time steps. It may be observed that the results of the BMR model match almost exactly with that of the full model (Table 8), with a maximum error of 0.06%. The designed ram velocities using the Aggregation, Marshall, Davison and Nicholson methods were also compared with those of the full model. These results are tabulated in Tables (9) through (12), respectively. Here again, the Aggregation model performed well in the initial few steps. But, after the seventh step the results from this model did not conform with that of the full model. This behavior of the aggregated model is due to the truncation of the higher eigenvalues of the system during the reduction process. The other models showed trends in close conformance with the full-size model. It is very likely that retaining more states in the reduced models would result in more accurate results.

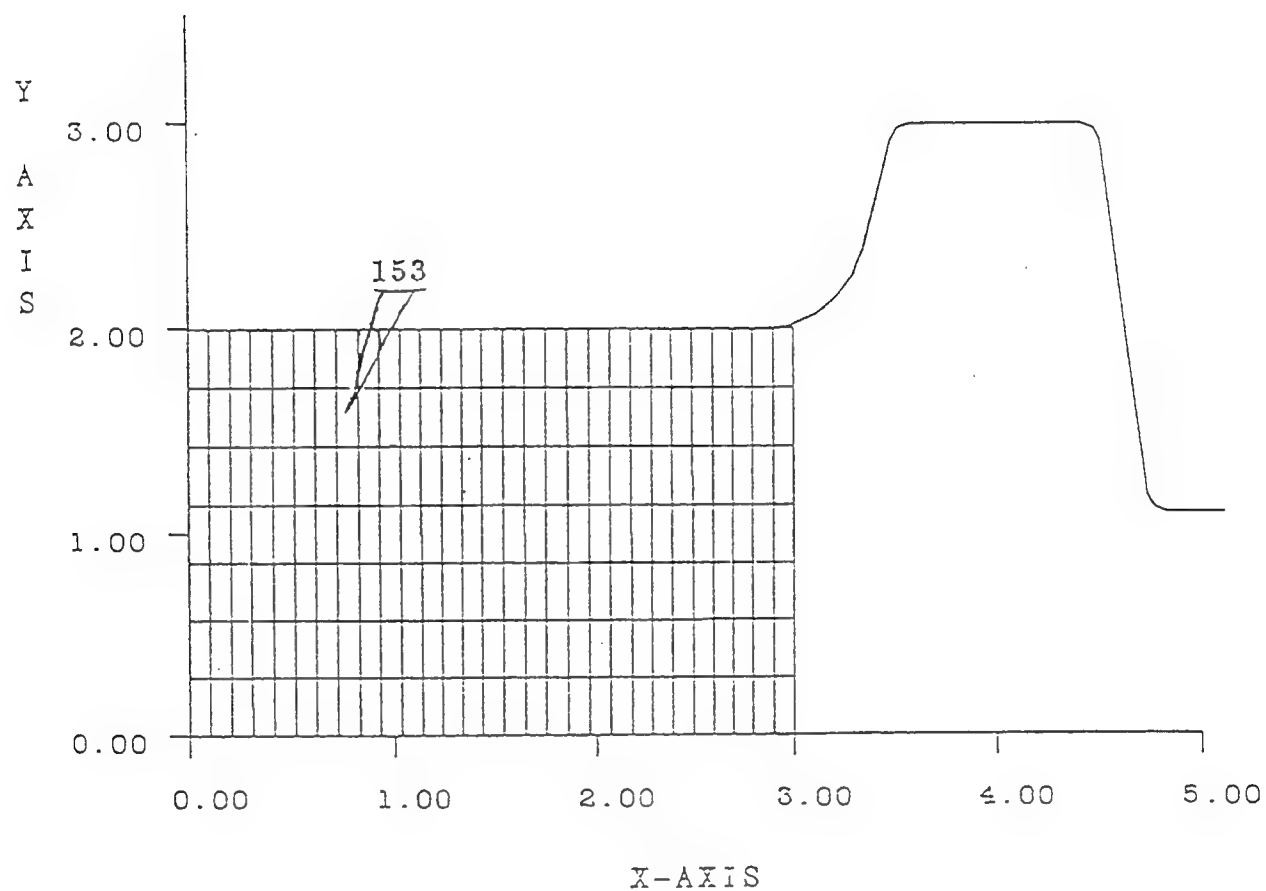


Figure 27: FEM discretization - Friction case

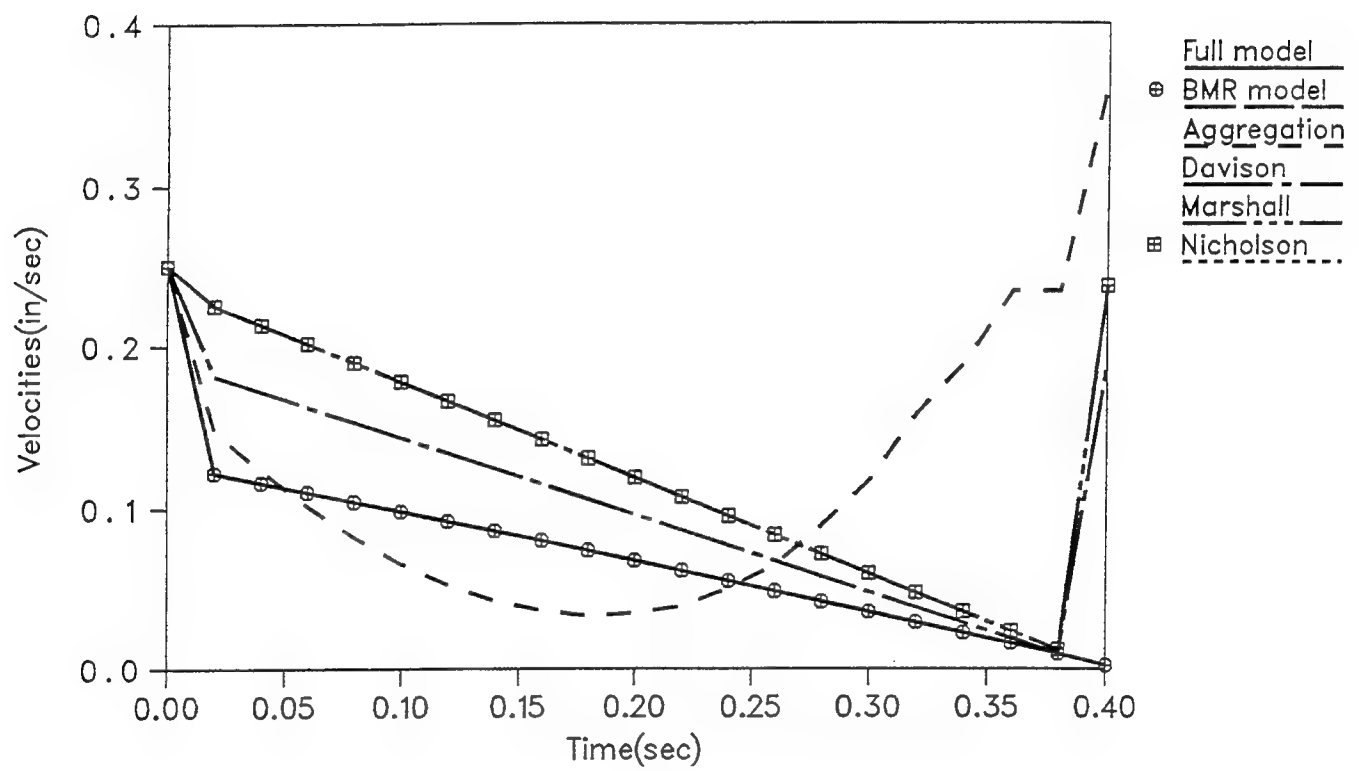


Figure 28: Comparison of velocities using reduced models and full model

Table 8. Comparison of optimized velocities for BMR model (Friction case)

Step No.	Time (sec)	Full Model (in/sec)	Red. Model (in/sec)	% error
1	0.02	-0.002341	-0.002342	0.0548
2	0.04	-0.009623	-0.009629	0.0570
3	0.06	-0.016222	-0.016229	0.0489
4	0.08	-0.022782	-0.022792	0.0423
5	0.10	-0.029304	-0.029315	0.0365
6	0.12	-0.035785	-0.035796	0.0313
7	0.14	-0.042225	-0.042236	0.0266
8	0.16	-0.048623	-0.048634	0.0223
9	0.18	-0.054980	-0.054990	0.0184
10	0.20	-0.061294	-0.061304	0.0149
11	0.22	-0.067566	-0.067574	0.0117
12	0.24	-0.073794	-0.073800	0.0088
13	0.26	-0.079979	-0.079984	0.0061
14	0.28	-0.086119	-0.086122	0.0038
15	0.30	-0.092215	-0.092217	0.0016
16	0.32	-0.098266	-0.098266	0.0003
17	0.34	-0.104272	-0.104270	-0.0020
18	0.36	-0.110232	-0.110229	-0.0035
19	0.38	-0.116147	-0.116141	-0.0048
20	0.40	-0.122016	-0.122008	-0.0060

Table 9. Comparison of optimized velocities for aggregation method (Friction case)

Step No.	Time (sec)	Full model (mm/sec)	Red. Model (mm/sec)	% Error
1	0.02	0.0993	0.2760	-177.9456
2	0.04	0.1037	0.2764	-166.5381
3	0.06	0.1083	0.2767	-155.4940
4	0.08	0.1133	0.2771	-144.5719
5	0.10	0.1186	0.2775	-133.9798
6	0.12	0.1243	0.2779	-123.5720
7	0.14	0.1303	0.2782	-113.5073
8	0.16	0.1368	0.2786	-103.6550
9	0.18	0.1436	0.2790	-94.2897
10	0.20	0.1510	0.2794	-85.0331
11	0.22	0.1588	0.2797	-76.1335
12	0.24	0.1671	0.2801	-67.6242
13	0.26	0.1760	0.2805	-59.3750
14	0.28	0.1855	0.2809	-51.4286
15	0.30	0.1956	0.2813	-43.8139
16	0.32	0.2064	0.2817	-36.4825
17	0.34	0.2179	0.2821	-29.4631
18	0.36	0.2302	0.2824	-22.6759
19	0.38	0.2434	0.2828	-16.1873
20	0.40	0.2574	0.2832	-10.0233

Table 10. Comparison of optimized velocities for Marshall's method (Friction case)

Step No.	Time (sec)	Full model (mm/sec)	Red. Model (mm/sec)	% Error
1	0.02	0.0993	0.2039	-105.3374
2	0.04	0.1037	0.2045	-97.2035
3	0.06	0.1083	0.2050	-89.2890
4	0.08	0.1133	0.2055	-81.3769
5	0.10	0.1186	0.2060	-73.6931
6	0.12	0.1243	0.2066	-66.2108
7	0.14	0.1303	0.2071	-58.9409
8	0.16	0.1368	0.2076	-51.7544
9	0.18	0.1436	0.2081	-44.9164
10	0.20	0.1510	0.2087	-38.2119
11	0.22	0.1588	0.2092	-31.7380
12	0.24	0.1671	0.2097	-25.4937
13	0.26	0.1760	0.2103	-19.4886
14	0.28	0.1855	0.2108	-13.6388
15	0.30	0.1956	0.2113	-8.0266
16	0.32	0.2064	0.2119	-2.6647
17	0.34	0.2179	0.2124	2.5241
18	0.36	0.2302	0.2129	7.5152
19	0.38	0.2434	0.2135	12.2843
20	0.40	0.2574	0.2140	16.8609

Table 11. Comparison of optimized velocities for Davison's method (Friction case)

Step No.	Time (sec)	Full model (mm/sec)	Red. Model (mm/sec)	% Error
1	0.02	0.0993	0.1233	-24.1692
2	0.04	0.1037	0.1234	-18.9971
3	0.06	0.1083	0.1235	-14.0351
4	0.08	0.1133	0.1236	-9.0909
5	0.10	0.1186	0.1237	-4.3002
6	0.12	0.1243	0.1238	0.4023
7	0.14	0.1303	0.1240	4.8350
8	0.16	0.1368	0.1241	9.2836
9	0.18	0.1436	0.1242	13.5097
10	0.20	0.1510	0.1243	17.6821
11	0.22	0.1588	0.1244	21.6625
12	0.24	0.1671	0.1245	25.4937
13	0.26	0.1760	0.1247	29.1477
14	0.28	0.1855	0.1248	32.7224
15	0.30	0.1956	0.1249	36.1452
16	0.32	0.2064	0.1250	39.4380
17	0.34	0.2179	0.1251	42.5883
18	0.36	0.2302	0.1253	45.5691
19	0.38	0.2434	0.1254	48.4799
20	0.40	0.2574	0.1255	51.2432

Table 12. Comparison of optimized velocities for Nicholson's method (Friction case)

Step No.	Time (sec)	Full model (mm/sec)	Red. Model (mm/sec)	% Error
1	0.02	0.0993	0.1233	-24.1692
2	0.04	0.1037	0.1234	-18.9971
3	0.06	0.1083	0.1235	-14.0351
4	0.08	0.1133	0.1236	-9.0909
5	0.10	0.1186	0.1237	-4.3002
6	0.12	0.1243	0.1238	0.4023
7	0.14	0.1303	0.1240	4.8350
8	0.16	0.1368	0.1241	9.2836
9	0.18	0.1436	0.1242	13.5097
10	0.20	0.1510	0.1243	17.6821
11	0.22	0.1588	0.1244	21.6625
12	0.24	0.1671	0.1245	25.4937
13	0.26	0.1760	0.1247	29.1477
14	0.28	0.1855	0.1248	32.7224
15	0.30	0.1956	0.1249	36.1452
16	0.32	0.2064	0.1250	39.4380
17	0.34	0.2179	0.1251	42.5883
18	0.36	0.2302	0.1253	45.5691
19	0.38	0.2434	0.1254	48.4799
20	0.40	0.2574	0.1255	51.2432

The reduced model constructed using the BMR method resulted in a velocity schedule very close to that of the full state model (Table 8), and the corresponding strain rate profile is depicted in Fig. 29.

7.7 Analysis of results

In this work, an efficient model reduction scheme suitable for the metal forming applications is identified. The methodology developed is general purpose and applicable to most metal forming processes such as forging, extrusion, upsetting and coining processes. Of the possible order reduction methods studied, the balanced model reduction (BMR) method was the most accurate scheme suitable for process control of metal forming operations. Because the BMR scheme is based on the controllable and observable properties of the original system, the designed velocities matched almost exactly with those of the full model. Another advantage of this method is that it can be used for a very large reductions in the number of states. Also, this method does not need any additional calculation of weighting matrices since it is based on the controllability of the original system. This results in a savings in computational time during simulation, as compared to the other model reduction methods.

The consolidated results are presented in Figures (25) and (29). In the first case, the discretized system resulted in 234 states, which was reduced to 15 states by using finite element condensation techniques. This was further reduced to four states by the model reduction schemes considered. The initial strain rate of the uncontrolled system was $0.0044/\text{sec}$ and the objective was to increase this to $0.005/\text{sec}$. Because the desired strain rate is higher than the initial strain rate, the control dictated a

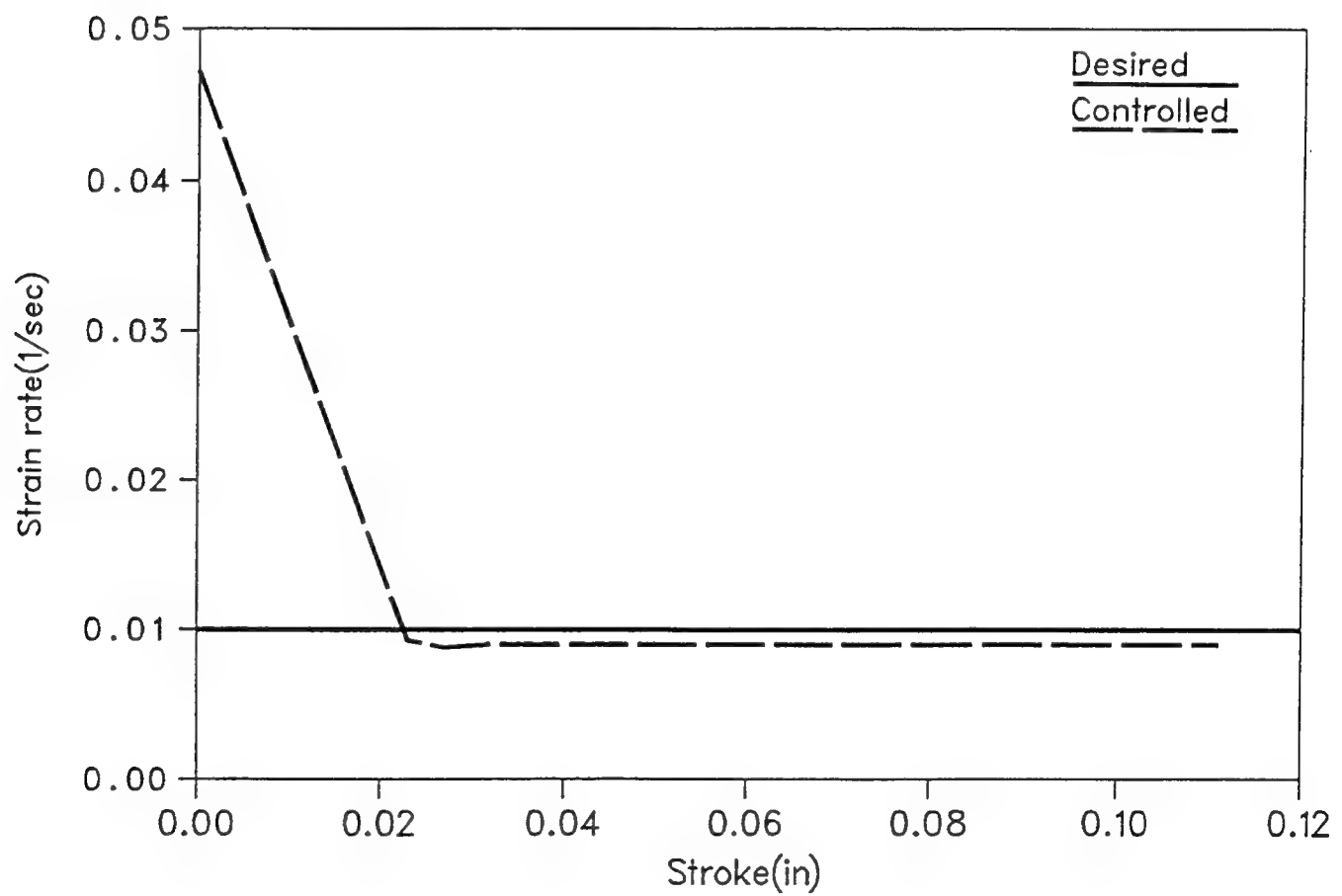


Figure 29: Comparison of desired and controlled strain rates

sharp increase in the velocity. The change in the velocity gradually reduced with die stroke, maintaining the strain rate at 0.005/sec. This trend was exhibited by all the reduced models except the Aggregated model. The reduced model constructed using the balanced model reduction scheme resulted in a design closest (comparatively) to that of the the full model. For the BMR model, the maximum deviation in velocities from the original (full-size model) design was 0.3%.

In the second case, the finite element model had 240 nodes, and the number of states in the original system was 480. The condensation scheme reduced this large number of states to 37 at the second step, and model reduction further reduced the number of states to 10. The initial strain rate of element 153 was 0.0996/sec, and the desired effective strain rate was 0.005/sec. Because a reduction in effective strain rate is desired, the designed velocities decreased sharply to ensure that the desired strain rate is achieved. This tendency was shown by all the reduced models except the Aggregation model. A characteristic feature of the modal analysis methods is that the steady state response matches with the parent model. Hence, the reduced model behaves similar to the full model after the settling time is reached. But in metal forming processes, the simulation time step cannot be large because of the nonlinearity of the system/process. Therefore, in general, modal analysis methods are not suitable for metal forming processes.

CHAPTER 8

Numerical Examples - Reduced Order Models

The condensed state space model representing the coupled thermomechanical forging system is first constructed. This model is further reduced by retaining the controllable and observable subspace of the system using the balanced state space representation. The process parameters are then designed using LQR theory as an off-line design tool. The design problem is posed as an output tracking problem and the trajectory to be tracked is the desired strain-rate profile of the element of interest. The state space model is updated at the end of each time step to accomodate the frequent changes in geometry and boundary conditions.

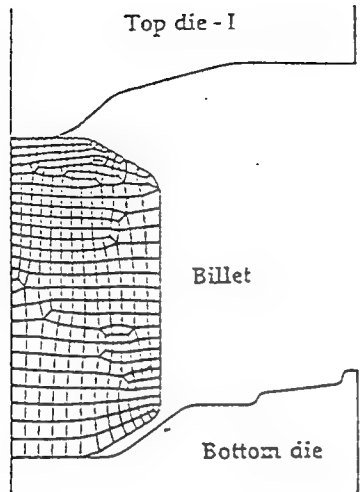
The design approach is demonstrated using two example cases. In the first example, the design of process parameters (die velocity) is performed while forging an integrated blade and rotor (IBR) disk under isothermal conditions. This problem is carried out with two different initial conditions. In the first case an initial die velocity of 1.0 in/sec was used, and in the second case, the design was carried out using an initial ram velocity of 0.5 in/sec. In both cases, the method was demonstrated using two different strain rate requirements. Also, the simulation was carried out only for 200 time steps, and not until completion. This is because the goal of these examples is limited to demonstrating the concept developed and not for simulating and analyzing the entire forging process. In the second example, die velocity design was performed under nonisothermal conditions for an engine disk

forging. For validation purposes the design obtained using the reduced model was compared with that obtained using the full model.

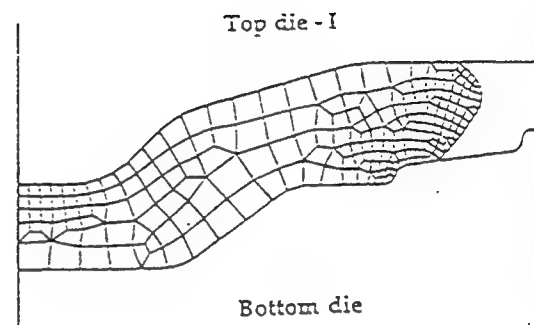
8.1 Isothermal design - IBR disk forging

Forging of an IBR disk is generally conducted in multiple stages because of the complexity and intricacy of the finished part. The die/billet shapes for this forging were determined by earlier researchers using a trial and error approach. Figure (30) shows the billet and die shapes used in simulating the IBR disk forging. Figures (30a) and (30b) show the start and finish of the first stage of forging. The second stage forging simulations are shown in Figures (30c) and (30d).

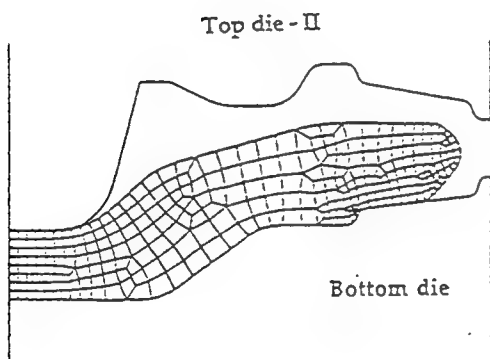
In this work, the billet and die shapes shown in Figure (31) were used for simulation while designing the process parameters. Though there is a considerable change in billet shape during the first stage of simulation, this process is similar to pure compression where only one mode of deformation is dominant. On the other hand, the second stage has multiple modes of deformation and constitutes a more challenging forging problem. As a result, the second stage of the IBR disk forging was selected for demonstrating the methodology proposed in this work. To evaluate the performance of the reduced order model, the same case was studied with two different initial ram velocities and with two different design (strain rate) requirements. Element 275 was chosen as the element of interest for this example (Figure 31). This element is ‘critical’ because it goes through a variety of deformation modes as the forging simulation progresses. A hypothetical rate dependent



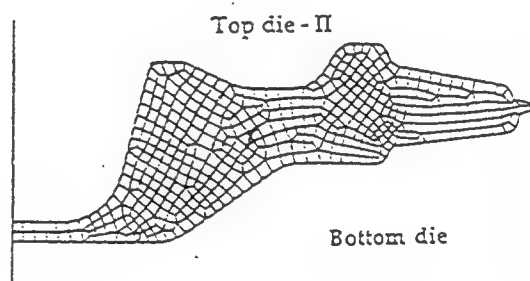
(a). Start of the first stage forging



(b). End of the first stage forging



(c). Start of the second stage forging



(d). End of the forging

Figure 30: Simulation of IBR disk forging

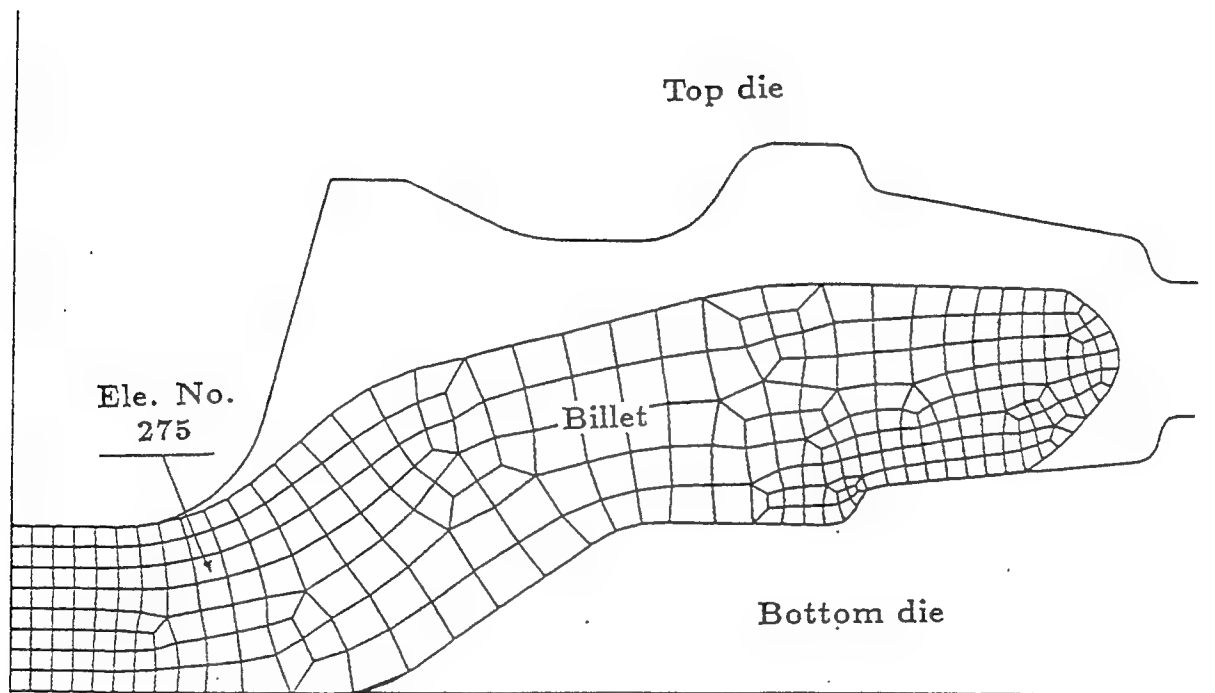


Figure 31: Finite element model of Integrated Blade and Rotor disk

material with constitutive equation $\bar{\sigma} = k\dot{\bar{\epsilon}}^g\bar{\epsilon}^h$ was used in the simulation [Ref. Eqn. (7.78)]. In this case, the proportionality constant k , the strain rate exponent g , and the strain sensitivity factor h , were assumed to be 10.0, 0.1, and 0, respectively. Due to the symmetry of the model only one half of the disk was modeled. The discretized workpiece had 302 quadrilateral elements and 347 nodes. A constant temperature of 1700°F was maintained in the workpiece for the entire isothermal forging process. The bottom die was kept stationary while the top die was allowed to move. Interface frictional conditions were enforced using a constant shear friction factor of 0.15.

In the first case the simulation was started with an initial die velocity of 1.0 in/sec. Two different strain-rate requirements of 0.2/sec and 0.5/sec were imposed on element 275. The 0.5/sec strain rate case was compared with the full state space model results and the designed velocities for 200 simulation time steps are shown in Figure (32). The full model results were used as the reference design values. From the figure it can be observed that the full model and reduced model results match exactly, and the difference in results obtained from the two models is zero. At the beginning of the process, the full state space model had 26 states and the controllable subspace (reduced order model) had 4 states. At the completion of 200 time steps, there were 34 states in the full model and 5 states in the reduced model. Figure (33) depicts the effective strain rate profile of element 275 for the the full and reduced models. The difference in results for the two models is again zero, because the balanced model consists of the controllable subspace of the full system and the weighting matrices (for control) used in both the simulations are the same. The fluctuation in die velocity/strain rate towards the end of the 200th step is because

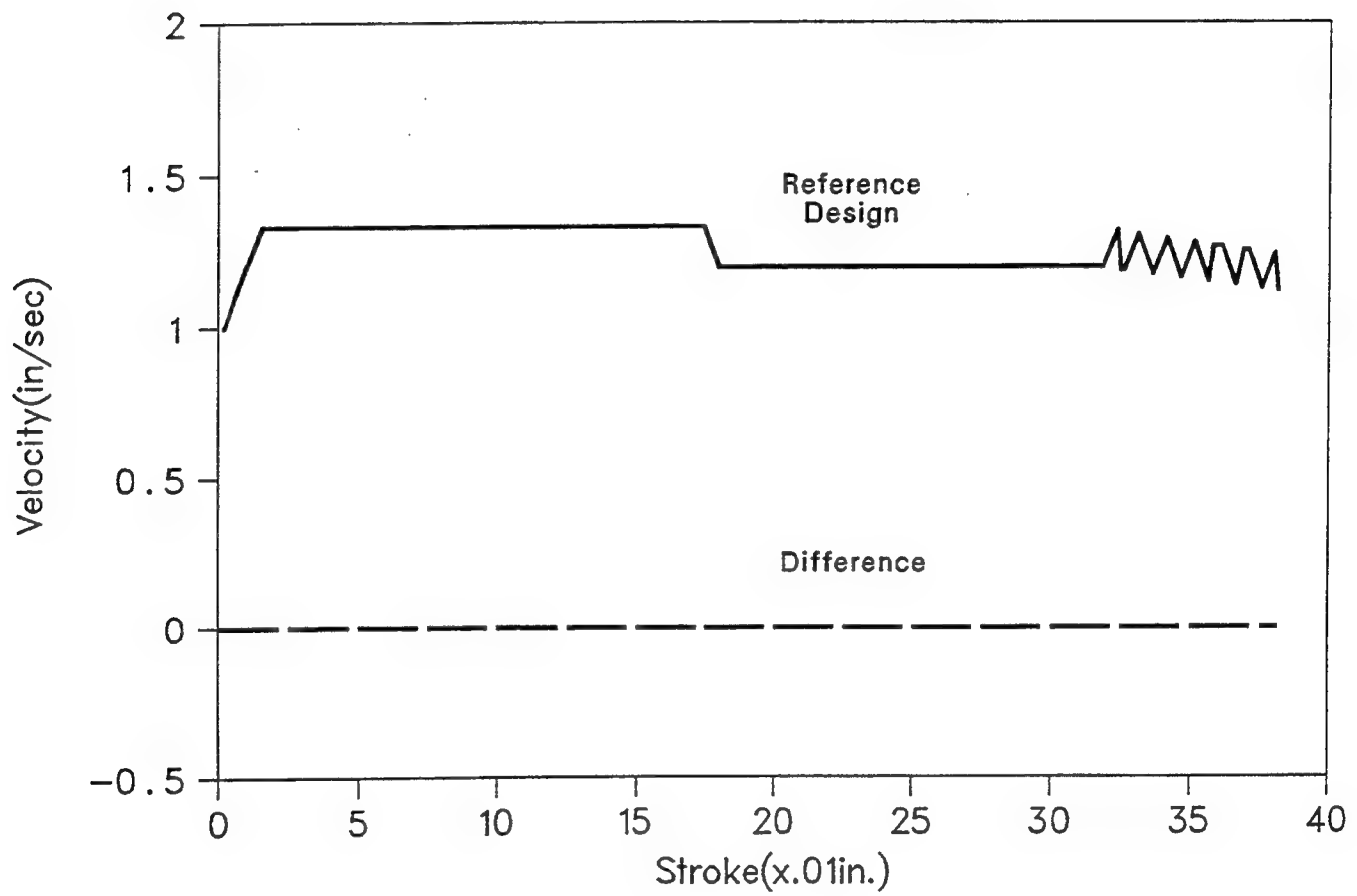


Figure 32: Die velocity profile for IBR disk forging (strain rate = 0.5)

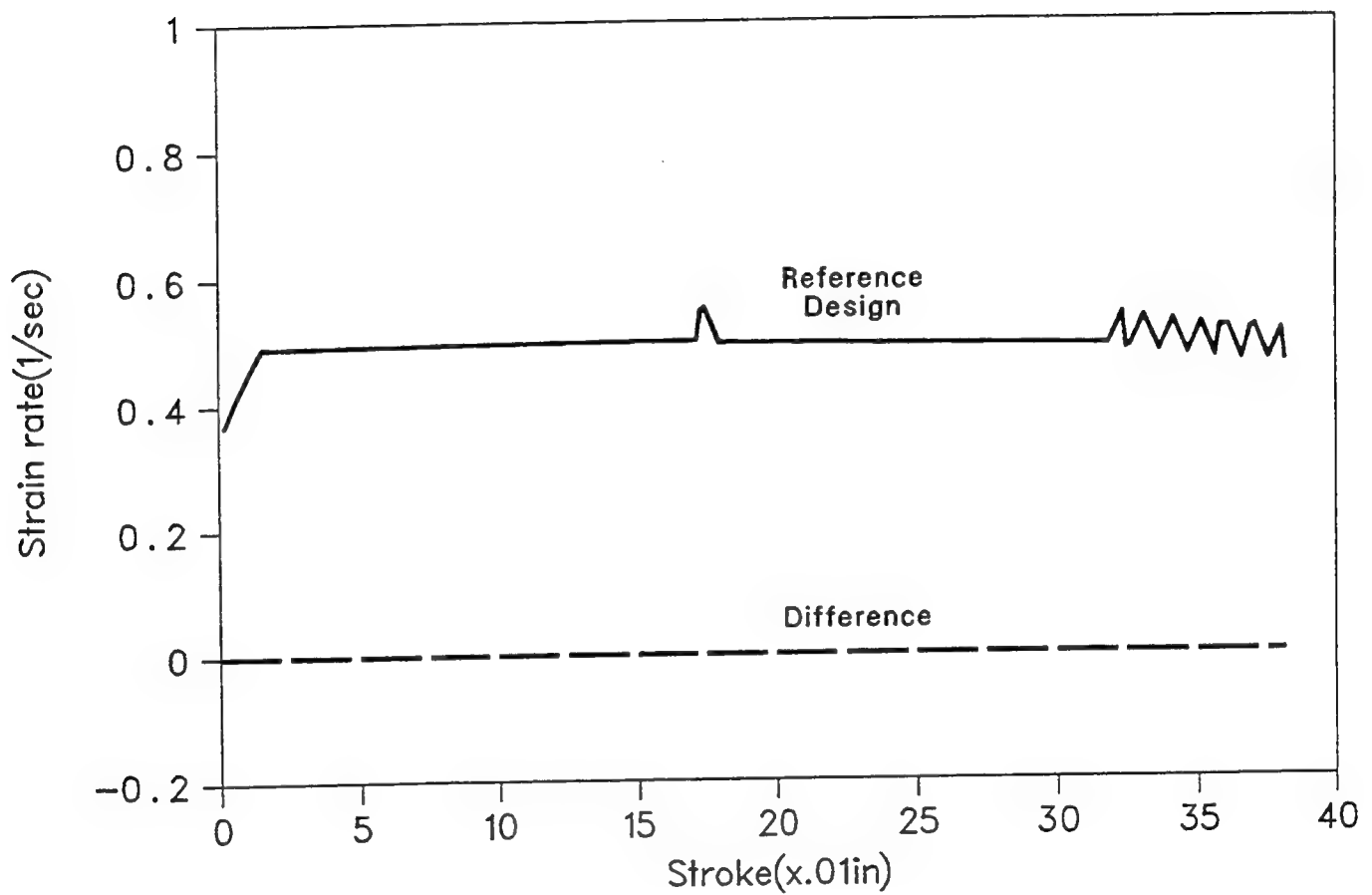


Figure 33: Strain rate profile for IBR disk forging (strain rate = 0.5)

of the change in boundary conditions of the system as nodes get detached and reattached to the die surface. With the same initial die velocity, a different design requirement of 0.2/sec was now imposed on element 275. The design procedure was then repeated for 200 simulation steps. The strain rate of element 275 obtained using the designed ram velocity schedule was compared with that obtained using a constant velocity of 1.0 in/sec in Figure (34). This figure shows a plot of the strain rate against die stroke upto a stroke length of 0.0993 in.

The design was continued for the strain-rate requirement of 0.5/sec, until elements distorted significantly and remesh was needed. The reduced model at this stroke (0.98 in.) had 5 states, while the full model had 66 states. The velocity and strain rate schedules for this example are described in Figure (35) and Figure (36), respectively. It may be observed that there is a sudden jump in strain-rate (Figure (37)) at a stroke of 0.17 in. due to the detaching of a node from the bottom die. Further, a series of oscillations in strain-rate may be observed at a stroke of 0.4 in. These oscillations may be attributed to the attaching of additional nodes to the die at this stroke. As new nodes come in contact with the die, the time step used in ALPID decreases considerably. The controller now has a smaller time duration to meet the strain rate requirement in the 'control' element. It thus makes large corrections in the input (die velocity). If these adjustments are not within the equipment acceleration limit, the die velocity tends to bounce back and forth between the acceleration bounds resulting in the fluctuations observed in Figure (37). For on-line control implementation, these oscillations must be smoothed about their mean value at the disturbance locations and then used.

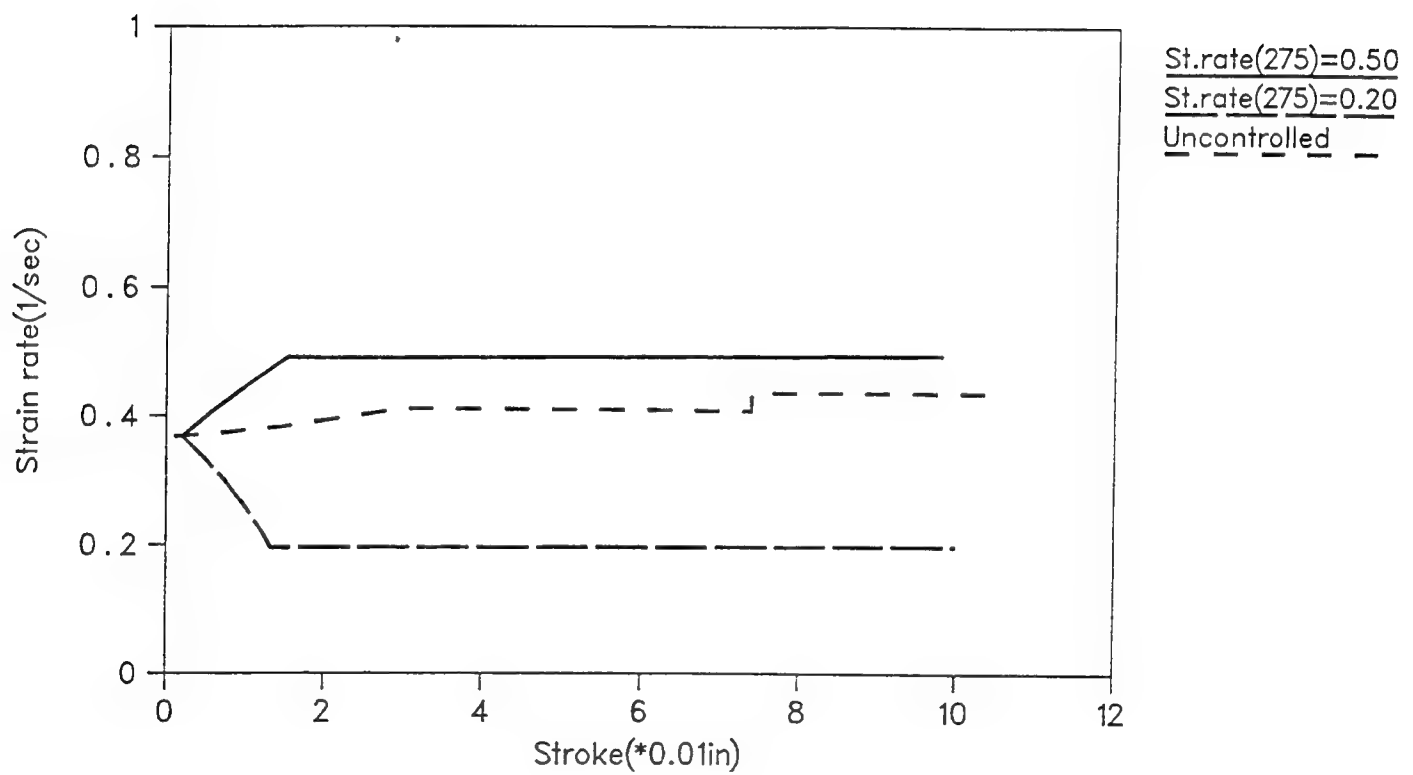


Figure 34: Comparison of strain rates for IBR forging using reduced order model

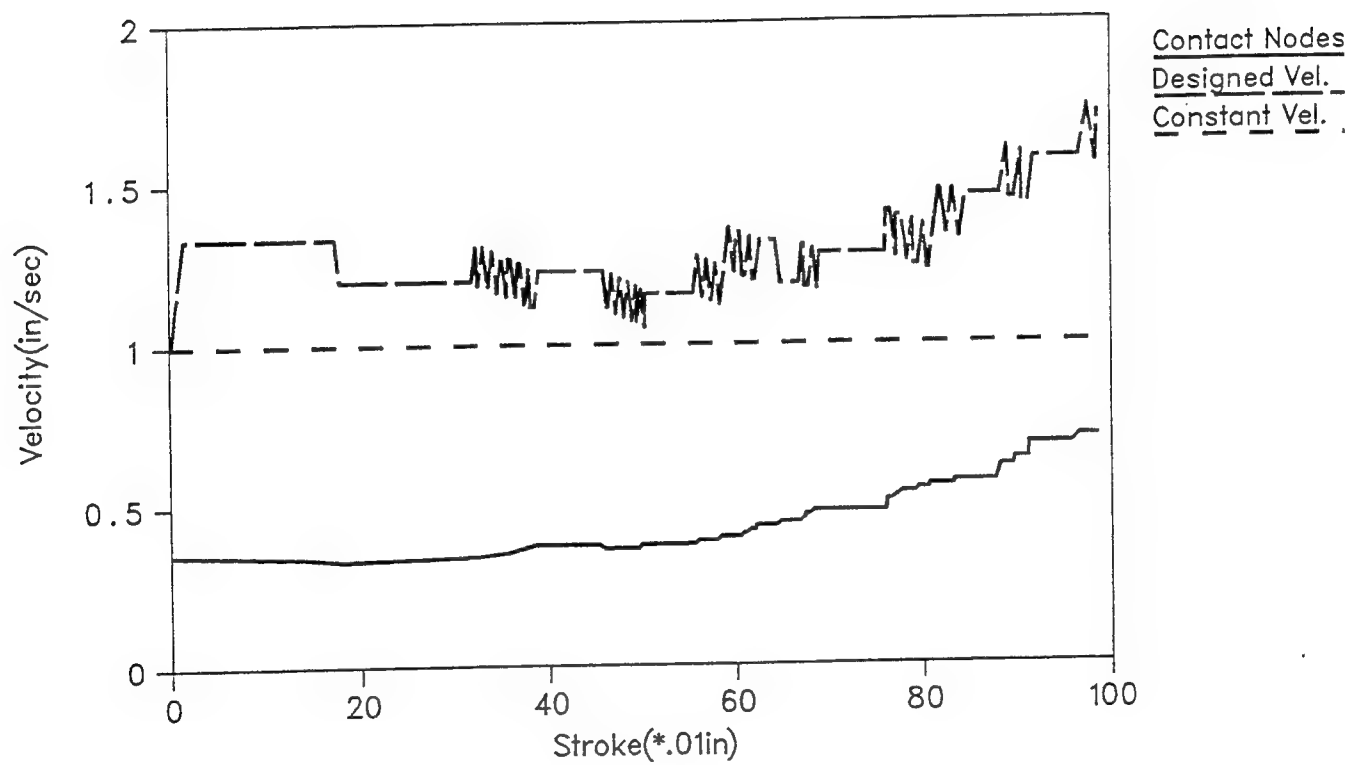


Figure 35: Die velocity profiles - Designed and constant velocity cases

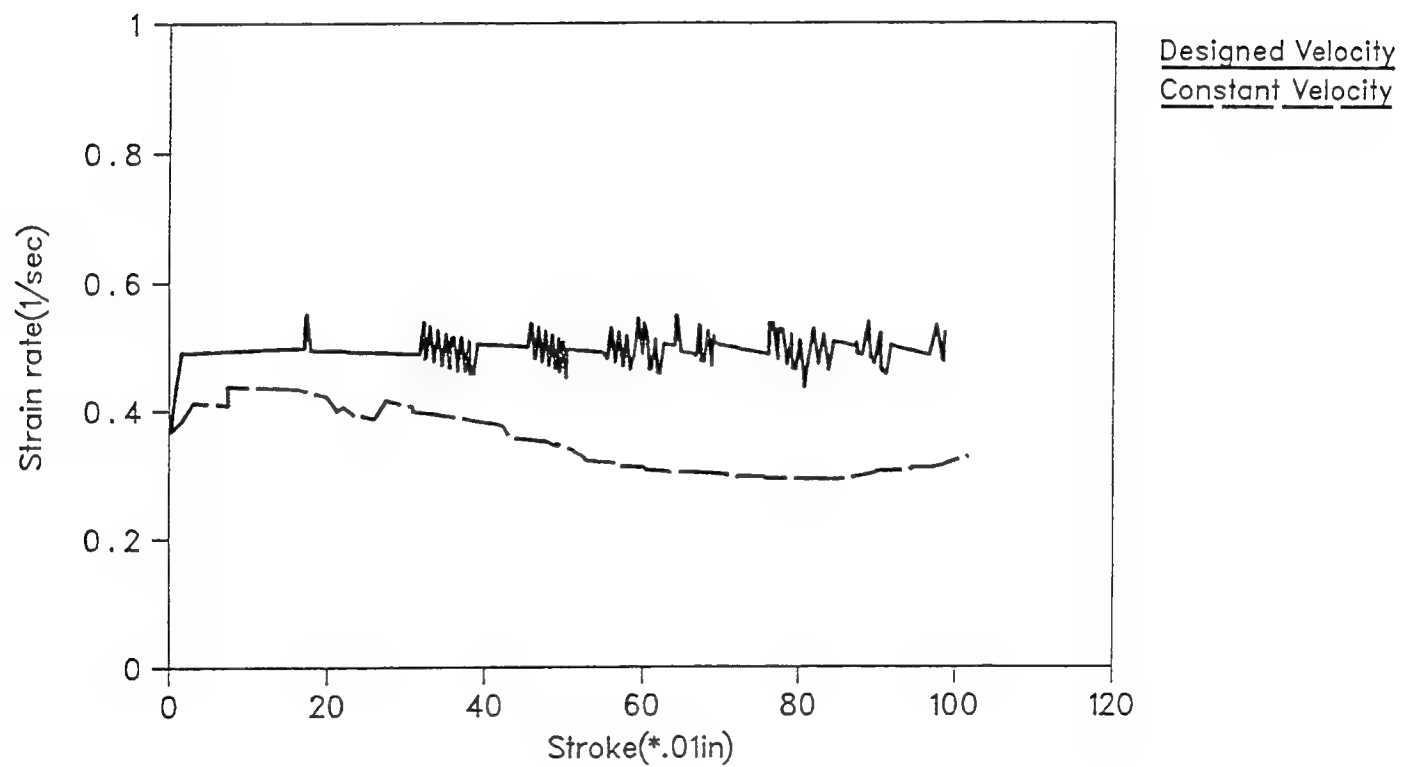


Figure 36: Strain rate profiles - Designed and constant velocity cases

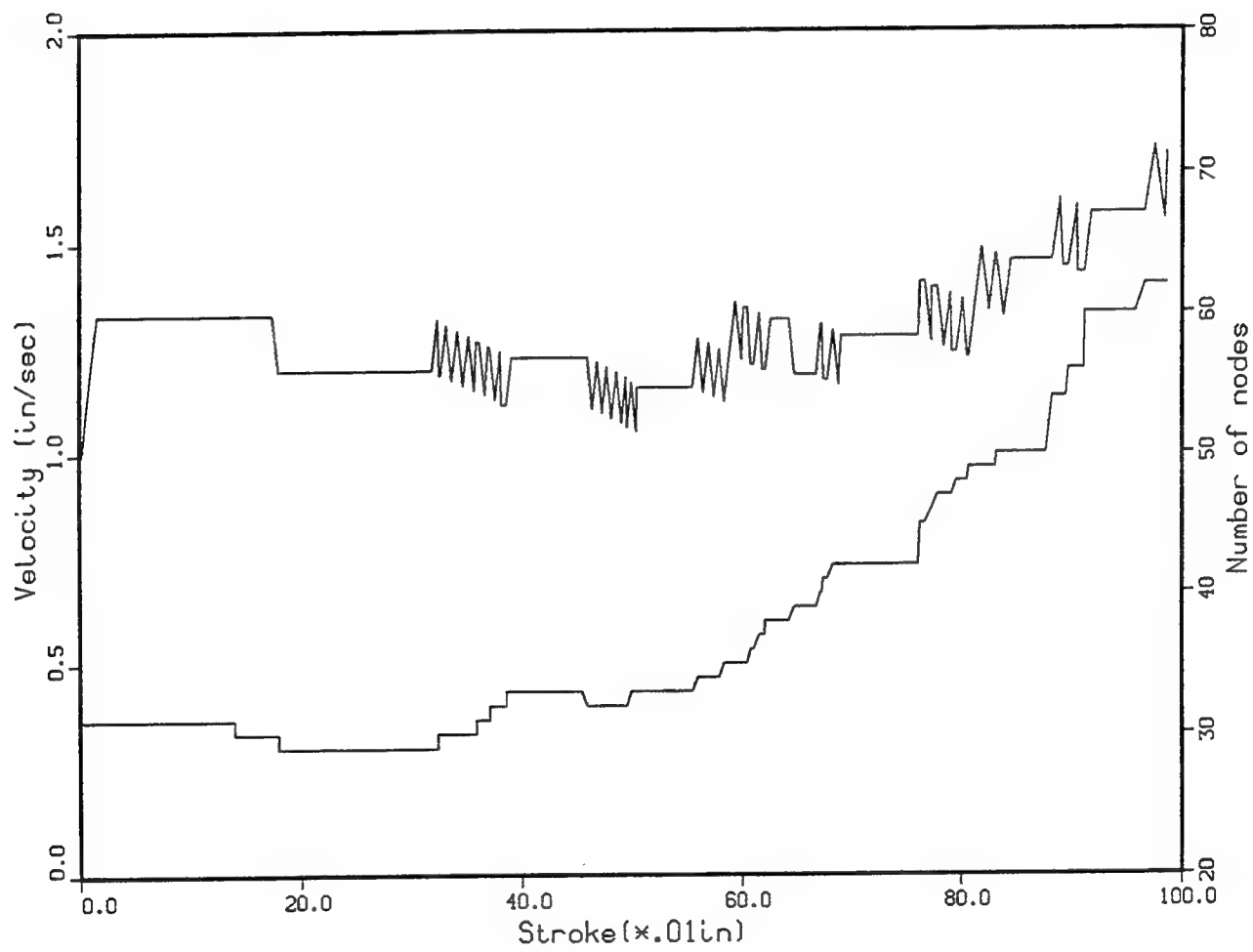


Figure 37: Comparison of designed velocities and contact nodes vs. stroke

In the second case, an initial die velocity of 0.5 in/sec was used with two different design requirements of 0.15/sec and 0.1/sec on the strain rate of element 275. Figure (38) shows a comparison between the strain rate profiles for the controlled and uncontrolled (constant velocity) cases for 200 simulation steps. The figure demonstrates the effectiveness of the reduced order model in meeting the design requirement under different initial conditions and confirms the stability of the proposed approach.

8.2 Non-isothermal design - Engine disk forging

In the second example, process parameter design for an engine disk forging was carried out under nonisothermal conditions. The finite element discretization of the billet and die for the engine disk are shown in Figure (39). An initial die temperature of 600°F and initial billet temperature of 1700°F was chosen for this simulation. Figure (39) also shows the location of the element of interest (element 23) and critical node (node 18) for this example. The critical node may be defined as the node at the die-billet interface whose temperature is to be tracked. Only the interface nodes qualify to be critical nodes because they go through a variety of heat transfer modes as deformation proceeds. The design requirement was to maintain the strain-rate of the element 23 at 0.7/sec. Only a quarter of the billet was modeled because of the inherent symmetry of the engine disk along the two cartesian axes. The billet was discretized using 50 quadrilateral elements and 66 nodes. The billet material used for this example was titanium alloy (Ti 6242), and

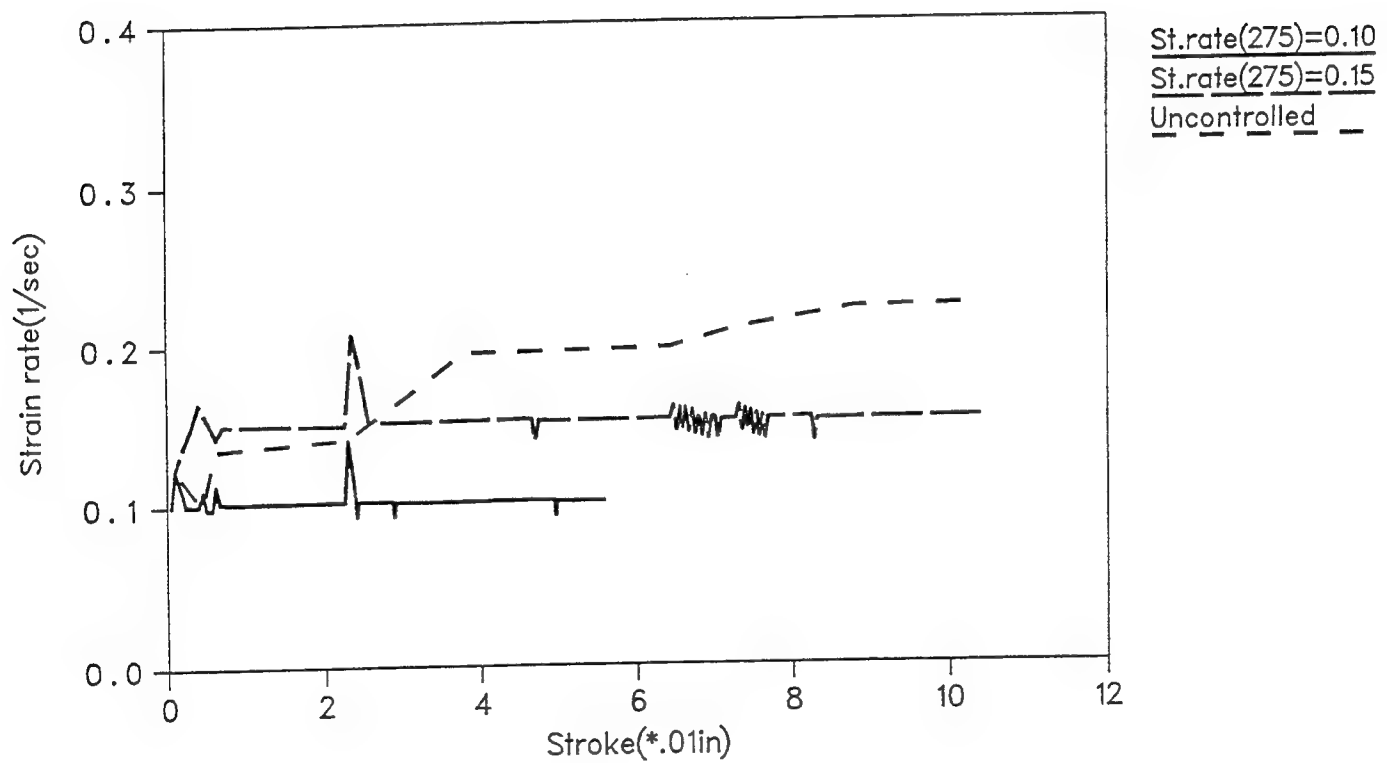


Figure 38: Comparison of strain rates for IBR disk forging

the design was started using a single die (top die) moving with a velocity of 1.0 in/sec.

The full-size state space model for this system (nonisothermal) resulted in 21 states. The number of states was further reduced to 10 by using the BMR method. Process parameter (die velocity) design was performed, and Figure (40) shows the resulting strain rate trajectory. In the figure, the results from the full state model were used as the reference. It may be observed that the full and reduced order models gave exactly the same results. The corresponding die velocity profiles for the two models (Figure (41)) also matched exactly. The temperature profile of node 18 was compared for the two models and is depicted in Figure (42). Again, it was observed that the results of the full-size and reduced order state space models match very well, with a maximum difference in nodal temperature of 0.25%. The simulation was carried out till the die was completely filled, and at the end of the simulation it was observed that the full model had 41 states while the reduced order model had a total of 11 states.

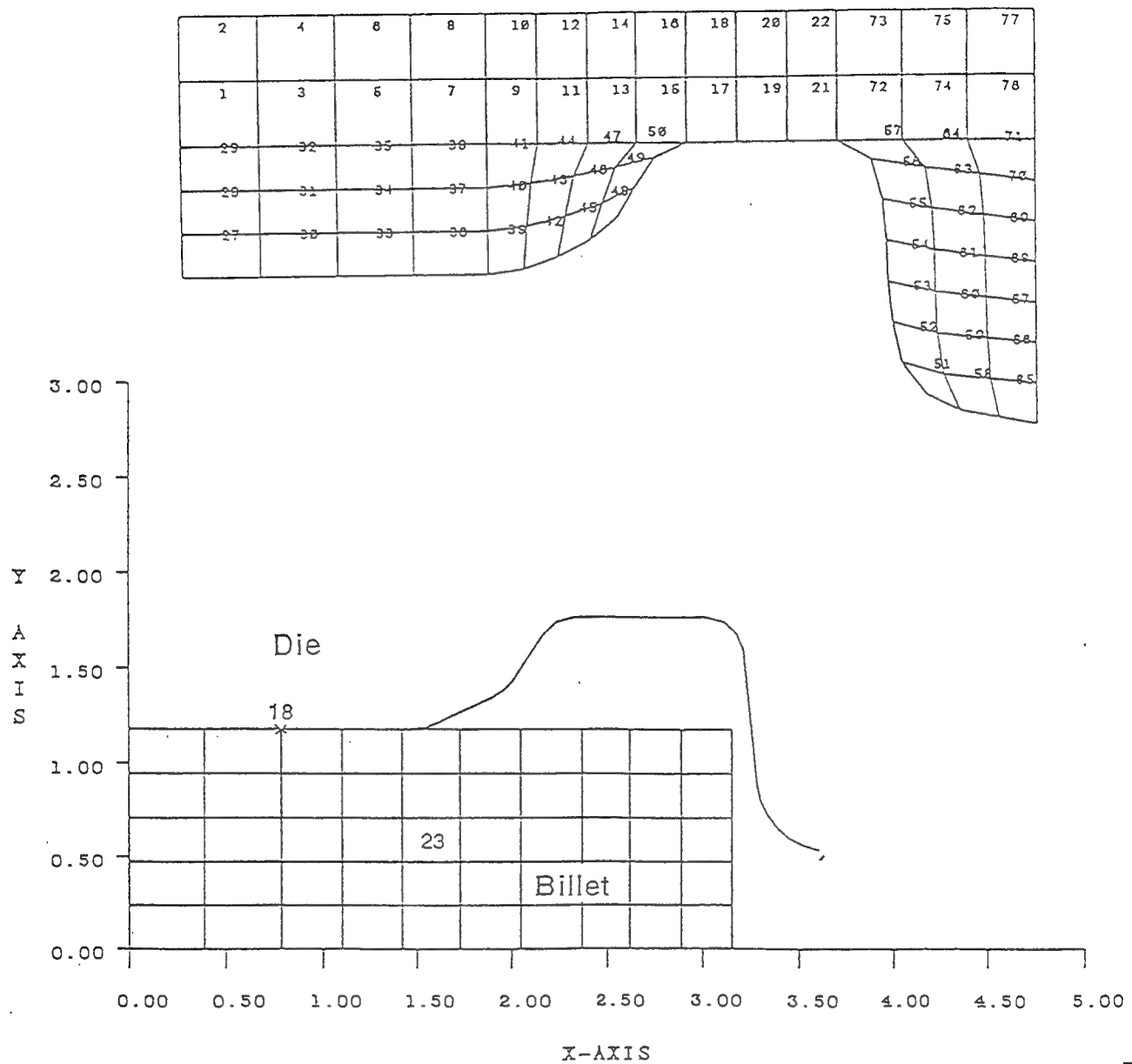


Figure 39: Finite element model of die and billet for engine disk

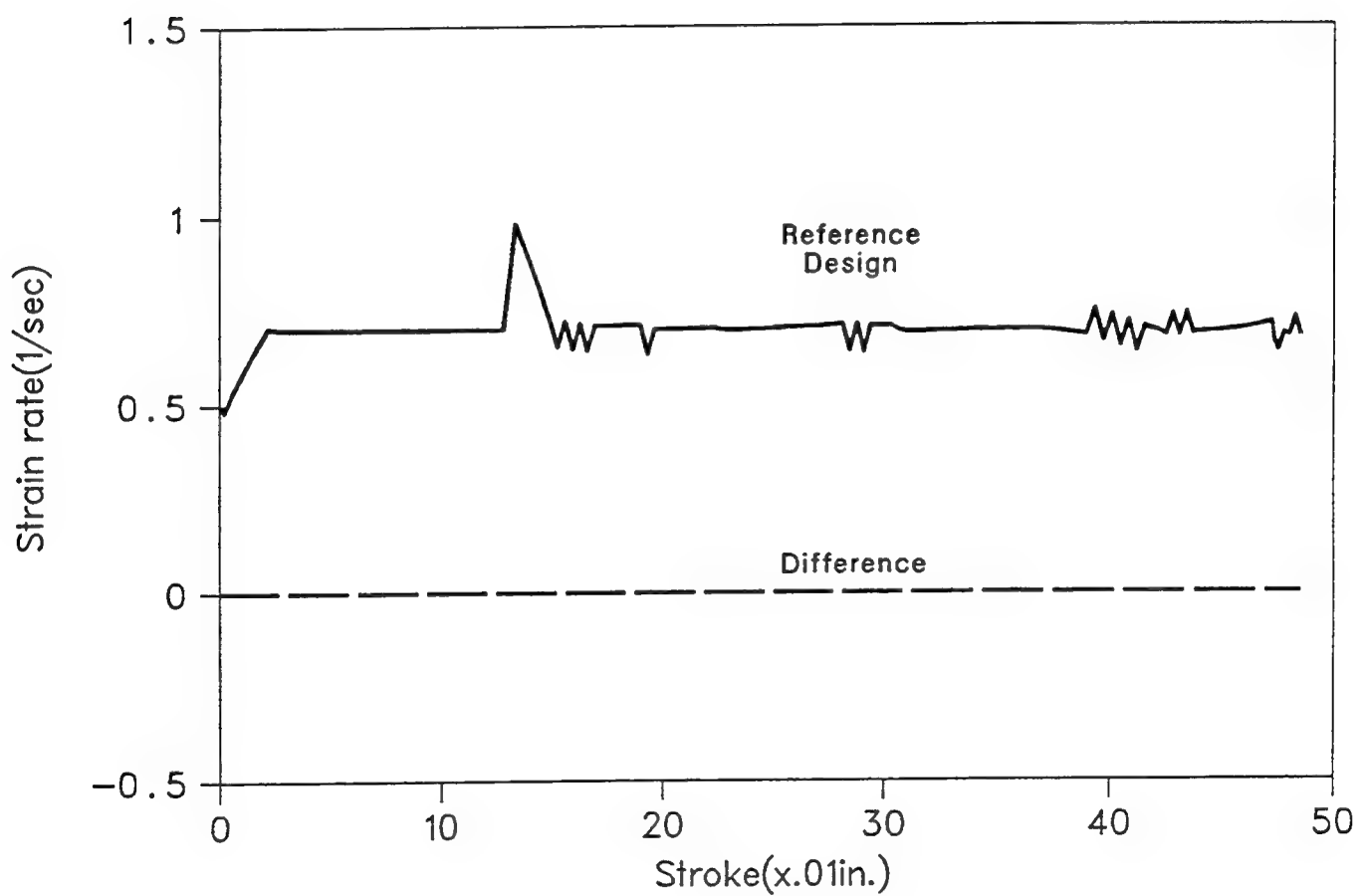


Figure 40: Comparison of strain rates for engine disk forging

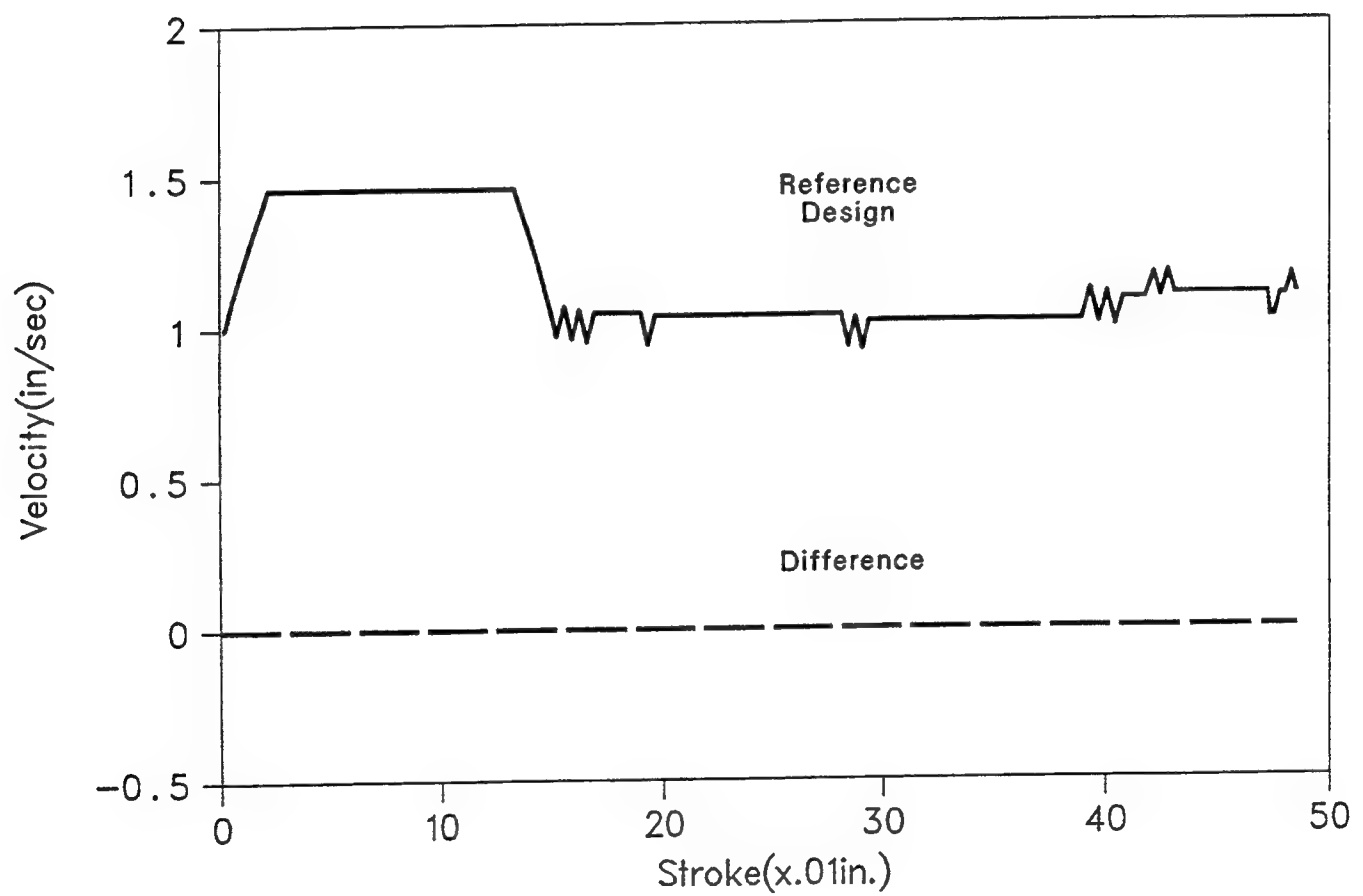


Figure 41: Comparison of die velocities for engine disk forging

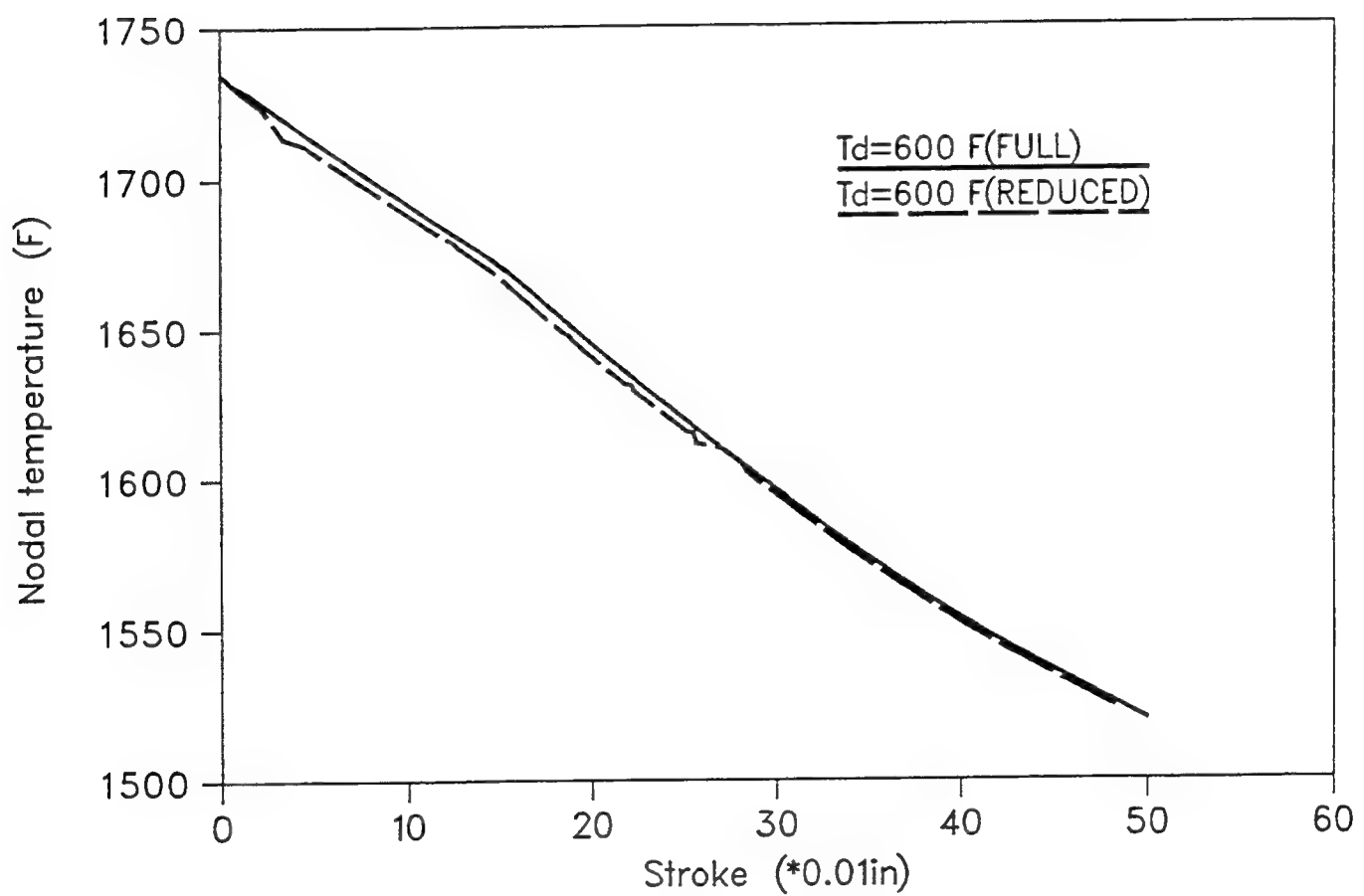


Figure 42: Comparison of nodal temps. (node 18) for engine disk forging

CHAPTER 9

Practical Aspects in Process Control Design

9.1 Smoothened die velocity profiles

The optimal control scheme described earlier worked satisfactorily for most metal forming problems. But, it was observed that simulations involving intricate and complex die/billet shapes resulted in frequent changes in the material flow direction and boundary conditions of the system. This implies that nodes get attached/detached from the die boundary at frequent intervals as the simulation progresses. This phenomenon causes the optimal control scheme to produce an oscillating die velocity schedule. In addition, there is a complex interplay of forces during die-fill which results in unsteady and non-uniform material flow. This again causes the control algorithm to produce a fluctuating die velocity during the final stages of the forming process. A fluctuating or oscillating die velocity schedule is impractical to implement on a hydraulic press. Therefore, designed velocity curves were smoothed locally using curve-fitting techniques before implementation. To check the effect of this approximation on the results obtained, the new velocity schedule was fed back into the system using the same design conditions and requirements as the original (control) simulation. Fig. 43 shows a comparison of the original (designed) and smoothed velocity profiles for an axisymmetric engine disk forging. The corresponding strain rate profiles are depicted in Fig. 44. It is observed that the strain rate obtained using the smoothed velocity profile satisfies the (strain rate) design requirement, and is also in close conformance with that obtained using the original velocity profile.

A smoothed velocity schedule was also produced for a plane strain channel section forging. Again, it was observed that the strain rate obtained met the design requirement satisfactorily, and was in conformance with that obtained using the original velocity. Figures 45 and 46 depict the die velocity and strain rate profiles for this example case. It may thus be concluded that the smoothed velocity curves are an acceptable approximation, and may be used for practical application of the control algorithm described in this work.

In addition to the advantage during implementation, the smoothed velocity profiles are also an asset while carrying out parametric studies for metal forming simulations. In such studies, generally, repetitive simulations must be performed, and previously constructed smoothed velocity profiles can directly be used for carrying out additional simulations, instead of using the computationally intensive control-based design methodology. This would save a considerable amount of computational time and effort during the simulation, since expensive numerical calculations involved in the design process may be avoided.

9.2 Stability and validity of the state space models

The results obtained using the control-based methodology depend, to a large extent, on the prevailing properties and characteristics of the metal forming system. This means that the designed velocities and the effectiveness of the control scheme are dependent on the system matrices (plant, input, and output matrices) and the weighting matrices used in the LQR design scheme. But, for simple forging simulations, having uniform and well distributed metal flow, it was observed that the system matrices did not change significantly from one time step to the next. Studies were thus carried out to determine the effect of using only one set of system matrices for the entire simulation, instead of building the state space model at every time step. This would again reduce the computational cost

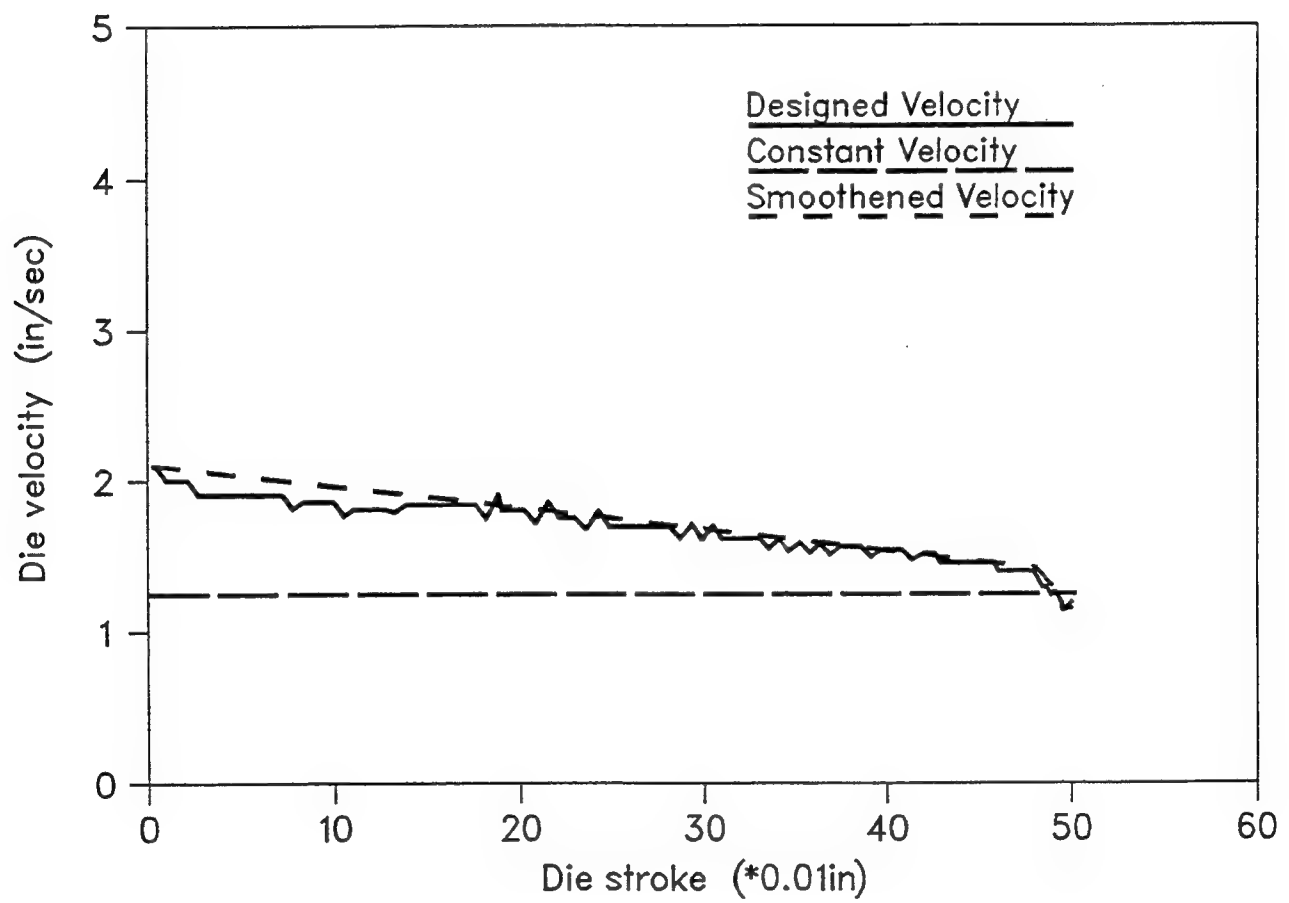


Figure 43: Engine disk forging - Velocity profiles

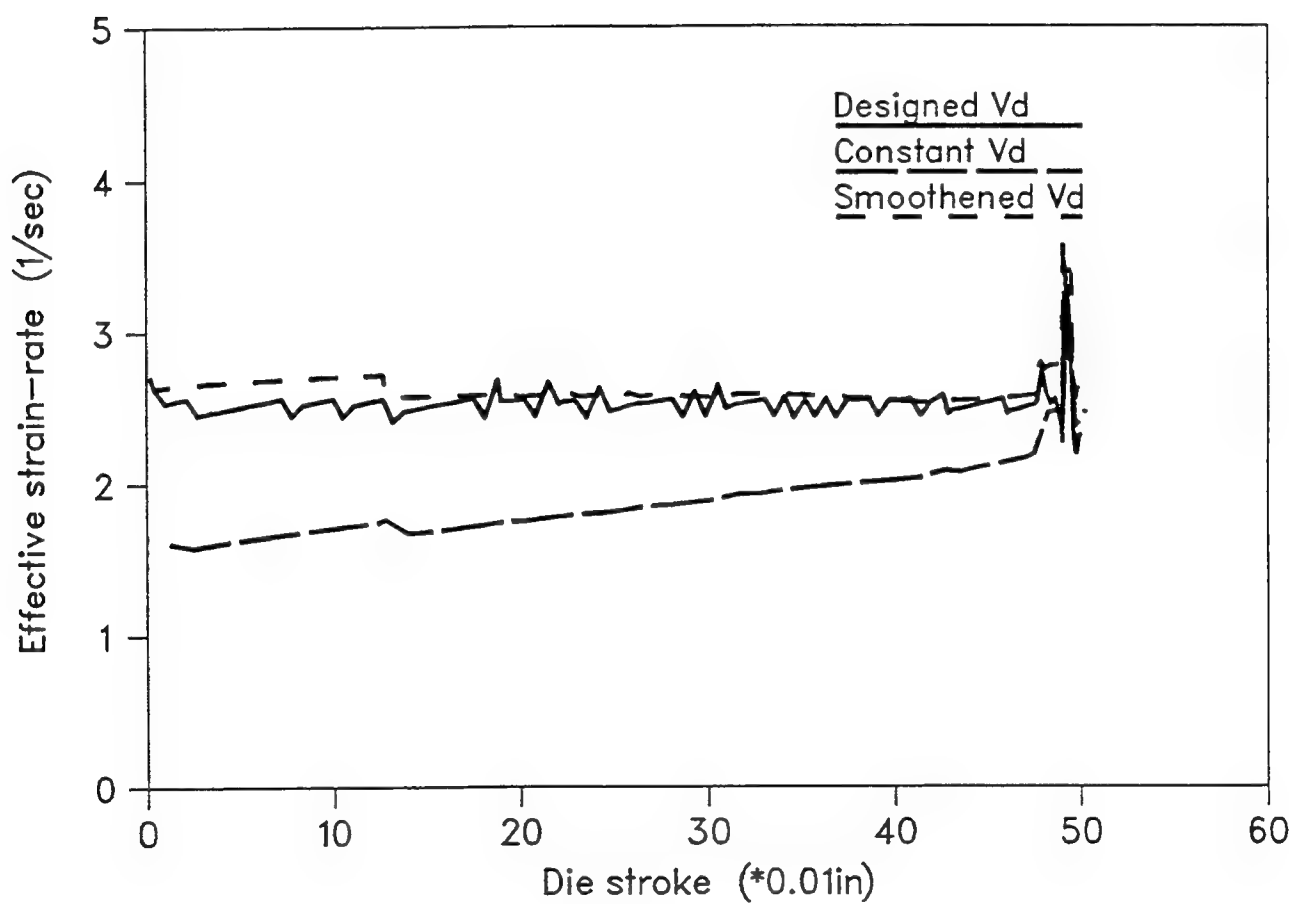


Figure 44: Engine disk forging - Strain rate profiles

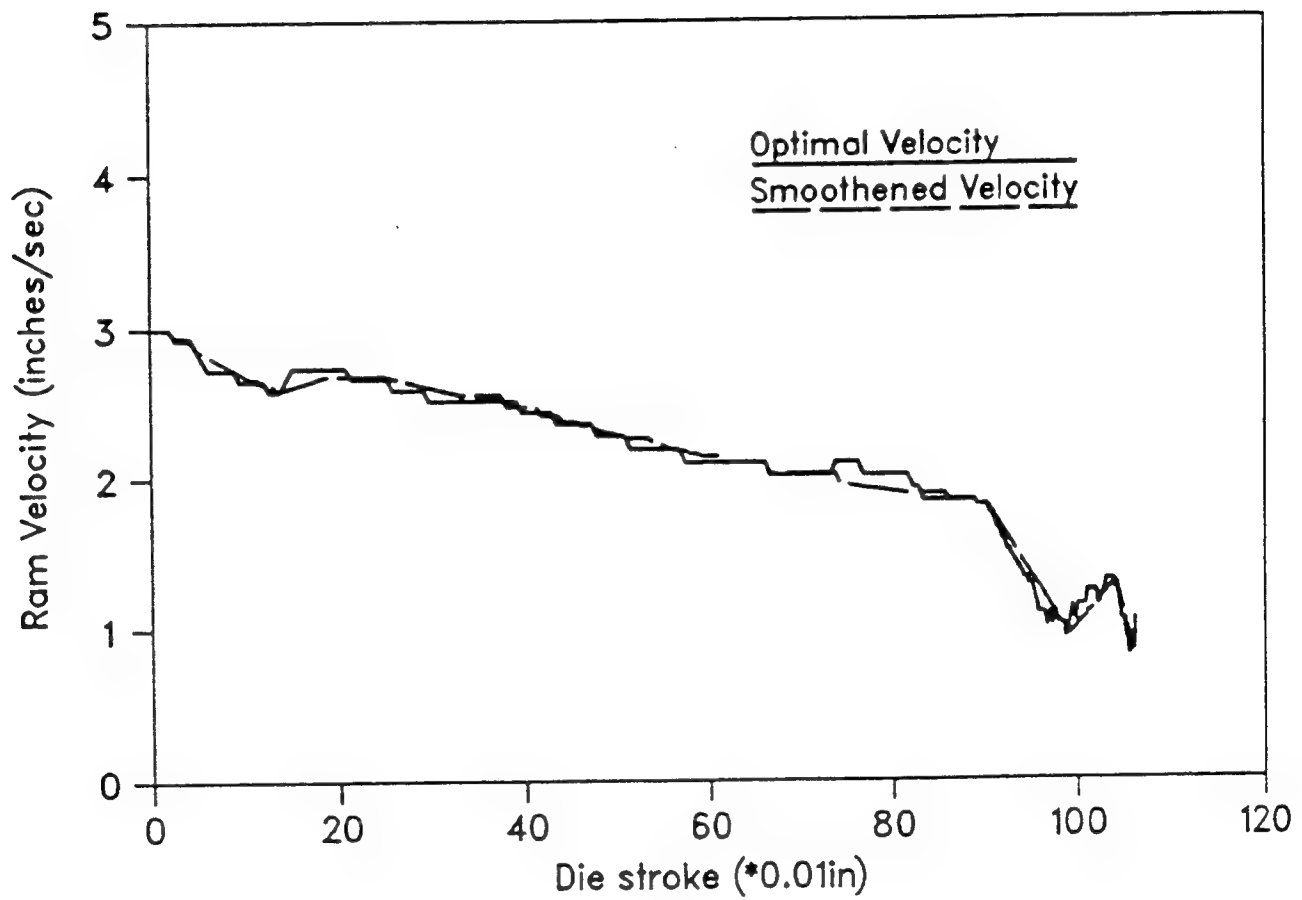


Figure 45: Channel section forging - Velocity profiles

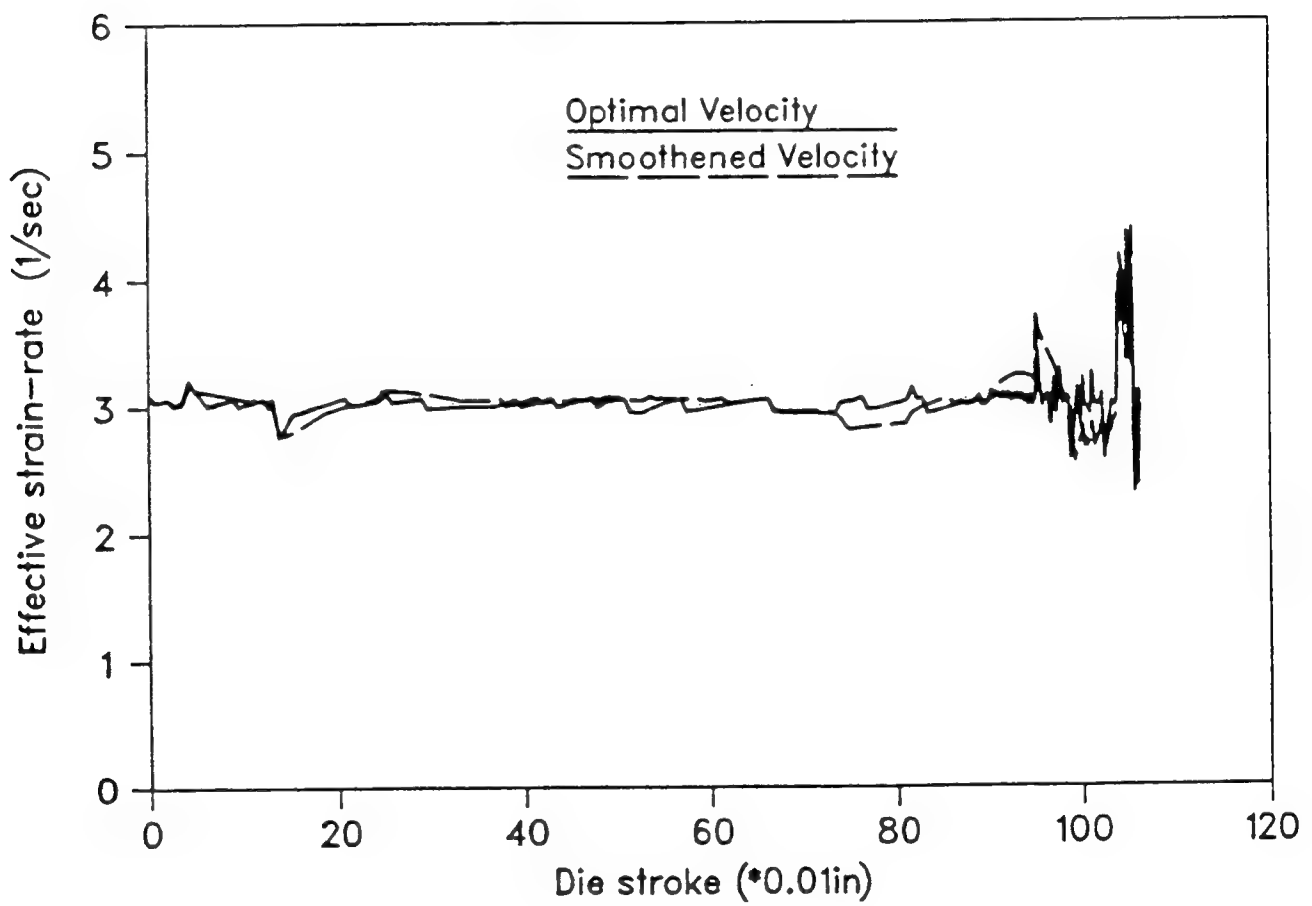


Figure 46: Channel section forging - Strain rate profiles

and time significantly. An axisymmetric engine disk forging was considered as the test case, and the design of velocities was carried out for the following three situations:

1. State space model built at every time step.
2. State space model built only once at the beginning of the simulation.
3. State space model built whenever boundary condition changes.

In Case 3, the boundary condition changed 12 times during the entire simulation, which lasted about 130 time steps. As a result, the state space model had to be built 12 times during the design process. On an average, each state space model was valid for about 10 simulation time steps for this example. Case 3 is also more accurate than Case 2 because it accounts for the change in the size of the system matrices as deformation progresses. In other words, in case 3, the system matrices are built and used (for designing the die velocity) whenever nodes attach/detach from the die surface. Figures 47 and 48 show the die velocity and strain rate profiles obtained for the above three cases. It may be observed from Fig. 47 that the die velocities designed for the above three cases match closely. Fig. 48 shows that the strain rate requirement is met effectively for all the three cases. Since the results from case 2 match so closely with that of the other two cases, it may be concluded that for this case the one state space model built at the beginning of the simulation was valid for the entire duration of the simulation. In addition, use of approximate system matrices for the entire simulation has a smoothening effect on the designed velocities, thereby reducing the fluctuations in the designed die velocities. This in itself is a big advantage, as explained in the previous section. It may thus be concluded that for simple forging problems, approximate system matrices may be used to design die velocities without radically altering the performance of the system. In addition, by

intelligently selecting points along the simulation path where the system matrices are to be built, a large amount of computational time may be saved without sacrificing the accuracy of the system.

The above argument may be extended and applied to the design of weighting matrices also. In the original design scheme, the weighting matrices for control are determined at every time step of the simulation. For systems behaving in a fairly linear and predictable manner, constant weighting matrices may be used for the entire simulation without affecting the results significantly. Figs. 49 and 50 show the velocities and (corresponding) strain rates obtained using constant and varying weighting matrices for an engine disk forging. In both cases, the conformance with the original results is very good. Therefore, it may be concluded that the use of constant weighting matrices in the control scheme is again an acceptable approximation.

All the above mentioned approximations made in the formulation and implementation procedures result in a large savings in computational time and effort during the simulation, while still realizing effective control and design. However, it must be noted that these practical aspects are related to the simulation and are not directly applicable to the actual forging process itself.

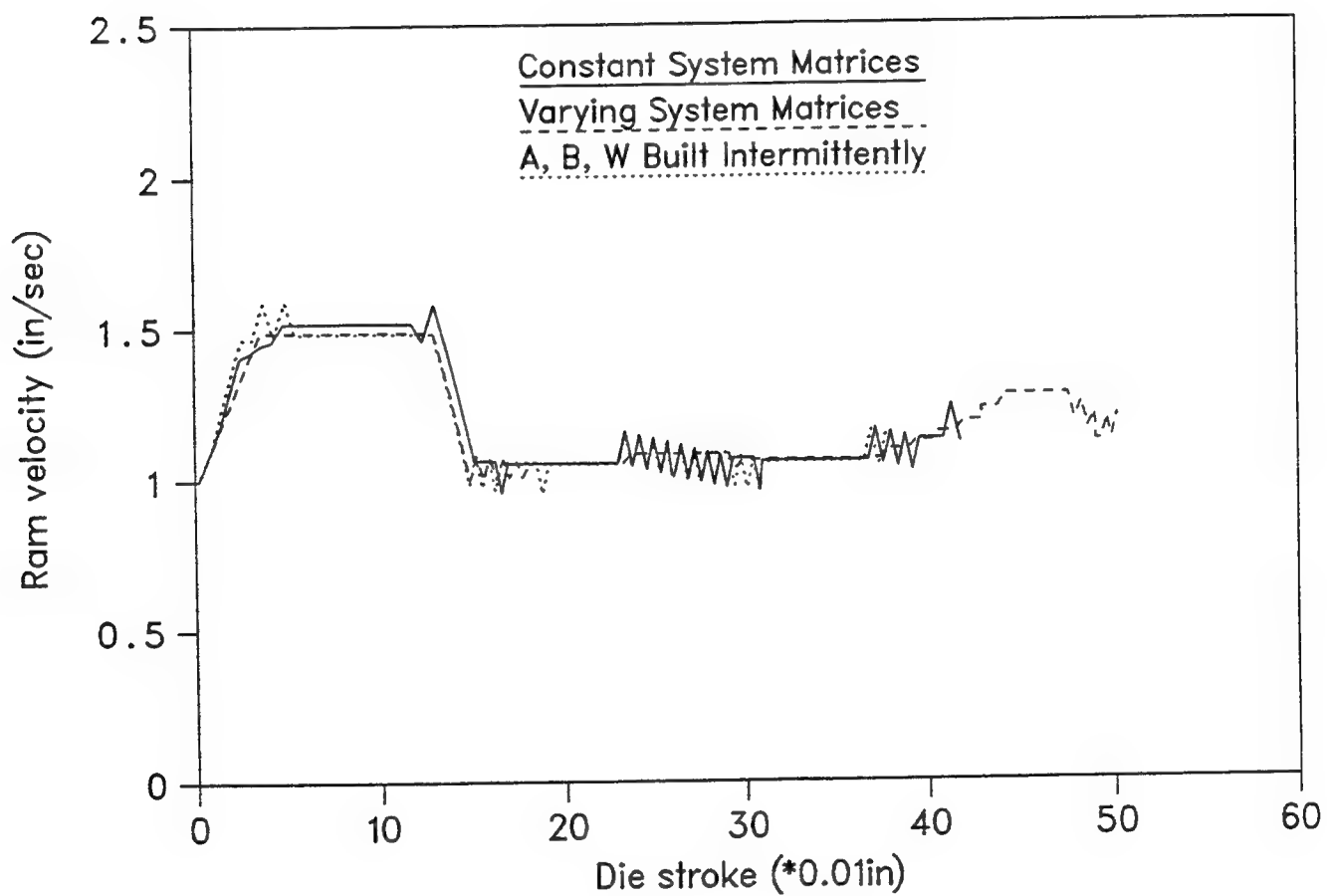


Figure 47: Die velocities using constant and varying system matrices

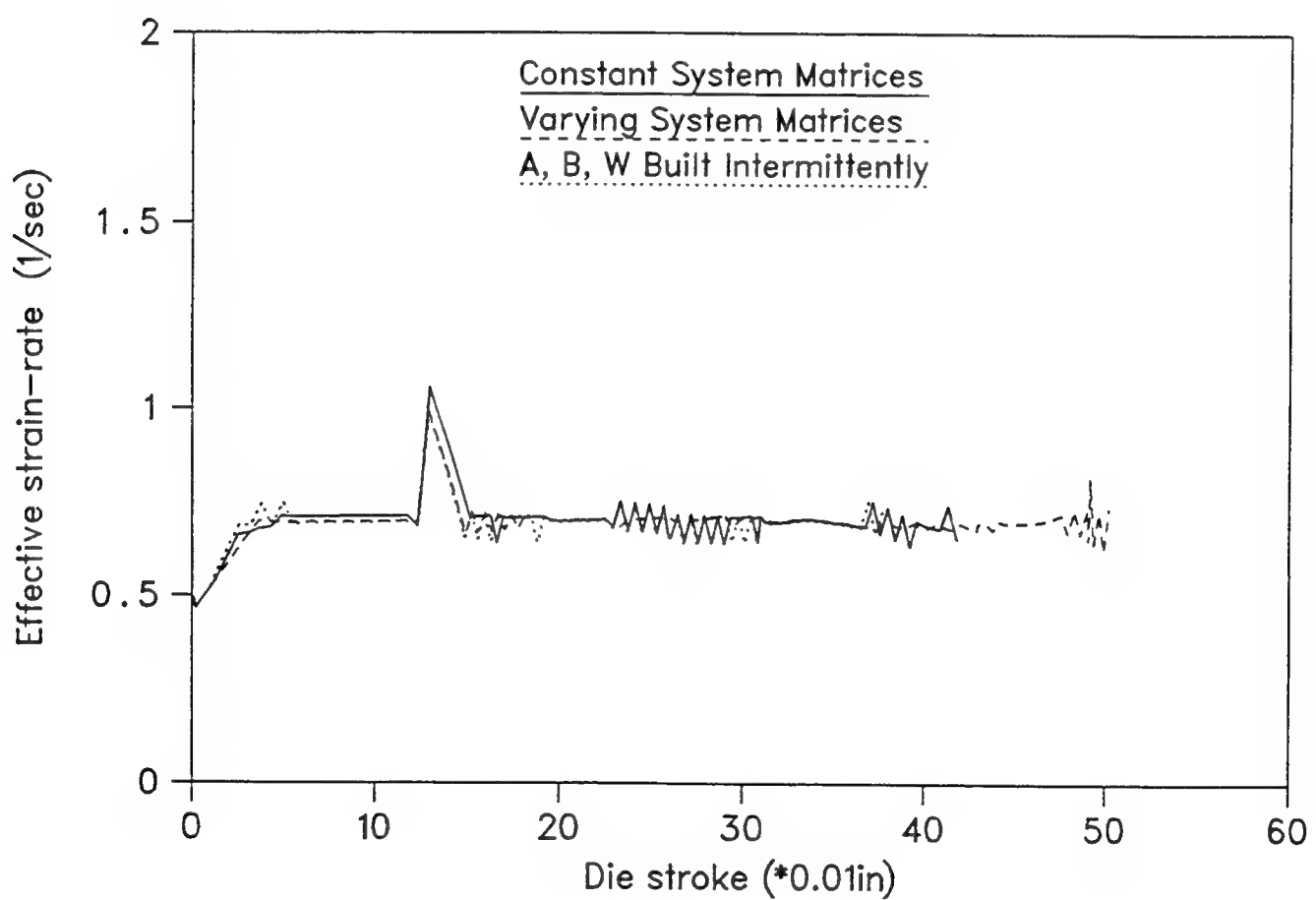


Figure 48: Strain rates using constant and varying system matrices

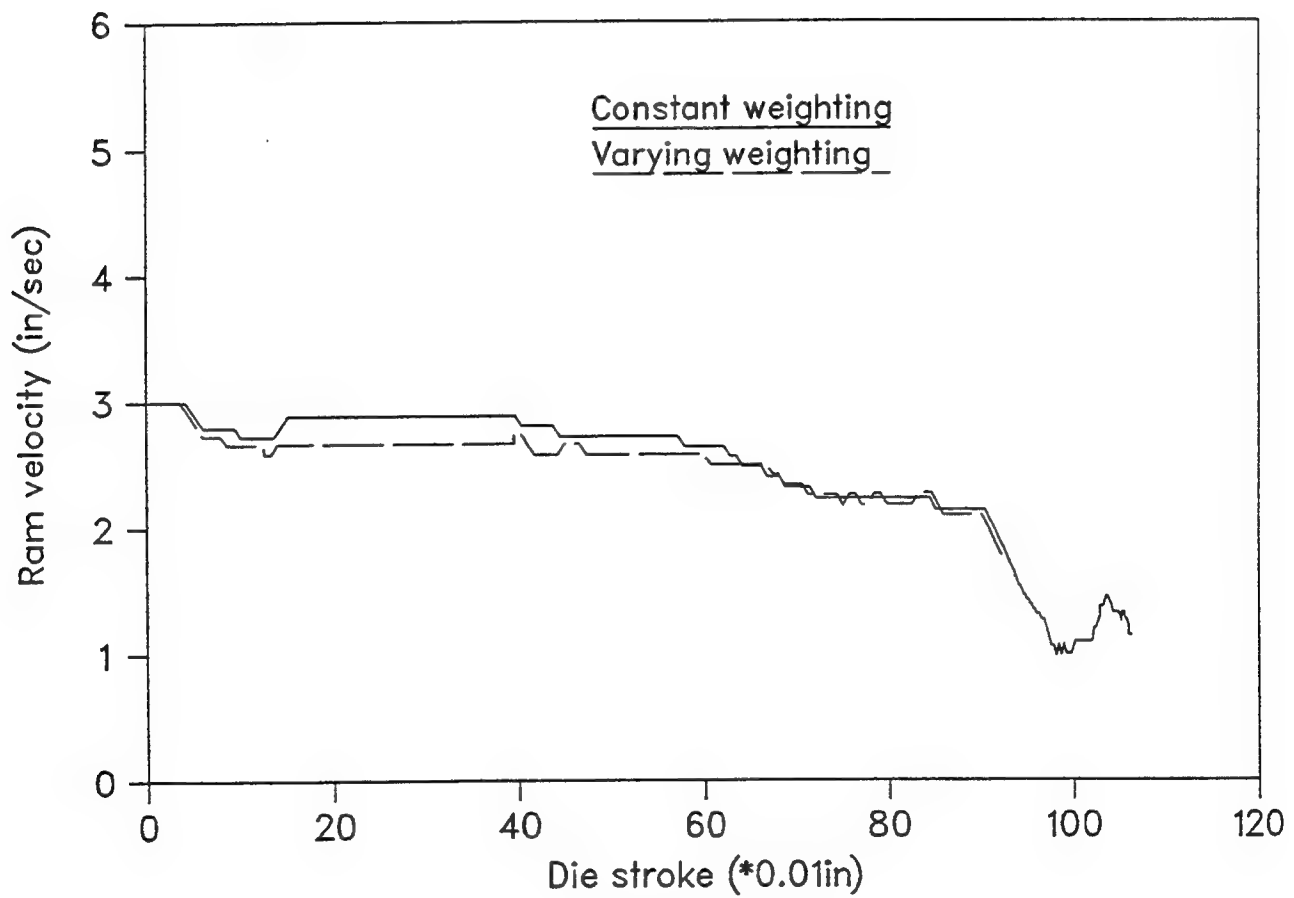


Figure 49: Die velocities using constant and varying weighting matrices

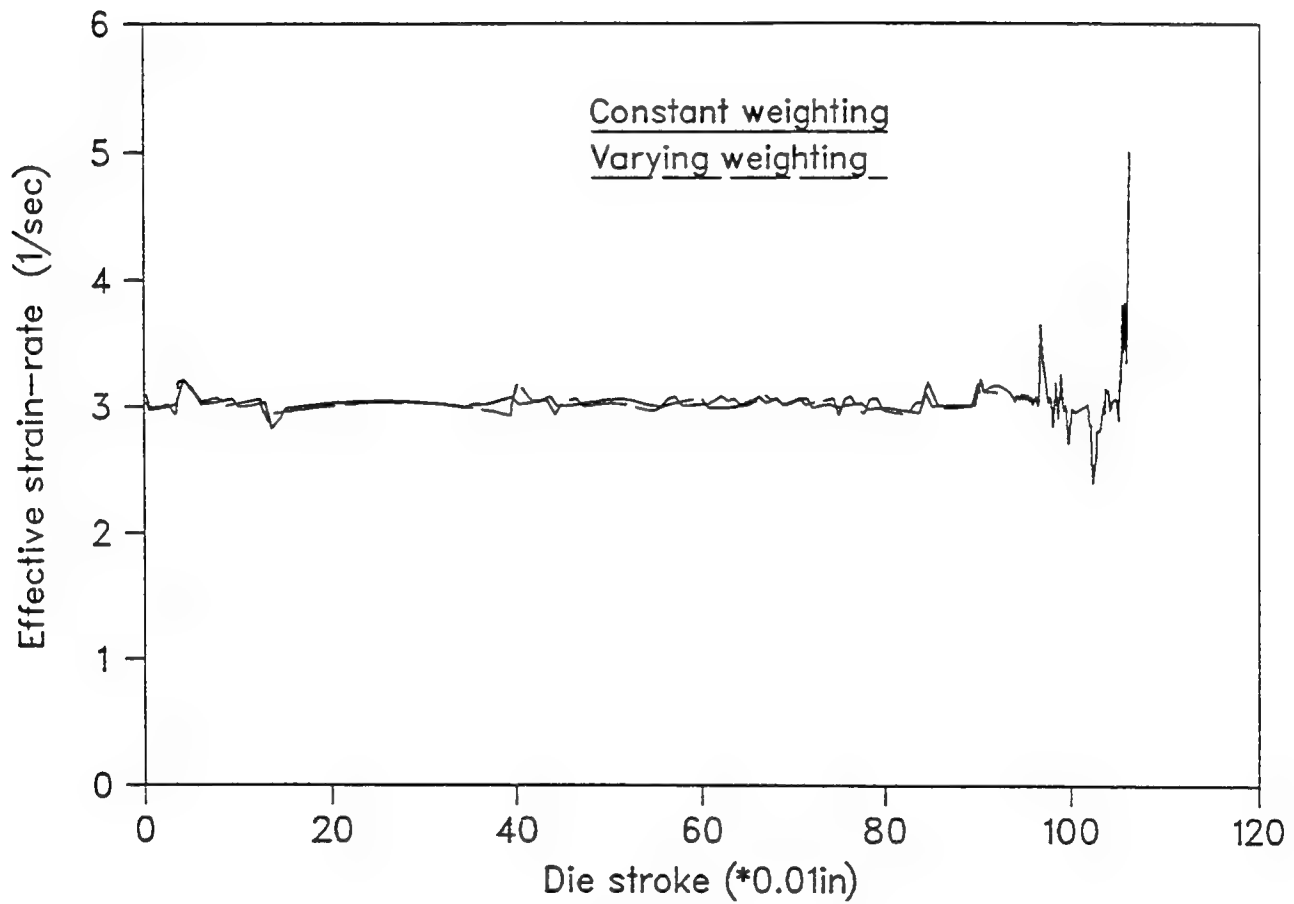


Figure 50: Strain rates using constant and varying weighting matrices

9.3 Eigen mode analysis for process characterization

This section presents a methodology for identifying the tension and compression zones in the workpiece material, based on the study of eigenmodes of the deforming system. The process of identification of the tension and compression zones is then related to the selection of favorable operating zones/conditions for the process, and for predicting the stability of the deforming material.

Elemental level eigenmode analysis

The derivation of the finite element governing equations for metal forming analysis have been described earlier in chapter 2 of this report. In the finite element formulation, the objective is to design admissible velocity fields by minimizing the potential energy of the system (Eq. (2.8)) while also maintaining the incompressibility condition on the velocity field. This is done by introducing a penalty constant for the volumetric component and converting the variational problem into a stationary value problem, whose first order variation (Eq. (2.10)) is stated as,

$$\delta\pi = \int_V \bar{\sigma} \delta \bar{\varepsilon} dV + K \int_V \varepsilon_V \delta \varepsilon \dot{V} dV - \int_{S_F} F_i \delta u_i dS = 0 \quad (9.1)$$

where K is the penalty parameter, and is generally a large positive quantity.

On the right hand side of Eq. (9.1), the first, second, and third terms represent the shear component, the volumetric component, and the work done by

external tractional forces, respectively. Because of the penalty parameter, the volumetric deformation component is easily separable from the shear deformation component. In a similar manner the stiffness matrix of the element can also be separated into the deformation part and volumetric part. The stiffness equations in metal forming analysis are nonlinear in nature, and the velocity field solution is generally obtained in an iterative manner. At the converged solution point, the stiffness matrix of any element may be represented as,

$$\mathbf{K}_C = \mathbf{K}_D + \mathbf{K}_{vo} \quad (9.2)$$

where \mathbf{K}_D is the deformation part of stiffness, \mathbf{K}_{vo} is the volumetric part of stiffness, and \mathbf{K}_C is the total elemental stiffness (volumetric and deformation parts combined). For a four-noded quadrilateral element, the volumetric strain is linearly distributed within the element. The penalty function constraint, $\int_V \dot{\epsilon}_V^2 dV$, requires the value of $\dot{\epsilon}_V$ to be zero at every point of the element because of the 'squared' term. This over-constraint condition is relaxed by using the one point numerical integration scheme, which is applied at the centroid of the element.

For identifying the tension and compression zones, the analysis is based on the volumetric component of the stiffness matrix. It has been observed that a distinct separation exists between the eigenvalues of the shear deformation part and the volumetric deformation part in the elemental level eigenvalue representation, as shown in Fig. 51. This figure shows the real eigenvalue spectrum of an element during the axisymmetric compression of a disk. In general, the deformation of the material can be characterized by three modes: the rigid body mode, the shear mode, and the volumetric mode. The rigid body mode is due to

1	- 4.48E-15	5	1.93E+00
2	1.32E-01	6	3.71E+00
3	2.32E-01	7	6.53E+00
4	8.93E-01	8	1.30E+03

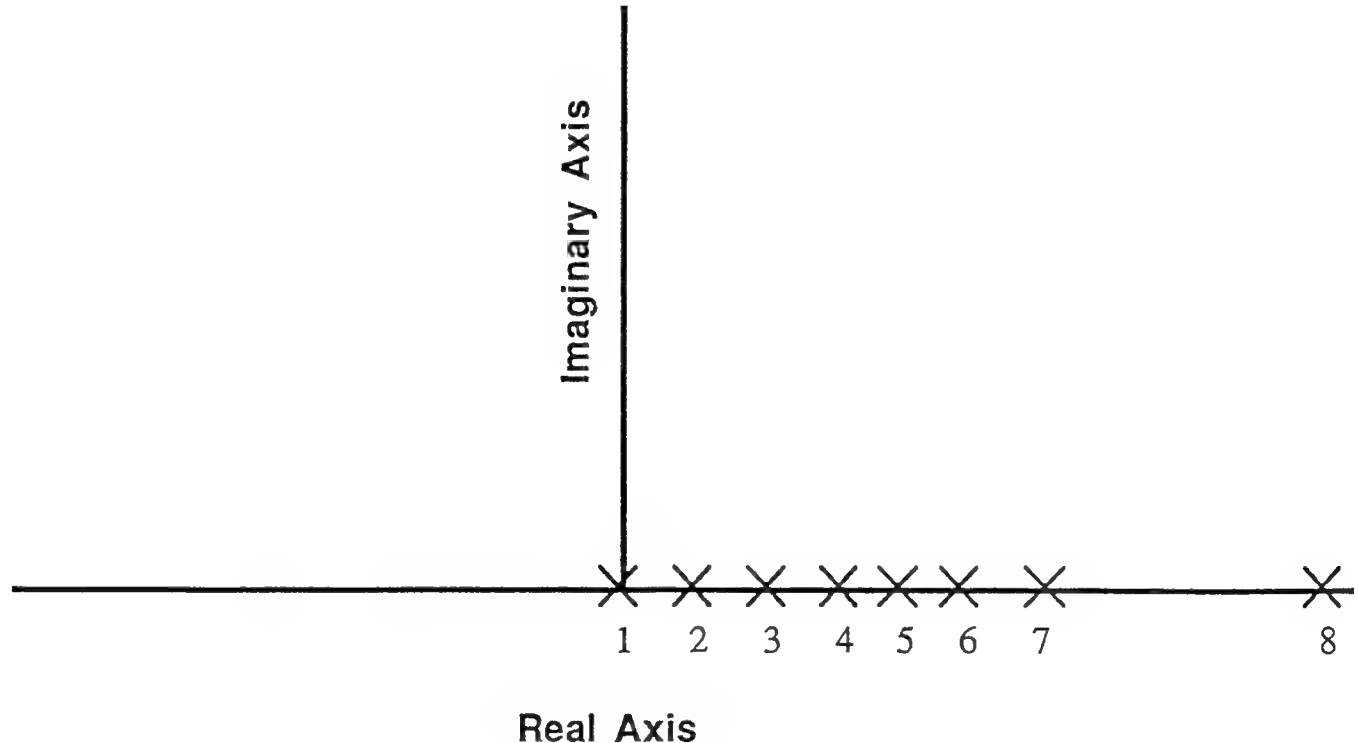


Fig 51. Eigenvalue spectrum of a generic elemental stiffness stiffness matrix

the rigid movement caused by adjacent elements. The shear mode is due to pure deformation of the material. The volumetric mode is a result of bulk deformation, which is not practical to have in any metal forming process. Therefore, in closed die forging the volume is maintained constant during deformation. This is achieved by using a large penalty constant as explained earlier. In the elemental level eigenvalue distribution, at least one eigenvalue and its corresponding eigenmode is due to the volumetric component of stiffness. Because the penalty constant is very large and applied to the volumetric deformation component, the corresponding eigenvalue will be the largest in the real eigenvalue spectrum. The eigenvalues are calculated by first computing the stiffness matrix \mathbf{K}_{vo} (Eq. (9.2)) and using an IMSL subroutine DEVCSF to extract these values from this matrix.

Once the eigenvalue representing the volumetric deformation component is identified, the corresponding eigenvector can easily be calculated. The elemental level representation of the eigenvalue problem is:

$$\mathbf{K}_{vo}\phi = \left[\int_A (K\mathbf{C}) dA \right] \phi \quad (9.3)$$

where K is the penalty constant, ϕ is the modal matrix having dimensions corresponding to the number of degrees of freedom (8 X 8) of each element, and \mathbf{C} is the volumetric gradient vector of size 1 X 8. Eq. (9.3) is of the form $\mathbf{Ax} = \Lambda x$, which is the general form of a standard eigenvalue problem where, Λ is the eigenvalue matrix, and \mathbf{x} is the modal matrix. Further, \mathbf{C} can be determined from the expression for the volumetric strain rate $\dot{\epsilon}_V$, as described below [27]:

$$\dot{\epsilon}_V = \dot{\epsilon}_x + \dot{\epsilon}_y + \dot{\epsilon}_z \quad (9.4)$$

In terms of nodal velocities, the volumetric strain rate is expressed as,

$$\dot{\epsilon}_V = \mathbf{C}^T \mathbf{V} = C_i v_i \quad i = 1, 2, 3 \quad (9.5)$$

where $C_i = B_{1i} + B_{2i} + B_{3i}$ and 'B' refers to the elements of the strain rate gradient matrix corresponding to the x, y and z coordinates. Now, the eigenmode problem may be formulated as,

$$S_e = \mathbf{C} \phi_V \alpha \quad (9.6)$$

where S_e is a scalar used for identifying the tension and compression zones, and ϕ_V is the volumetric deformation mode of the elemental stiffness. α , the scalar term, is calculated from the volumetric eigenmodes as,

$$\alpha = \phi_V^T \mathbf{V} \quad (9.7)$$

where \mathbf{V} is the elemental nodal velocity vector. The value of S_e determines whether the element is in tension or compression. The general rule is,

$$If \quad \mathbf{C} \phi_V \phi_V^T \mathbf{V} > 0 \quad \text{the element is in tension}$$

$$If \quad \mathbf{C} \phi_V \phi_V^T \mathbf{V} < 0 \quad \text{the element is in compression}$$

The product of \mathbf{C} and \mathbf{V} gives the volumetric strain rate of the element which is a scalar, and the product of the eigenvectors (ϕ_V) is another positive scalar, representing the extent of the deformation. Because the product of these two scalar quantities gives the volumetric strain of the element, S_e can indicate whether the element is in tension or compression.

Global level eigenmode analysis

As explained in chapter 2, the equilibrium equations dealt with in metal forming processes are nonlinear, and the solution to these equations is obtained in an iterative manner. The velocity solution is actually obtained by linearizing the equilibrium equations and applying suitable convergence criteria. The linearization is achieved by a Taylor series expansion (Eq. (2.14)) about the assumed velocity solution as shown below:

$$\left[\frac{\partial \pi}{\partial v_I} \right]_{v=v_0} + \left[\frac{\partial^2 \pi}{\partial v_I \partial v_J} \right]_{v=v_0} \Delta v_J = 0 \quad (9.8)$$

where v_0 is the converged solution point, and Δv_J is the first order correction of the velocity v . Eq. (9.8) can be rewritten by taking the first derivative term to the right hand side as,

$$\mathbf{K} \Delta \mathbf{v} = \mathbf{f} \quad (9.9)$$

The linearized form of the system of equations is given as,

$$\mathbf{K}_S \mathbf{v} + \mathbf{K}_T \Delta \mathbf{v} = \mathbf{F} + \mathbf{f} \quad (9.10)$$

where \mathbf{K}_S is the secant stiffness matrix at the converged solution point of the previous iteration, \mathbf{K}_T is the gradient stiffness matrix at the current iterative step, \mathbf{F} is the force vector, and \mathbf{f} is the change in force due to a change in the nodal velocity.

Using the discrete representation of the quantities involved in the stiffness equation developed in chapter 2 (Eq. (2.12)), we have [27],

$$\frac{\partial \pi}{\partial v_I} = \frac{\partial \pi_D}{\partial v_I} + \frac{\partial \pi_P}{\partial v_I} + \frac{\partial \pi_{S_F}}{\partial v_I} \quad (9.11)$$

where the first term on the right hand side of the above equation is the load vector due to deviatoric stresses, the second term is the load due to hydrostatic stress, and the third term is the applied nodal point force. These three terms are added up to give the additional force term \mathbf{f} . The second derivative terms of π are expressed as (Eq. 2.21),

$$\frac{\partial^2 \pi}{\partial v_I v_J} = \int_V \frac{\bar{\sigma}}{\bar{\epsilon}} P_{IJ} dV + \int_V \left(\frac{1}{\bar{\epsilon}} \frac{\partial \bar{\sigma}}{\partial \bar{\epsilon}} - \frac{\bar{\sigma}}{\bar{\epsilon}^2} \right) \frac{1}{\bar{\epsilon}} P_{IK} v_K v_M P_{MJ} dV + \int_V K \mathbf{C}_J \mathbf{C}_I dV \quad (9.12)$$

The third term in the above equation is the gradient matrix due to volumetric deformation. This part of the gradient stiffness is easily separable from the other parts due to its association with the penalty parameter, and is used for global level eigenvalue analysis. The stiffness terms are first computed at the elemental level and then assembled into the global stiffness matrix (Eq. 2.13). This assembled stiffness matrix has both the shear and volumetric components together. Consequently, the real eigenvalue spectrum of the stiffness has two parts. These parts again are distinct and can be easily identified and separated because of the penalty parameter associated with the volumetric part.

In the global level eigenvalue analysis, the first step is to identify the eigenvalues related to $\mathbf{K}_{\mathbf{V}\mathbf{O}}$ and calculate the corresponding eigenvectors matrix $\Phi_{\mathbf{V}}$. The next step in this procedure is to compute α for each volumetric deformation mode, by taking the product of the eigenvector and the nodal velocities as explained in the previous section. This computation results in a vector given by,

$$\alpha = \Phi_{\mathbf{V}}^T \mathbf{V} \quad (9.13)$$

The volumetric gradient matrix, C , for each element is assembled as a global matrix \mathbf{C}_G of dimension equal to total number of degrees of freedom of the system. This matrix is sparsely populated and has values only at eight places, the rest of the terms in a given row being zeros. These eight values correspond to the degrees of freedom of the element under consideration. Now, the scalar S is calculated for each element as,

$$S = \mathbf{C}_G \Phi \mathbf{v} \alpha \quad (9.14)$$

Because \mathbf{C}_G is assembled row wise, only the degrees of freedom corresponding to the element under consideration are made active. Eq. (9.14) actually gives the element volumetric strain. Therefore, the sign of the scalar, S , provides information whether the element is in tension or compression.

Numerical examples

The methodology developed is demonstrated using two numerical examples presented in this section. The results are validated by two methods: The actual computation of the volumetric strain and the g ratio method presented by Chen et. al. [83]. The first method is simple and easy to implement because the volumetric strain rate can directly be calculated using Eq. (9.5). To obtain the volumetric strain, the calculated volumetric strain rate is multiplied by the simulation time step (size) which is a positive quantity. In general, the volumetric strain determines whether volume is gained or lost, and this in turn can help predict whether the element is in tension or compression. If the calculated value

(of volumetric strain) is greater than zero, the element is in tension. Otherwise, the concerned element is in compression.

The other validation method used in this work is the *g* ratio method which is briefly explained in this section. The *g* ratio is defined as [83],

$$g = \frac{\sigma_m}{\bar{\sigma}} \quad (9.15)$$

where σ_m is the mean or hydrostatic stress, and $\bar{\sigma}$ is the effective stress. The hydrostatic stress in turn is calculated as,

$$\sigma_m = \frac{1}{3} (\sigma_1 + \sigma_2 + \sigma_3) \quad (9.16)$$

where σ_1, σ_2 and σ_3 are the principle stresses.

The Dynamic Material Model (DMM) developed by Prasad et. al. [84], and Gegel [85] provides useful macroscopic information for identifying favorable processing zones in the workpiece material during deformation. This procedure models the relationship between the constitutive behavior, hot workability, and microstructure development. The modeling is based on four criteria: range of strain rate sensitivity, stability criteria relating the variations of strain rate sensitivity with $\log \dot{\epsilon}$, the lower limit on the temperature sensitivity on flow stress, and the stability criteria relating the variations of the entropy with $\log \dot{\epsilon}$. According to the authors, the rate sensitivity should lie between 0 and 1, and the lower limit on entropy should be 1, for stable deforming operations. Further, for stable processing conditions, the following relations should hold good:

$$\frac{\partial m}{\partial \log \dot{\epsilon}} < 0 \quad \text{and} \quad \frac{\partial s}{\partial \log \dot{\epsilon}} < 0 \quad (9.17)$$

where s is the entropy of the system and m is the strain rate sensitivity index. By analogy, Chen et. al. [83], considered the stress ratio parameter (g) as a measure of stability, and concluded that,

$$\text{If } g < 0, \quad \frac{\partial s}{\partial \log \dot{\epsilon}} < 0 \quad \text{the element is stable} \quad (9.18)$$

and

$$\text{If } g > 0, \quad \frac{\partial s}{\partial \log \dot{\epsilon}} > 0 \quad \text{the element is not stable.} \quad (9.19)$$

Hence, the g ratio can be used as a reference for dynamically determining favorable processing conditions during deformation. If the g ratio value is less than $\frac{1}{3}$, the state of stress is considered compressive, otherwise, the state of the stress is considered tensile.

Example 1: H-block compression

In this example, the closed die forging of a H-block is simulated using the nonlinear finite element code ALPID (Fig. 52). Isothermal simulation conditions were assumed, with a initial billet temperature of 1700°F . A constant shear friction factor ($m=0.3$) was assumed at the die/billet interface. A Titanium alloy was used as the workpiece material. A ram velocity of 0.12 mm/sec was used at the start of the simulation. Because of the symmetry of deformation, only a quarter section of the workpiece is modeled and analyzed, while maintaining symmetric boundary conditions along the X and Y axes. The simulation is carried out for 15 steps, and the billet deformation is predicted. The results of the elemental and global level analyses are compared with the stress ratio method, and presented

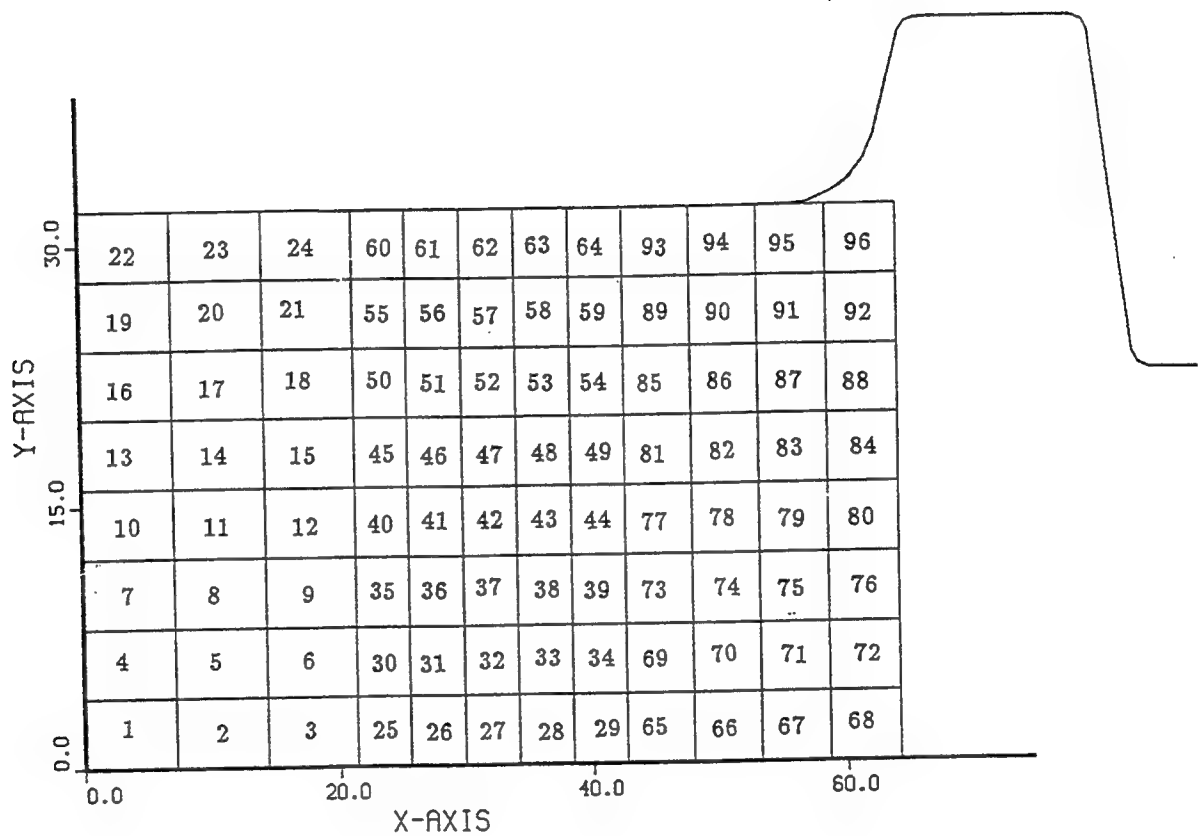
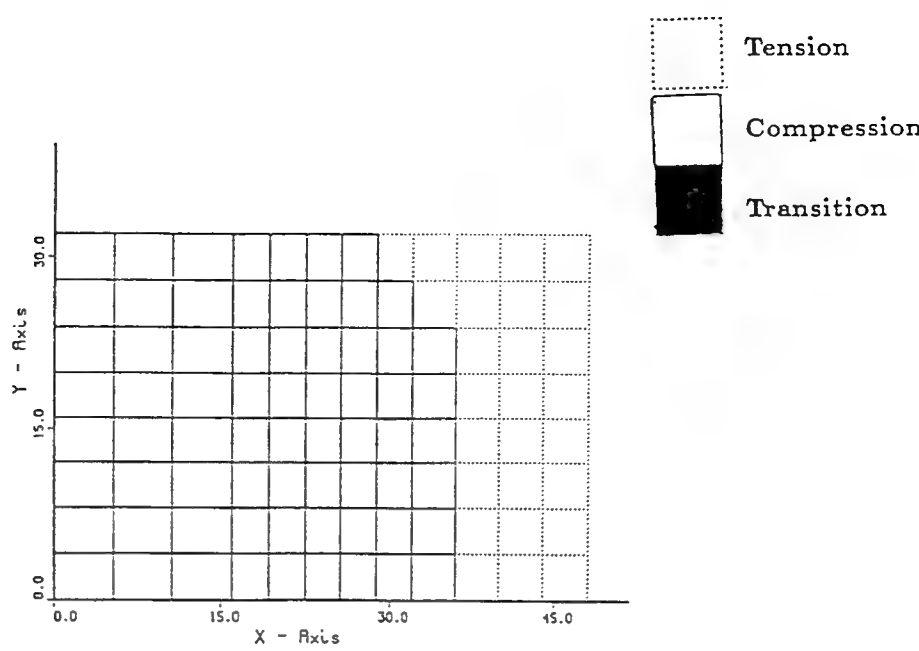
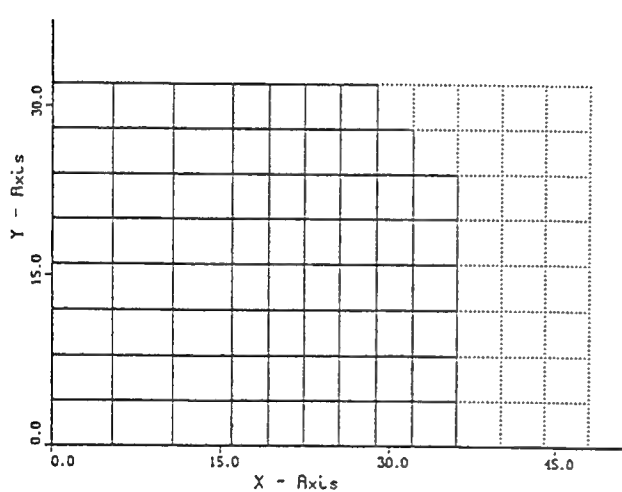


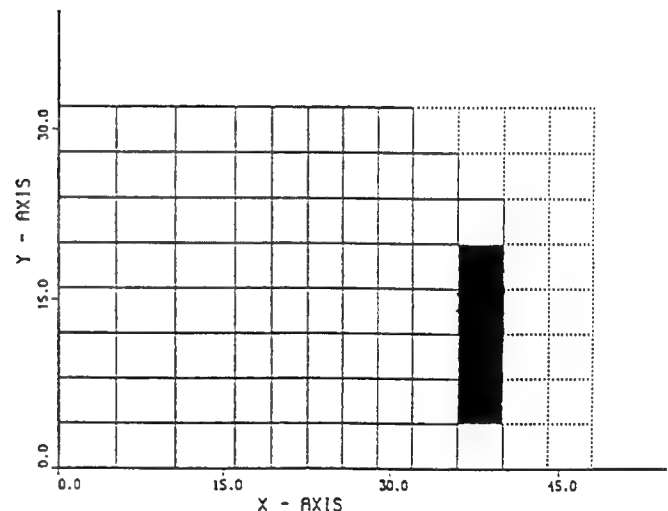
Fig 52. H-Block compression: Finite element model



(a).



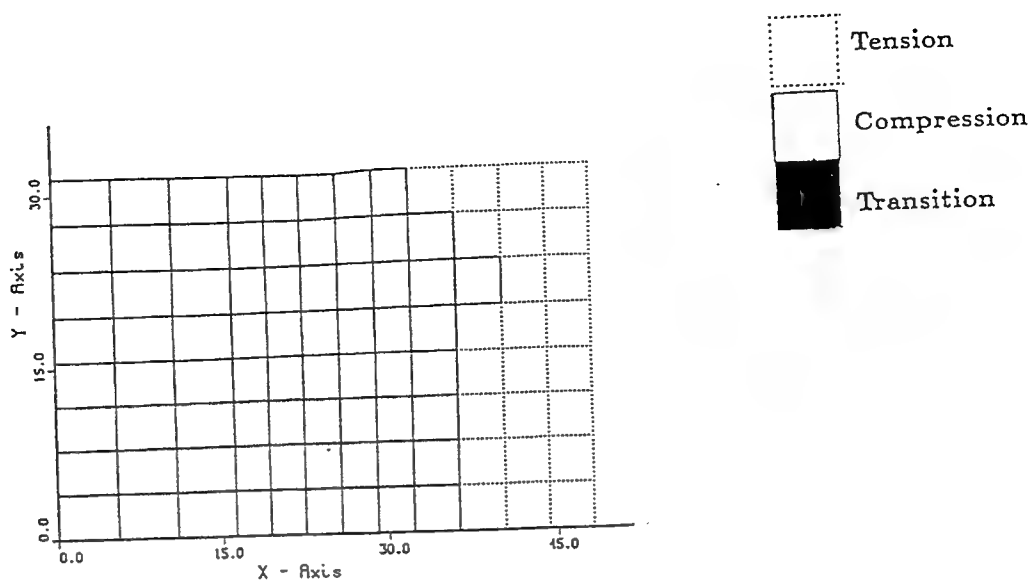
(b).



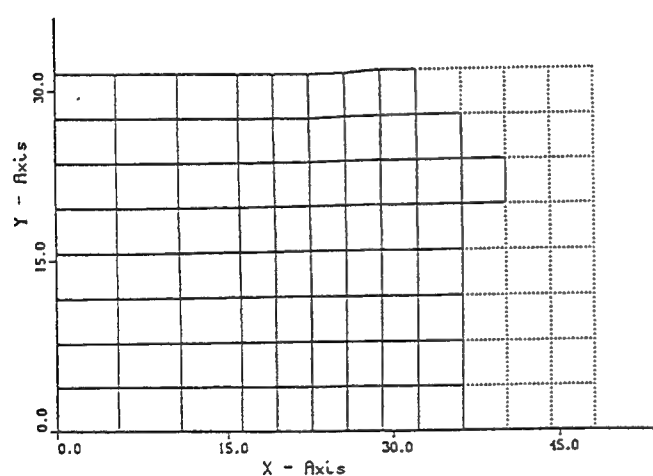
(c).

Fig 53. Stability predictions for H-Block compression (Step 1)

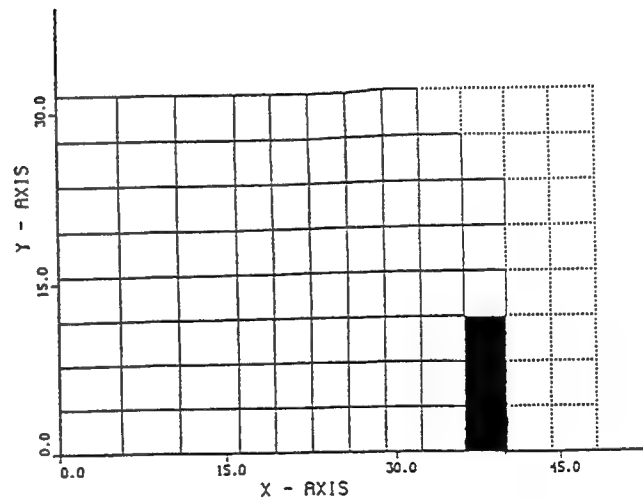
(a) Stress ratio method (b) Elemental analysis (c) Global analysis



(a).



(b).



(c).

Fig 54. Stability predictions for H-Block compression (Step 15)
 (a) Stress ratio method (b) Elemental analysis (c) Global analysis

in Figs. 53 and 54. Figs. 53a and 54a show the predictions of the stress ratio method. Figs. 53b and 54b show the results of elemental level analysis, while Figs. 53c and 54c show the results of global level analysis. The elemental level results exactly match the prediction made by the stress ratio method. In case of the global level analysis, the results match in most of the elements except for three or four elements which are in a state of transition between the compression and tension zones as indicated in Figs. 53c and 54c. This discrepancy could be due to the coupling of modes of deformation in the billet (i.e., coupling of the deformation and shear modes).

Example 2: Disk forging

In this example, the closed die forging of a circular billet of radius 52 mm is simulated under plane strain conditions. Two dies are used in simulating the process. The top die is given an initial velocity of 1.0 mm/sec, while the bottom die is kept stationary. A half-model is used for simulation of the process because of the symmetry in deformation (Fig. 55). Symmetrical boundary conditions are applied for the nodes along the Y-axis. The billet is modeled with 97 elements. A rate sensitive billet material having the following constitutive relationship is used for the simulation:

$$\bar{\sigma} = K \bar{\epsilon}^n \dot{\epsilon}^m + c \quad (9.19)$$

For the current example the constant K is 10.0, the strain rate hardening sensitivity index, m , is 0.1, the strain hardening index, n , is 0 and the constant c is 0. The simulation is carried out under isothermal conditions for 10 steps, each

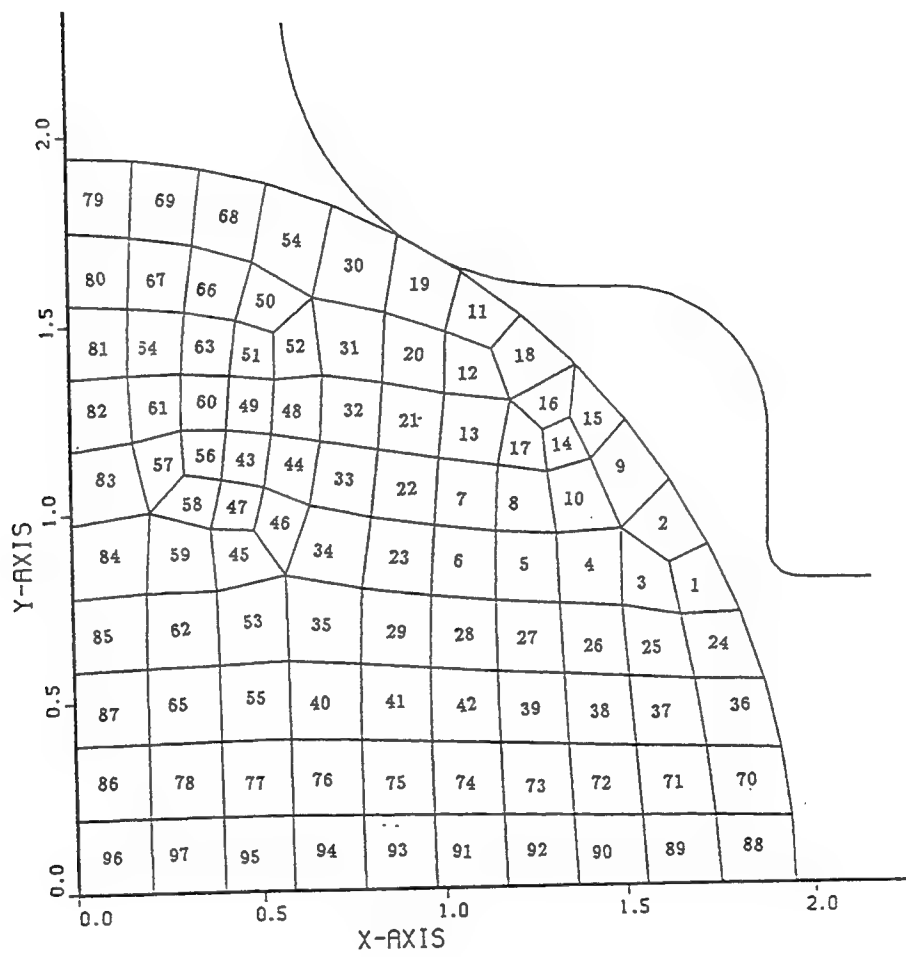
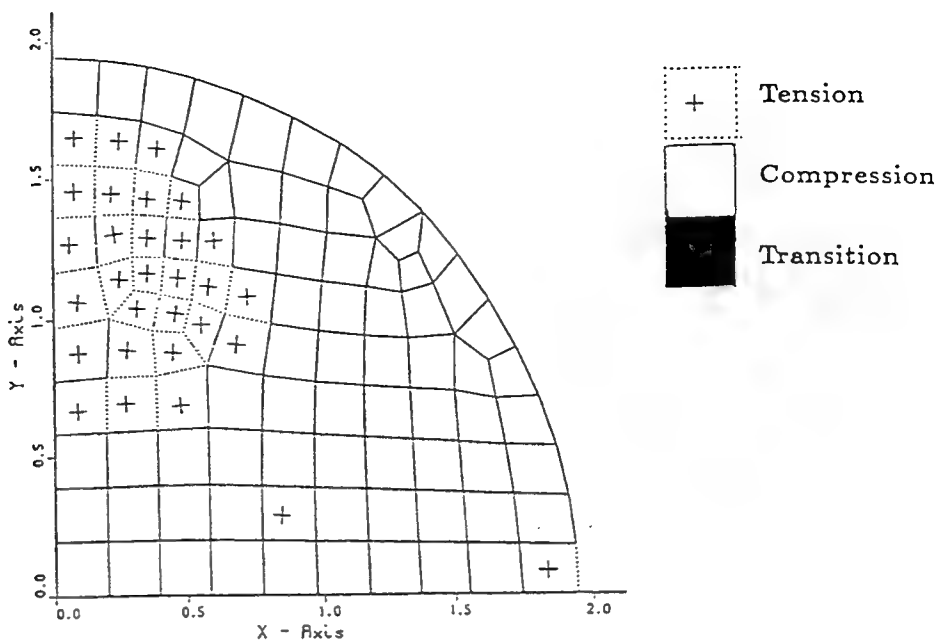
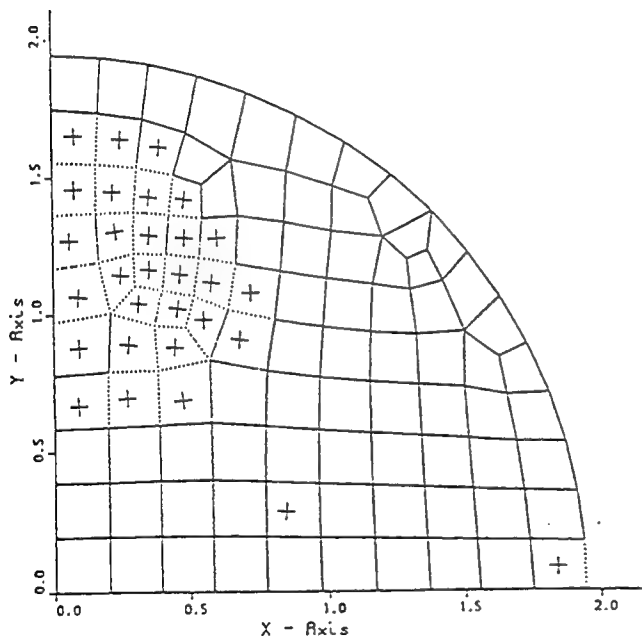


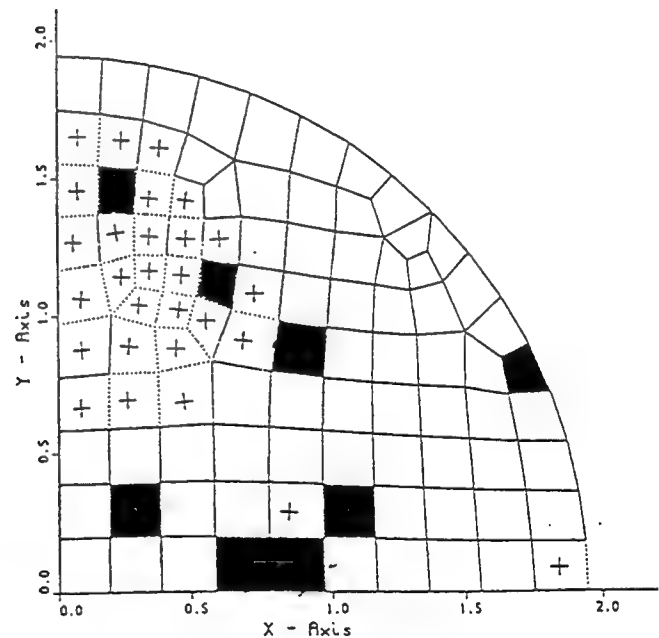
Fig 55. Plane strain compression: Finite element model



(a).

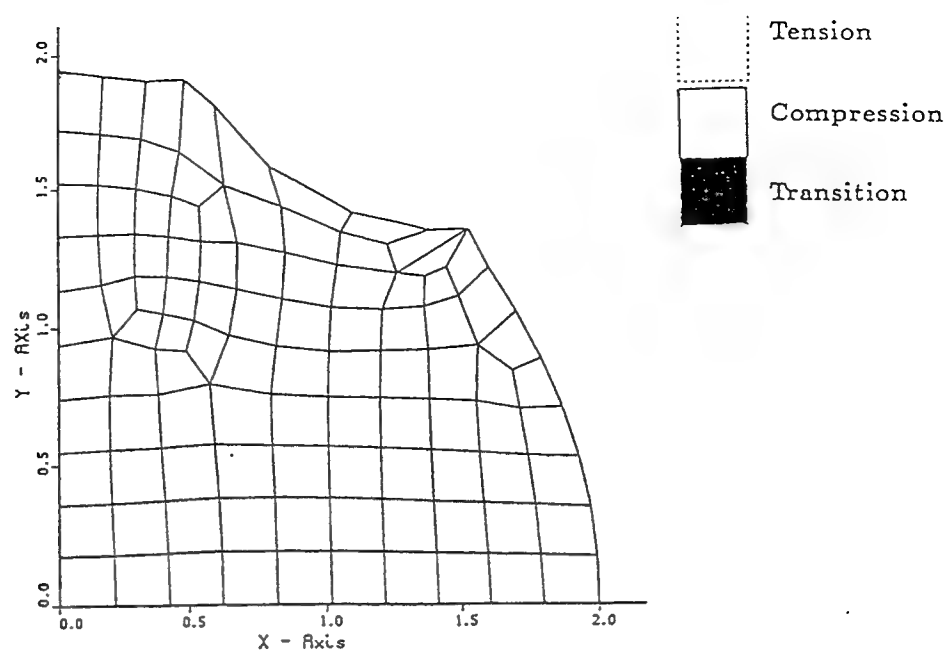


(b).

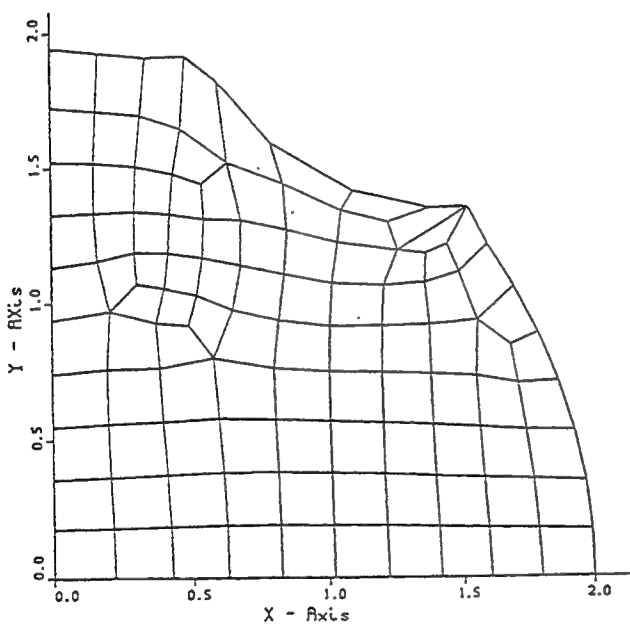


(c).

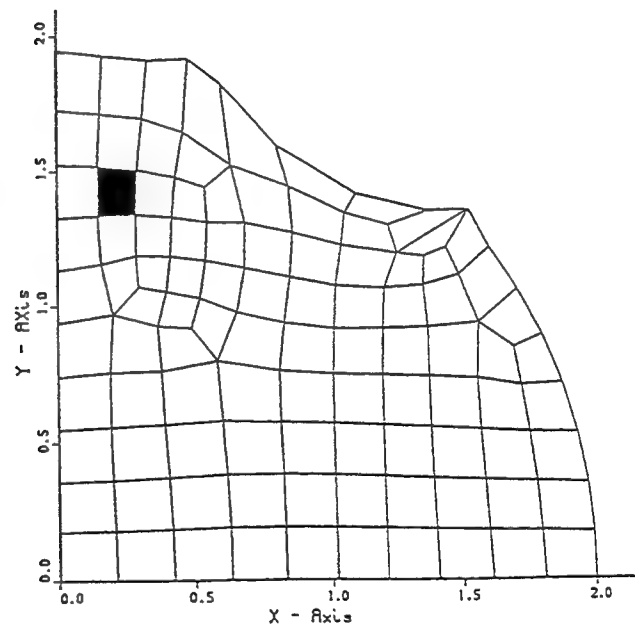
Fig 56. Stability predictions for plane strain compression (Step 1)
 (a) Stress ratio method (b) Elemental analysis (c) Global analysis



(a).



(b).



(c).

Fig 57. Stability predictions for plane strain compression (Step 10)
 (a) Stress ratio method (b) Elemental analysis (c) Global analysis

of step size 0.1 sec. The elemental level analysis results again compared very well with that of the stress ratio method. The global level eigenmode analysis results along with the stress ratio results are presented in Figs. 56 and 57. The results of the global analysis matched that of the stress ratio method for most of the elements except the ones indicated Figs. 56c and 57c. The uncharacteristic behavior of some of these elements is again attributed to the coupling of deformation modes within the workpiece material.

Summary

In this work an attempt was made to relate the deformation modes of the forging system with the tensile and compressive behavior of the material. Identifying the tension and compression zones can be directly related to the stability of the system under deformation. Because identifying the zones is carried out using the stiffness matrices, the predictions depend closely on the stability of the stiffness matrices. Hence, the volumetric modes calculated in a particular step can be used for several steps by calculating the stability margins of the stiffness matrices in that step and by confirming that in the succeeding steps the stiffness matrices do not exceed the stability margins.

The elemental analysis showed a clear separation of modes, namely, the rigid body mode, shear deformation mode and the volumetric deformation mode. Each one is characterized by a different location in the real eigenvalue spectrum. The predictions made using the elemental level analysis matched very well with the

predictions of the stress ratio method and with the volumetric strain calculation. The global level formulation was also tested and compared with the stress ratio method. There was some discrepancy in the predictions of the two methods. These differences may be attributed to the coupling of shear and volumetric deformations.

Out of the three modes of deformation, the rigid body modes clearly separate from the other two modes. Between the shear and volumetric modes, a coupling exists for certain problems whose geometry and processes are complex. From the stiffness calculations, it is clear that the bulk and volumetric strain rates are involved in the deformation process. Both of these are functions of the strain rate components $\dot{\epsilon}_x$, $\dot{\epsilon}_y$, and $\dot{\epsilon}_z$. Due to this nature of the stiffness matrix coupling exists between the shear and the volumetric deformation modes. This coupling is not shown very well in the elemental analysis because each element is treated individually. Because the global analysis is based on the volumetric deformation of the entire billet, the coupling of the modes is more pronounced.

CHAPTER 10

Summary and Conclusions

The forging of complex geometries using expensive alloys under optimum processing conditions is critical to produce defect-free and cost-effective products. This work presents an innovative methodology for process modeling and control using a multidisciplinary approach based on nonlinear finite element methods and optimal control theory. From the finite element governing equations of the metal forming system, a state space model is built. This model only retains the critical states of the system (after condensing out from the system the unwanted and non-critical states), and has lower number of degrees of freedom as compared to the corresponding finite element model. This model is further reduced using sophisticated model reduction methods if required. The state equations are solved using the LQR design scheme to obtain the optimal process parameters (die velocity and initial die temperature).

This methodology has been implemented by means of a computer program, COPP, developed during the course of this work. COPP is built using ALPID subroutines, and can be used with isothermal and nonisothermal forgings to obtain optimal ram velocity schedules and temperature trajectories. Several design problems have been solved to substantiate and validate the methodology developed. Both strain rate and nodal temperature have been effectively controlled to satisfy the design requirements, and the performance of the process has been considerably improved. From this study, the following conclusions can be drawn:

1. The condensed state space model describes the forging process behavior very well as discussed in section 6.1 (model validation) of this report. This is further supported by the numerical examples described in sections 6.2 through 6.5.
2. Optimal die velocity profiles may be used to control the strain rate in the workpiece, as well as reduce the temperature gradient and temperature range for any given forging process. Typically 5 % to 10 % reduction in temperature gradient was observed. At the same time, the temperature range reduction varied from 15 % to 20 % for the examples considered in this work.
4. Optimizing the initial die temperature directly influences the die-workpiece boundary temperature and reduces the temperature range in the billet. For the numerical examples considered in this work the temperature range was typically reduced by about 15 % due to the optimal design and/or selection of the initial die temperature.
5. In some cases, additional benefits such as a reduction in die loads and process time were also observed. Depending on the processing conditions chosen, the process time was reduced by upto 25 % in some cases, while the die load in most examples was reduced by 15 % to 20 %.

Among the model reduction methods studied, the balanced model reduction (BMR) method was found to be the most effective in representing metal forming processes. In future, other order reduction methods also need to be explored for this purpose. Some of the issues that require further investigation are:

- i. Issues pertaining to the stability and performance robustness of the metal forming system.
- ii. Extending this design procedure to suit on-line control applications.
- iii. Extending this methodology and making it applicable to other unit forming processes.
- iv Integrating preform shape design and staging criteria with the process control concepts developed in this work.

CHAPTER 11

References

1. Lahoti, G. D., and Altan, T., "Research to develop process models for producing a dual property Titanium alloy compressor disk," *AFMAL-TR-79-4156*, Wright Patterson Air Force Base, Dayton, Ohio, 1979.
2. Devadas, C., Samarasekera I. V., and Hawbolt E. B., "The thermal and metallurgical state of steel strip during hot rolling: Part III, Microstructural Evolution," *Metallurgical Transactions*, Vol. 22A, Feb 1991, pp. 335-348.
3. Sastry, S. M. L., Lederich, R. J., Mackay, T. L., and Kerr, W. R., "Generalized relations between metallurgical and process parameters for superplastic forming of Titanium alloy," *Experimetal Verification of Process Models*, American Society for Metals, 1983, pp. 70-93.
4. Dadras, P., and Thomas, J. F. JR., "Characterization and modeling for forging deformation of Ti-6Al-2Sn-4Zr-2Mo-0.1Si," *Metallurgical Transactions*, Vol. 12A, Nov 1981, pp. 1867-1875.
5. Cohen, R. E., and Durham, D. R., "Microstructure as a criterion for the selection of hot working process parameters for plain medium carbon steel," *Journal of Materials and Technology*, Vol. 112, 1990, pp. 90-94.

6. Seetharaman, V., Malas, J. C., and Lombard, C. M., "Hot extrusion of a Ti-Al-Nb-Mn alloy," *Materials Research Society Proceedings*, Vol. 213, 1991, pp. 889-891.
7. Prasad, Y. V. R. K., Gegel, H. C., Doraivelu, S. M., Malas, J. C., Morgan, J. T., Lark, K. A., and Barker, D. R., "Modeling of dynamic material behaviour in hot deformation forging of Ti-6242," *Metallurgical Transactions*, Vol. 15A, Oct 1984.
8. Biswas, S. K., and Rooks, B. W., "Application of modular approach to estimate load and energy in closed die forging," *Proc. 13th International Machine Tool Design and Research Conference*, 1973, pp. 445-453.
9. Lui, S. W., and Das, M. K., "Interactive design of axisymmetric forging dies using a desk top computer," *Journal of Mechanical Working Technology*, Vol. 5, 1981, pp. 88-103.
10. Altan, T., Lahoti, G. D., and Nagpal V., "Application of process modeling in massive forming process, Process Modeling Tools," *ASM Material & Process Congress Proceedings*, 1980, pp. 77-99.
11. Shahaf M., Bercovier, M., Guez, D., and Blades, I., "Interactive simulation of a forging process for blades," *Numerical Methods in Industrial Forming Process*, 1982, pp. 343-350.
12. Kudo, H., "Some analytical and experimental studies of axisymmetric cold forging and extrusion-I," *Int. J. Mech. Sci.*, Vol. 2, 1960, pp. 102.

13. Kudo, H., "Some analytical and experimental studies of axisymmetric cold forging and extrusion-II," *Int. J. Mech. Sci.*, Vol. 3, 1960, pp. 91.
14. Nagpal, V., "General kinematically admissible velocity fields for some axisymmetric and metal forming problems," *ASME Trans., Journal of Engineering for Industry*, Nov 1974, pp. 1197-1201.
15. McDermott, R. P., and Bramley, A. N., "An elemental upper-bound technique for general use in forging analysis," *Proc. 15th M. T. D. R. Conference*, 1974, pp. 437.
16. Oh, S. I., and Kobayashi, S., "An approximate method for a three dimensional analysis of rolling," *Int. J. Mech. Sci.*, Vol. 17, 1975, pp. 293.
17. Juneja, B. L., "Forging of polygonal discs with barrelling," *Int. J. Machine Tool Des. Res.*, Vol. 13, 1973, pp. 87.
18. Yang, D. Y., and Lee, C. H., "Analysis of three-dimensional extrusion of sections through curved dies by conformal transformation," *Int. J. Mech. Sci.*, Vol. 20, 1978, pp. 111.
19. Kudo, H., "Upper bound approach to metal forming processes - To date and future," *Metal Forming and Impact Mechanics*, edited by Reid, S. R., Pergamon Press, Oxford, pp. 19.
20. Zienkiewicz, O. C., and Godbole, P. N., "Flow of plastic and viscoplastic solids, with special reference to extrusion and forming process," *Int. J. Num. Meth. Engg.*, Vol. 8, 1974, pp. 3-16.

21. Zienkiewicz, O. C., Jain, P. C., and Onak, E., "Flow of solids during forming and extrusion: Some aspects of numerical solutions," *Int. J. Solids and Structures*, Vol. 14, 1978, pp. 15-38.
22. Lee, C. H., and Kobayashi, S., "New solutions to rigid plastic deformation problems using a matrix method," *Trans. ASME, J. Engr. for Ind.*, Vol. 95, 1973, pp. 865-873.
23. Kobayashi, S., "Rigid plastic finite element analysis of axisymmetric metal forming process," *Numerical Modeling of Manufacturing Process*, ASME PVP-PB-025, 1977, pp. 49-68.
24. Oh, S. I., Rebelo, N., and Kobayashi, S., "Finite element formulation for the analysis of plastic deformation of rate-sensitive materials in metal forming," *Metal Forming Plasticity - IUTAM Symposium*, Tutzing, Germany, 1978, pp. 273-291.
25. Oh, S. I., Lahoti, G. D., and Altan, T., "Application of finite element method to industrial metal forming process," *Numerical Methods in Industrial Forming Process*, Pineridge Press Ltd., Swansea, U. K., 1982, pp. 145-153.
26. Oh, S. I., Lahoti, G. D., and Altan, T., "ALPID- A general purpose FEM program for metal forming," *Proceedings of NAMRC-IX*, May 1981, State College, Pennsylvania, pp. 83.
27. Kobayashi, S., Oh, S. I., and Altan, T., "Metal forming and the finite element method," Oxford University Press, 1989.

28. Duggirala, R., "Design of forging dies for forming flashless ring gear blanks using finite element methods," *J. Materials Shaping Technology*, Vol. 7, No. 1, 1989, pp. 33-47.
29. Dexter, R. J., Chan, K. S., and Couts, W. H., "Elastic-viscoplastic finite element analysis of a forging die," *Int. J. Mech. Sci.*, Vol. 33, No. 8, pp. 659-674.
30. Haque, I., Jackson, J. E. Jr., Gangjee, T., and Raikar A., "Empirical and finite element approaches to forging die design: A state of the art survey," *J. Materials Shaping Technology*, Vol. 5, No. 1, 1987, pp. 23-33.
31. Wu, W. T., and Oh, S. I., "ALPIDT: A general purpose FEM code for simulation of nonisothermal forming processes," Proc. NAMRXC XIII Conference, Berkeley, California, 1985.
32. Oh, S. I., Park, J. J., Kobayashi, S., and Altan, T., "Application of FEM modeling to simulate metal flow in forging a Titanium alloy engine disk," *Trans. ASME, J. Engr. Ind.*, Vol. 105, 1983, pp. 251.
33. Zienkiewicz, O. C., Onate, E., and Heinrich, J. C., "Plastic flow in forming, I. Coupled thermal behavior in extrusion. II. Thin sheet forming," *Applications of Numerical Methods to Forming Processes*, ASME, AMD, Vol. 28, 1978, pp. 107.
34. Tang, M. C., and Kobayashi, S., "An investigation of the shell nosing process by the finite element method, Part 2: Nosing at elevated temperatures (Hot

nosing)," *J. of Engr. for Industry, Trans. ASME*, Vol. 104(3), 1982, pp. 312-318.

35. Argyris, J. H., and Doltsins, J. Sr., "On the natural formulation and analysis of large deformation coupled thermal mechanical problems," *Comp. Meth. Appl. Mech. Eng.*, Vol. 25, 1981, pp. 195.
36. Boer, C. R., Rydstad, H., and Schroder, G., "Choosing optimal forging conditions in isothermal and hot-die forging," *J. Applied Metalworking*, Vol. 3, No. 4, 1985, pp. 421-431.
37. Lanka, S., Srinivasan, R., and Grandhi, R. V., "A design approach for intermediate die shapes in plane strain forging," *J. Mater. Shaping Technol.*, Sept 1991, pp. 193-206.
38. Malas, J. C., "A thermodynamic and continuum approach to the design and control of precision forging processes," M. S. Thesis, Wright State University, Dayton, Ohio, 1985.
39. Hong, B. S., "Numerical simulation of stability control in sheet metal forming," M. S. Thesis, Massachusetts Institute of Technology, Cambridge, Massachusetts, 1990.
40. Park, J. J., Rebelo, N., Kobayashi, S., "A new approach to preform design in metal forming with the finite element method," *Int. J. Machine Tool Des. Res.*, Vol. 23, 1983, pp. 71.

41. Han, S. C., Grandhi, R. V., and Srinivasan, R., "Optimum design of forging die shapes using nonlinear finite element analysis," *AIAA Journal*, Vol. 31, 1993, pp. 774-781.
42. Grandhi, R. V., Kumar, A., Chaudhary, A., and Malas, J. C., "State space representation and optimal control of nonlinear material deformation using the finite element method," *Int. J. Num. Meth. Engg.*, Vol. 36, 1993, pp. 1967-1986.
43. Balas, M. J., "Trends in large space structure control theory: Fondest hopes, wildest dreams," *IEEE Transactions on Automatic Control*, Vol. AC-27, No. 3, 1982, pp. 522-535.
44. Marshall, S. A., "An approximate method for reducing the order of a linear system," *Control Engineering*, Vol. 10, 1966, pp. 642-643.
45. Akoi, M., "Control of large-scale systems by aggregation," *IEEE Transactions on Automatic Control*, Vol. AC-13, 1968, pp. 246-253.
46. Akoi, M., "Some approximation methods for estimation and control of large scale systems," *IEEE Transactions on Automatic Control*, Vol. AC-23, No. 2, April 1978, pp. 173-182.
47. Rao, S. V., Ngo, K., Berg, J. L., and Das, A., "Derivation of reduced order models for large flexible structures," *AIAA Guidance, Navigation and Control Conference*, New Orleans, 1991, pp. 72-82.

48. Safonov, M. G., Chiang, R. Y., and Flashner, H., " H^∞ robust control synthesis for a large space structure," *American Control Conference*, Atlanta, Georgia, Vol. 3, 1988, pp. 2038-2045.
49. Ben Jaafar, M. T., Pasquetti, R. and Petit, D., "Model reduction for thermal diffusion: Application of the Eitelberg, Marshall and Aggregation methods to a heat transmission tube model," *International Journal for Numerical Methods in Engineering*, Vol. 29, 1990, pp. 599 - 617.
50. Wanxie, Z., Jiahao, L., and Chunhang, Q., "Computational structural mechanics and optimal control - The simulation of sub-structural chain theory to LQ optimal control problems," *International Journal for Numerical Methods in Engineering*, Vol. 33, No. 1, 1992, pp. 197-212.
51. Chang, C., and Engblom, J. J., "Nonlinear dynamical response of impulsively loaded structure - A reduced basis approach," *AIAA Journal*, Vol. 29, No. 4, 1991, pp. 613-618.
52. Gregory, C. Z. Jr., "Reduction of large flexible spacecraft models using internal balancing theory," *AIAA Journal of Guidance, Control and Dynamics*, Vol. 7, No. 6, 1984, pp. 725-732.
53. Yae, K. H., Inman, J. D., "Flexible-body dynamics modeling with a reduced-order model," *Advances in Design Automation*, Edited by B. Ravani, ASME, DE-Vol. 23-2, 1990, pp. 87-91.

54. Adams, R. J., Buffington, J. M., Sparks, A. G., and Banda, S. S., "An introduction to multivariable flight control system design," Report No. WL-TR-93-3110, Wright Patterson Air Force Base, Dayton, Ohio, 1992.

55. Mahmoud, M. S., Hassan, M. F., and Darwish, M. G., Large-scale control systems, Marcel Dekker Inc., 1985.

56. Mahmoud, M. S., and Singh, M. G., Large scale systems Modeling, Pergamon Press, 1981.

57. Pernebo, L., and Silverman, L. M., "Model reduction via balanced state space representations," *IEEE Transaction on Automatic Control*, Vol. AC-27, April 1982, pp. 382-387.

58. "MME-ALPID User's Manual," UES, Inc., Processing Science Division, Dayton, Ohio.

59. Boer, C. R., Rebelo, N., Rydstad, H., and Schroder, G., "Process modeling of metal forming and thermomechanical treatment," Springer-Verlag, 1986, pp. 192.

60. Anderson, B. D., and Moore, J. B., "Optimal Control - Linear Quadratic Methods," Prentice Hall, 1990.

61. Davison, E. J., and Goldberg, A., "Robust control of a general servomechanism problem: The servo compensator," *Automatica*, Vol. 11, 1975, pp. 461-471.

62. Meng, X., "Modern Control Theory II," Beijing University of Aeronautics and Astronautics Press, Beijing, 1984.

63. Van Loan, C., "Computing integrals involving the matrix exponential," *IEEE Trans. on Automat. Control* Vol. AC-23, No.3, June 1978, pp. 395-404.

64. Kirk, D., "Theory of optimal control: An introduction," Prentice-Hall, 1970, pp. 221.

65. Skelton, R. E., *Dynamic Systems Control*, Published by John Wiley & Sons Inc., 1988.

66. Kumar, A., Grandhi, R. V., Chaudhary, A., and Irwin, D., "Modeling and design of control parameters in metal forming processes", *Transactions, Canadian Society of Mechanical Engineers*, Vol. 17, No. 4A, 1993, 613-631.

67. Cheng, H., Grandhi, R. V., and Malas, J. C., "Design of optimal process parameters for non-isothermal forging", *International Journal for Numerical Methods in Engineering*, Vol. 37, 1994, pp. 155-177.

68. Moore, B. C., "Principal component analysis in linear systems: Controllability, observability, and model reduction", *IEEE Transactions on Automatic Control*, Vol. AC-26, No. 1, Feb 1981, pp. 17-31.

69. Bryson, E. A. Jr., and Ho, Y., *Applied optimal control: Optimization, estimation and Control*, Blaisdell Publishing Company, 1969, pp. 148-149.

70. Duggirala, R., "Using finite element method in metal forming process," *Journal of Metals*, Vol. 42, No. 2, 1990, pp. 24-27.

71. Duggirala, R. and Badawy, A., "Finite element method approach to forging process design," *Journal of Materials Shaping Technology*, Vol. 6, No. 2, 1988, pp. 81-89.

72. Howson, T. E., Delgado, H. E., "Computer modeling metal flow in forging," *Journal of Metals*, Vol. 41, No. 2, 1989, pp. 32-34.

73. Grandhi, R. V., Modukuru, S. C., and Malas, J. C., " Integrated strength and manufacturing process design using shape optimization approach," *Trans. of ASME, Journal of Mechanical Design*, Vol. 115, Mar 1993, pp. 125-131.

74. Surdon, C. and Chenot, J. L., "Finite element calculation of three dimensional hot forging," *International J. for Numerical Methods in Engineering*, Vol. 24, No. 8, 1987, pp. 2107-2117.

75. Zienkiewicz, O. C., Huang, G. C. and Liu, Y. C., "Adaptive FEM computation of forming processes - Application to porous and non-porous materials," *International Journal for Numerical Methods in Engineering*, Vol. 30, No. 8, 1990, pp. 1527-1553.

76. Shabaik, A. H., "Analysis of forming processes: Experimental and numerical methods," *Journal of Materials Processing Technology*, Vol. 24, 1990, pp. 15-25.

77. Heinstein, H. W., and Yang, H. T. Y., "Plane strain finite element simulation of shear band formation during metal forming," *International Journal for Numerical Methods in Engineering*, Vol. 33, No. 1, 1992, pp. 719-737.

78. Hardt, D. E. and Lee, G. Y., "Closed-loop control of sheet metal stability during stamping," *Proceedings NAMRC-XIII*, Berkeley, CA, 1985, pp. 315-322.

79. Kim, S. and Stelson, K. A., "Finite element method for the analysis of a material property identification algorithm for pressbrake bending," *Transactions of ASME, Journal of Engineering for Industry*, Vol. 110, 1988, pp. 219-222.

80. Frangomeni, J. M., Hilbery, B. M., Sanders, T. H., and Gaitatzes, A. G., "Integration of microstructural development and properties design into the CAD/CAM environment," *Microstructural Development and Control in Materials Processing*, Edited by Durham, D. R. and Saigal, A., Vol. 14, 1989, pp. 1-9.

81. Larrabee, G. D. and Stelson, K. A., "Digital image shape measurement for the monitoring and control of non-homogeneous axisymmetric plastic deformation," *American Control Conference*, Minneapolis, Minnesota, Vol. 2, 1988, pp. 729-734.

82. Malas, J. C., and Seetharaman, V., "Using material behavior models to develop process control strategies," *Journal of Metals*, Vol. 44, No. 6, 1992, pp. 8-13.

83. Chen, H. L., Lehnhoff, T. F. and Dorivalu, S. M., "A stress ratio parameter for studying the workability of metals - Tension and Compression", *Journal of Material Shaping Technology*, Vol. 8, No. 2, 1990), pp. 111 - 122.

84. Prasad, Y. V. R. K., Gegel, H. L., Doraivelu, S. M., Malas, J. C., Morgan, J. T., Lark, K. A., et al., "Modeling of dynamic material behavior in hot deformation: Forging of Ti6242", *Metallurgical Transactions A*, Vol. 15, 1984, pp. 1883 - 1892.

85. Gegel, H. L., "Synthesis of atomistics and continuum modeling to describe microstructure", *Computer Simulations in Material Science*, ed. Arsenault, R. J., Beeler, J. R., and Easterling, D. M., *ASM*, 1987, pp. 291 - 344.

Appendix A - Project Overview

Metal forming processes generally involve the plastic deformation of a material having a relatively simple geometry into a product of relatively complex configuration in one or more operations. In metal forming technology, proper design and control of the process requires, among other things, the determination of the deformation mechanics involved in the process. For example, in a forming process such as forging, the properties, quality, and integrity of the final product are determined by factors such as workpiece/die geometry, material properties, frictional conditions, ram velocity schedule, and die/billet temperature profiles. Without the knowledge of the influence of these variables on the process mechanics it would not be possible to design the dies and equipment adequately, and/or predict and prevent the occurrence of defects.

The entire design process is depicted in Fig. A1. In this flowchart, the highlighted box shows the control methodology developed and presented in this report. Using this methodology, optimal ram velocity profiles and initial die temperatures may be designed for any generic forming process, with constraints on elemental strain rates and nodal temperatures within the deforming workpiece. The exact design procedure is described in detail elsewhere in this report. Fig. A2 briefly describes the design procedure by means of a flow diagram and also indicates the chapter (of this report) in which each of the design procedures is elaborated upon.

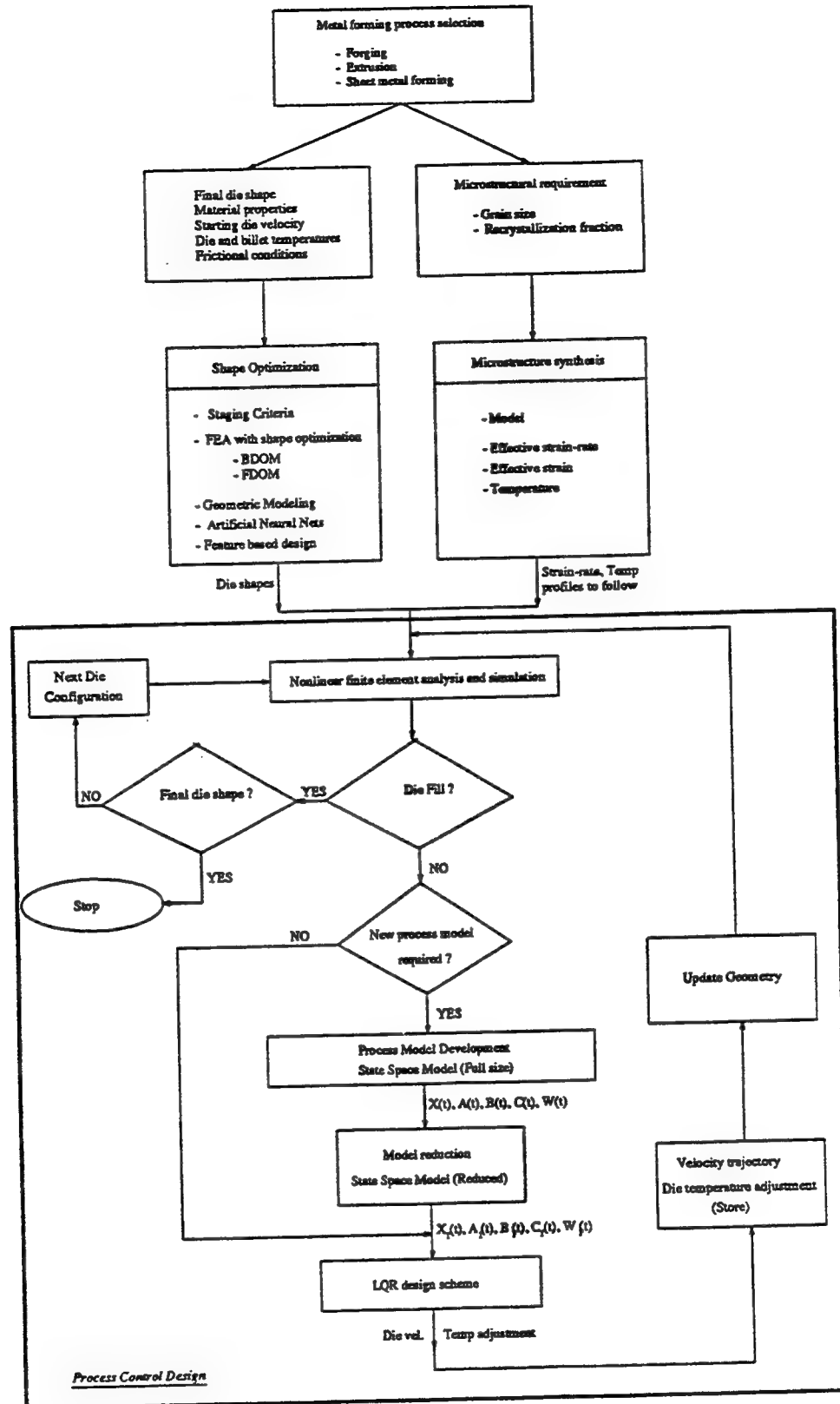


Fig A1. Process control of metal forming operations - Project overview

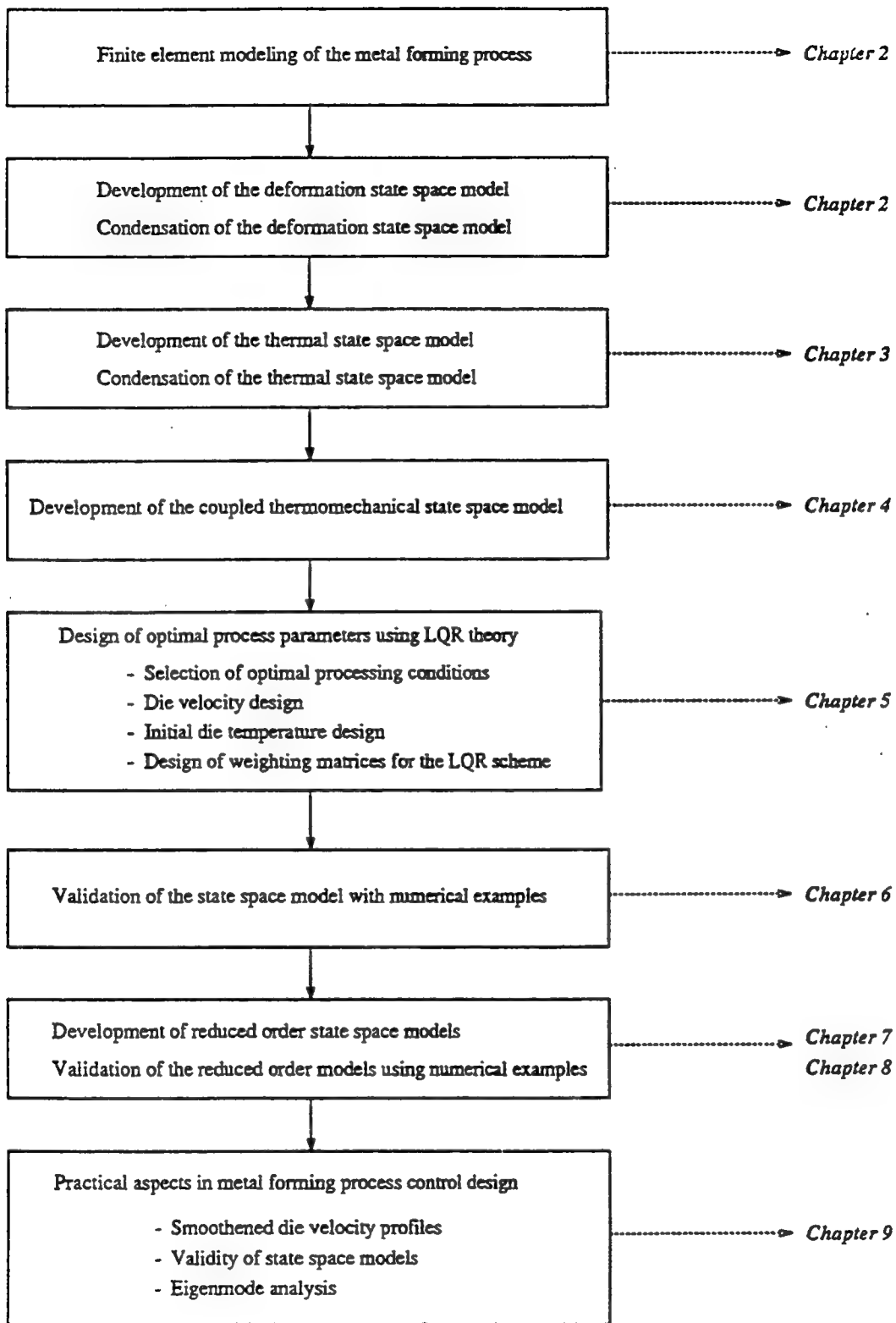


Fig A.2. Description and organization of the metal forming process control work

Appendix B - User's Manual for COPP

A general purpose program COPP (Control of Optimal Processing Parameters) has been developed for designing optimal die velocities and initial die temperature for forging processes. This program has been coded using FORTRAN 77, and uses ALPID (Analysis of Large Plastic Incremental Deformation) subroutines for finite element simulation and analysis. A control module has been integrated into the program for implementing the optimal design strategy described in chapter 2. Because the control module uses IMSL subroutines during the design process, access to IMSL subroutines is necessary while linking this program. This program runs on VAX systems because ALPID makes use of some VAX system commands during the simulation. General exposure to ALPID and its postprocessor (FEMGRA) are required for using this program.

COPP can be used with both isothermal and nonisothermal forgings. For isothermal forging operations COPP requires an ALPID deformation input file, and for nonisothermal forgings it requires both ALPID deformation and temperature input files. For more information regarding the ALPID input files the reader is referred to the ALPID user's manual [43]. In addition to these files COPP also requires a small input data file called 'control.dat', which has information regarding the design requirements and element(s)/node(s) to be controlled. After the program is run, it creates an output file called 'output.dat' which contains the designed (optimal) velocity, strain rate of the 'control' element, initial die temperature adjustment, and other relevant information. This manual presents

the format for the input/output files and also contains a few sample data files for the reader's reference.

General format for the input file 'control.dat'

ISO
ICNTL
NUMD, IDDIE, IDPICK, NUMELE
VDOT, SMAX
NUME, NUMVI
NELMZ(NUME)
EPSLMT(NUME)
NPVI(NUMVI)
NUMT
NTEMP(NUMT)
GT(NUMT)
COEF(4,NUMDIE)

Note:

The variables with parentheses are arrays, and the quantity within the parentheses gives the size of the array(s).

Description of the input variables

ISO : 0–Isothermal process, 1–Nonisothermal process

ICNTL : 0–Simulation only (No design required)
1–Optimal design required
(This means die velocity and/or initial die temperature need to be designed)

NUMD : Number of control input(s)
1–Only die velocity (or initial die temperature) needs to be designed
2–Both die velocity and initial die temperature need to be designed

IDDIE : Number of dies requiring initial die temperature design

IDPICK : 0–User selects the ‘element of interest’ and/or ‘critical node’
1–User selects the ‘critical node’ and the program selects the ‘element of interest’
(The program normally picks the non-perimeter element having the largest strain rate in the billet as the ‘element of interest’)
2–User selects the ‘element of interest’ and the program selects the ‘critical node’
(The program normally picks the node having the lowest temperature in the billet as the ‘critical node’)
3–Program selects the ‘element of interest’ and ‘critical node’

NUMELE : Number of elements used to discretize the billet

VDOT : Machine’s maximum acceleration capability
(This restricts the amount by which the die velocity can change in a given time step)

SMAX : Stroke at which the simulation is to be stopped

NUME : Number of ‘elements of interest’

NUMVI : Number of nodes constituting the 'element(s) of interest'
(If NUME is 1, NUMVI would be 4, for a four-noded quadrilateral element)

NELMZ : The element numbers of the elements of interest separated by commas
(Maximum of NUME sets)

EPSLMT : The desired effective strain rate values for the (corresponding) 'elements of interest' separated by commas (Maximum of NUME columns)

NPVI : The node numbers constituting the 'element(s) of interest'
(separated by commas up to NUMVI columns)
(Note: The node numbers for any element have to be in the ccw direction)

NUMT : Number of critical nodal temperatures to be controlled

NTEMP : The node numbers of the 'critical' nodes,
(separated by commas up to NUMT columns)

GT : Desired temperature gradient reduction(s) (≤ 0.03)
(separated by commas up to NUMT columns)

COEF : Coefficients of the desired temperature profile
(4 coefficients are needed for a 3rd order polynomial. These have to be specified in sequence starting with the constant term)

Note:

1. In the above nomenclature 'element of interest' refers to the element whose strain rate is being controlled (or needs to be controlled). Perimeter elements

are generally not picked as 'elements of interest'. Also, 'critical node' refers to the die-contacting boundary node whose temperature is being tracked (or needs to be tracked). The present version of the program can have, at most, one 'element of interest' and one 'critical node' during the design process.

2. If ISO=0,

All temperature related inputs may be omitted.

3. If ICNTL=0,

EPSLMT, GT may be omitted.

4. If IDDIE=0,

COEF may be omitted.

5. If IDPICK=1 or 3,

NUME, NUMVI, NELMZ, NPVI may be omitted.

6. If IDPICK=2 or 3,

NUMT, NTEMP may be omitted.

Sample data file: Isothermal case

(Die velocity design only)

```
ISO
0

ICNTL
1

NUMD,      IDDIE, IDPICK, NUMELE
1,          0,      0,      50

VDOT,      SMAX
15,        0.5

NUME,      NUMVI
1,          4

NELMZ(NUME)
23

EPSLMT(NUME)
0.5

NPVI(NUMVI)
27,28,33,34
```

In the above input file, element 23 has been specified as the 'element of interest', and it's strain rate must be maintained at 0.5 1/sec. Refer section 6.3 for more information regarding the design of die velocities for isothermal forging processes.

Sample output file ('output.dat'): Isothermal case

(Die velocity design for 5 simulation steps)

* PROCESS PARAMETERS *

ST*100	T*10	VRAM	EPS	23	EPS	0	EPS	0	EPS	0	EPS	0
0.100	0.0100	1.0000	0.49341	0.00000	0.00000	0.00000	0.00000	0.00000	0.00000	0.00000	0.00000	
0.200	0.0200	1.0000	0.46508	0.00000	0.00000	0.00000	0.00000	0.00000	0.00000	0.00000	0.00000	
0.549	0.0533	1.0481	0.49065	0.00000	0.00000	0.00000	0.00000	0.00000	0.00000	0.00000	0.00000	
0.916	0.0883	1.0481	0.48903	0.00000	0.00000	0.00000	0.00000	0.00000	0.00000	0.00000	0.00000	
1.300	0.1232	1.1005	0.51541	0.00000	0.00000	0.00000	0.00000	0.00000	0.00000	0.00000	0.00000	

In the above output file, the first column gives the stroke (ST), the second column gives the time (T), and the third column gives the optimal die velocity (VRAM) corresponding to that stroke or time. It may be noted that the stroke and time have been multiplied by suitable scaling factors for convenience. The fourth column in the output file gives the strain rate of element 23, which was specified as the 'control element' in the input data file. It is also observed that the strain rate of this element is maintained more or less at 0.5 1/sec as specified by the design requirement. The last four columns in the output file are meant for the strain rates of other 'control elements'. But, at present these columns do not have any significance because the program (COPP) is capable of having only one 'control' element at any given time.

Sample data file: Non-isothermal case

(Die velocity design only)

```
ISO
1

ICNTL
1

NUMD,      IDDIE, IDPICK, NUMELE
1,          0,      0,      50

VDOT,      SMAX
15,        0.5

NUME,      NUMVI
1,          4

NELMZ(NUME)
23

EPSLMT(NUME)
0.7

NPVI(NUMVI)
27,28,33,34

NUMT
1

NTEMP(NUMT)
18

GT(NUMT)
0.01
```

In the above input file, element 23 is specified as the 'control' element, and node 18 is specified as the 'critical' node. Also, it is required to maintain the strain rate of element 23 at 0.7 1/sec, and reduce the (nodal) temperature gradient of node 18 by 1 % at every time step. Refer sections 6.2 and 6.4 for more information regarding the design of die velocities for nonisothermal forging processes.

Sample output file ('output.dat'): Non-isothermal case

(Die velocity for 5 simulation steps)

* PROCESS PARAMETERS *

	ST*100	T*10	VRAM	EPS 23	EPS 0	EPS 0	EPS 0	EPS 0	TEMP 18	TEMP 0	TEMP 0	TEMP 0	TEMP 0
	0.100	0.0100	1.0000	0.50017	0.00000	0.00000	0.00000	0.00000	1734.34	0.00	0.00	0.00	0.00
0.00	0.00	0.00											
	0.200	0.0200	1.0000	0.48265	0.00000	0.00000	0.00000	0.00000	1733.68	0.00	0.00	0.00	0.00
0.00	0.00	0.00											
	0.540	0.0533	1.0193	0.49242	0.00000	0.00000	0.00000	0.00000	1731.50	0.00	0.00	0.00	0.00
0.00	0.00	0.00											
	0.896	0.0873	1.0495	0.50697	0.00000	0.00000	0.00000	0.00000	1729.28	0.00	0.00	0.00	0.00
0.00	0.00	0.00											
	1.277	0.1223	1.0895	0.52627	0.00000	0.00000	0.00000	0.00000	1727.02	0.00	0.00	0.00	0.00
0.00	0.00	0.00											

The output file shown above has 14 columns. The first two columns contain the stroke (ST) and time (T), respectively. The third column gives the optimal ram velocity (VRAM) for the process, and the fourth column contains the strain rate of element 23 ('control element') due to the designed velocity schedule. Column 9 give temperature of node 18 ('critical node) at every time step of the simulation. The columns containing zeros are not relevant at this stage and may be ignored.

Sample data file: Non-isothermal case

(Die velocity design & initial die temperature design)

```
ISO
1

ICNTL
1

NUMD,          IDDIE, IDPICK, NUMELE
2,            1,      0,      50

VDOT,          SMAX
15,           0.5

NUME,          NUMVI
1,            4

NELMZ(NUME)
23

EPSLMT(NUME)
0.7

NPVI(NUMVI)
27,28,33,34

NUMT
1

NTEMP(NUMT)
18

GT(NUMT)
0.01

COEF(4,NUMDIE)
1735,-550,355,-25
```

The above input file is similar to the one shown earlier for nonisothermal die velocity design. But here, in addition to die velocity, it is specified that initial die temperature also needs to be designed. In this case there are two control inputs (instead of one, as in the previous case), namely the die velocity and the initial

die temperature adjustment. Here again, element 23 and node 18 are specified as the 'control' element and 'critical' node, respectively. The design requirements are to maintain a strain rate of 0.7 1/ sec in element 23, and reduce the temperature gradient at node 18 by 1% at every simulation time step. The last line in the data file gives the coefficients of a third order polynomial (in sequence) starting with the coefficient of the constant term. This polynomial specifies the temperature trajectory to be tracked by node 18 in order to meet the design goals. The reader is referred to section 6.5 of this report for more details on the initial die temperature design procedure.

Sample output file ('output.dat'): Non-isothermal case

(Die velocity & initial die temperature design for 5 simulation steps)

```
*****
*      PROCESS PARAMETERS      *
*****
ST*100    T*10    DIE-TEMP+
0.100    0.0100   0.00   0.00
0.200    0.0200   0.00   0.00
0.550    0.0533   304.58  0.00
0.936    0.0883   182.50  0.00
1.382    0.1251   179.66  0.00
```

In the output file shown above, the first column gives the stroke (ST), and the second column gives the time (T). The third column gives the initial die temperature adjustment value. The average of the initial die temperature adjustments for all the time steps, needs to be added to the original initial die temperature, to get the optimal initial die temperature. In addition to designing the initial die temperature, die velocity design is also done in this example. The reader is referred to section 5.2 and section 6.5 for further information on initial die temperature design.

Appendix C - User's Manual for Reduced Order Models

The reduced order state space models described earlier are obtained using the BMR (Balanced Model Reduction) method. A FORTRAN subroutine REDMOD has been developed for this purpose. The subroutine REDMOD takes in the full size state space matrices and returns the reduced order matrices. This subroutine has been integrated into the program COPP for designing optimal process parameters using reduced order state space models. The rest of the program including the control design strategy is similar to that used in COPP for the full-size state space models. The program with the capability to reduce the size of the state space system has been named MODRED (Model Reduction).

The following common blocks and subroutine call statements are needed to link the reduced order model routine (REDMOD) to the full state space model program.

C

C COMMON BLOCK FOR FULL STATE MODEL

C

COMMON /FULL/ AA(NN,NN),BB(NN),CC(NN,NN),WW(NN),NDD

COMMON /OPTL/ VGOOD(5),B(MS,5),NUMDX

COMMON /CSYC/ CSYS(MS,MS),EBI(MS,MS)

COMMON /MORE/ IMRE

CALL REDMOD(IPQ)

SUBROUTINE REDMOD(IPQ)

C

C COMMON BLOCK FOR FULL STATE MODEL

C

COMMON /FULL/ AA(NN,NN),BB(NN),CC(NN,NN),WW(NN),NDD

COMMON /OPTL/ VGOOD(5),B(MS,5),NUMDX

a. In the common block FULL (added in the control subroutine),

AA : A copy of the Plant matrix.

BB : A copy of the Input matrix.

CC : A copy of the Output matrix.

WW : A copy of the Constant perturbation term in the system.

NN : Maximum allowable size of the full system.

NDD : Number of rows in the **C** matrix (This depends on the number of outputs).

b. In the common block CSYC (added in the control subroutine),

CSYS : The reduced model of the output matrix is written in this array.

EBI : Array to store the inverse of the transformation matrix used in the balanced representation.

c. In the common block **OPTL** (added to the control subroutine),

VGOOD : Vector to store the designed process parameter(s).

B : Reduced order model of the input matrix is stored in this array.

NUDX : Number of design variables.

d. In the common block **MORE** (added to the control subroutine),

IMRE : If **IMRE** = 1, model reduction is performed. Otherwise, model reduction is not performed.

e. From the CALL statement,

IPQ : Goes in to the subroutine MODRED as the size of the full state model and returns as the size of the reduced model.

NOTE : – After the call statement for generating the reduced order models, the full state vector and the input matrix need to be multiplied with the inverse of the transformation matrix **EBI**.

The data files required for running MODRED are the same as those used for COPP. The only difference in this case is that the file 'control.dat' has an additional input variable called **IMRE** appended at the end of the data file. This

variable acts as a switch to turn the model reduction capability 'on' (IMRE = 1) or 'off' (IMRE = 0). The output of this program ('output.dat') is also the same as in the case of COPP (Appendix B).